Università degli Studi di Roma
“La Sapienza”

Effects of induced structural modifications in manganites and related compounds: the Jahn-Teller distortion of MnO_6 octahedra

Thesis submitted for the degree of
“Doctor Philosophiæ” in Physics
October 2004

Candidate
Andrea Sacchetti

Supervisor
Prof. Paolo Postorino

Coordinator
Prof. Valeria Ferrari

Strain experiments in 55 B.C.

Contents

Introduction

In recent years remarkable experimental and theoretical efforts have been devoted to the study of hole-doped rare-earth pseudocubic manganites ($Re_{1-x}Ae_x\mathrm{MnO}_3$, Re=trivalent rare-earth and Ae=divalent alkali-earth) exhibiting colossal magneto-resistance (CMR). This property, namely a pronounced dependence of the resistivity on applied magnetic field, promises important applications in the fields of magnetic sensors and memories. Besides the potential technical applications, the interest in these compounds is brought about by the complex and intriguing physics which determines their properties. Indeed, strong coupling among lattice, electronic, and spin degrees of freedom has to be accounted for to understand the microscopic origin of the peculiar transport properties. Therefore, manganites provide a natural "laboratory" for studying fundamental condensed-matter physics. A large number of pseudocubic manganites in the CMR doping region ($0.2 \lesssim x \lesssim 0.5$) undergo a transition from a high-temperature paramagnetic insulating phase to a low-temperature ferromagnetic metallic one at $T = T_C = T_{IM} = 150 - 370$ K. It is well established that the transition and the transport properties of manganites are determined by the competition between the charge-delocalizing double-exchange mechanism and the localizing electron-phonon coupling (EPC) triggered by the Jahn-Teller (JT) distortion of the MnO_6 octahedral units, which compose the structure of pseudocubic manganites.

Hydrostatic pressure is a powerful tool for tuning the JT distortion in manganites. In fact the lattice contraction forces symmetrization of the octahedra reducing the JT distortion and thus the EPC. A similar effect is observed when the radius r_A of the ion occupying the rare-earth site is increased (internal chemical pressure). Pressure data on manganites are in large part limited to the low pressure range (0-2 GPa) and from these data the equivalence between hydrostatic pressure and chemical pressure has been claimed. The investigation of manganites in the high-pressure regime ($P > 2$ GPa), exploiting diamond anvil cells, started in 2000 when our group established a research activity on this subject, which the present Ph.D. thesis is part of. The first results, obtained by means of Raman and infrared spectroscopy, showed an anomalous behavior of the JT phonon in $La_{0.75}Ca_{0.25}MnO_3$ and saturation of the pressure-induced charge delocalization in the high-pressure regime suggesting the absence of any pressure-induced IM transition up to 14 GPa. Since the aforementioned $P - r_A$ equivalence predicts a pressure-induced IM transition at around 5-6 GPa, the high-pressure data questioned the validity of this equivalence in the high-pressure regime.

The present Ph.D. thesis aims at addressing the questions left open by the existing studies, exploiting the high-pressure technique to deeply investigate the link between electronic and vibrational properties with focusing on the role of JT distortions on the physical properties of manganites and related materials. The study has been carried out mainly by means of Raman and infrared spectroscopies and X-ray diffraction. Raman spectroscopy is an important technique to measure the MnO_6 octahedron phonon-spectrum and it can provide direct information on the JT effect. On the other hand, infrared spectroscopy is sensitive to the charge delocalization process and, in particular, temperature dependent infrared measurements provide good estimates of the metal-insulator transition temperature T_{IM}. The capability of obtaining these data is very important in the study of manganites since high-pressure conductivity measurements are still in a pioneeristic phase and might provide questionable results.

In order to obtain detailed information on the JT effect in manganites, four different ways of inducing structural deformations in bulk and film samples were applied in the present study, namely:

1. Hydrostatic pressure (almost isotropic compression).
2. Oxygen non-stoichiometry (modification of hole doping with negligible structural changes).
3. Substrate-film lattice mismatch (anisotropic compression).
4. Change of the MnO_6 octahedral arrangement (non-pseudocubic compounds with MnO_6 octahedra).

The above-discussed role of hydrostatic pressure in the study of manganites was extensively exploited in the present study (point 1). In particular, the high-pressure technique was applied to stoichiometric $La_{0.75}Ca_{0.25}MnO_3$ (LC25S) and $La_{0.80}Ca_{0.20}MnO_3$ (LC20S) and oxygen-deficient $La_{0.80}Ca_{0.20}MnO_{2.92}$ (LC20D) manganites (point 2). The variation of oxygen stoichiometry strongly modifies the number of charge carriers, although inducing negligible structural changes, thus representing an efficient tool for the disentanglement of the two effects induced by Ca-substitution, namely hole-doping and r_A modulation. In order to get a deeper insight in the anomalous high-pressure behavior observed in LC25S, high-pressure investigations of the JT effect and charge delocalization were carried out by means of Raman and infrared spectroscopy on LC25S, LC20S, and LC20D. High-pressure Raman measurements were carried out on LC20S and LC20D with the purpose of observing the doping effect on the pressure induced quenching of the JT distortion. In parallel, the high-pressure far-infrared absorption spectrum of three manganites (LC25S, LC20S, and LC20D) was investigated, for the first time, exploiting synchrotron radiation. With the aim to test the proposed absence of pressure-induced IM transition in LC25S, a temperature and pressure dependent infrared study was performed on this compound in order to obtain the $P-T$ phase diagram over a wide pressure range. A simple theoretical model was also developed for the description of the phase diagram.

Manganite thin-films (point 3) were also studied in order to investigate the effect of the anisotropic substrate-induced strain. Interest in manganites films is brought about by the fact that the large part of manganites potential applications are based on thin-films devices. The thickness dependence of the phonon spectrum was investigated down to 40 Å in order to get a comparison between the anisotropic substrate-induced strain and the isotropic pressure-induced one.

Finally $LiMn_2O_4$ (LMO) spinel and hexagonal $SrMnO_3$ (SMO) were also studied (point 4). In analogy with manganites, these two compounds contain MnO_6 octahedra but their is structure is not pseudocubic. It is worth to note that in pseudocubic manganites the octahedra are all corner-sharing whereas LMO and SMO contain edge- and face-sharing octahedra respectively. Besides the possible comparison with pseudocubic manganites, these two compounds are interesting on their own. In fact, Li-spinels like LMO have potential applications in rechargeable batteries technology whereas SMO is the end-member of a family of electron-doped $Sr_{1-x}Ce_xMnO_3$ manganites for which the fundamental physics has still to be understood in detail. High-pressure X-ray diffraction measurements on LMO, as well as Raman measurements on LMO and SMO were thus carried out. This study can represent a fruitful starting point for the development of a new research activity focused at Li-spinels and electron doped manganites.

The results of the present Ph.D. thesis definitively confirm the previously observed high-pressure anomalies and the proposed onset of an unpredicted localizing mechanism which competes with charge delocalization at high pressure. In particular, the $P-T$ phase diagram of LC25S has been determined up to 11 GPa and the absence of a room-temperature pressure-induced IM transition has been confirmed. The analysis of the phase diagram suggests the existence of a universal behavior of $T_{IM}(P)$ for a large class of manganites. Moreover, the theoretical model here developed for the description of the phase diagram suggests the antiferromagnetic coupling as a good candidate for the high-pressure localizing mechanism. The high-pressure far-infrared measurements represent an important technical achievement demonstrating the feasibility of this kind of challenging experiment and, from the physical point of view, qualitatively confirming the proposed universal behavior for $T_{IM}(P)$. The measurements on manganites thin films represent a good technical result and the comparison with high-pressure data suggests a somehow universal scaling for the strain effect in manganites. Finally, the study of related compounds provides an interesting comparison with pseudocubic manganites and opens new perspectives for future research projects.

The results of the present work have been the subject of the following publications:

R1 "Pressure-induced charge delocalization in manganites studied by means of infrared spectroscopy", P. Postorino, A. Congeduti, P. Dore, F.A. Gorelli, A. Nucara, A. Sacchetti, and L. Ulivi, *High Pressure Res.* **22**, 139 (2002).

R2 "Pressure tuning of the electron-phonon coupling: the insulator to metal transition in manganites", P. Postorino, A. Congeduti, P. Dore, A. Sacchetti, F.A. Gorelli, L. Ulivi, A. Kumar, and D.D. Sarma, *Phys. Rev. Lett.* **91**, 175501 (2003).

R3 "Pressure and temperature dependence of optical phonons in $La_{0.75}Ca_{0.25}MnO_3$", A. Sacchetti, P. Dore, P. Postorino, and A. Congeduti, *J. Phys. Chem. Solids* **65**, 1431 (2004).

R4 "Microraman spectroscopy on $LiMn_2O_4$: warnings on laser-induced thermal decomposition", A. Paolone, A. Sacchetti, T. Corridoni, P. Postorino, R. Cantelli, G. Rousse, and C. Masquelier, *Solid State Ionics* **170**, 135 (2004).

R5 "Study of the infrared phonons in the $La_{0.7}Sr_{0.3}MnO_3$ manganite by means of reflectance measurements on epitaxial thin films ", P. Dore, A. Funaro, A. Sacchetti, M. Angeloni, and G. Balestrino, *Eur. Phys. J. B* **37**, 339 (2004).

R6 "High-pressure far-infrared measurements at SINBAD", M. Cestelli Guidi, A. Nucara, P. Calvani, P. Postorino, A. Sacchetti, A. Congeduti, M. Piccinini, A. Marcelli, and E. Burattini, *Infrared Phys. Techn.* **45**, 365 (2004).

R7 "Competitive effects on the high-pressure phase diagram of manganites", P. Postorino, A. Sacchetti, M. Capone, and P. Dore, *Phys. Status Solidi B* **241**, 3381 (2004).

R8 "Stabilization of the orthorhombic phase of $LiMn_2O_4$ by means of high pressure", A. Paolone, A. Sacchetti, P. Postorino, R. Cantelli, A. Congeduti, G. Rousse, and C. Masquelier, *Solid State Ionics* **00**, 0000 (2004).

R9 "Far infrared synchrotron radiation spectroscopy of solids in normal and extreme conditions", M. Piccinini, M. Cestelli Guidi, A. Marcelli, P. Calvani, E. Burattini, A. Nucara, P. Postorino, A. Sacchetti, E. Arcangeletti, E. Sheregii, J. Polit, and A. Kisiel, *Phys. Status Solidi C* **00**, 0000 (2004).

R10 "Evidence of phase separation in the $P-T$ phase diagram of the $La_{0.75}Ca_{0.25}MnO_3$ manganite by infrared measurements", P. Dore, A. Sacchetti, P. Postorino, A. Congeduti, F.A. Gorelli, and L. Ulivi, *J. Supercond.* **00**, 0000 (2004).

R11 "Comment on Effect of chromium substitution on the lattice vibration of spinel lithium manganate: a new interpretation of the raman spectrum of $LiMn_2O_4$", A. Paolone, A. Sacchetti, R. Cantelli, and P. Postorino, submitted to *J. Phys. Chem. B.*

R12 "High-pressure phase diagram of manganites: a two-site model study", A. Sacchetti, P. Postorino, and M. Capone, submitted to *Phys. Rev. B* & cond-mat/0402279.

R13 "Raman spectroscopy: a direct probe of substrate-induced strain in ultra-thin $La_{0.7}Sr_{0.3}MnO_3$ films", P. Dore, P.Postorino, A. Sacchetti, R. Giambelluca, M. Angeloni, and G. Balestrino, submitted to *Appl. Phys. Lett.*

This Ph.D. thesis is organized in the following structure.

Physical background and state of the art

- In Chapter 1, the general properties of rare-earth manganites are described. In particular the structure and doping-temperature phase diagram will be described and the theoretical models developed for the description of the physical properties of manganites will be reviewed.

- In Chapter 2, several ways of inducing structural modifications in manganites are discussed. In particular the effects of pressure, oxygen deficiency, and substrate-induced strain on the physical properties of manganites will be described. The properties of related compounds with similar structural properties are also briefly reviewed.

Results of the present work

- In Chapter 3, the experimental techniques employed throughout the measurements performed in this Ph.D. thesis are described. The reader can safely skip this chapter and if necessary read only the parts indicated by successive cross-references.

- In Chapter 4, a brief review of Raman data on manganites existing in the literature is first presented. The **high-pressure Raman** measurements performed on two $\mathrm{La}_{1-x}\mathrm{Ca}_x\mathrm{MnO}_{3-\delta}$ samples are then reported and discussed.

- In Chapter 5, the most relevant infrared measurements on manganites reported in the literature are reviewed. The **pressure and temperature** dependent **mid-infrared** absorption measurements on $\mathrm{La}_{0.75}\mathrm{Ca}_{0.25}\mathrm{MnO}_3$ are reported and the $P-T$ phase diagram so obtained is presented. Finally, **high-pressure far-infrared** absorption measurements on three $\mathrm{La}_{1-x}\mathrm{Ca}_x\mathrm{MnO}_{3-\delta}$ samples performed exploiting **synchrotron radiation** are reported.

- In Chapter 6, **infrared** and **Raman** measurements on $\mathrm{La}_{0.7}\mathrm{Sr}_{0.3}\mathrm{MnO}_3$ **thin films** grown on SrTiO_3 and LaAlO_3 substrates are reported and discussed.

- In Chapter 7, **high-temperature high-pressure X-ray diffraction** measurements on **$\mathrm{LiMn}_2\mathrm{O}_4$** devoted to the determination of the structural $P-T$ phase diagram are reported. **Raman** measurements on the same compound are also presented. Finally **Raman** data on **$SrMnO_3$** obtained are reported. A **polarization analysis** devoted to phonon-assignment in the hexagonal compound was performed and Raman measurements in the **100-360 K temperature** range were carried out.

- In Chapter 8, the results obtained in chaps.4-7 are compared and discussed. Finally conclusions and future perspectives are presented.

Labels employed in the thesis

In the second part of the thesis, the names of the studied samples are reported with labels. A table containing the meanings of the employed labels is reported here for easy referencing.

Label	Sample
LC25S	$La_{0.75}Ca_{0.25}MnO_3$
LC20S	$La_{0.80}Ca_{0.20}MnO_3$
LC20D	$La_{0.80}Ca_{0.20}MnO_{2.92}$
LSMO	$La_{0.7}Sr_{0.3}MnO_3$
LMO	$LiMn_2O_4$
SMO	$SrMnO_3$
STO	$SrTiO_3$
LAO	$LaAlO_3$

Chapter 1

Properties of Rare-Earth Manganites

Rare-earth manganites have been object of many theoretical and experimental investigations in the last fifteen years, owing to the interesting phenomenon of Colossal Magneto-Resistance (CMR), i.e. the dramatic decrease of the resistance with applied magnetic field [1]. The CMR effect makes manganites very promising from the application point of view in fields such as magnetic sensors and memories [2, 3]. Moreover, the physics underlying the properties of these compounds represents a challenging problem owing to the presence of an interplay between charge, spin, lattice, and orbital degrees of freedom [4]. This competition between different effects with similar energy scale is typical of many other strongly-correlated electron systems such as superconducting cuprates [4].

Despite the strong effort devoted to the study of manganites, we are still far apart from a complete understanding of the physics which rules their properties. In this chapter, we review the main properties of rare-earth manganites and the theoretical models developed in order to give a description of these compounds.

1.1 Structural properties of rare-earth manganites

Rare-earth manganites have general chemical formula $Re_{1-x}Ae_x$ $\mathrm{MnO_3}$ where Re is a trivalent rare-earth and Ae is a dopant divalent alkali earth. They belong to the crystallographic class of *perovskites*, i.e. the compounds with general chemical formula ABX_3 where A and B are cations and X is an anion (typically oxygen). The perovskite structure is represented in fig.1.1, where the presence of BX_6 octahedra in the structure is evidenced. These octahedra form the skeleton of the perovskite structure. In rare-earth manganites, distortions from the ideal cubic perovskite structure are often observed, with consequent reduction of symmetry from cubic to orthorhombic, rhombohedral, tetragonal, or monoclinic symmetry. These distortions are usually quite small and one can talk of a *pseudocubic* structure. The stability of a perovskite depends on the possibility of forming the BX_6 array, which is stable only when the A ion is neither too large nor too small. Indeed the BX bond lengths and BXB bond angles tend to readjust in order to accommodate the A ion in the structure. Therefore, there is a limiting value for the dimension of the A ion for the perovskite structure to be stable, defined by the tolerance factor:

$$TF = \frac{r_A + r_X}{\sqrt{2}(r_B + r_X)} \tag{1.1}$$

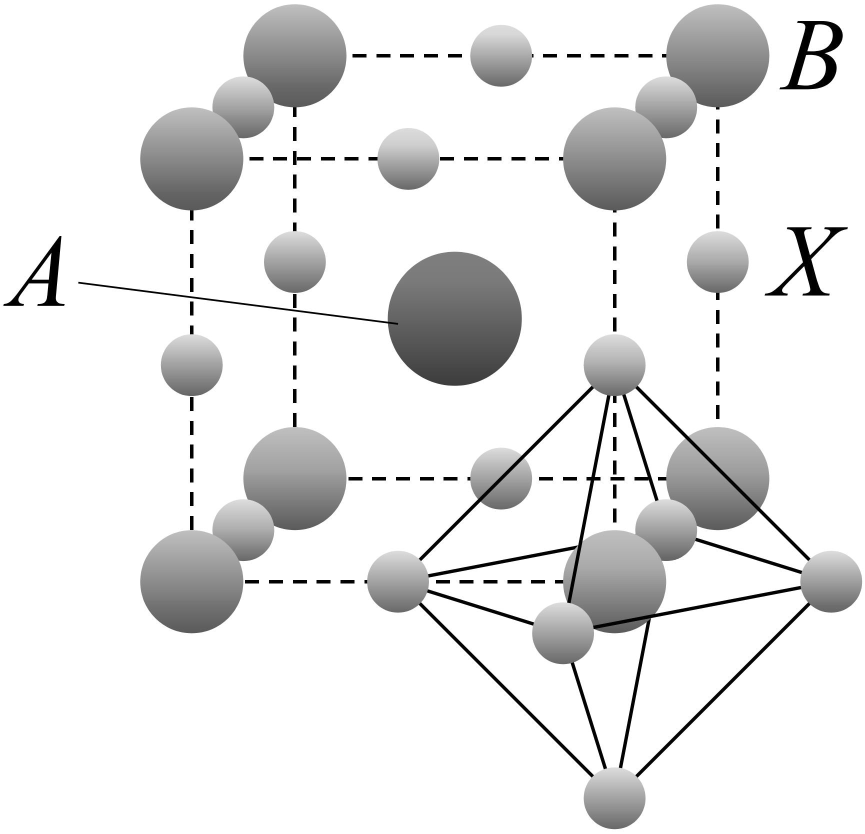

FIGURE 1.1: Structure of a cubic ABX_3 perovskite.

where r_A, r_B, and r_X are the ionic radii of the A, B, and X atoms respectively. $TF = 1$ implies a perfect cubic perovskite, whereas for $TF < 1$ the A ion is too small to fill the space between the BX_6 octahedra which tend to tilt in order to occupy the available space. On the other hand, for $TF > 1$ or $TF < 0.75$ the pseudocubic structure is generally unstable.

1.1.1 The Jahn-Teller effect

The departure of the tolerance factor from unity is not the only cause of structural distortion from ideal cubic structure in manganites. An important role in these compounds is played also by the presence of a strong coupling between electronic and lattice degrees of freedom.

Let us consider the electronic structure of the parent undoped compound $Re\mathrm{MnO_3}$: in the ionic approximation, there will be Re^{3+}, Mn^{3+}, and O^{2-} ions. The most important orbitals in describing these systems are the $3d$ manganese orbitals which are five-fold degenerate. This degeneracy is partially removed by the crystal field, which in a cubic structure, lowers the three d_{xy}, d_{xz}, and d_{yz} orbitals with respect to the remaining two $d_{x^2-y^2}$ and $d_{3z^2-r^2}$ [5]. Once mixing with oxygen p-orbitals is considered, the three low lying and the two upper orbitals assume the t_{2g} and e_g symmetry respectively. This schematization also holds in a pseudocubic structure. The four valence electrons of the Mn^{3+} ion have aligned spins owing to a strong Hund-rule coupling. Therefore, three of them occupy the t_{2g} levels, forming a 3/2 spin core, and the fourth occupies one of the e_g levels with spin parallel to the other three. It can be shown that the resulting electronic structure is unstable owing to the degeneracy of the e_g levels.

The Jahn-Teller theorem states that a non-linear molecule with a degenerate electronic ground-state is unstable with respect to ionic displacements which remove the electronic degeneracy [6]. This theorem can be extended also to a crystal and in particular, in manganites, the degeneracy of the e_g levels can be removed by an asymmetric distortion of the $\mathrm{MnO_6}$ octahedron surrounding the Mn^{3+} ion (see fig.1.2). It is important to note that the octahedral distortion (Jahn-Teller distortion), in a first approximation, can be described as linear combination of the three normal coordinates of the undistorted octahedron: the totally symmetrical (A_{1g} symmetry) breathing Q_1 (which gives no splitting of the e_g levels), the basal-plane distortion Q_2, and the Q_3 stretching modes (see fig.1.3). Only the latter two modes (both having E_g symmetry) break the degeneracy of the e_g levels, leading to the Jahn-Teller (JT) effect. By means of a simplified calculation, it can be shown

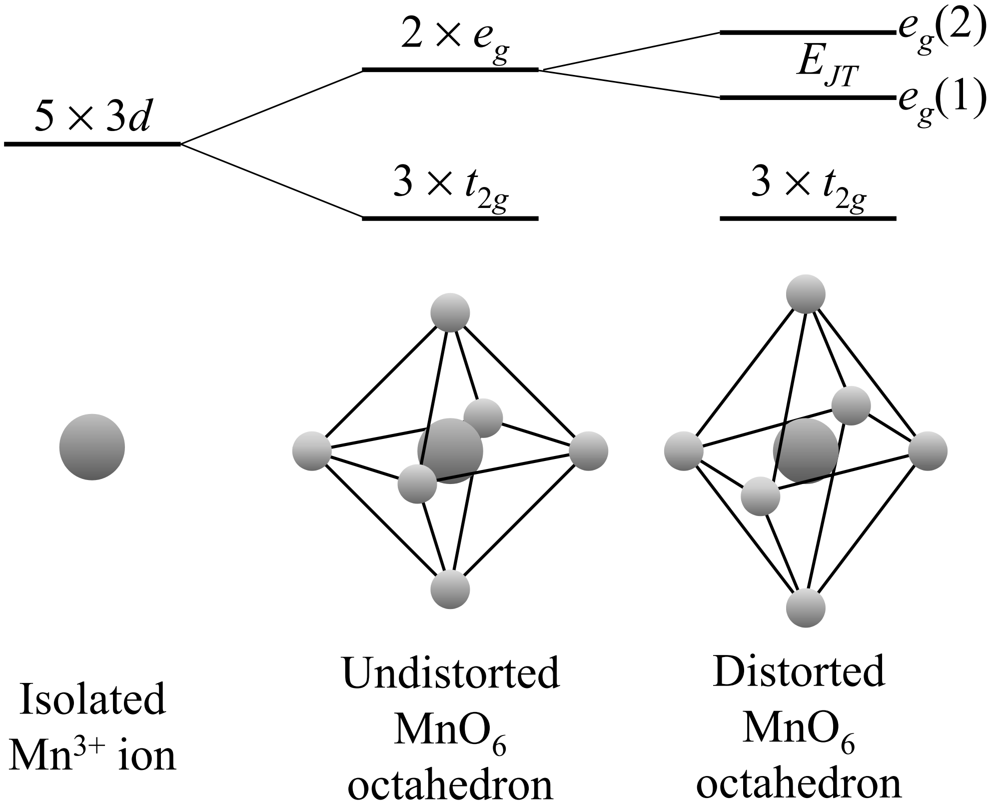

FIGURE 1.2: Jahn-Teller effect in ReMnO$_3$.

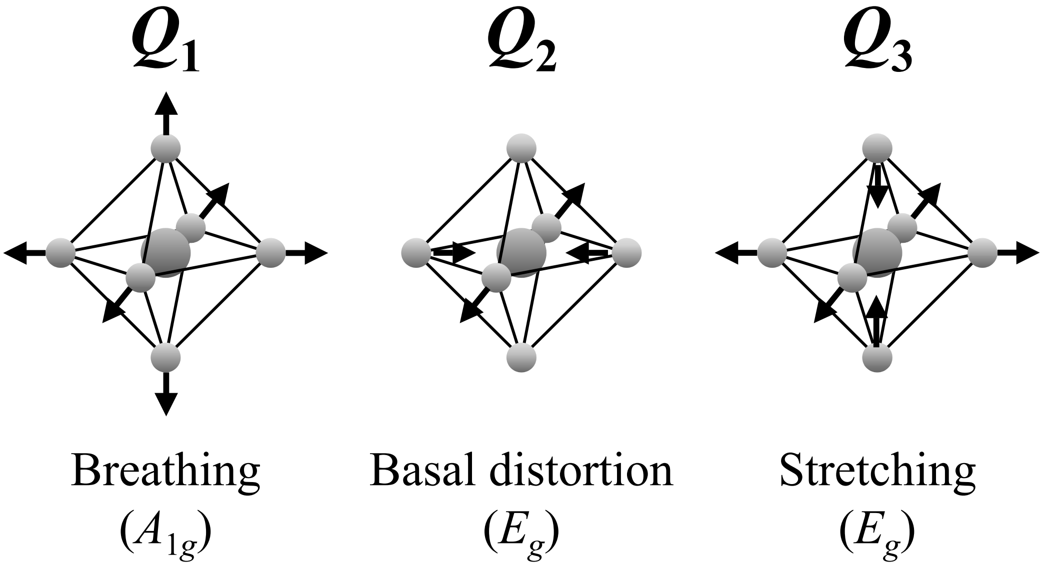

FIGURE 1.3: Octahedral normal coordinates describing the Jahn-Teller distortion.

that the JT distortion affects the frequencies of the two normal modes of E_g symmetry. Let us expand the potential energy W "seen" by the nuclei for a given electronic level in series of the ionic normal coordinates of the undistorted system $\underline{Q} = \{Q_\alpha, \alpha = 1, 2, ...\}$:

$$W(\underline{Q}) \simeq W_0 + \sum_\alpha \frac{\partial W}{\partial Q_\alpha} Q_\alpha + \sum_{\alpha\beta} \frac{\partial^2 W}{\partial Q_\alpha \partial Q_\beta} Q_\alpha Q_\beta \tag{1.2}$$

If the electronic level is non-degenerate, the linear terms in eq.1.2 vanish and the dynamical matrix (i.e. the quadratic term in eq.1.2) reduces to the diagonal form. Instead in the degenerate case, there are always non-vanishing linear terms [6] and in general the dynamical matrix is no more diagonal. Therefore, the equilibrium values of Q_α are modified (leading to the JT distortion) and mixing coupling terms of the type $(\partial^2 W/\partial Q_\alpha \partial Q_\beta) Q_\alpha Q_\beta$ with $\alpha \neq \beta$ appear. As an example, we can consider a simple model in which there are only two normal coordinates x and B. If x removes the electronic degeneracy while B does not, and there is a coupling $\Gamma = \partial^2 W/\partial x \partial B$ between them, the ionic potential energy in presence of degeneracy reads [7]:

$$W(x, B) = \frac{1}{2} k x^2 + \frac{1}{2} k_B B^2 - g x + \Gamma x B \tag{1.3}$$

where k and k_B are the spring constants of x and B normal coordinates respectively and $g = \partial W/\partial x$ is the JT term. Minimization of eq.1.3 leads to:

$$B = -\Gamma x / k_B \tag{1.4}$$

$$W(x) = \frac{1}{2}\left(k - \frac{\Gamma^2}{k_B}\right) x^2 - g x = \frac{1}{2} k' (x - x_0)^2 + E_{JT} \tag{1.5}$$

where $k' = k - \Gamma^2/k_B$, $x_0 = g/k'$, and $E_{JT} = g^2/2k'$. It is well evident that, besides the shift of the equilibrium positions from $B = 0$ and $x = 0$, another important consequence of the JT effect is the reduction of the spring constant k, and thus of the vibrational frequency of the JT active normal mode, with respect to the undistorted case. This finding will be very important in the discussion of the results of this thesis.

The JT effect induces a strong interplay between electronic and ionic degrees of freedom. In particular, we will see in detail in sec.1.3.3 the consequences of this effect on the conducting properties of manganites.

1.2 Ca and Sr doped $\mathrm{LaMnO_3}$

In the previous section, we discussed the electronic properties of the undoped rare-earth manganites $Re\mathrm{MnO_3}$. This is the case of parent compound $\mathrm{LaMnO_3}$ which is an orthorhombic (space group $Pnma$) insulating and paramagnetic (PM) system which enters an A-type antiferromagnetic (AF) phase below $T_N = 140$ K [2]. The insulating nature of $\mathrm{LaMnO_3}$ is due to the JT effect. Indeed, bearing in mind that the external valence orbitals are the e_g levels, in absence of the JT effect, they would give rise to an half-filled band and thus to a metallic state. The JT effect splits the e_g band leading to a lower full band and an upper empty one, and thus to an insulating state [1].

Doping $\mathrm{LaMnO_3}$ with partial substitution of La with a divalent metal (Ca, Sr, Ba, Pb, etc...) creates holes in the valence band and drives the system towards a metallic phase. In the ionic approximation, the presence of a divalent dopant converts part of the $\mathrm{Mn^{3+}}$ into $\mathrm{Mn^{4+}}$, thus removing part of the distorted $\mathrm{MnO_6}$ octahedra. Moreover chemical doping varies the tolerance factor owing to the different ionic size of $\mathrm{La^{3+}}$ and the dopant ion and also owing to the large difference in the ionic sizes of $\mathrm{Mn^{3+}}$ and $\mathrm{Mn^{4+}}$ ions. On the basis of the above considerations, chemical doping with a divalent metal, besides charge doping, can induce structural modifications in $\mathrm{LaMnO_3}$. Doped manganites often exhibit the CMR effect.

The spectacular magnetoresistance effect of manganites is one of the strongest every observed [1]. This effect can be quantified by means of the magnetoresistance ratio:

$$M.R. = \frac{R_0 - R_H}{R_0} \tag{1.6}$$

where R_H is the resistance in presence of a magnetic field of magnitude H and R_0 is the resistance in zero field. In manganites the magnetoresistance ratio can reach values larger than 90% which are much larger than those observed in other magnetoresistive materials such as permalloy ($M.R. = 2 - 3\%$) or Ni-Cu multilayers ($M.R. = 40\%$) [1].

Besides the intrinsic scientific interest on the CMR effect, the strong effort devoted to the study of CMR manganites is due to the possible applications of these systems. Since a moderate magnetic field (≈ 1 T) can induce a dramatic drop of the resistance, it is possible in principle to obtain a very sensible magnetic field sensor based on a manganite. Since the CMR is maximum around the Curie temperature T_C ($\approx 200 - 300$ K in La-Ca manganites),

---

[1] This picture has been questioned by Loa et. al. who pointed out that Hubbard repulsion plays a dominant role and that $\mathrm{LaMnO_3}$ is probably a Mott insulator [8].

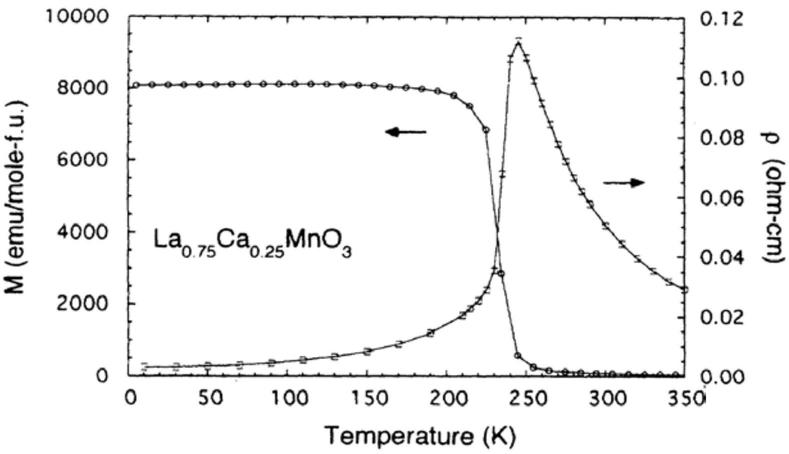

FIGURE 1.4: Temperature dependence of the magnetization and the resistivity for $La_{0.75}Ca_{0.25}MnO_3$ [9].

manganite-based devices can work around room temperature and can have application in magnetic memories technology [3].

In discussing the conducting properties of doped manganites, we will talk of a metal and of an insulator, even if a rigorous definition of what is a metal or an insulator is possible only at $T = 0$. Therefore in this context we will use a more phenomenological definition based on the temperature dependence of the resistivity $\rho(T)$ and we will talk of a metal when $d\rho/dT > 0$ and of an insulator when $d\rho/dT < 0$. As a typical example, the temperature dependence of magnetization and resistivity of $La_{0.75}Ca_{0.25}MnO_3$ is shown in fig.1.4 [9]. It is well evident that the resistivity $\rho(T)$ shows a maximum in correspondence of the onset of the magnetization $M(T)$. Therefore, in the PM phase ($M(T) = 0$) the system is insulating ($d\rho/dT < 0$), while in the FM phase ($M(T) \neq 0$) it is metallic ($d\rho/dT > 0$). Since the magnetic and conducting transition are almost coincident, the Curie temperature T_C and the insulator to metal (IM) transition temperature T_{IM} are very close one to each other. The approximate coincidence of the two transition is a common feature in manganites.

In the present Ph.D. thesis, $La_{1-x}Ca_xMnO_3$ and $La_{1-x}Sr_xMnO_3$ manganite families have been studied. In the following sections we will discuss the doping-temperature phase diagrams of these two systems.

1.2.1 Phase diagram of $La_{1-x}Ca_xMnO_3$

The $La_{1-x}Ca_xMnO_3$ systems is probably the most studied manganite family in the literature owing to the very large magneto-resistance observed in this

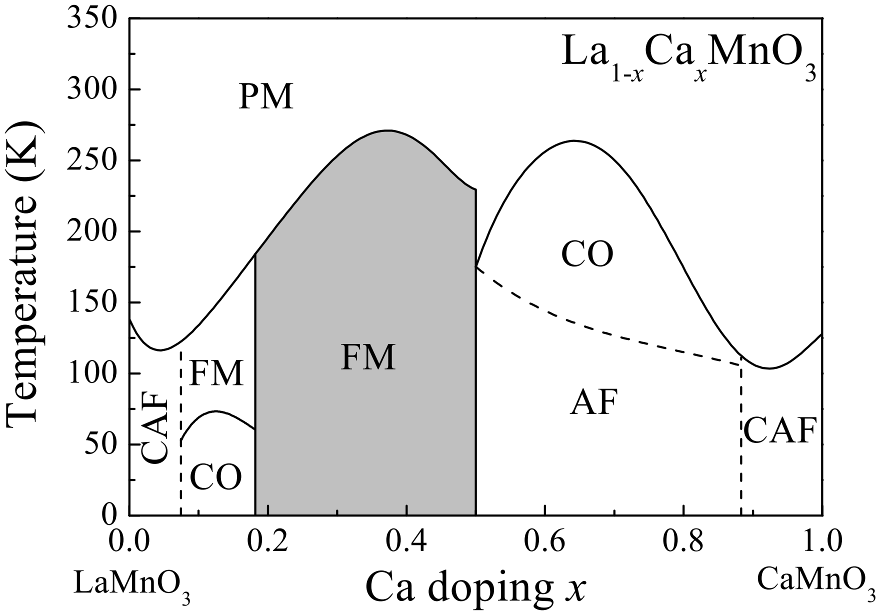

FIGURE 1.5: Doping vs. temperature phase diagram of La$_{1-x}$Ca$_x$MnO$_3$. PM=Paramagnet, CAF=Canted Antiferromagnet, FM=Ferromagnet, CO=Charge Ordered phase, AF=Antiferromagnet. In the shaded gray region the phase is metallic and it is insulating in the other regions [2].

compound (the resistance decreases of more than one order of magnitude in La$_{2/3}$Ca$_{1/3}$MnO$_3$ with an applied magnetic field of 2 T) [10]. The $x - T$ phase diagram of La$_{1-x}$Ca$_x$MnO$_3$ is shown in fig.1.5 [2]. At high temperature the system is a PM insulator over the whole doping range, while at low temperature the magneto-conducting properties strongly depend on x. The ground-state ($T = 0$) is antiferromagnetic (AF) within $0 \leq x \lesssim 0.1$ and $0.5 \lesssim x \leq 1$ and ferromagnetic (FM) elsewhere. A metallic ground-state is observed only for $0.2 \lesssim x \lesssim 0.5$ whereas several intermediate phases appear between the ground state and the high-temperature PM insulating phase within the non-metallic doping regions. In particular, within the doping regions close to the pure end compounds, on decreasing T transitions to AF canted phases[2] and charge-ordered phases[3] are observed. The $x = 1$ end-member CaMnO$_3$ is a G-type antiferromagnet with $T_N \simeq 130$ K. It is worth to note that in the $0.2 \lesssim x \lesssim 0.5$ doping region, the system undergoes a magneto-conductive transition from the high-temperature PM insulating phase to the low temperature FM metallic one (see fig.1.4 as an example).

The Ca-doping does not induce any structural transition and La$_{1-x}$Ca$_x$-

---

[2] The existence of canted phases in manganites has been recently revised in terms of an inhomogeneous phase consisting of a mixture of ferromagnetic and AF phases [4].

[3] In CO state the charge carriers are localized on Mn ions forming a periodic array.

MnO_3 remains orthorhombic (*Pnma* space group) over the whole doping range. Indeed, although Ca^{2+} is smaller than La^{3+}, the difference in their ionic radii estimated for 12-fold coordination is only 2% [11].

1.2.2 Phase diagram of $La_{1-x}Sr_xMnO_3$

$La_{1-x}Sr_xMnO_3$ is another widely studied manganite in the literature, owing to its large magnetoresistance effect accompanied by large T_C values. The $x-T$ phase diagram of $La_{1-x}Sr_xMnO_3$ is shown in fig.1.6 [12]. It is worth to note that, owing to the large ionic size of Sr^{2+} with respect to La^{3+}, $La_{1-x}Sr_xMnO_3$ undergoes structural transitions with increasing x. At low doping ($x < 0.2$) the structure is orthorhombic (space group *Pnma*) with $a < c$ (O-structure) near $x = 0$ and $a > c$ (O' structure) near $x = 0.2$. For $0.2 \lesssim x < 0.5$ the structure is rhombohedral (space group $R\overline{3}c$) and at $x > 0.5$ it becomes tetragonal (space group $I4/mmm$) at high temperature, while at

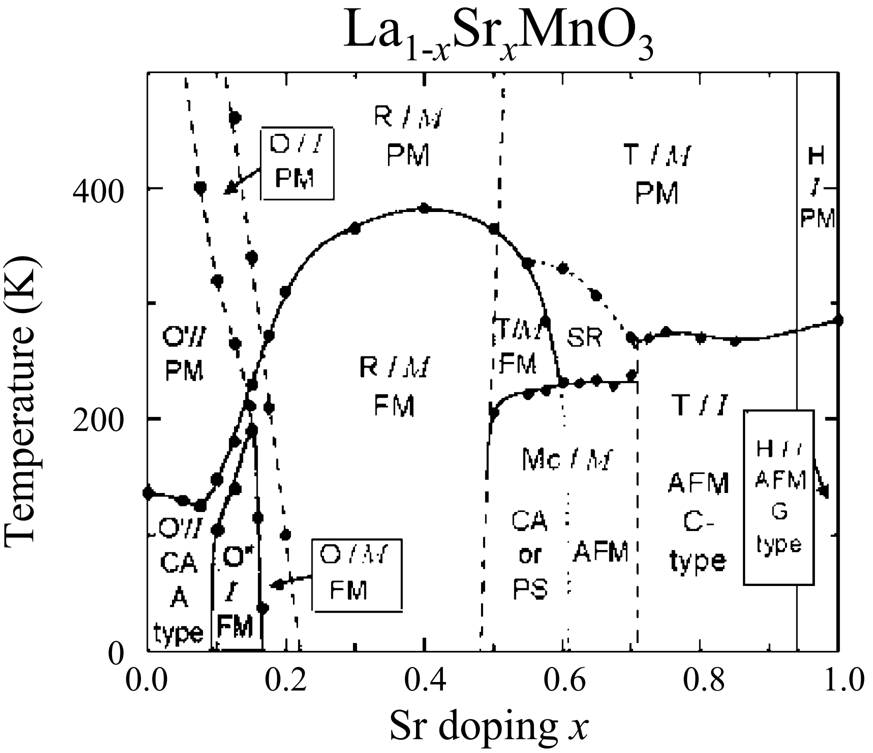

FIGURE 1.6: Doping vs. temperature phase diagram of $La_{1-x}Sr_xMnO_3$. In each region the structural (O and O'=orthorhombic, R=rhombhedral, T=tetragonal, Mc=monoclinic, H=hexagonal), conducting (I=insulator, M=metal), and magnetic (PM=paramgnetic, FM=ferromagnetic, AFM=antiferromagnetic, CA=canted state, PS=phase-separated range) phase are indicated [12].

low temperature it is monoclinic (space group $P2_1/m$) for $0.5 < x < 0.7$ and tetragonal for $0.7 < x < 1$. The end member $SrMnO_3$ is hexagonal (space group $P6_3/mmc$) but it can be synthesized also in the cubic structure, as we will discuss in detail in sect.2.6.2.

As already seen in the case of $La_{1-x}Ca_xMnO_3$, the high temperature phase of $La_{1-x}Sr_xMnO_3$ is PM over the whole doping range, whereas it is insulating only for $x \lesssim 0.1$ and presents a PM metallic regime for $0.1 \lesssim x < 1$. The low temperature phase is more complicated. At low doping there is a canted insulating AF phase which becomes FM at $x = 0.1$. Similarly to the case of Ca-doped $LaMnO_3$ for $0.2 < x < 0.5$ the system is FM and metallic but in this region the temperature-induced magnetic transition is not accompanied by a conducting one. In the $0.5 < x < 0.7$ range, the low temperature phase of $La_{1-x}Sr_xMnO_3$ is quite complicated with possible presence of phase separation between different magnetic and conducting regimes. At large doping ($x > 0.7$) there is an insulating C-type AF phase at low temperature. The end member $SrMnO_3$ is insulating at all temperatures and it undergoes a transition from a high temperature PM phase to a low temperature G-type AF phase. The properties of $SrMnO_3$ will be discussed in detail in sect.2.6.2.

1.3 Theoretical model for manganites

As discussed in the previous section, the phase-diagrams of Ca and Sr doped $LaMnO_3$ are very rich. In this Ph.D. thesis we will mainly focus our attention on the CMR doping region and in this section we give a description of the models developed in order to describe the physics of manganites in this regime.

1.3.1 Double exchange model

A good qualitative description of the CMR effect is given by the double exchange (DE) model [13]. In this model the motion of the e_g electrons is described in the matrix of the t_{2g} orbitals which, as discussed in sect. 1.1.1, form a polarizable core of spin 3/2. Let us consider two Mn^{4+} ions connected by the O^{2-} ion between them, and an extra electron which can occupy the e_g orbital of either the two Mn ions. There are two possible configurations for the electron: $Mn^{3+}O^{2-}Mn^{4+}$ (wavefunction Ψ_1) and $Mn^{4+}O^{2-}Mn^{3+}$ (wavefunction Ψ_2). These two wavefunctions are degenerate and can be written more explicitly as:

$$\Psi_1 = \psi^p \psi_1^d \quad \Psi_2 = \psi^p \psi_2^d \tag{1.7}$$

where ψ^p is the wavefunction of the oxygen p-orbital while ψ_1^d and ψ_2^d are the wavefunctions of the d-orbitals of the two manganese ions. Since Ψ_1 and Ψ_2 are degenerate, the total wavefunction can be written as an hybridization function:

$$\Psi_\pm = N_\pm(\Psi_1 \pm \Psi_2) = N_\pm(\psi^p\psi_1^d \pm \psi^p\psi_2^d) \tag{1.8}$$

where $N_\pm$ is a normalization constant. If we now introduce a spin-independent interaction hamiltonian H_{12} between the electrons and treat it with standard perturbation theory, there will be an exchange term J given by:

$$J = \int \psi_1^d(\vec{r}_1, \sigma_1)\psi^p(\vec{r}_2, \sigma_2)H_{12}(\vec{r}_1, \vec{r}_2)\psi^p(\vec{r}_1, \sigma_1)\psi_2^d(\vec{r}_2, \sigma_2)d^3r_1d^3r_2 \tag{1.9}$$

This term represents the transfer of the electron from a manganese ion and simultaneously the hopping of another electron from the oxygen ion to the second manganese ion. The net result is a charge transfer between the manganese ions. It is easy to show that the transfer probability is maximum when the spin of the two manganese ions are parallel, therefore a FM phase favors charge transport. Since the spins of each single manganese ion are aligned owing to the Hund's rule, in the $J \to +\infty$ limit (DE limit), the hopping of an electron from a Mn^{3+} to a Mn^{4+} by means of the O^{2-} in between them is possible only if the spins of the core t_{2g} electrons of the two manganese ions are aligned (see fig.1.7). From a more formal point of view, the DE model

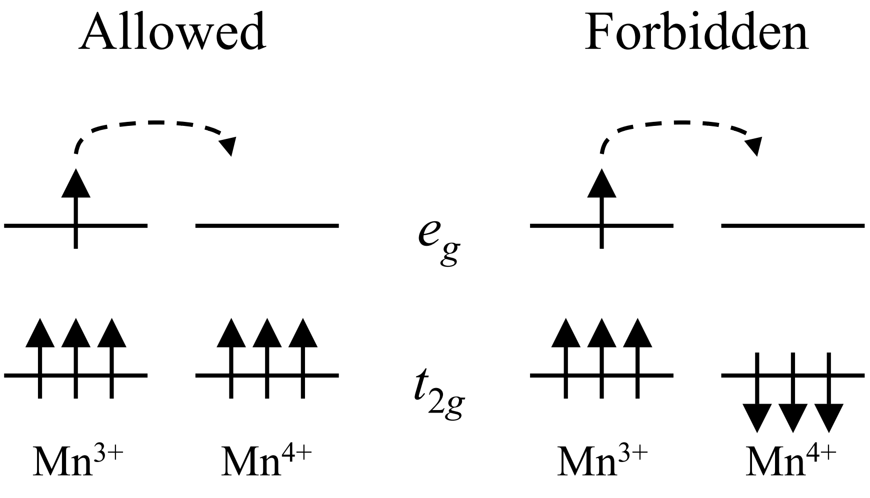

FIGURE 1.7: Schematic representation of the double exchange model.

can be represented by means of the hamiltonian [14]:

$$H_{DE} = -t \sum_{<ij>} c_i^\dagger c_j - J_H \sum_i \vec{S}_i \cdot \vec{\sigma}_i \tag{1.10}$$

where t is the effective hopping integral between nearest-neighbor Mn-ions, c_i is the e_g-electron annihilation operator on site i, and the sum in the first term runs over nearest neighbor sites. In the second term, J_H is the Hund's rule coupling, $\vec{S}_i$ is the total t_{2g} core spin on site i, and $\vec{\sigma}_i$ is the e_g electron spin on site i. The first term in eq.1.10 is the standard hopping term for an electron on a cubic lattice with hopping amplitude t, while the second term represents the Hund coupling between the $S = 3/2$ core spin in the localized t_{2g} orbitals and the spin of the delocalized e_g orbitals. This term adds an energy penalty for an electron with spin aligned with the corresponding core spin hopping to a site where the core spin has a different orientation.

The DE model explains qualitatively both the CMR effect and the IM transition occurring around T_C in $La_{1-x}Ca_xMnO_3$ (see sect.1.2). The CMR is described in the framework of the DE model as follows: a magnetic field induces alignment of the core spins, thus enhancing electron mobility and reducing the resistivity. On the other hand, the temperature-induced IM transition can be described considering that, starting from the PM phase, where spins are disordered and charge mobility is suppressed, cooling the system down to T_C, spin alignment is favored and thus charge mobility is increased.

DE is the first step to understand the physics of CMR manganites. As we will discuss in detail in next sections, a proper description of these systems requires the introduction of other physical effects such as the super-exchange coupling and electron-phonon coupling.

1.3.2 The Heisenberg term

The first limit of the DE model described in the previous section is that it always predicts a FM ground state. Bearing in mind the typical phase diagram of rare-earths manganites (see sect.1.2), it is well evident that away from the CMR doping region ($0.2 \lesssim x \lesssim 0.5$) the ground state is in general AF. In particular the $x = 1$ end members of the phase diagrams are typically G-type antiferromagnets. A simple way to take into account the existence of AF phases is the introduction of an Heisenberg term between the t_{2g} core spins [4]:

$$H_{AF} = J_{AF} \sum_{<ij>} \vec{S}_i \cdot \vec{S}_j \tag{1.11}$$

where J_{AF} is the Heisenberg coupling and $\vec{S}_i$ is the core spin on site i. This term naturally arises taking into account the super-exchange (SE) interaction between nearest-neighbor t_{2g} orbitals of Mn mediated by the oxygen. We recall that the SE interaction results from second-order perturbation treatment of the hopping term for localized orbitals (such as the t_{2g} in manganites) in the presence of a strong on-site Coulomb repulsion. The perturbation represented by hopping brakes the degeneracy between FM and AF states reducing the energy of the latter by an amount of the order of t^2/U, where t is the hopping integral and U is the on-site repulsion energy. Thus the Heisenberg coupling is typically of the order of t^2/U.

The introduction of the Heisenberg term is fundamental for the description of the AF phases and can in principle play a role also in the CMR regime where the ground state is FM [4].

1.3.3 Electron-phonon coupling

The second limit of the DE model is that it is not able to quantitatively reproduce the experimental results. For instance, the T_C values calculated in the framework of DE only are typically one order of magnitude larger than those obtained experimentally [15]. Moreover, the resistivity predicted by DE in the PM phase is much smaller than the real values and hardly compatible with an insulating state [15]. Both these considerations indicate that an extra physical effect inducing charge-carrier localization must be taken into account. It is largely accepted that this localizing mechanism is represented by the electron-phonon coupling triggered by the JT distortion (see sect.1.1.1), as proposed by Millis et al. [15] and strongly supported by a large number of experimental investigation. The presence of a long-range coherent JT distortion was observed in undoped $LaMnO_3$ [16] as well as incoherent distortions in the CMR doping region were observed by means of EXAFS measurements [17]. As discussed in sect.1.1.1, the JT effect introduces a coupling between ionic and electronic degrees of freedom. There is a large number of experimental investigations evidencing this effect. Radaelli et al. observed structural anomalies in orthorhombic $La_{0.75}Ca_{0.25}MnO_3$ in correspondence of the magneto-conducting transition (from insulating paramagnet to metallic ferromagnet) at $T = T_C$ [9]. In fig.1.8 the temperature dependence of the lattice parameters and of the unit cell volume obtained in ref. [9] are shown. A monotonic decrease with decreasing temperature of all the three lattice parameters, and thus of the volume, is well evident, but there is also a change in slope for all these quantities for $T = T_C$. This result

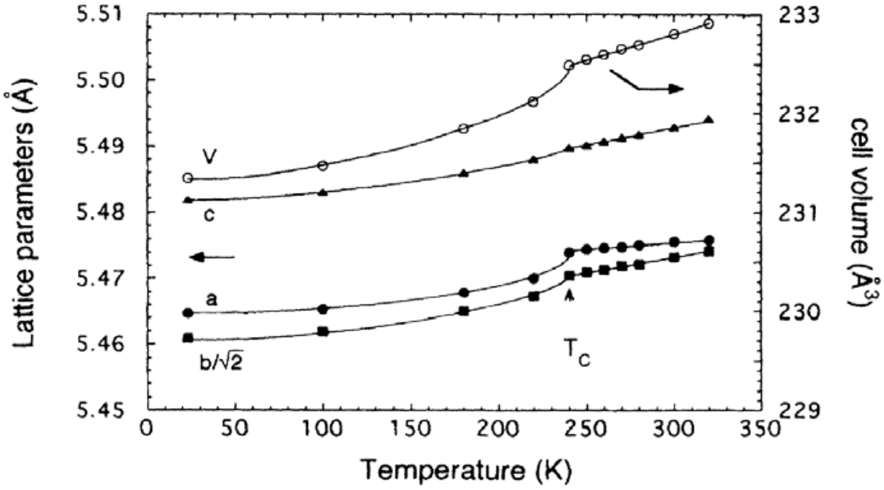

Figure 1.8: Temperature dependence of lattice parameters and unit cell volume in $La_{0.75}Ca_{0.25}MnO_3$ [9].

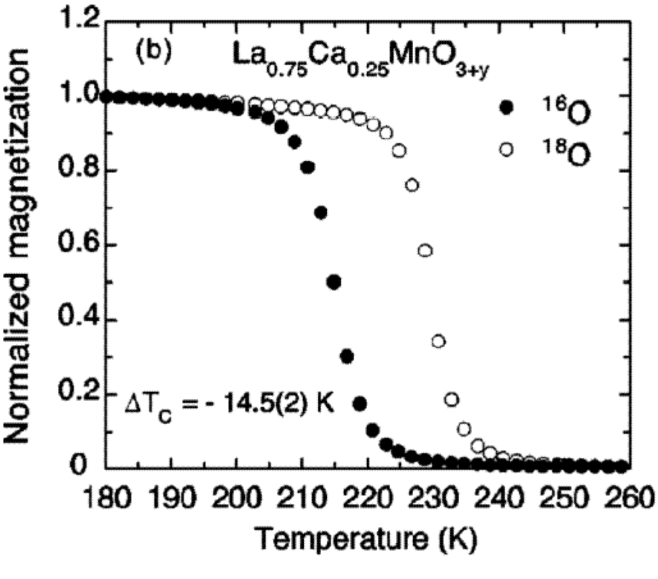

Figure 1.9: Temperature dependence of magnetization of $La_{0.65}Ca_{0.35}MnO_3$ containing ^{16}O (full symbols) and ^{18}O (open symbols) [18].

clearly indicates the presence of an interplay between lattice and electronic properties, but the most evident experimental observation of this coupling is given by the presence of a strong isotopic effect on T_C. Zaho et al. measured the magnetization of two samples of $La_{0.65}Ca_{0.35}MnO_3$ one containing natural ^{16}O isotope and the other obtained substituting a large fraction (∼90%) of ^{16}O with ^{18}O [18]. The results are shown in fig.1.9 where it is well evident a large shift of the flex-point of the $M(T)$ curve between the two samples. It is important to note that a back-exchange procedure in the isotopic sample $La_{0.65}Ca_{0.35}Mn^{18}O_3$ (i.e. a reversed substitution of ^{18}O with ^{16}O) gives a sample whose magnetization is almost identical to that of the natural sample [18]. Therefore, the observed effect is ascribed to the change in the oxygen mass with no spurious effects given by the oxygen exchange procedure. The isotopic shift of T_C clearly shows the presence of strong interplay between electronic and ionic dynamics, i.e. electron-phonon coupling (EPC).

The role of EPC triggered by the JT distortion was theoretically investigated by Millis et al. who proposed that the presence of the JT effect can renormalize the electron energy reducing its mobility [15]. The electron hopping in the lattice induces a JT distortion of the surrounding ions which produces a potential well where the electron tends to self-trap. Therefore, when the electron hops from a site to a nearest neighbor, the distortion on the starting site relaxes and it is instead induced in the arriving site. The net effect is that the lattice distortion tends to follow the electron and the electron mobility is reduced (i.e. its effective mass is increased). The ensemble of the electron and lattice distortion can be described in terms of a quasi-particle named “polaron”. The polaron theory is usually developed in two limiting cases: the charge-lattice coupling is short-ranged (small polaron [19]) or long-ranged (large polaron [20]). In the case of small polarons the charge is severely localized in the local potential well given by the distortion and has so large effective mass that no band-like coherent motion is allowed and only thermal hopping is possible [19]. In the case of large polarons, the distortion simply dresses the charge-carrier enhancing its effective mass and band-like coherent motion is possible [20]. The IM transition in manganites is often described in terms of a crossover from small to large polaron.

The EPC can be described adding a JT term to eq.1.10 [15]:

$$H_{JT} = g \sum_{iab\sigma} c^{\dagger}_{ia\sigma} \vec{\tau}_{ab} c_{ib\sigma} \cdot \vec{r}_i + \frac{1}{2} k \sum_i r_i^2 \tag{1.12}$$

where g is the electron-phonon coupling restoring force, $c_{ia\sigma}$ is the electron annihilation operator on orbital a of site i with spin σ, $\vec{\tau}_{ab}$ is the vector of Pauli matrices in orbital space, $\vec{r}_i$ is the 2-fold vector describing the lattice distortion at site i, and k is the lattice spring constant. The hamiltonian $H = H_{DE} + H_{JT}$ was studied by Millis and co-workers who found that magnetic and conducting properties of the system are regulated by the dimensionless parameter $\lambda = g^2/kt$ which represents the ratio between the energy g^2/k gained by the electron self-trapping and the hopping integral t related to the electron kinetic energy. In particular there can be identified three regimes [15]:

- Weak coupling ($\lambda \ll 1$): the lattice distortion decreases with decreasing temperature and the resistivity $\rho(T)$ decreases linearly with decreasing temperature (metallic behavior).
- Intermediate coupling ($\lambda \approx 1$): the lattice distortion is non-zero even at $T = 0$ but it is not sufficient for localizing particles near the Fermi energy; the resistivity increases as T decreases but it does not diverge for $T = 0$ (anomalous insulating behavior).
- Strong coupling ($\lambda \gg 1$): the lattice distortion is large enough to open a gap in the band structure and $\rho(T)$ diverges as T tends to 0 (insulating behavior).

The properties of the system are thus determined by λ and T as shown by the $\lambda - T$ phase diagram of fig.1.10 obtained by solving the hamiltonian H [15].

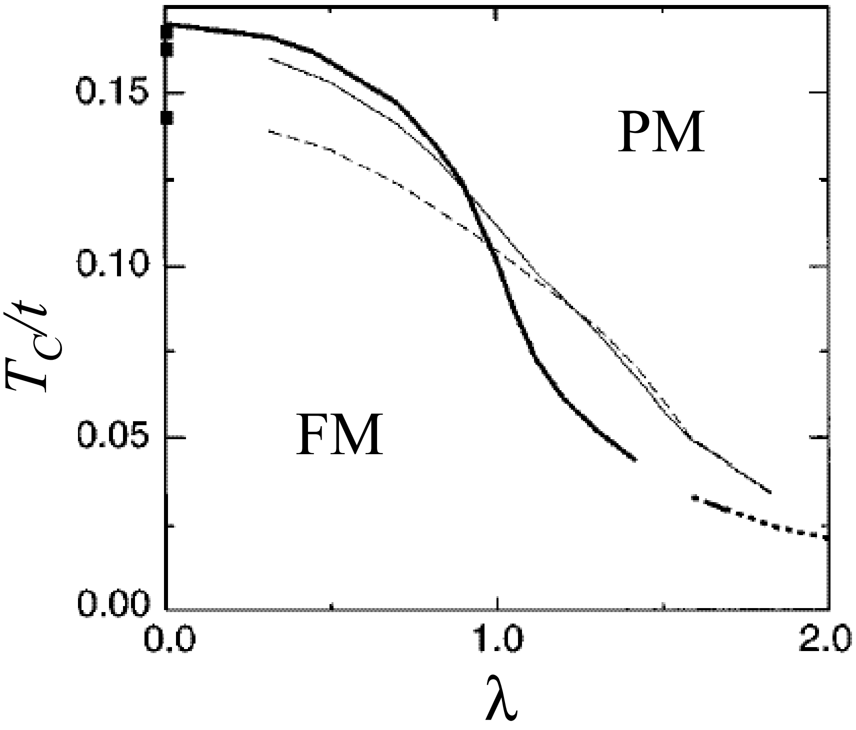

FIGURE 1.10: Curie temperature T_C as a function of the dimensionless electron-phonon coupling λ for different electron densities: $n = 1$ (thick solid line), $n = 0.75$ (light solid line), and $n = 0.5$ (light dashed line). FM=ferromagnetic phase, PM=paramagnetic phase [15].

The model proposed by Millis et al. [15] improves the DE model and better describes the physics of CMR manganites. If we introduce an effective λ defined as $\lambda_{eff} = g^2/kE_{kin}$ where E_{kin} is the kinetic energy of the electron, λ_{eff} can be tuned both by temperature and magnetic field which act on the electron kinetic energy. Therefore, both temperature and magnetic field can drive λ_{eff} from one regime to another, thus explaining the CMR effect and the IM transition. As we will discuss in detail in the next chapter, structural modification can vary λ by means of modulation of the localization energy g^2/k thus modifying the conducting properties of the system.

Chapter 2

Structural Modifications in Manganites

In sect.1.3.3 we have discussed the fundamental role played by EPC in the physics of manganites. Owing to the presence of this effect, the structure is very important in determining the magnetic and conducting properties of manganites. In this chapter we will discuss the effect of different kinds of structural modification on the physical properties of CMR manganites and in particular on the transition temperature T_C. We will discuss the competition between charge and structural effect induced by doping, focusing on the effect of oxygen vacancies and of different chemical doping. We will compare these results with the modifications which can be obtained by means of hydrostatic pressure and substrate-induced strain in thin films. Finally the role of the pseudocubic lattice of the MnO_6 octahedra in manganites will be discussed in comparison with systems containing MnO_6 octahedra in non-pseudocubic network.

2.1 Structural effects on T_C

One of the most important parameter characterizing properties of CMR manganites is the Curie temperature T_C which is directly related to the charge delocalization. In particular, as discussed in par.1.2, in $La_{1-x}Ca_xMnO_3$ the magnetic transition is accompanied by a simultaneous IM transition and thus T_C is actually coincident with the IM transition temperature T_{IM}. Therefore, structural effects, which affect charge delocalization by means of EPC, are expected to have large effect on T_C.

In a pure DE model, T_C is simply proportional to the electron bandwidth

[14] which in turn is proportional to the hopping integral t between nearest neighbor Mn ions mediated by the interposed O ion. It is easy to understand that t should depend on the structure and in particular on the Mn-O bond length d and on the Mn-O-Mn bond angle Θ. It can be shown that in manganites this dependence can be estimated in terms of [21]:

$$t \propto d^{-7/2} \cos^2 \Theta \tag{2.1}$$

Therefore T_C is expressed by [22]:

$$T_C \propto t \propto d^{-7/2} \cos^2 \Theta \tag{2.2}$$

It is important to note that eq.2.2 does not contain the effect of EPC which is fundamental in a correct description of charge-carrier dynamics, as discussed in par.1.3.3. In a first-order approximation, the introduction of EPC has the effect of reducing the electron bandwidth by a factor $\xi = \mathrm{e}^{-E_P/\omega}$ [23] where E_P is the polaron self-trapping energy and ω is the frequency of the phonon describing the distortion. Therefore eq.2.2 can be rewritten as:

$$T_C \propto t\xi = t\mathrm{e}^{-E_P/\omega} \tag{2.3}$$

As expected, eqs.2.1 and 2.3 show that the structure can strongly affect T_C. Indeed, besides d and Θ which obviously depend on the structure, also E_P and ω are related to the lattice and thus to the structural properties.

A more rigorous treatment of the dependence of T_C on structural properties was developed by Millis et al. in ref. [24], where the presence of two distinct structural contributions to T_C, due to isotropic and biaxial strain, was evidenced. In a cubic environment, these two contributions are described by the T_C dependence on the bulk strain ε_B and on the biaxial strain ε_X:

$$T_C(\varepsilon_B, \varepsilon_X) = T_C(0,0)\left(1 + \Delta_1 \varepsilon_B + \frac{1}{2}\Delta_2 \varepsilon_X^2\right) \tag{2.4}$$

where:

$$\Delta_1 = \frac{1}{T_C(0,0)} \frac{dT_C}{d\varepsilon_B}\bigg|_{(0,0)} \qquad \Delta_2 = \frac{1}{T_C(0,0)} \frac{d^2 T_C}{d\varepsilon_X^2}\bigg|_{(0,0)} \tag{2.5}$$

The first-order term in ε_X is zero owing to the cubic symmetry [24]. Simple consideration on bulk modulus, thermal expansion, and specific heat allowed Millis et al. to estimate $\Delta_1 \simeq 6$ and $\Delta_2 \simeq 1400$ in $La_{0.83}Sr_{0.17}MnO_3$. Therefore $\Delta_2 \gg \Delta_1^2$, indicating that the biaxial contribution to T_C is very large, owing to the JT effect [24].

2.2 Hole-doping versus oxygen deficiency

As discussed in sect.1.2, hole doping of $LaMnO_3$ with a divalent metal, modifies the tolerance factor and thus can induce structural modifications. A possible way for partially decouple the charge and structural effects induced by doping is the variation of oxygen stoichiometry creating oxygen vacancies in the structure. Let us consider a series of $Re_{1-x}Ae_x\mathrm{MnO}_{3-\delta}$ samples with different values of the oxygen deficiency δ: since oxygen is an electron acceptor, starting from the stoichiometric ($\delta = 0$) sample, on increasing δ the number of holes in the conduction band will be decreased from x owing to the presence of two extra electrons for each oxygen vacancy. The resulting hole density x_{eff} can be then estimated as:

$$x_{eff} = x - 2\delta \tag{2.6}$$

It is important to note that oxygen deficiency induces structural effects in the manganite in two competing ways [25]:

- *Compressive effect:* the oxygen vacancy itself leaves free space in the structure and the lattice tends to contract.

- *Tensile effect:* the reduced number of O^{2-} ions increases the number of Mn^{3+} ions which are larger than Mn^{4+} ions and thus the lattice tends to expand in order to allocate them.

The competition between these two effects leads to a quite small net distortion of the lattice. As an example, comparing $La_{0.8}Ca_{0.2}MnO_3$ ($x_{eff} = 0.20$) with $La_{0.8}Ca_{0.2}MnO_{2.92}$ ($x_{eff} = 0.04$), the large difference in hole doping is accompanied by a small variation of the unit cell volume ($\Delta V/V = 0.8\%$ [26]) thus indicating negligible structural modifications. On the other hand, the same hole-density variation induced by means of calcium doping (i.e changing x from 0.20 to 0.04) implies a larger volume change of 2.5% [25].

There is not a large number of studies on oxygen-deficient manganites in the literature. Oxygen vacancies have typically a moderate effect on magnetic properties of FM manganites with a small reduction of magnetization whereas the effect on conducting properties is typically dramatic with a remarkable reduction of conductivity [26, 27]. At large δ, $Re_{1-x}Ae_x\mathrm{MnO}_{3-\delta}$ manganites show inhomogeneities with behaviors typical of a spin glass [27,28]. In fig.2.1 the $T - \delta$ phase diagram of $La_{0.70}Ca_{0.30}MnO_{3-\delta}$ is shown [27]. It is well evident that for $\delta \lesssim 0.06$ the magnetic transition is only slightly affected by the

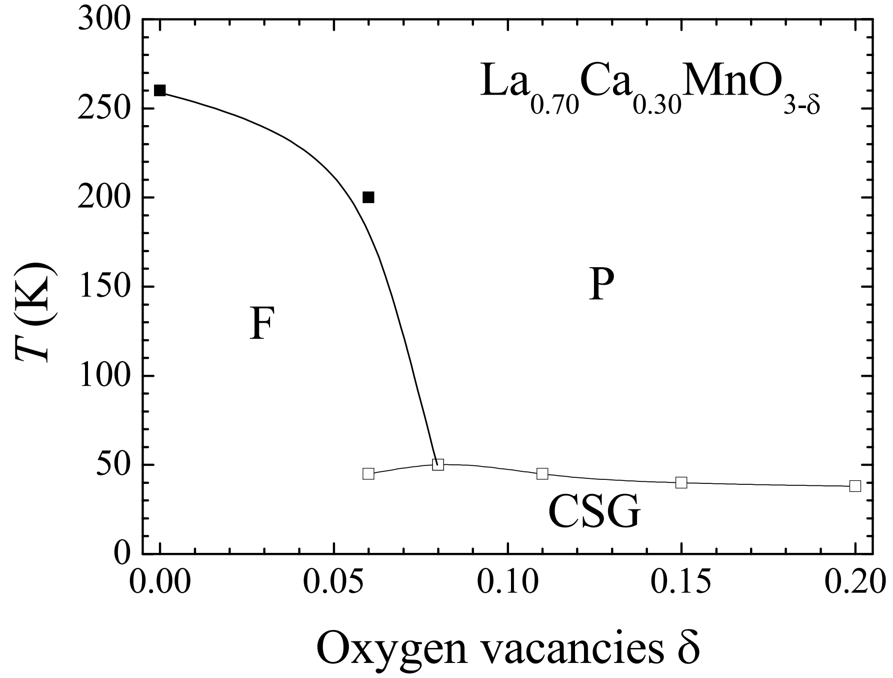

FIGURE 2.1: Temperature vs. number of oxygen vacancies phase diagram of $La_{0.70}Ca_{0.30}MnO_{3-\delta}$. F=Ferromagnet, P=Paramagnet, CSG=Cluster Spin Glass. Solid lines are guides to eyes [27].

oxygen-deficiency, while at larger δ the PM phase persists down to low temperatures and the ground-state FM phase is replaced by an inhomogeneous spin-glass. In the low δ regime, the IM transition is rapidly suppressed and almost disappears at $\delta \approx 0.06$ [27]. Therefore, FM insulating phases can be obtained by means of oxygen vacancies.

2.3 Internal chemical pressure

As discussed in par.1.1, a relevant parameter determining the structural properties of manganites is the tolerance factor TF, defined in eq.1.1, which depends on the ionic radii of the ions composing the manganite [2]. The average radius r_A of the ion at the A-site in the ABX_3 perovskite structure can be continuously tuned in manganites series of the type $(Re_{1-y}Re'_y)_{1-x}Ae_x\text{MnO}_3$ where Re and Re' are two trivalent rare-earths with different ionic radii and Ae is a divalent metal. Varying y with x kept fixed, allows a continuous tuning of the tolerance factor with no variation of the doping level and thus of the hole density [1]. This is a method for varying the *internal chemical pres-*

---

[1] The same effect can be obtained by varying y with x fixed in $Re_{1-x}(Ae_{1-y}Ae'_y)_x\text{MnO}_3$ series where Ae and Ae' are two divalent metals with different ionic radii.

sure exerted on the MnO_6 octahedra skeletal array by the atoms occupying the A-site [2].

Hwang et al. [29] measured magnetization and resistivity of several samples of $Re_{1-x}Ae_xMnO_3$ where Re (Ae) is a proper mixture of trivalent rare-earths (divalent metals) ions, with x fixed at 0.3. A wide range of the A-site ionic radius r_A was explored, allowing the determination of the tolerance factor vs. temperature phase-diagram shown in fig.2.2. For $TF < 0.91$ the low-temperature phase is a FM insulator, while at larger TF a metallic phase is observed. T_C systematically increases with increasing TF up to $TF = 0.93$ and then it slightly decreases. The observed behavior can be explained considering the r_A dependence of the Mn-O bond lengths and Mn-O-Mn bond angles determined by Radaelli et al. and shown in fig.2.3 [30]. On increasing r_A, the average bond angle Θ increases systematically in the whole range, while the average bond length d decreases down to $r_A = 1.24$ Å and then suddenly increases. The increase of r_A reduces the free volume available around the MnO_6 octahedra, thus forcing a symmetrization of the structure

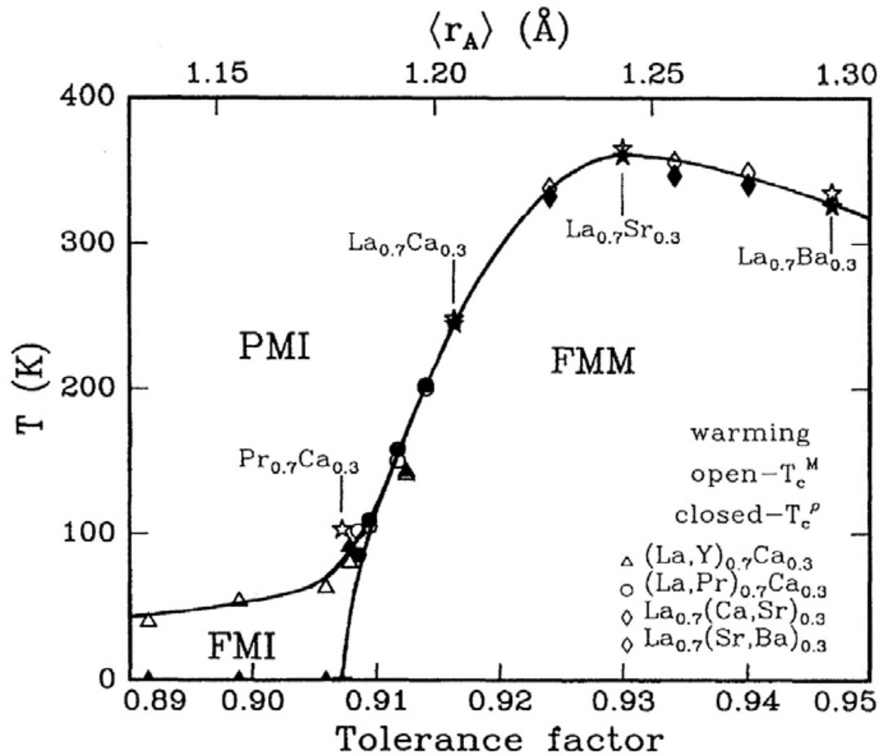

FIGURE 2.2: Temperature vs. tolerance factor (or A-site ionic radius) phase diagram of $Re_{0.7}Ae_{0.3}MnO_3$ (see text). PMI=Paramagnetic insulator, FMI=Ferromagnetic insulator, FMM=Ferromagnetic metal. Transition temperatures have been determined from magnetization (open symbols) and from resistivity (full symbols). Solid lines are guides to eyes [29].

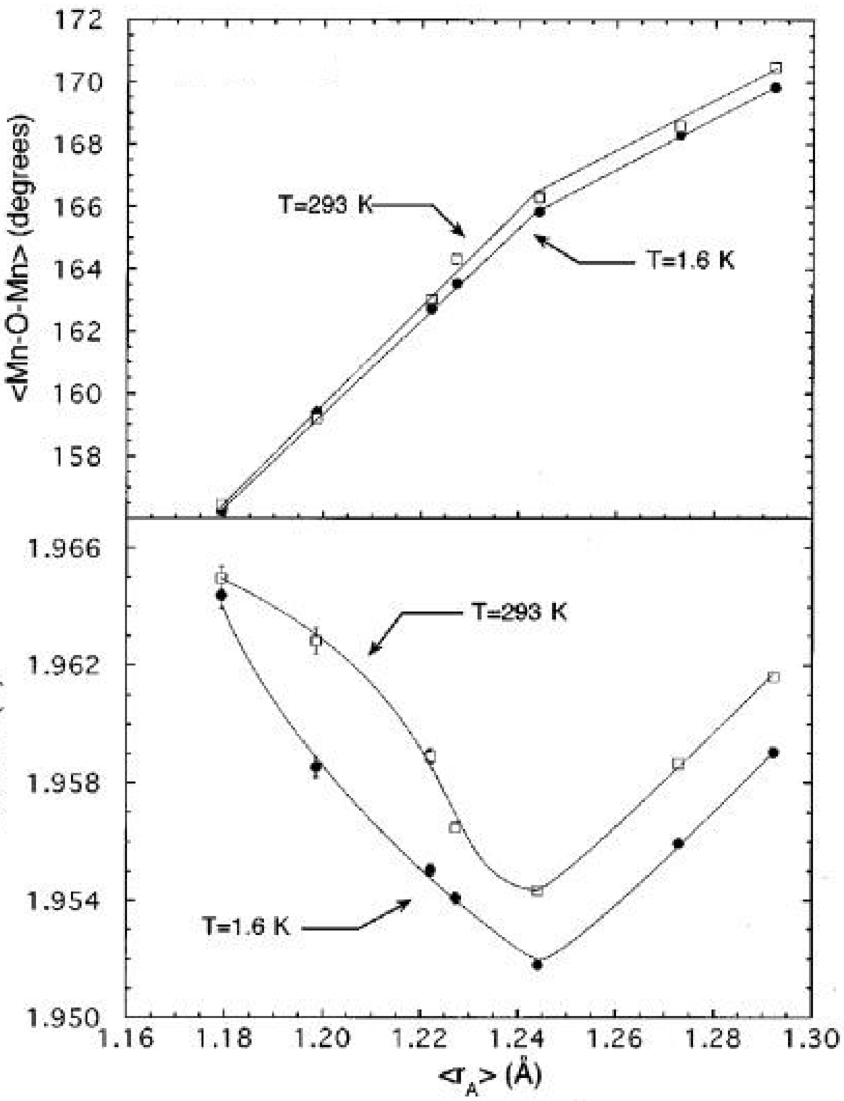

FIGURE 2.3: Average Mn-O-Mn bond angle (top panel) and Mn-O bond length (bottom panel) of $Re_{0.7}Ae_{0.3}$MnO$_3$ as a function of r_A at 1.6 K (full symbols) and 293 K (open symbols). Solid lines are guides to eyes [30].

(i.e. an increase of the bond angles towards 180°) and a reduction of the bond lengths. When r_A exceeds a critical value (≈ 1.24 Å) the bond lengths start to increase in order to allocate in the structure the large ion at the A-site. As discussed in sect.2.1, the bandwidth dependence on the structure is summarized in eq.2.1 and it increases when d decreases and/or when Θ increases towards 180°. Therefore the T_C increase for $TF < 0.93$ is qualitatively explained by the r_A dependence of Θ and d, while the slight decrease at larger TF can be ascribed to the d increase at $r_A > 1.24$ Å (corresponding to $TF = 0.93$). From the quantitative point of view, eq.2.2 cannot explain the observed behavior since, starting from the structural data shown in fig.2.3, it predicts a T_C increase of only 4% in the explored r_A range, whereas the observed T_C increases by a factor 5. This difference can be ascribed to the EPC contribution which is strongly reduced on increasing r_A. Indeed, since the reduction of the free volume around the MnO_6 octahedra forces their symmetrization, the JT distortions are (at least partially) removed and the EPC strength is reduced. The symmetrization of the octahedra is demonstrated by the r_A dependence of the three independent Mn-O distances existing in the orthorhombic *Pnma* structure shown in fig.2.4 [30]. At low r_A there are three distinct Mn-O bond lengths which tend to converge to a single value at $r_A \approx 1.23$ Å where the structure changes from orthorhombic (*Pnma* space group) to a more symmetric rhombohedral ($R\overline{3}c$ space group) one.

It is worth to note that, besides the steric effect (i.e. the bare-bandwidth increase) and the EPC reduction, the variation of r_A can affect T_C also by means of configurational disorder induced by chemical doping [31, 32]. It was indeed shown that samples with large variance of r_A have T_C's a factor 7 smaller than samples with the same x and average r_A and smaller r_A variance [32]. We will see in the next section that a possible way to overcome this effect is the use of external hydrostatic pressure which acts on the structure in a way similar to r_A and represents a *clean tool*, i.e. it does not introduce disorder in the system.

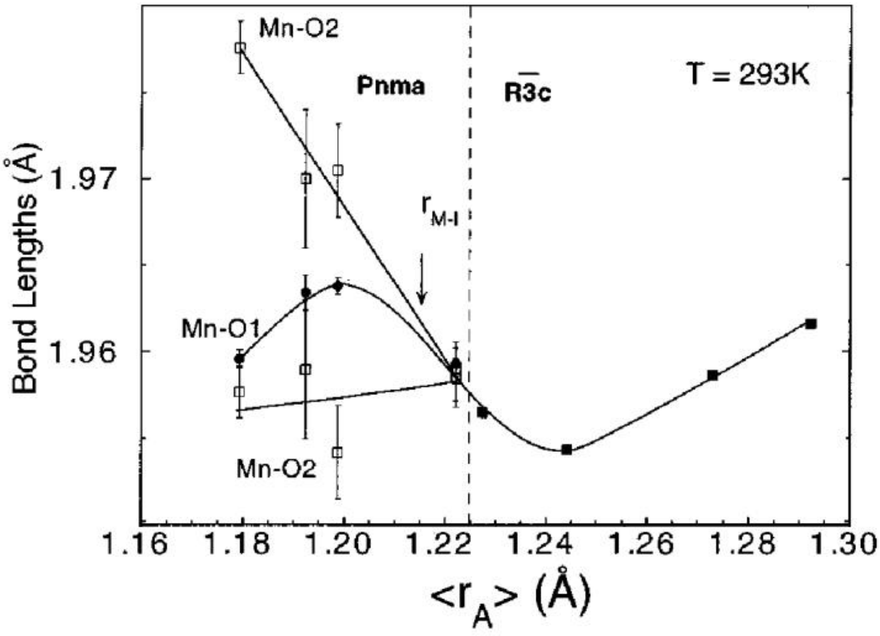

FIGURE 2.4: Mn-O bond lengths of $Re_{0.7}Ae_{0.3}MnO_3$ as a function of r_A at 293 K. Solid lines are guides to eyes [30].

2.4 External hydrostatic pressure

As above mentioned, external pressure P is a good tool for tuning the structure of manganites. There is a large number of experimental investigations showing that external pressure enhances the metallic character of the system, although a large part of them are limited to the 0-2 GPa range [30, 33–48]. Similarly to the increase of r_A, external pressure reduces the free volume around the MnO_6 octahedra forcing their symmetrization.

The T_C dependence on r_A for $Re_{0.7}Ae_{0.3}MnO_3$ is shown in fig.2.5 [34]. A moderate pressure ($P < 2$ GPa) was also applied to a part of the samples and the corresponding pressure-dependent T_C values are also shown in fig.2.5. It is well evident that the effect of external pressure is very similar to that of internal pressure. Indeed data obtained on applying pressure can be properly scaled on r_A-dependent results by means of the conversion factor $\beta = 3.75 \times$

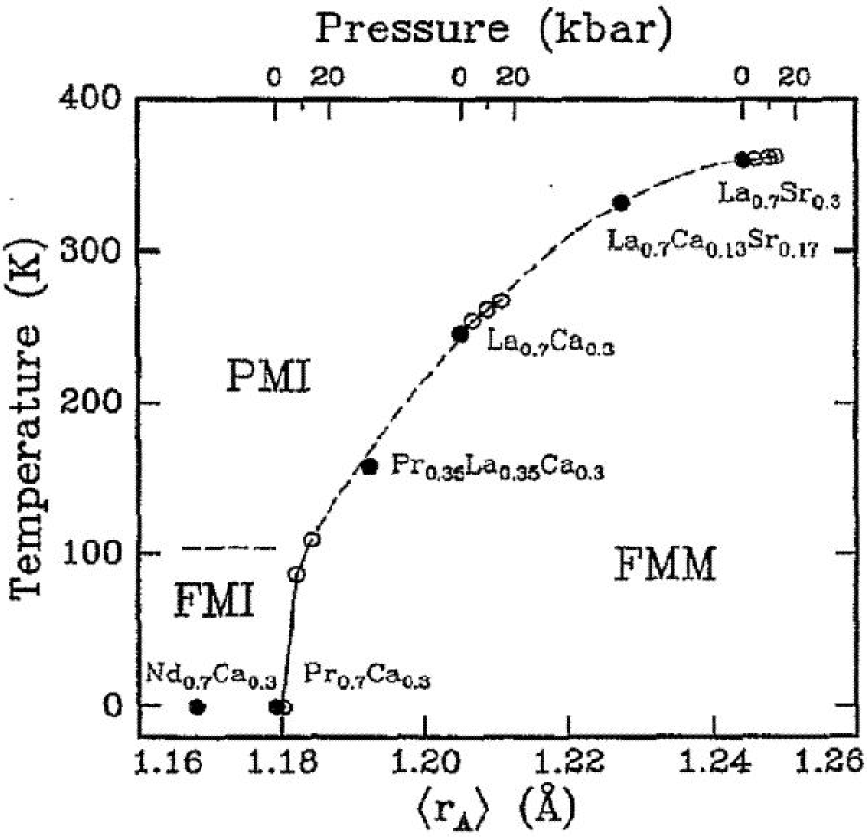

FIGURE 2.5: T_C dependence on r_A (solid symbols, bottom scale) for $Re_{0.7}Ae_{0.3}MnO_3$. Pressure dependent data (open symbols, top scale) are also plotted exploiting the conversion factor (see text). PMI=Paramagnetic insulator, FMI=Ferromagnetic insulator, FMM=Ferromagnetic metal. Lines are guides to eyes [34].

10^{-3} Å/GPa between P and r_A [34].

The similarity between the effect of P and r_A is evidenced also by the structural data shown in fig.2.6, where the average Mn-O bond length d and Mn-O-Mn bond angle Θ for several $x = 0.3$ manganites is shown [30]. It is well evident that, similarly to the case of the r_A dependence, Θ slightly increases and d strongly decreases on pressure. Therefore the pressure-induced enhancement of T_C can be at least partially ascribed to the increase of the bare bandwidth.

A comparison between the pressure dependence of T_C directly measured and calculated from structural data by means of eq.2.2, has been performed by Lauhkin et al. and is shown in fig.2.7 [22]. The logarithmic slope $d\ln T_C/dP$ of $T_C(P)$ is plotted for several $x = 0.33$ manganites as a function of T_C and compared with the corresponding estimates obtained from structural data. It is well evident that the T_C slope of the measured data is much larger than that of the estimate obtained from eq.2.2, thus indicating that, also in the case of pressure dependent data, the steric effect is not sufficient for describing the T_C behavior and the role of EPC must be taken into account [22]. Moreover fig.2.7 shows that on increasing T_C the measured and calculated slopes get closer one to each other, thus indicating that EPC effect becomes less important for larger T_C values (i.e. for the most metallic systems).

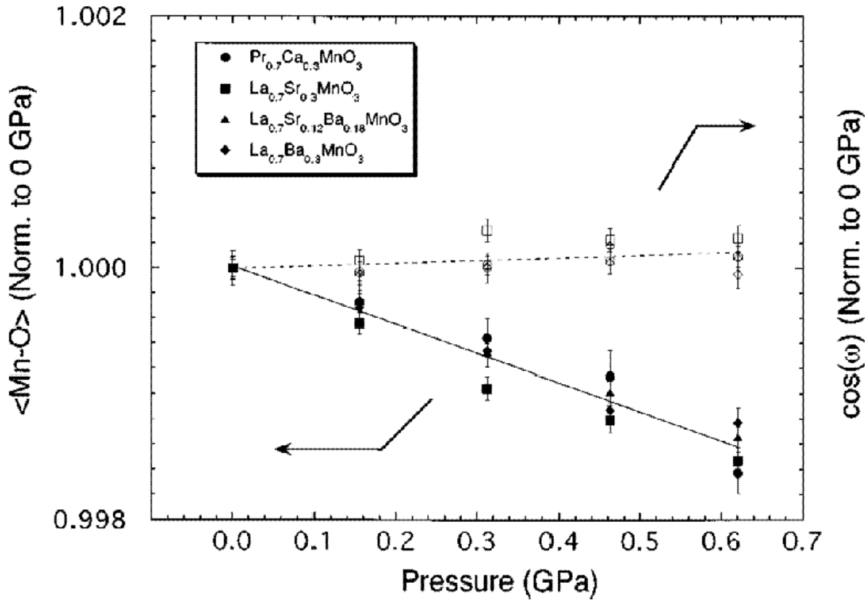

FIGURE 2.6: Pressure dependence of average Mn-O bond length (full symbols) and Mn-O-Mn bond angle (open symbols) for several manganites with $x = 0.3$. Lines are guides to eyes [30].

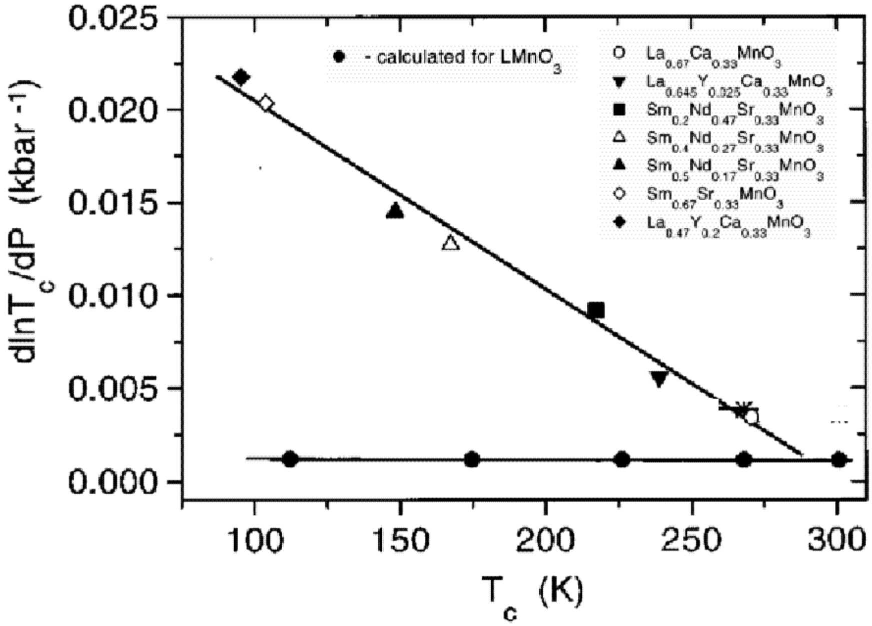

FIGURE 2.7: Calculated (full circles) and measured (other symbols) $d \ln T_C/dP$ as a function of T_C for several manganites with $x = 0.33$. Lines are guides to eyes [22].

The pressure dependence of T_C has been measured for various manganites in the 0-2 GPa pressure range [22,34,36,39,40,43–46,48]. The resulting slopes dT_C/dP as a function of T_C are plotted in fig.2.8. There is clear indication of a kind of universal trend for dT_C/dP vs. T_C (at least for orthorhombic manganites) which strongly decreases on increasing T_C thus indicating that the pressure effect is smaller in the most metallic samples. It is important to note that results on rhombohedral $La_{1-x}Sr_xMnO_3$ samples show a different trend probably owing to the different structure. Since the steric effect seems not to strongly depend on T_C (see fig.2.6 and 2.7), the decrease in dT_C/dP on increasing T_C can be ascribed to a smaller role of the EPC in the systems with the largest T_C.

As discussed above, the major part of the experimental investigations on manganites is limited to the low-pressure range (0-2 GPa). Only recently the study has been extended to higher pressure by means of diamond anvil cells. Bearing in mind the universal trend supposed in discussing fig.2.8, it can be shown that, if it holds also at high pressure, the $T_C(P)$ behavior cannot be simply linear. Indeed, since on increasing T_C, dT_C/dP should decrease, the $T_C(P)$ curve should bend down on increasing P. Therefore high pressure studies are very important to understand the role of structural effect, and in particular of EPC, in the physics of manganites.

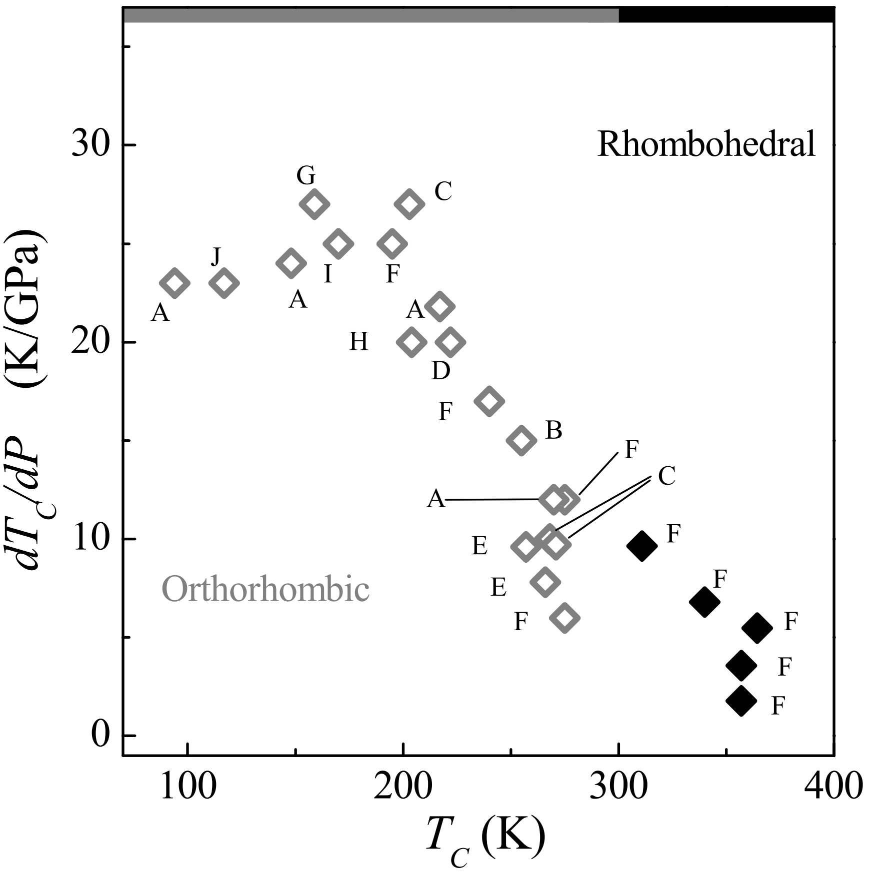

FIGURE 2.8: dT_C/dP as a function of T_C measured in the low pressure regime for several orthorhombic (open symbols) and rhombohedral (full symbols) manganites. References: A= [22], B= [34], C= [48], D= [39], E= [46], F= [36], G= [40], H= [43], I= [44], J= [45].

The first high-pressure study of manganites above 2 GPa was published in 2001 [49] by our group and was followed by other papers [50, 51] in the framework of a research project, in which this Ph.D. thesis is inserted, focused on the high-pressure properties of manganites.

The first of these paper reports high-pressure Raman measurements on $La_{0.75}Ca_{0.25}MnO_3$ [49]. From these data an anomalous high-pressure behavior of the Raman-active JT phonon was observed. This result was interpreted in terms of the onset of an unexpected mechanism which competes with charge delocalization at high pressure. The onset of this mechanism prevents the metallization which can be expected extrapolating the low-pressure data. This paper will be discussed in more detail in sect.4.1.1. These Raman results have been successively confirmed by high-pressure infrared absorption measurements on the same sample [51]. A progressive reduction of the charge-delocalization tendency at high pressure was observed, confirming

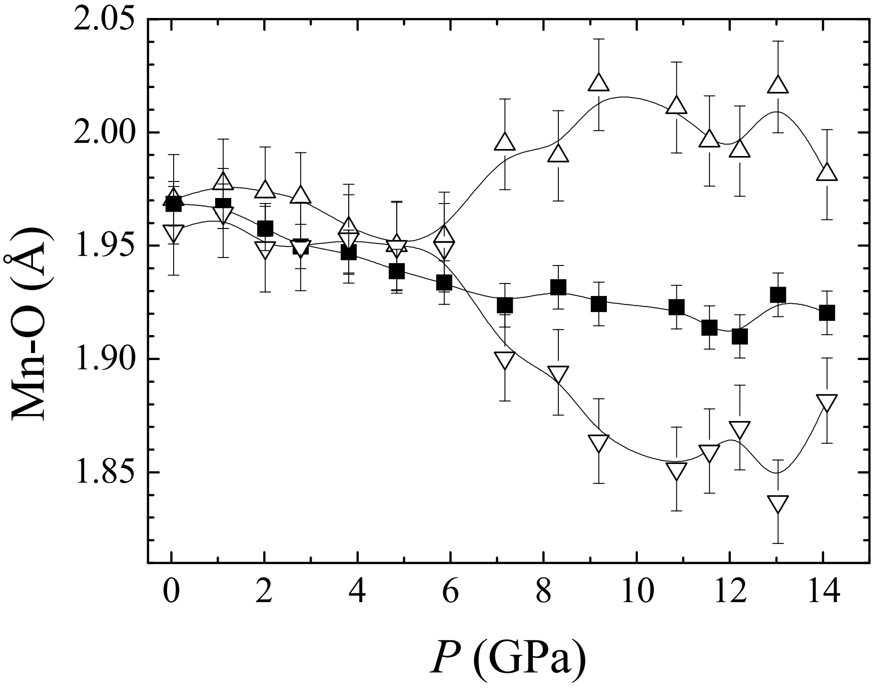

FIGURE 2.9: Pressure dependence of the three Mn-O bond lengths in $La_{0.75}Ca_{0.25}MnO_3$ at room temperature. Lines are guides to eyes [52].

the absence of a pressure-induced IM transition up to 10 GPa. These results will be discussed in sect.5.1. Finally, the comparison between the high pressure properties of pseudocubic $La_{0.75}Ca_{0.25}MnO_3$ with that of layered $Sr_{1.5}La_{0.5}MnO_4$ evidenced the importance of the role played by the MnO_6 octahedra arrangement in determining the charge delocalization processes in manganites [50, 51]. The relevance of the MnO_6 octahedra arrangement will be discussed in more detail in sect.2.6

Loa et al. studied undoped $LaMnO_3$ in the high pressure regime by means of optical and Raman spectroscopy, resistivity measurements, and X-ray diffraction [8]. A pressure-induced suppression of the static JT distortions was observed at around 18 GPa. On the other hand, Meneghini et al. observed the onset of a large coherent JT distortion in $La_{0.75}Ca_{0.25}MnO_3$ at 7-8 GPa [52]. In fig.2.9 the pressure dependence of the three Mn-O bond lengths of orthorhombic $La_{0.75}Ca_{0.25}MnO_3$ determined from Rietveld refinement of X-ray diffraction patterns is shown. It is well evident that that the three Mn-O bond lengths are almost identical[2] for $P < 7 - 8$ GPa, while at higher pressure they clearly separate indicating the onset of a coherent JT distortion [52]. This effect was interpreted with the activation at high

---

[2] The JT distortion at ambient pressure has a small coherence length and thus it is difficult to be detected with high-pressure X-ray diffraction.

pressure of an unpredicted localizing mechanism which competes with the natural delocalizing tendency.

When this Ph.D. thesis started, the above-discussed papers were the only results above 2 GPa reported in the literature. In 2003 and 2004, several papers reporting on manganites at pressures above 2 GPa appeared [53–59]. A localizing effect in the high pressure regime was observed in several manganites by means of resistivity measurements which allowed the determination of $T_C(P)$ [53–57]. In fig.2.10, the pressure dependence of T_C in $La_{60}Y_{0.07}Ca_{0.33}MnO_3$ is shown [53]. It is well evident that T_C first increases with increasing pressure up to $P \simeq 4$ GPa where $T_C(P)$ shows a maximum and then starts to decrease. It is important to note that high-pressure resistivity measurements can be in principle affected by inter-grain effects and much care must be taken when interpreting this kind of results. Nevertheless, these data confirm the onset at high pressure of a localizing mechanism which induces the decrease in T_C.

A possible explanation of the high pressure behavior comes from high-pressure neutron diffraction measurements on $La_{0.67}Ca_{0.33}MnO_3$ shown in fig.2.11 [58]. Comparing the spectra at 0 GPa and 3.8 GPa, it is well evident that two diffraction peaks ascribable to AF ordering appear at high pressure.

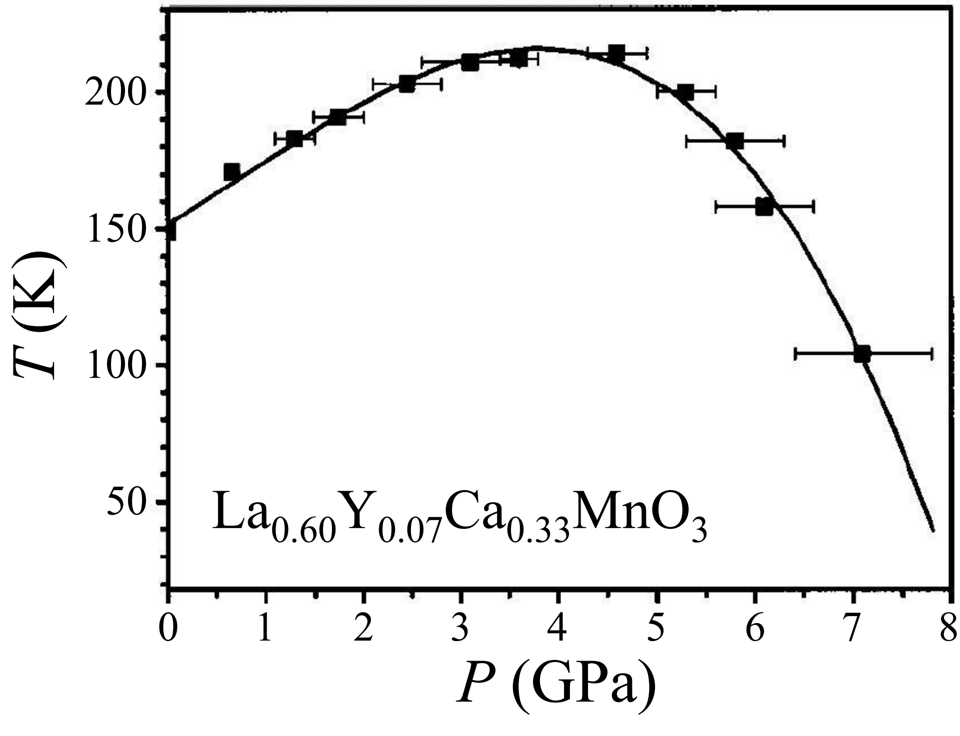

Figure 2.10: Pressure dependence of T_C for $La_{60}Y_{0.07}Ca_{0.33}MnO_3$. Line is a third-order polynomial fit [53].

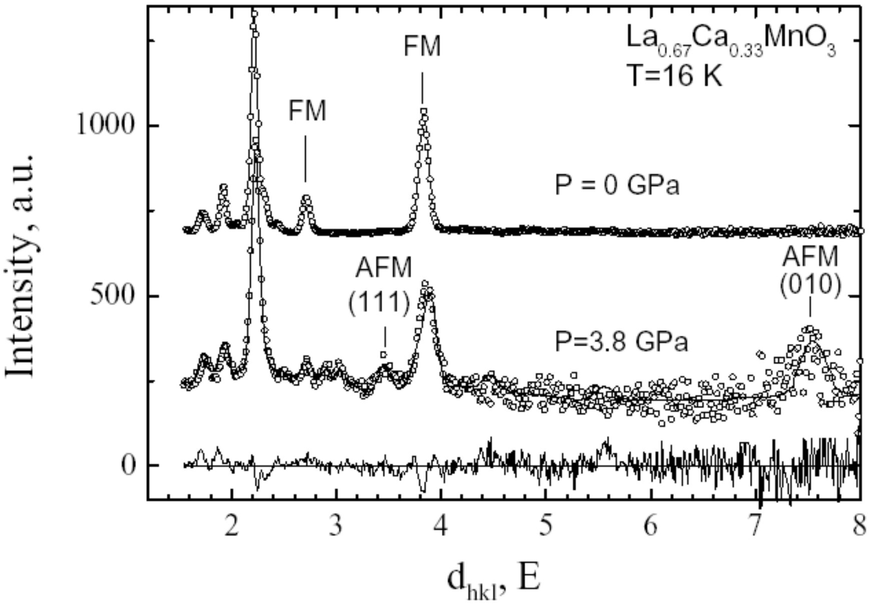

FIGURE 2.11: Neutron diffraction patterns of $La_{0.67}Ca_{0.33}MnO_3$ at 16 K and at 0 and 3.8 GPa (open circles) and relative Rietveld refinements (solid lines). The difference between experimental data and refinement at 3.8 GPa is also shown. FM and AFM indicate the peaks associated with ferromagnetic and antiferromagnetic ordering respectively [58].

One of the purpose of the present Ph.D. thesis is to investigate the nature of the high-pressure anomalies and to verify the role of the AF interaction.

2.5 Anisotropic strain in manganites thin films

Besides the strong experimental effort devoted to the study of manganite bulk-samples, a lot of investigations in the literature are focused on thin-films. Indeed films and multi-layers are very promising from the point of view of applications based on tunnelling effects in artificial hetero-junctions [60]. Moreover, the difference between the physical properties of thin films and bulk samples attracted much attention in the manganites community.

Manganites films can be deposited on various kind of substrates, typically of perovskite-like compounds such as $SrTiO_3$, $LaAlO_3$, and $NdGaO_3$ which are available in single-crystal form [60]. The choice of the substrate is very important since it can strongly influence the physical properties of the film. Indeed, since manganite properties are strongly dependent on the structure, the strain due to the lattice mismatch at film-substrate interface alters dramatically the magneto-conducting properties of the film. The strain of the film ε can be quantified by [60]:

$$\varepsilon = \frac{a_{sub} - a_{bulk}}{a_{sub}} \tag{2.7}$$

where a_{sub} and a_{bulk} are the pseudocubic lattice parameters of the substrate and of the bulk manganite respectively. As an example, the strain effect induced by different substrates on $La_{0.7}Sr_{0.3}MnO_3$ ($a_{bulk} = 3.870$ Å) is schematically represented in fig.2.12: $SrTiO_3$ ($a_{sub} = 3.905$) induces a tensile stress ($\varepsilon \simeq +0.9\%$) compensated by a reduction of the unit cell along the growth direction; $NdGaO_3$ ($a_{sub} \simeq 3.864$ Å) induces a negligible strain ($\varepsilon \simeq 0.1\%$); while $LaAlO_3$ ($a_{sub} = 3.788$ Å) induces a compressive stress ($\varepsilon \simeq -2.2\%$) with consequent expansion along the growth direction [60]. Substrate-induced strain effects have been observed in a large number of manganite films. For instance, the thickness dependence of the lattice parameters of $La_{0.67}Sr_{0.33}MnO_3$ grown on $LaAlO_3$ is shown in the left panel of fig.2.13 [61]. On decreasing thickness, the strain strongly increases and the manganite lattice parameters deviate significantly from the bulk value. Moreover, for small film thickness, the in-plane lattice parameter is almost identical to that of the substrate. In the right panel of fig.2.13 the thickness dependence of the out-of-plane lattice parameter c for $Pr_{0.67}Sr_{0.33}MnO_3$

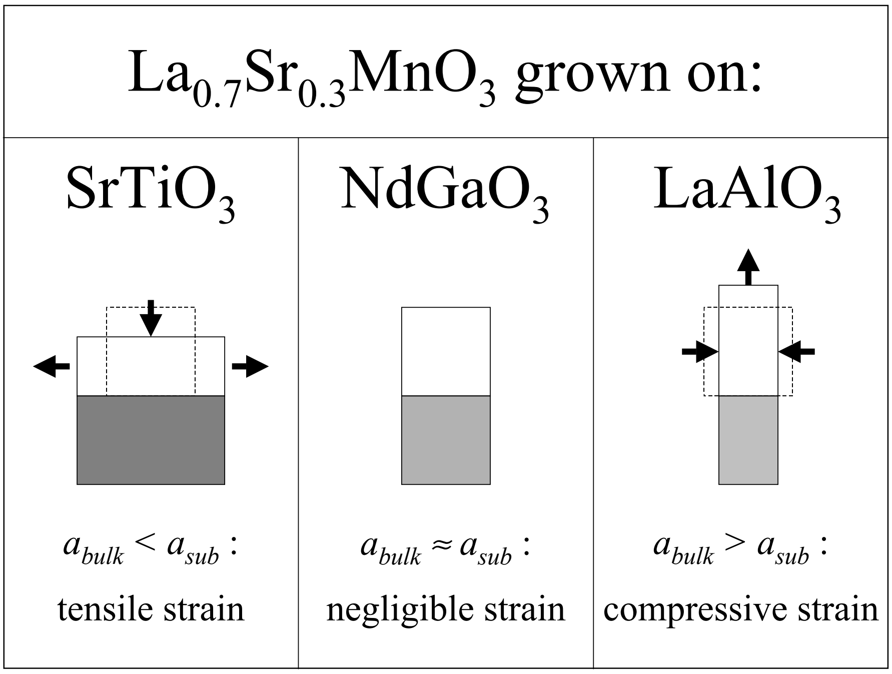

FIGURE 2.12: Schematization of the strain effect induced by different substrates on $La_{0.7}Sr_{0.3}MnO_3$. Dashed boxes represent the bulk unit cell.

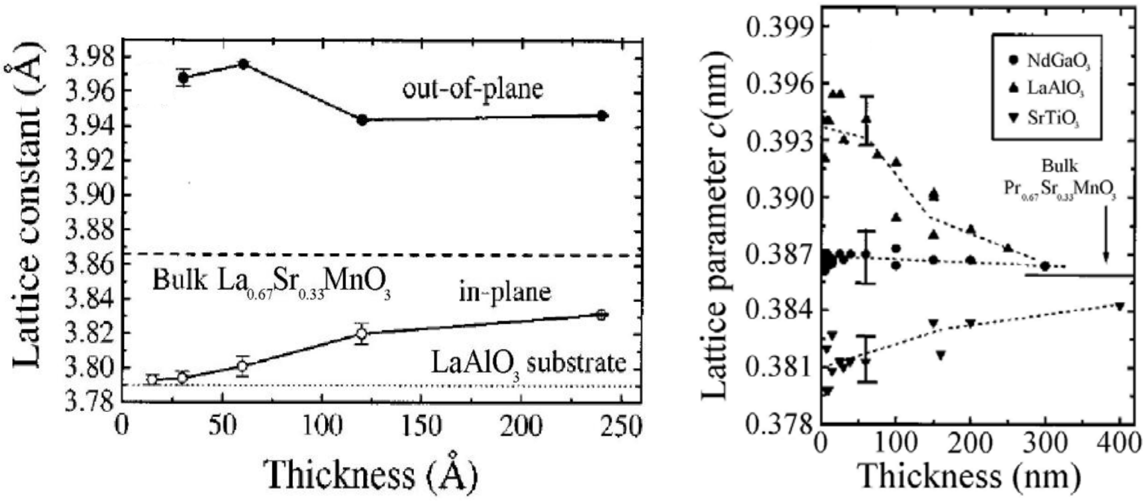

FIGURE 2.13: Thickness dependence of in-plane and out-of-plane lattice parameters for $La_{0.67}Sr_{0.33}MnO_3$ grown on $LaAlO_3$ (left panel) [61] and of out-of plane lattice parameter for $Pr_{0.67}Sr_{0.33}MnO_3$ grown on several substrates (right panel) [62]. Lines are guides to eyes.

grown on $SrTiO_3$, $NdGaO_3$, and $LaAlO_3$ is shown [62]. The strain effect is well evident also in this case: the compressive stress induced by $LaAlO_3$ substrate enhances c on decreasing film thickness, while $SrTiO_3$ induces the opposite effect, and $NdGaO_3$ has negligible effect on c which is almost constant. It is worth to note that for all the three substrates c converges to the bulk value on increasing film thickness. These findings clearly indicate that the structure of thick films is almost relaxed and shows negligible strain, while decreasing thickness below a certain critical value, strain effects become evident and the structure significantly deviates from that of the bulk.

The effect of the substrate on the film can be divided into two kinds of strain: the planar strains ε_{xx} and ε_{yy} along the film plane xy and the axial strain ε_{zz} along the growth direction z. Since the substrate is typically pseudocubic, the planar strain is almost isotropic: $\varepsilon_{xx} = \varepsilon_{yy}$, while the axial strain is related to the planar one by means of:

$$\varepsilon_{zz} = -\frac{2\nu}{1-\nu}\varepsilon_{xx} \tag{2.8}$$

where ν is the Poisson's ratio. The planar and axial strains can be estimated starting from:

$$\varepsilon_{xx} = \frac{a_{bulk} - a_{film}}{a_{bulk}} \qquad \varepsilon_{zz} = \frac{a_{bulk} - c_{film}}{a_{bulk}} \tag{2.9}$$

where a_{film} and c_{film} are the film lattice parameters along the film plane and the growth direction respectively.

As discussed above, strain affects also the magneto-transport properties of the film. In fig.2.14(a) the temperature dependence of resistivity of $La_{0.67}Ca_{0.33}MnO_3$ films with different thickness grown on $SrTiO_3$ is shown [63]. In the same figure, panel (b) shows the temperature dependence of the magnetization of the same films of panel (a) [63]. It is well evident that on decreasing thickness the overall resistivity $\rho(T)$ strongly increases and correspondingly the magnetization $M(T)$ decreases. Moreover, the two characteristic temperatures T_P and T_C (corresponding to the maximum in $\rho(T)$ and to the onset of $M(T)$ respectively) both decrease with decreasing temperature as shown in the inset of fig.2.14(a) [63]. It is worth to note that the thinnest film shows no metallic phase in the whole temperature range.

The $La_{0.7}Sr_{0.3}MnO_3$ films studied in this Ph.D. thesis were grown by means of Pulsed Laser Deposition (PLD) [64] by the group of Prof. G.

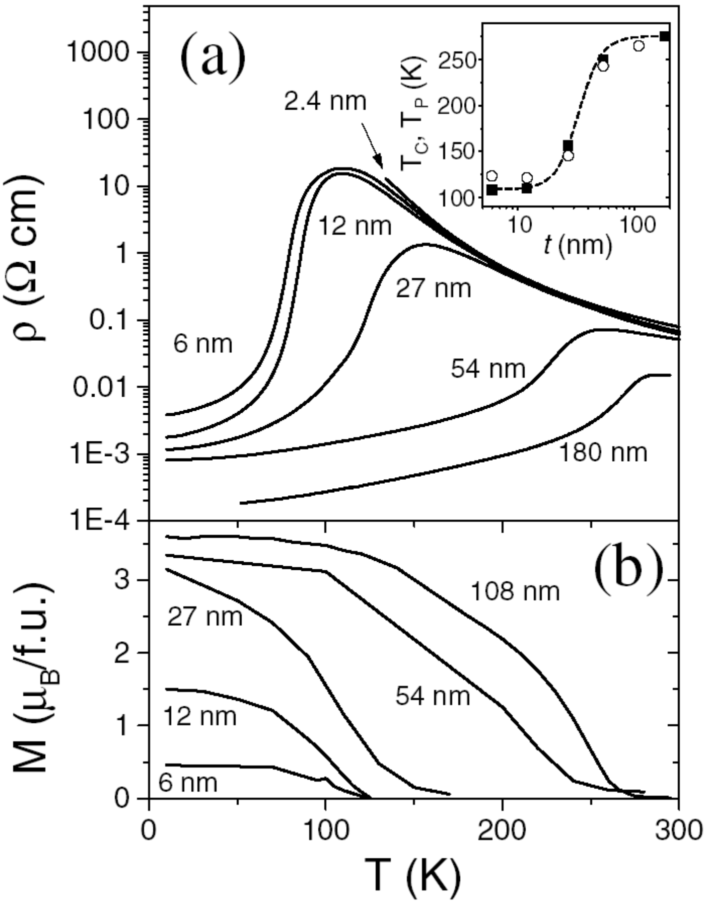

Figure 2.14: Temperature dependence of the resistivity (a) and magnetization (b) of $La_{0.67}Ca_{0.33}MnO_3$ films of different thickness grown on $SrTiO_3$. Inset: thickness dependence of the transition temperature determined from resistivity (full squares) and from magnetization (open circles) [63].

Balestrino (University of “Tor Vergata”, Rome). In this technique, a bulk target of the sample is placed inside a high-vacuum chamber at several centimeters from the heated substrate. A high-power pulsed laser is focused on the target which is vaporized by each laser pulse forming a dynamic plasma which condensates on the substrate forming a layer of the film. Epitaxial films with carefully controlled stoichiometry and thickness can thus be produced. The films so obtained show a behavior similar to that above described either when grown on $LaAlO_3$ or on $SrTiO_3$. The thickness dependence of T_C for these films is shown in fig.2.15. It is well evident that on decreasing thickness T_C first slightly decreases and then almost abruptly drops to zero indicating the disruption of the magneto-conducting properties of the film.

The whole of these results clearly indicate that, besides structural effects, the substrate-induced strain strongly affects both the FM and metallic properties of very thin films.

Recently many authors pointed out that substrate-induced strain is insufficient in describing the thickness dependence of the film properties [60,64,65]. Attempts to fit the Curie temperature by means of eq.2.4 were unsuccessful since the predicted T_C dependence on strain is much weaker than the observed one. Moreover, a strong thickness dependence of T_C was observed also in almost unstrained films such as $La_{2/3}Ca_{1/3}MnO_3$ grown on $NdGaO_3$ [66]. These

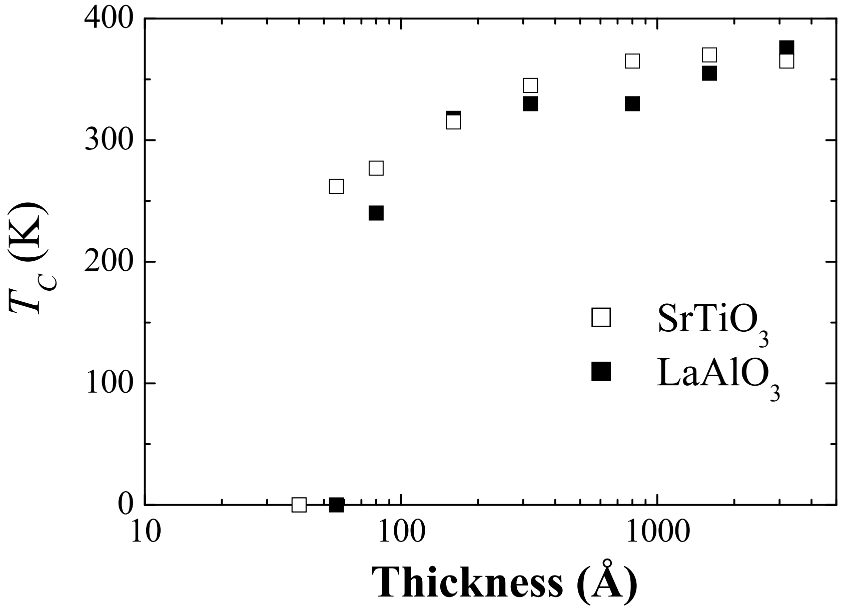

FIGURE 2.15: Thickness dependence of T_C for the first series of $La_{0.7}Sr_{0.3}MnO_3$ thin films grown on $SrTiO_3$ (open symbols) and on $LaAlO_3$ (full symbols) studied in the present Ph.D. thesis [64].

discrepancies have been ascribed to the presence at the film-substrate interface of an insulating *dead layer* a few nanometers thick [60,64,65]. The origin of this dead layer is still unclear but there are some indications that it is induced by a *phase separation* effect between insulating and conducting phases at the interface [65, 66]. Moreover, it is worth to note that film's properties strongly depend also on growth conditions. Indeed the experimental values reported for the relevant parameters (transition temperatures, critical thicknesses, etc.) spread over a wide range even for nominally identical films [60]. These discrepancies are probably ascribable to several uncontrolled growth parameters such as oxygen or cation stoichiometry or substrate quality.

2.6 Non-pseudocubic arrangements of MnO_6 octahedra

The structural effect on manganites is strongly correlated to the specific MnO_6 octahedral array. As discussed in sect.2.3 and 2.4, increasing pressure (both internal or external) reduces the free volume around the octahedra and forces their symmetrization. This effect is observed in manganites with a pseudocubic lattice of octahedra and in principle can be reduced or even suppressed in a different structure. It is therefore important to investigate the role of the octahedral array and in particular to study systems containing MnO_6 octahedral units in a non-pseudocubic environment. For instance, interesting results have been obtained on layered manganites. A combined X-ray and Raman high-pressure study pointed out the importance of the dimensionality of the octahedral array in determining magnetic and transport properties of manganites [50].

In the present Ph.D. thesis, the attention was focused on studying two systems ($LiMn_2O_4$ spinel and hexagonal $SrMnO_3$) in which the octahedral network is still tri-dimensional, but the arrangement contains either edge-sharing or face-sharing octahedra in contrast to the pseudocubic structure where the octahedra are all corner-sharing. The properties of these two systems are briefly described in setcs.2.6.1 and 2.6.2.

2.6.1 $LiMn_2O_4$ spinel

An interesting MnO_6-based compound is the $LiMn_2O_4$ spinel. This system has attracted a lot of attention in the last years owing to its possible application as a cathode material for Li-based rechargeable batteries [67]. The structure of $LiMn_2O_4$ is that of the cubic spinel $MgAl_2O_4$ (space group $Fd\bar{3}m$) and it is shown from two different perspectives in fig.2.16. As apparent, LiO_4 tetrahedra and MnO_6 octahedra characterize the structure which is substantially composed by an alternative stacking of two kind of layers as shown in fig.2.17. The octahedra share an edge with each nearest neighbor, while the tetrahedra share their corners with the octahedra. It is worth to note that the LiO_4 tetrahedra are regular (i.e. the O-Li-O angles are 109.47°), while the octahedra are slightly distorted. The octahedral distortion, schematically represented in fig.2.18, can be ascribed, in this compound, to the JT effect. Indeed, the average Mn valence is 3.5 and thus, in the ionic approximation, there are both Mn^{3+} (JT ions) and Mn^{4+} (non-JT ions) in the structure.

$LiMn_2O_4$ is an insulator with no long-range magnetic order [68, 69]. The Curie-Wiess behavior indicates short-range AF interactions. These probably arise from SE coupling with geometrical frustration due to the 90° value of the Mn-O-Mn angles in the spinel structure [69].

One of the most interesting feature of $LiMn_2O_4$ is that it undergoes a structural transition around room temperature [70]. Indeed the low temperature phase is orthorhombic (space group $Fddd$) [71] with an enlargement of the unit cell from the $a \times a \times a$ cubic cell to the $3a \times 3a \times a$ orthorhombic cell (i.e. the orthorhombic cell is equivalent to nine cubic cells). Superstructure peaks appear in the diffraction patterns on crossing the transition temperature [71]. The temperature dependence of both the lattice parameters and

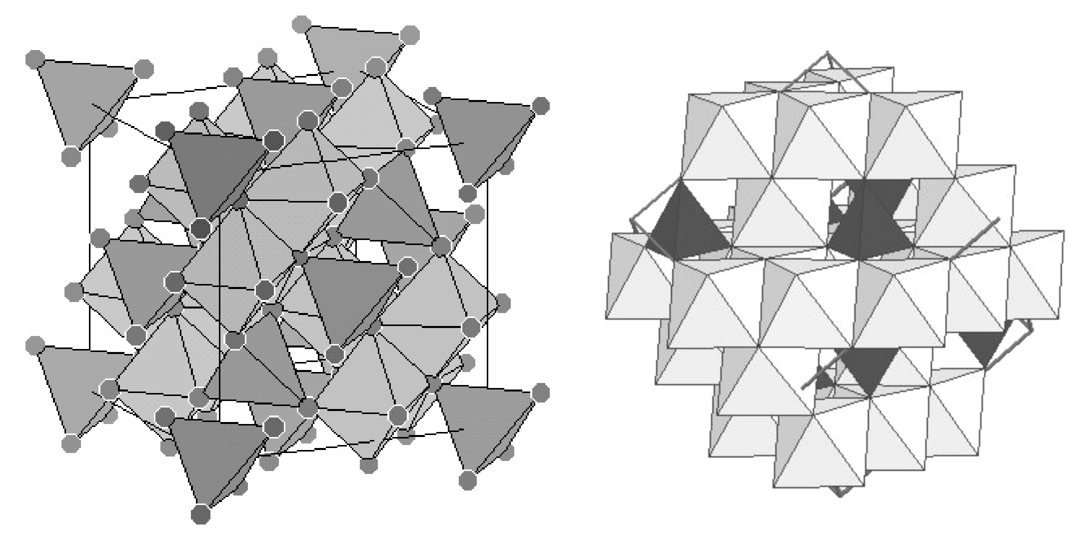

FIGURE 2.16: Representation of the spinel structure from two different perspectives. The LiO_4 tetrahedra (dark) and MnO_6 octahedra (light) are evidenced.

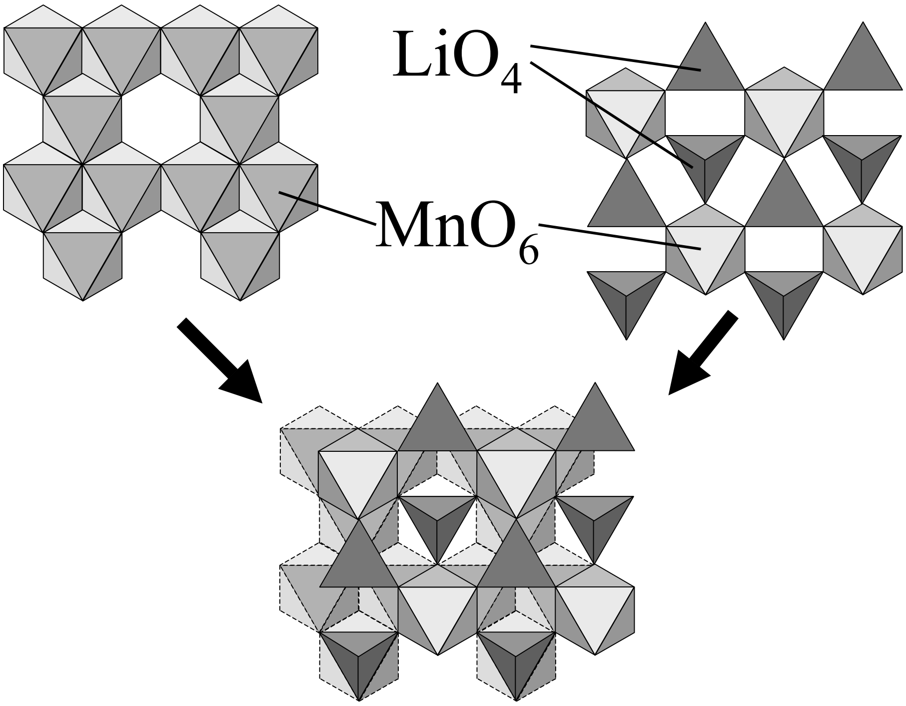

Figure 2.17: Representation of the two kind of layers composing the spinel structure (top) and their overlap (bottom).

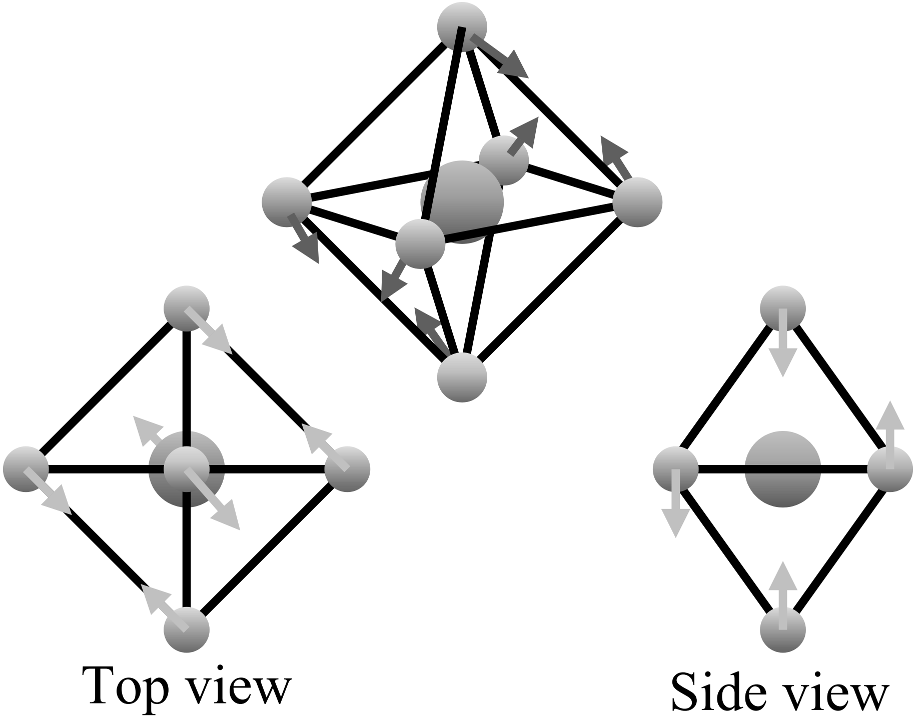

Figure 2.18: Distortion of the MnO$_6$ octahedra in the spinel structure.

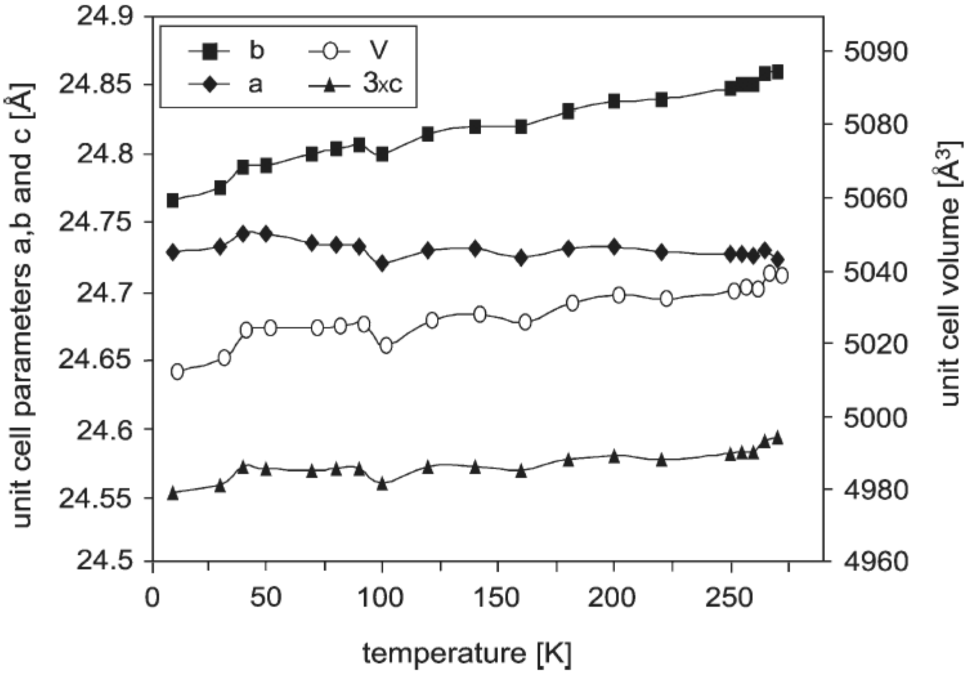

FIGURE 2.19: Temperature dependence of the lattice parameters and unit-cell volume of $LiMn_2O_4$ in the low-temperature orthorhombic phase [72].

of the unit-cell volume in the orthorhombic phase are shown in fig.2.19 [72]. It is worth to note that the unit cell volume in the orthorhombic phase is very close to nine times that of the cubic phase ($a = 8.2413$ Å at $T = 360$ K [72]). The transition shows a first-order nature with a 15-20 K thermal hysteresis and affects the conductivity. The temperature dependence of the resistivity is shown in fig.2.20 [68]. A large increase in resistivity (about one order of magnitude) at the transition with a pronounced thermal hysteresis is apparent.

The structural transition has been ascribed to a charge-ordering process similar to $La_{0.5}Ca_{0.5}MnO_3$ (see sect.1.2.1): the Mn^{3+} and Mn^{4+} order periodically[3] causing a remarkable resistivity increase [71]. A cooperative JT distortion of the MnO_6 octahedra is thus established in the low temperature phase.

$LiMn_2O_4$, similarly to manganites, shows two phases which are characterized by high and low JT distortions. The main difference is that the effect of temperature in manganites and in $LiMn_2O_4$ is reversed. The study of $LiMn_2O_4$ could allow investigation of the JT effect unscreened by the DE mechanism and intercalated in a different MnO_6 octahedra environment.

---

[3] The charge ordering process in $LiMn_2O_4$ is not complete and the periodic array consists of Mn^{+4} ions and Mn ions with fractional charge between +3 and +4 [71].

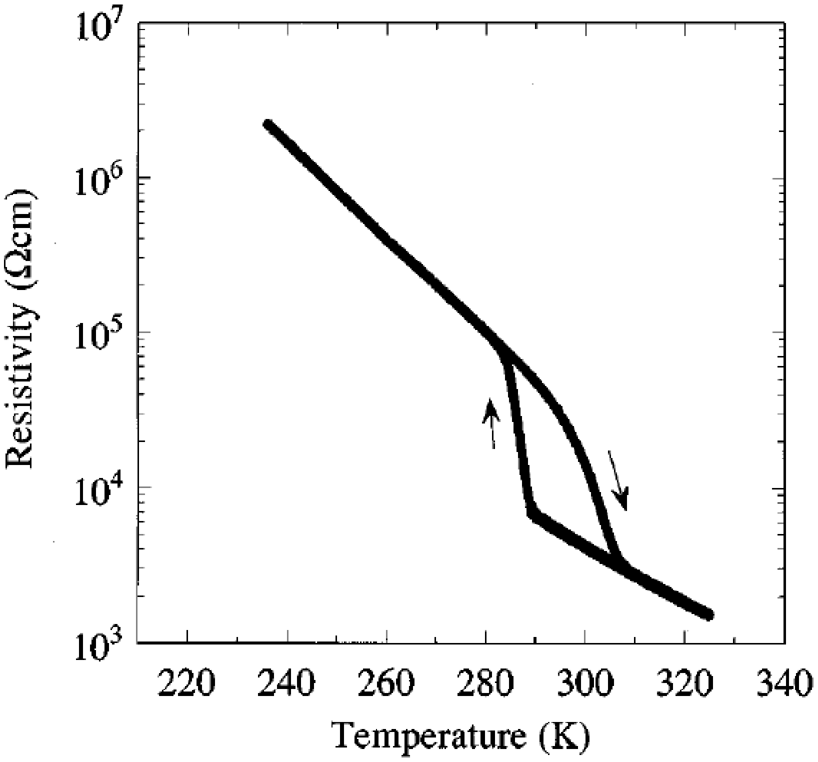

FIGURE 2.20: Temperature dependence of the resistivity of $LiMn_2O_4$ taken on cooling and warming [68].

2.6.2 Cubic and hexagonal $SrMnO_3$

As discussed in sect.1.1, the stability of the octahedral array, and thus of the perovskite structure of ABX_3 compounds, is determined by the tolerance factor TF (see eq.1.1). In particular, when the A ion is large, $TF > 1$ and the perovskite structure is usually substituted by an hexagonal one. In this case there is large number of possible hexagonal structures which are distinguished by the stacking of the AX_3 layers [73]. The three different types of AX_3 layers are shown in fig.2.21 and each hexagonal structure is represented by a particular stacking of layers. It is worth to note that in all the possible structures MnO_6 octahedral units are still present. The cubic perovskite structure and the close-packed hexagonal structure can be represented by an *abc* or an *ab* stacking of the layers, respectively. Between these two limiting cases, there is a large variety of intermediate hexagonal structure composed by long layers blocks [73] as shown in fig.2.22. It is well evident that in this kind of structures there are chains of face-sharing octahedra connected by corner-sharing octahedra. The distance between two B ions is larger for corner-sharing octahedra than for face-sharing ones, therefore in the latter

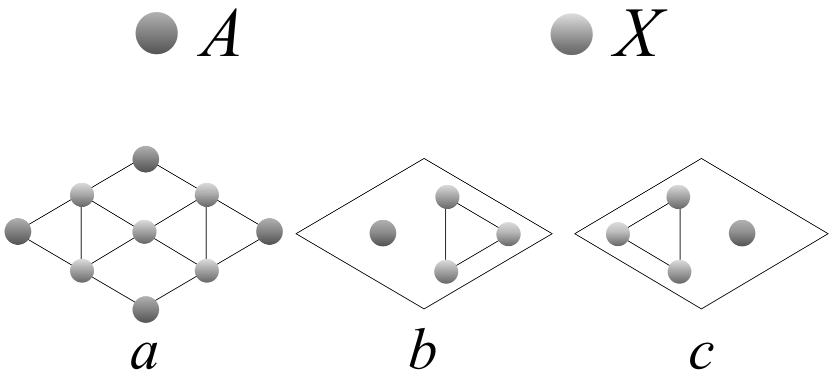

FIGURE 2.21: Representation of the three kinds of AX_3 layers composing the possible hexagonal structures of ABX_3 compounds.

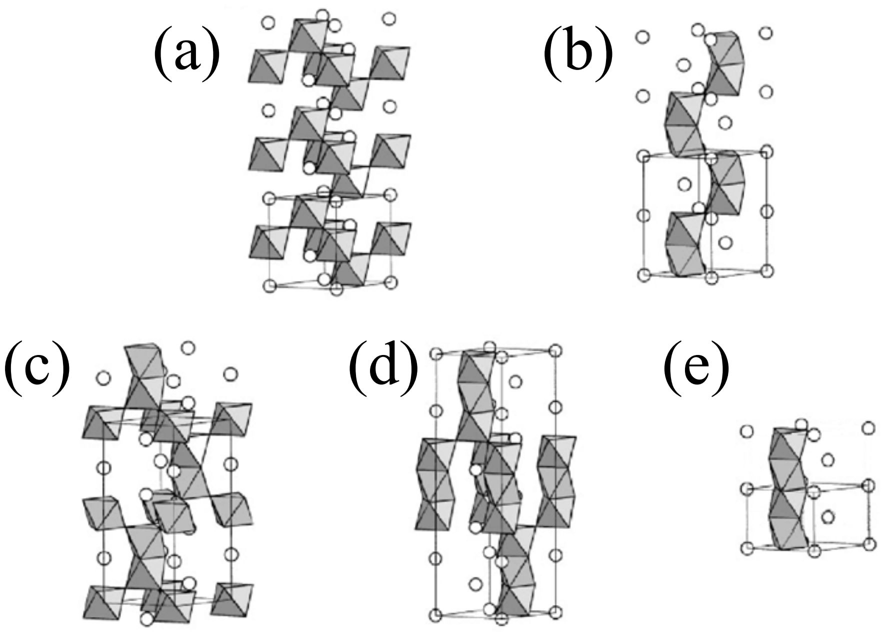

FIGURE 2.22: Examples of the structures obtainable by means of different stacking of AX_3 layers. (a) cubic (b) 4-layer hexagonal (c) 6-layer hexagonal (d) 9-layer hexagonal (e) close-packed hexagonal.

case the Coulomb repulsion between B cations is larger. The X anions change their position in order to screen the repulsion and thus the octahedra distort [74]. The number of B cations contained in a single chain of face-sharing octahedra changes continuously from 1 in the cubic structure to ∞ in the close-packed hexagonal structure. Therefore, in the latter case the distortion is maximum and it decreases on evolving the structure towards the cubic one [74].

$SrMnO_3$, besides representing the end-member of the $La_{1-x}Sr_xMnO_3$ family, is a very interesting compound from the structural point of view. Indeed for this compound the tolerance factor is very close to unity ($TF = 1.05$) and thus it can be synthesized in both the cubic ($Pmmm$ space group) and 4-layer hexagonal ($P6_3/mmc$ space group) structure [75] (see fig.2.23). The latter is obtained by means of an *abac* stacking of the SrO_3 layers. Owing to these two possible structures, the study of $SrMnO_3$ could represent a good tool in investigating the role of the MnO_6 octahedra arrangement in the physics of manganites.

The magnetic phase of $SrMnO_3$ is a G-type antiferromagnet for both cubic and hexagonal structure with $T_N = 260$ K [76] and 278 K [77] respectively. The conductivity is quite low in both phases showing insulating behavior, but interestingly the cubic compound shows a conductivity about two orders of magnitude larger than that of the hexagonal compound [78]. It is important to note that, since the Mn^{4+} ions are in octahedral coordination in both structures, a $t_{2g}^3 e_g^0$ electronic configuration can be expected for these compounds. Therefore, there should be a filled t_{2g} and an empty e_g bands and thus an insulating state. Moreover, no DE mechanism is expected in these systems (owing to the absence of e_g itinerant electrons) and the AF phase is probably ascribable to SE interaction. Finally the different conductivity of the two compounds is probably due to the presence in the hexagonal structure of 90° Mn-O-Mn angles which strongly suppress the Mn-Mn effective hopping integral (see eq.2.1). In analogy with the iso-structural compound $BaRuO_3$ [79],

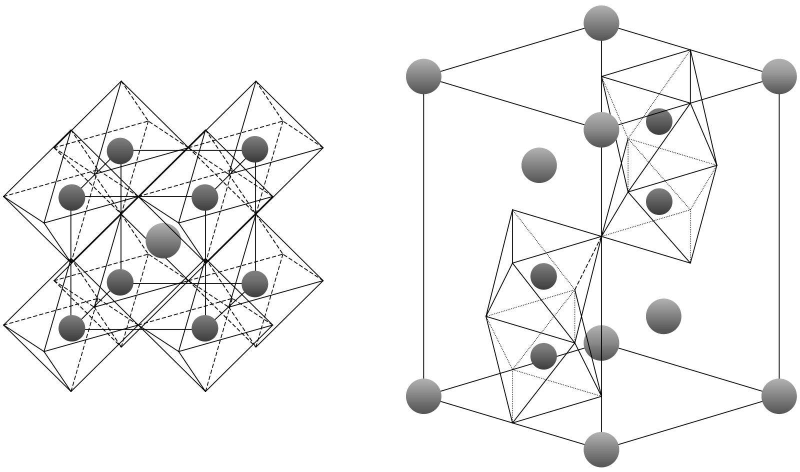

FIGURE 2.23: The two possible structures of $SrMnO_3$: cubic (left) and 4-layer hexagonal (right).

a direct-exchange mechanism between Mn ions inside face-sharing octahedra can also be present.

The difference in the conducting properties of the two possible structures of $SrMnO_3$ indicate that the role of the octahedra arrangement is very important in determining the transport properties of manganites. Since there is neither DE mechanism nor JT effect in $SrMnO_3$, a low-temperature study on this system could provide a deep inside in the AF interaction of manganites and its connection with the octahedral array.

Chapter 3

Experimental Techniques

In this chapter a brief description of the various experimental apparatuses employed in the present work is reported. In particular the principles of diamond anvil cell for high-pressure generation is described and the different Raman, infrared and X-ray diffraction setups used are described. Finally a schematic measurement plan is reported.

3.1 The high-pressure diamond anvil cell

The diamond anvil cell (DAC) is a very simple but powerful tool for investigation of matter under extreme pressure [80]. The working principle is very simple and is shown in fig.3.1. A metallic plate with a small hole in the center is paced between two diamond anvils and a moderate force is exerted on the external faces of the diamonds. The large ratio between the surface of the external and internal anvil faces strongly amplifies the effect of the external force leading to very large pressure inside the hole. The metallic plate acts as a gasket and avoids anvil failure and sample's lost. The maximum pressure depends on several factors such as the dimensions of the diamond and of the hole, the material of the gasket, the friction between diamond and gasket (which exerts a force which compensates to the internal pressure) and the quality of the diamond. Pressure of several tenths of GPa can be applied and with particular technical implementations the Mbar range was reached [1].

Diamonds are very suitable for anvils owing to their hardness and transparency to electromagnetic ration in a wide frequency range. Therefore the natural applications of DAC are spectroscopic techniques such as Raman and

---

[1] The maximum pressure reached with a DAC is of about 3.4 Mbar [81].

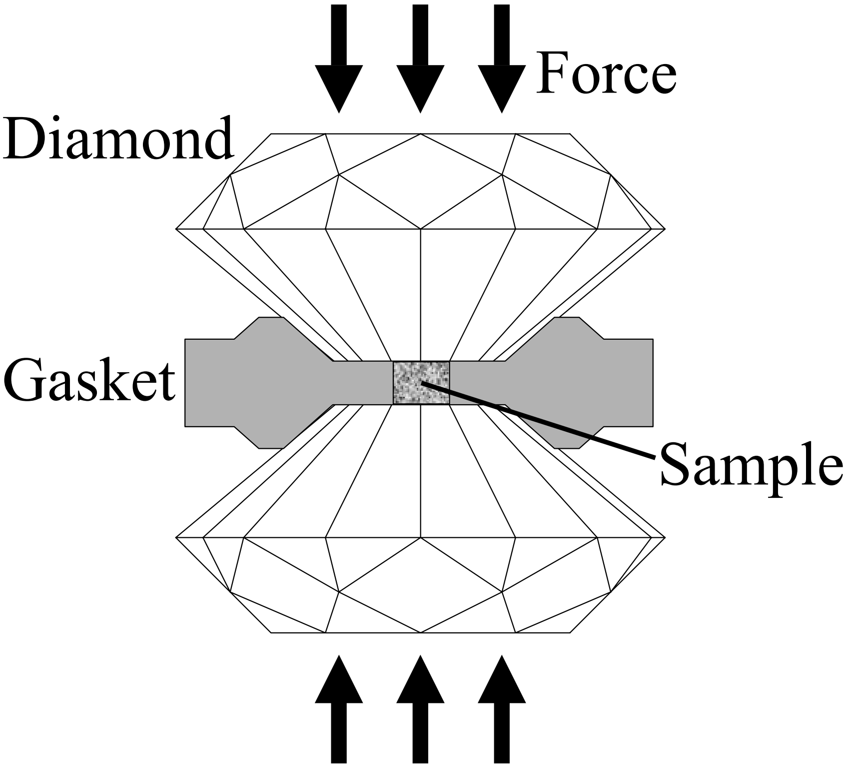

Figure 3.1: Schematic representation of the working principle of the diamond anvil cell.

infrared spectroscopy and X-ray diffraction and absorption [80]. The inner face of the diamond (culet) is a 16-side polygon with a 200-800 μm typical diameter. The external face diameter is 2-4 mm large and the diamond is typically 1-3 mm thick. The quality of diamonds depends on the number of impurities and vacancies in the crystal. For Raman and X-ray measurements, type Ia diamonds can be employed, while infrared spectroscopy requires more expensive and higher quality type IIa diamonds.

The typical infrared transmission and reflection of diamond are shown in fig.3.2 [82]. Apart from the strong multiphonon absorption in the 1900-2600 cm^{-1} range, it is well evident the high transparency in the far- and mid-infrared region. Diamonds are also very suitable for Raman spectroscopy owing to their large transparency in the visible light region. The only disadvantage is the presence of the strong one-phonon Raman contribution at around 1300 cm^{-1} which prevents the spectrum reliability in the 1200-1500 cm^{-1} range.

The gasket material can be either molybdenum (for measurements in the 0-5 GPa range), or stainless steal (0-20 GPa), or rhenium (0-50 GPa).

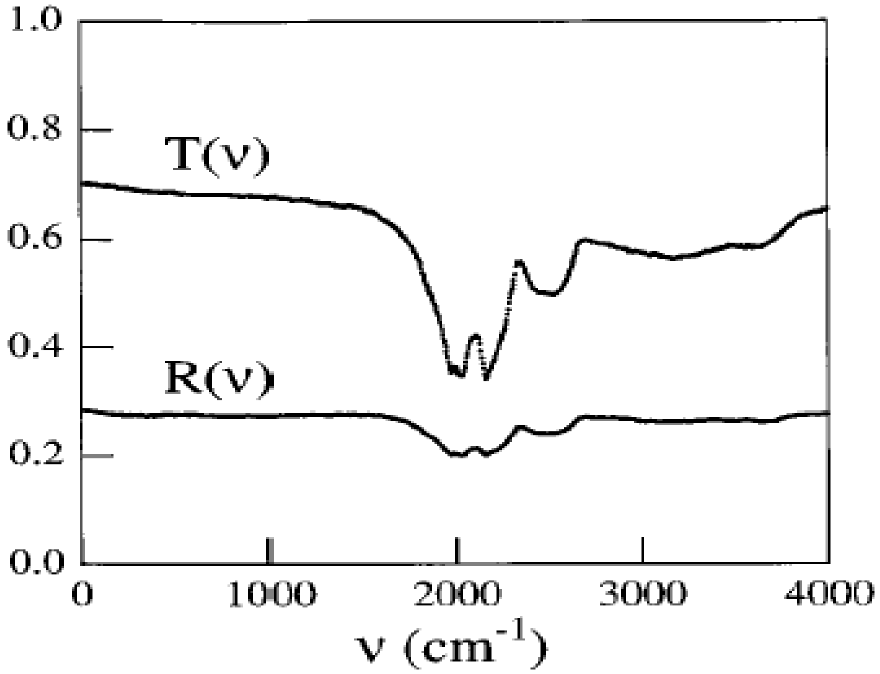

Figure 3.2: Infrared reflection and transmission in the 0-4000 cm^{-1} range of a diamond plate 0.5 mm thick [82].

Gasket thickness is typically of 40-100 μm and gasket hole diameter ranges from 100 μm to 400 μm. The sample chamber dimension is thus very small and all experiments should deal with this limitation. Gaskets are prepared by pre-indenting a 200 μm thick foil between the diamonds until the desired thickness is reached. Owing to the out-flowing of gasket material during the indenting procedure, the indented gasket has a characteristic crater-like shape which perfectly allocates the diamonds and ensures massive support. Finally a hole is made at the center of the indented gasket by means of electro-erosion.

Together with the sample, a proper hydrostatic medium must be placed inside the gasket in order to avoid pressure gradients in the sample chamber, at least in the cases in which the sample is not hydrostatic itself. Very good hydrostatic media are liquid noble gases (Ar, Xe, or Ne) or nitrogen but they require a cryogenic or high-pressure DAC-loading device. For pressure up to 20 GPa, alkali halides (NaCl, KBr, or CsI) can be employed. It is quite obvious that the hydrostatic medium must me transparent to electromagnetic radiation used in the experiment. In mid infrared measurements KBr (transparent down to 500 cm^{-1}) can be employed, while in the far infrared region CsI (down to 200 cm^{-1}) or even petroleum-jelly grease (transparent in the whole far-infrared region) can be used. For Raman measurements NaCl works well, while in X-ray experiments silicon oil can be employed.

Diamonds are mounted on two hard hemispheres of tungsten carbide. The hemispheres are placed on two mechanical supports (piston and cylinder) which ensure precise movement of the diamonds along their axis. The mechanical efficiency of the DAC is fundamental for reaching high pressures. In temperature dependent measurements, low thermal expansion materials must be chosen. Several devices are employed for generating the external force. They can be either mechanical (pistons or screws) or pneumatic [80]. The latter choice consists on flowing a gas (typically helium) at a moderate pressure (0-200 bar) inside a metallic membrane tightly screwed on the cylinder and able to expand against the piston. This system allows fine regulation of the pressure and remote control which is very important when performing measurements at low temperature.

3.1.1 Ruby fluorescence for pressure determination

One of the main problem of the early studies with DACs was the pressure determination. The discovery of the ruby fluorescence technique strongly extended the possibility of these devices. This technique is based on the strong dependence of the fluorescence lines of ruby (Al_2O_3 with Cr^{3+} impurities) on the interatomic distances and thus on pressure. The main advantages are that this fluorescence signal is very strong and composed by two narrow lines (see fig.3.3) [80]. Owing the very large strength of the signal, it can be well detected even from a very small ($\sim 10\ \mu$m diameter) ruby sphere which can be thus safely placed in the gasket hole without altering the measurement. The fluorescence can be thus excited by a laser precisely focused on the small ruby and detected by a monochromator.

Both the fluorescence lines increase their peak wavelength on increasing pressure. The pressure calibration is typically performed by means of the stronger R_1 line whose pressure dependence was established and improved during the years by extrapolating state-equations and non hydrostatic data from shock-wave experiments [83,84]. The most widely used ruby calibration scale is shown in fig.3.4 [84]. From this calibration the pressure can be obtained from the wavelength shift $\Delta\lambda$ from:

$$P(\Delta\lambda) = \frac{A}{B}\left[\left(1+\frac{\Delta\lambda}{\lambda_0}\right)^B - 1\right] \tag{3.1}$$

where $A = 1904$ GPa and $B = 7.665$ are constants [84] and $\lambda_0 = 694.2$ nm is the R_1 line peak wavelength at ambient pressure. In 0-30 GPa regime, eq.3.1

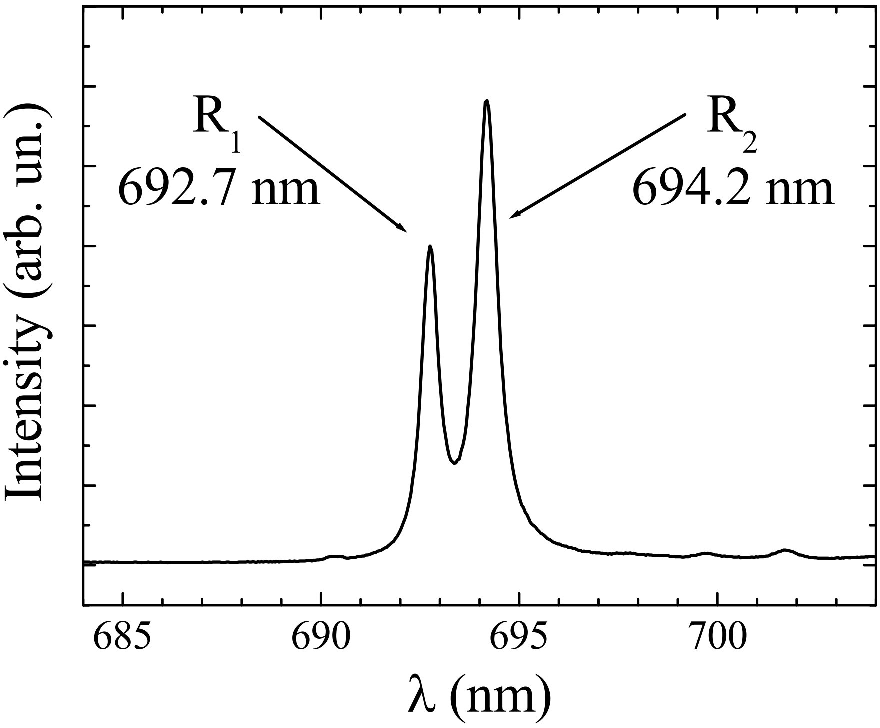

FIGURE 3.3: Ambient pressure room-temperature fluorescence spectrum of ruby.

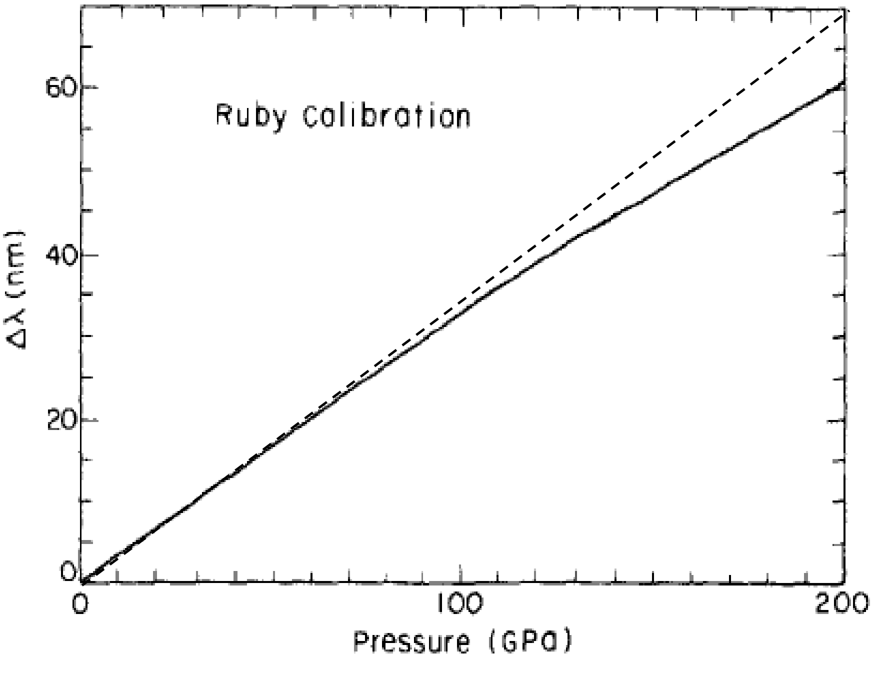

FIGURE 3.4: Pressure dependence of the wavelength shift of the R_1 ruby fluorescence line (solid line) [84] and linear approximation in the low pressure regime (dashed line) [83].

can be approximated with a linear dependence [83]:

$$P = \alpha \Delta \lambda \tag{3.2}$$

with $\alpha = 2.74$ GPa/nm. The ruby fluorescence technique ensure pressure indetermination of ±0.1 GPa in the 0-10 GPa range, ±0.5 GPa for pressure up to 30 GPa, and ±1 GPa or more at higher pressure.

Since the R_1 line depends on temperature also, a correction to eq.3.1 (or equivalently to eq.3.2) must be applied when working at variable temperature. The temperature-induced wavelength shift was measured at ambient pressure and fitted to a cubic law [85]:

$$\Delta \lambda(T) = C_1(T - T_0) + C_2(T - T_0)^2 + C_3(T - T_0)^3 \tag{3.3}$$

where $C_1 = 0.00696$ nm/K, $C_2 = 7.76671 \cdot 10^{-6}$ nm/K^2, $C_3 = -1.697 \cdot 10^{-8}$ nm/K^3, and $T_0 = 298$ K [85]. Assuming that the temperature-induced shift is pressure independent, eq.3.1 or 3.2 can be simply corrected by subtracting from $\Delta\lambda$ the thermal contribution given by eq.3.3.

3.2 Raman setup

All Raman measurements reported in this work have been performed by means of a commercial LABRAM-infinity micro-Raman apparatus. This instrument was installed in our laboratory at the end of 2002 and part of the work done during this Ph.D. thesis was devoted to the setup the apparatus and the preliminary test measurements. The optical scheme is shown in fig.3.5. The light emitted by the He-Ne laser (632.81 nm wavelength) is filtered, if needed, by filters with attenuation factors from 1 to 10^{-4} and reflected by the notch-filter inside the microscope. Objectives with 10× to 50× magnifications can be used for the microscope which focuses the laser onto the sample and collects the backscattered light sending it again on the notch-filter. In transmission mode the notch filter efficiently rejects the elastic Rayleigh contribution and transmits the Raman signal above ~ 200 cm^{-1}. Before entering the monochromator, the light is focused into an adjustable pinhole which provides the confocal effect, i.e. the possibility, by adjusting the pinhole, of selecting along the optical axis the region of the sample from which the scattered light is collected and analyzed. Two monochromators (with 600 or 1800 lines/mm) can be used and they both can be rotated in order to select the spectral range. Photons are revealed by a cooled multichannel charge coupled device (CCD) detector. The spectrum of a neon lamp was used for frequency calibration.

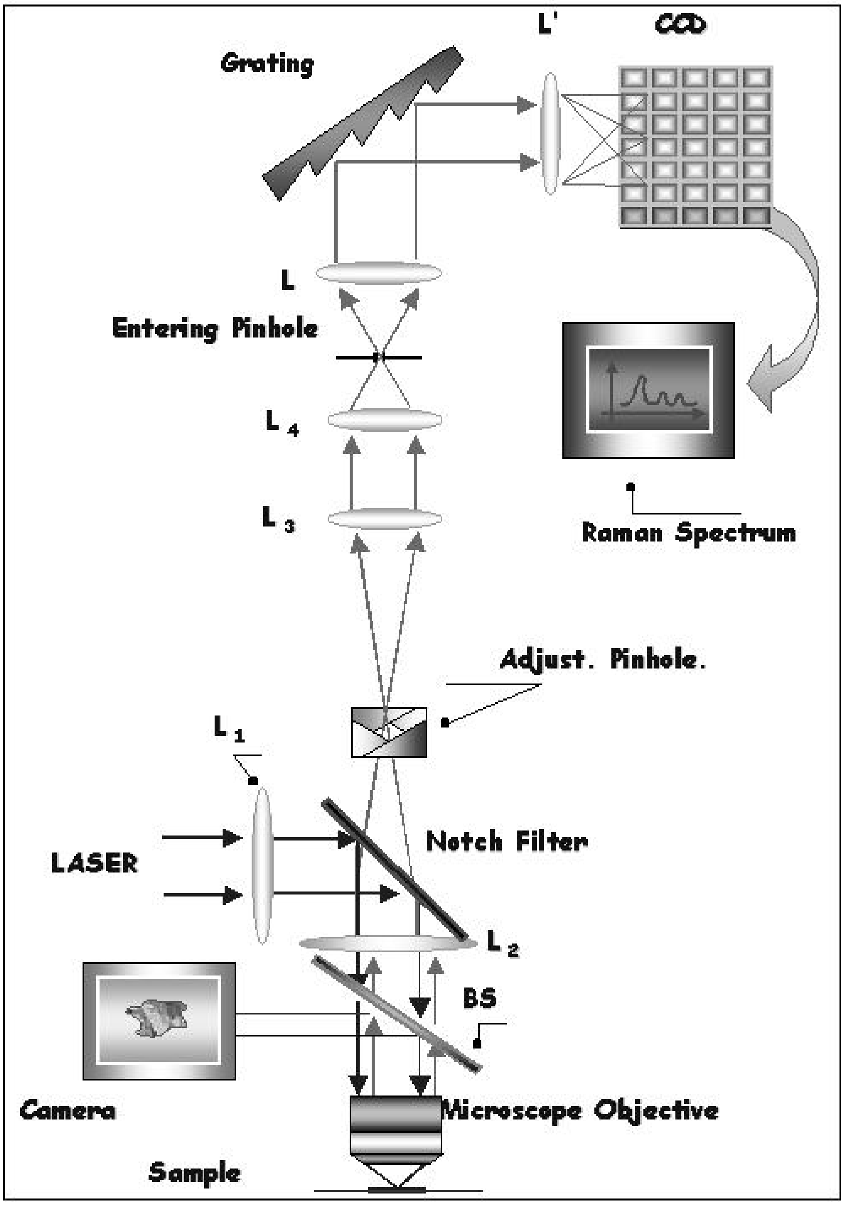

FIGURE 3.5: Optical scheme of the micro-Raman spectrometer employed in the present work.

3.2.1 High-pressure Raman setup

For the high pressure measurements, a 20× objective with 22 mm focal length was used and the pinhole was adjusted in order to collect light from a region of only few microns along the optical axis thus suppressing possible spurious signal from diamond and hydrostatic medium. In this configuration the laser spot on the sample is only few microns diameter. The 1800 lines/mm grating was chosen obtaining a total resolution of about 3 cm^{-1}.

A BETSA DAC with 45° conical aperture and equipped with type IIa low fluorescence diamonds with 800 μm culet diameter was employed in these measurements. The gasket was made of stainless steal with a 400 μm diameter hole. The samples were finely milled (average grain size of 1 μm) and placed at the center of a NaCl pellet (which acts as hydrostatic medium) presynthesized at high-pressure inside the gasket hole. This procedure ensures good hydrostatic conditions and the high thermal conductivity of diamond prevents strong heating of the sample impinged by the laser spot. A small ruby chip was also placed inside the gasket hole for pressure calibration. Ruby fluorescence was directly measured by means of the Raman spectrometer.

3.2.2 Low temperature Raman setup

For the low-temperature Raman measurements, the same spectrometer described in sect.3.2 was employed. A commercial OXFORD MicrostatHe liquid nitrogen continuous-flux cryostat was employed for cooling the sample. Thermoregulation was performed by means of a fine regulation of the nitrogen flux and an electrical heater placed on the cold finger of the cryostat. A platinum thermometer was placed as close as possible to the sample for temperature determination. This experimental setup allows temperature dependent measurements in the 100-360 K range with an accuracy of about ±2 K. The cryostat was equipped with quartz windows which are about 15 mm far from the sample. Therefore the 20× objective with 22 mm focal length was employed.

3.3 High-pressure low-temperature infrared setup

The temperature and pressure dependent infrared absorption measurements were performed at European Laboratories for Non-linear Optics (LENS) in Florence where a Bruker 120HR fast Fourier transform interferometer dedicated to high-pressure absorption measurements is available. This apparatus is equipped with an home-made beam-condenser based on elliptical mirrors and schematically represented in fig.3.6. The two elliptic mirrors provide high magnification of the incoming beam and large collecting angle for the outgoing beam, thus leading to a 5× gain in the intensity transmitted by the DAC in the mid-infrared region (500-5000 cm^{-1}). For the experiment presented in this thesis, the interferometer was equipped with a KBr beam-splitter,

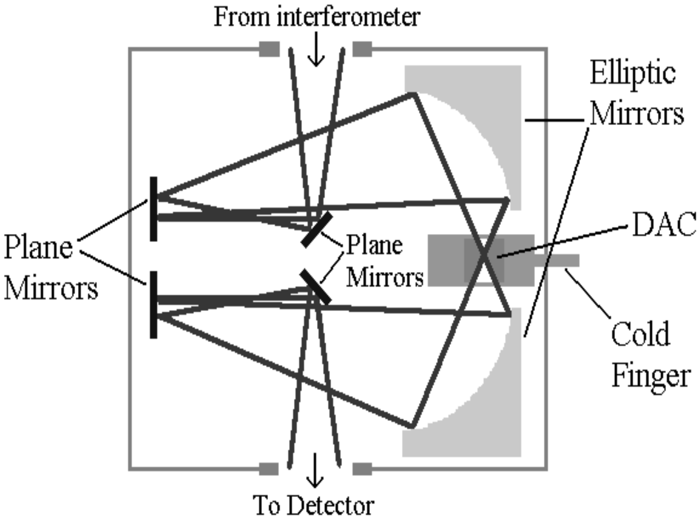

FIGURE 3.6: Schematic representation of the beam condenser installed on the Bruker 120HR interferometer.

a HgCdTe detector, and a Globar lamp as light source. This configuration allows measurements in the 500-4500 cm^{-1} range.

A cryocooler is coupled to the interferometer with the cold finger placed directly inside the vacuum sample compartment. The DAC is mounted at the end of the cold finger and a silicon-diode thermometer is placed as close as possible to the gasket. This system ensures a thermal reproducibility with an accuracy of 2 K. A DAC by LOTO was employed and it was equipped with type IIa diamonds with 600 μm culet diameter. The gasket was made of stainless steel with a hole of 300 μm diameter and 50 μm thick. The sample was finely powdered (average grain size of 1 μm) and smeared on the top surface of a KBr pellet pre-sintered in the hole gasket. With this procedure, small sample thickness can be obtained whereas dishomogeneity and fractures can be present in the sample. Fractures, if present, can be removed adding small quantity of sample and pressing between the diamonds. A small ruby chip was placed on the other side of the KBr pellet for pressure calibration. The ruby fluorescence lines were excited by means of an argon laser whose beam is inserted in the optical path of the interferometer by means of a movable plane mirror. This system, exploiting the beam condenser of the interferometer, provides focusing of the incoming light, collection of the backscattered fluorescence and allows visual observation of the sample. The collected ruby fluorescence is sent, by means of a 300 μm optical fiber, to a fixed grating spectrometer equipped with a cooled CCD detector with dedicated computer and software for pressure calibration.

3.4 High-pressure synchrotron radiation infrared setup

Far-infrared absorption measurements in a DAC is a challenging problem. In particular, when working on strongly absorbing samples such as manganites, these kind of experiments are almost impossible using conventional far-infrared sources which are not enough intense and brilliant to be used with the small sample contained in the DAC. This problem can be overcome exploiting the high brilliance of synchrotron sources.

In the present thesis, far-infrared absorption measurements at high pressure on three manganite samples have been performed on the SINBAD (Synchrotron INfrared Beamline At DAΦNE) infrared beamline at DAΦNE $e^+ - e^-$ collider in Frascati (Rome). In this line, the synchrotron radiation is extracted from the electron orbit by means of a bending magnet and sent to the interferometer through a 25 m optical line ending with a wedged diamond window.

The interferometer is a wish-bone Bruker Equinox 55 with corner-cube retro-reflectors and it was equipped with a silicon-mylar broad band beamsplitter and a liquid helium cooled bolometer as detector. With this experimental setup, the 30-700 cm^{-1} spectral range can be explored. In the far-infrared region, the intensity measured through pinholes of a few hundreds μm diameter using synchrotron radiation is at least one order of magnitude larger than that measured using a conventional mercury lamp. The DAC is mounted on a motorized stage inside the vacuum sample compartment of the interferometer. A couple of motorized mirrors allows acquisition of reference spectra on a parallel channel at each measurement, thus allowing correction of spurious effects due to fluctuations of the synchrotron source.

The DAC used for these measurement is the same described in sect.3.2.1. Petroleum-jelly (Apiezon-L) which has a 90% transmittance in the 0-700 cm^{-1} range was used as hydrostatic medium [86]. Since the pressure medium is not solid, the DAC-loading procedure described in the previous section cannot be employed and an alternative approach was used. The samples were finely milled and pressed between the diamond anvils thus obtaining a compact and thin sample slab with thickness of 4-5 μm. This slab was then carefully shaped for fitting inside the gasket hole. With this procedure sample homogeneity is quite good except for the presence of unavoidable small-fractures in the slab. Petroleum jelly and several ruby chips were then placed inside the gasket hole.

Ruby fluorescence was measured by means of a dedicated device schemat-

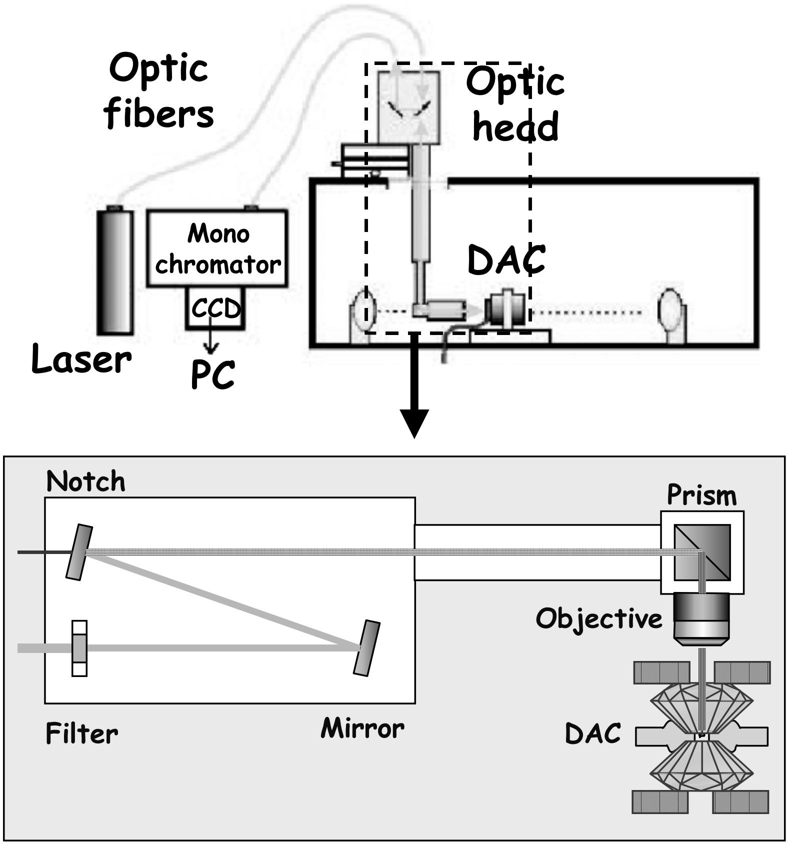

Figure 3.7: Top: Schematic representation of the pressure gauge used in the far-infrared synchrotron radiation high pressure measurements. Bottom: scheme of the optic head of the pressure gauge.

ically represented in fig.3.7. The 514 nm line of an argon laser is collected by the incoming optic fiber and focused into the DAC by the objective of the optic head (schematically represent at bottom of fig.3.7). The backscattered signal collected by the objective is sent by a notch beam-splitter to the outgoing fiber which is coupled to the spectrometer. The spectrometer is composed by a TRIAX monochromator equipped with a 1800 lines/mm grating a CCD detector whose output signal is analyzed by a dedicated elaborator.

3.5 High-pressure X-ray diffraction setup

X-ray diffraction measurements were performed in collaboration with the group of Prof. J.P. Itié at LURE synchrotron facility (Paris) on the DW11 station of the DCI storage ring. The white beam emerging from the wiggler is collimated down to 50 × 50 μm^2 with successive slits. The diffracted spectra are collected by a germanium detector in the 10-40 keV range at a diffraction angle of about 5°. A copper sheet placed inside the DAC was used for calibration of the diffraction angle.

Several BETSA DACs equipped with type Ia diamonds with 400-600 μm culet diameter were employed and the gaskets were made of rhenium. Finely milled sample was placed inside the gasket hole together with several ruby chips and silicon oil as hydrostatic medium. Ruby fluorescence was measured by means of dedicated optical apparatus similar to that employed in the far-infrared measurements (see sect.3.4).

A resistor heater was employed for heating the whole DAC above room temperature. Temperature was measured by means of a thermocouple placed as close as possible to the gasket obtaining an uncertainty of ±5 K.

3.6 List of measurements

Exploiting the aforementioned experimental techniques, the following measurements have been performed in the present thesis:

- Room temperature high-pressure Raman spectroscopy on $La_{0.80}Ca_{0.20}$-$MnO_{3-\delta}$ (δ=0.00, 0.08).
- Pressure (0-11 GPa) and temperature (130-320 K) dependent mid-infrared absorption on $La_{0.75}Ca_{0.25}MnO_3$. The results obtained from these data have been also the object of a theoretical model developed for their description.
- Room-temperature high-pressure far-infrared absorption on $La_{1-x}Ca_x$-$MnO_{3-\delta}$ (three samples: $x = 0.25$, $\delta = 0.00$; $x = 0.20$, $\delta = 0.00$; $x = 0.20$, $\delta = 0.08$) by means of synchrotron radiation.
- Far infrared reflectivity on $La_{0.70}Sr_{0.30}MnO_3$ thin films with thickness from 320 Å to 6800 Å grown on $SrTiO_3$ and $LaAlO_3$ substrates.
- Room temperature Raman spectroscopy on $La_{0.70}Sr_{0.30}MnO_3$ thin films with thickness from 40 Å to 1000 Å grown on $LaAlO_3$.
- High-temperature (300-450 K) and high-pressure (0-20 GPa) X-ray diffraction measurements on $LiMn_2O_4$.
- Raman measurements on $LiMn_2O_4$ as a function of incident laser power.

- Room temperature Raman spectroscopy on $SrMnO_3$ and polarization analysis for the hexagonal compound.
- Low temperature (100-360 K) Raman spectroscopy on hexagonal and cubic $SrMnO_3$.

These measurements are reported in chap.4-7, while the conclusions which can be drawn from the whole of these results are reported in chap.8.

3.7 List of samples

The samples of manganites and related compounds investigated during the present Ph.D. thesis are listed in tab.3.1. The samples were obtained exploiting the collaboration with the groups headed by the people reported in the last column.

Sample	Label	Form	Collaboration
$La_{0.75}Ca_{0.25}MnO_3$	LC25S	bulk	Prof. D.D. Sarma[1]
$La_{0.80}Ca_{0.20}MnO_3$	LC20S	bulk	Prof. D. Emin[2]
$La_{0.80}Ca_{0.20}MnO_{2.92}$	LC20D	bulk	Prof. D. Emin[2]
$La_{0.7}Sr_{0.3}MnO_3$	LSMO	films	Prof. G. Balestrino[3]
$LiMn_2O_4$	LMO	bulk	Prof. C. Masquelier[4]
$SrMnO_3$	SMO	bulk	Prof. B. Raveau[5]

Table 3.1: List of the samples studied in the present Ph.D. thesis. Bulk samples are all poly-crystalline. Film samples have been grown with different thickness on $SrTiO_3$ and $LaAlO_3$ substrates. Samples were provided by the collaborations with the groups headed by the people reported in the last column. Affiliations: 1 Indian Institute of Science, Bangalore, India; 2 Sandia National Laboratories, Albuquerque, U.S.A.; 3 Università di “Tor Vergata”, Roma, Italy; 4 Université de Picardie “Jules Verne”, Amien Cedex, France; 5 ISMRA-CRISMAT Laboratory, Caen, France.

Chapter 4

Raman Measurements at High-Pressure

In this chapter we start presenting the results of the present work. In the first section, we will present a brief survey of the Raman measurements on bulk manganites available in the literature which are relevant in discussing our results. In particular, the only two published paper reporting on high-pressure Raman measurements on manganites will be discussed. In the second section, results obtained in this Ph.D. thesis on $La_{1-x}Ca_xMnO_{3-\delta}$ at room temperature as a function of pressure will be presented and discussed.

4.1 Survey of Raman spectroscopy on manganites

Raman spectroscopy is a powerful tool in the study of manganites being able to observe phonon modes and in particular, as we will see, a JT mode. In orthorhombic manganite of *Pnma* space group, there are 60 phonons at the Γ-point of the Brollouin zone. Among these modes, 24 are Raman active ($7A_g + 5B_{1g} + 7B_{2g} + 5B_{3g}$) and include 16 octahedral modes, i.e. modes which involve only movements within the MnO_6 octahedral units [87]. The atomic displacements in these octahedral modes are shown in fig.4.1.

A polarization-dependent Raman experiment on $LaMnO_3$ single crystal was performed by Iliev et al. and their results are shown in fig.4.2 [87]. The analysis in polarization of the measured spectra and the comparison with a lattice dynamics calculation allowed the assignment of the four main bands which characterize the unpolarized Raman spectrum. The main peaks, cen-

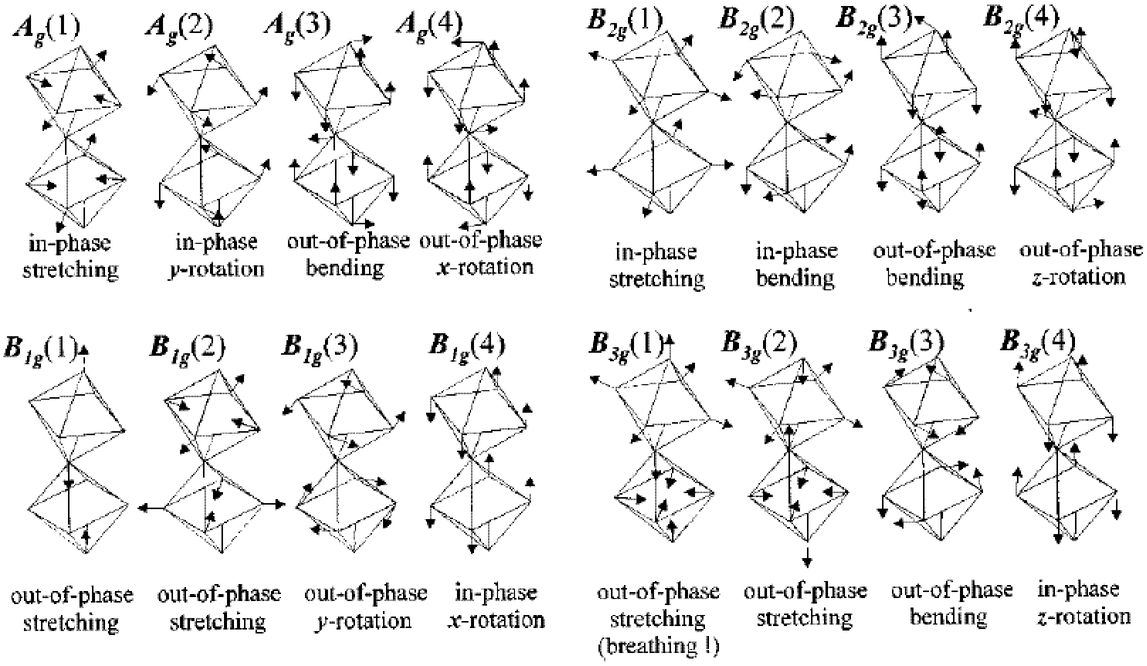

FIGURE 4.1: Atomic displacements in octahedral Raman-active modes of the orthorhombic perovskite [87].

tered at 275, 314, 490, and 611 cm^{-1}, are assigned to the $A_g(4)$ (x-rotation), $B_{3g}(4)$ (z-rotation), $A_g(3)$ (bending), and $B_{2g}(1)$ (stretching) modes respectively (following the notation of fig.4.1) [87]. It is worth to note that the two high frequency phonons are associated to modifications of the strong Mn-O bond, while the two low frequency ones are assigned to rigid rotations of the octahedra. In particular, the $B_{2g}(1)$ stretching mode is associated to a deformation of the base of the octahedron and it can be shown that it is JT-splitting active, i.e. is one of the mode composing the JT distortion induced by the extra electron in Mn^{3+} ions (see sect.1.1.1). This phonon will be called *JT phonon* in the following. The comparison between the spectra of the fully JT-distorted $LaMnO_3$ and of the undistorted $CaMnO_3$ [88, 89] show that the presence of the JT distortion gives rise to quite broad phonon bands. The EPC triggered by the JT distortions indeed activates efficient decay channel for the phonons thus reducing their lifetime.

Doping dependence

The spectrum of lightly doped $LaMnO_3$ resembles that of the parent compound with typically four main phonon bands centered at around 250, 350, 500, and 600 cm^{-1}. A strong reduction of intensity and a further broadening of the phonon bands is observed on increasing doping. In fig.4.3 the Raman

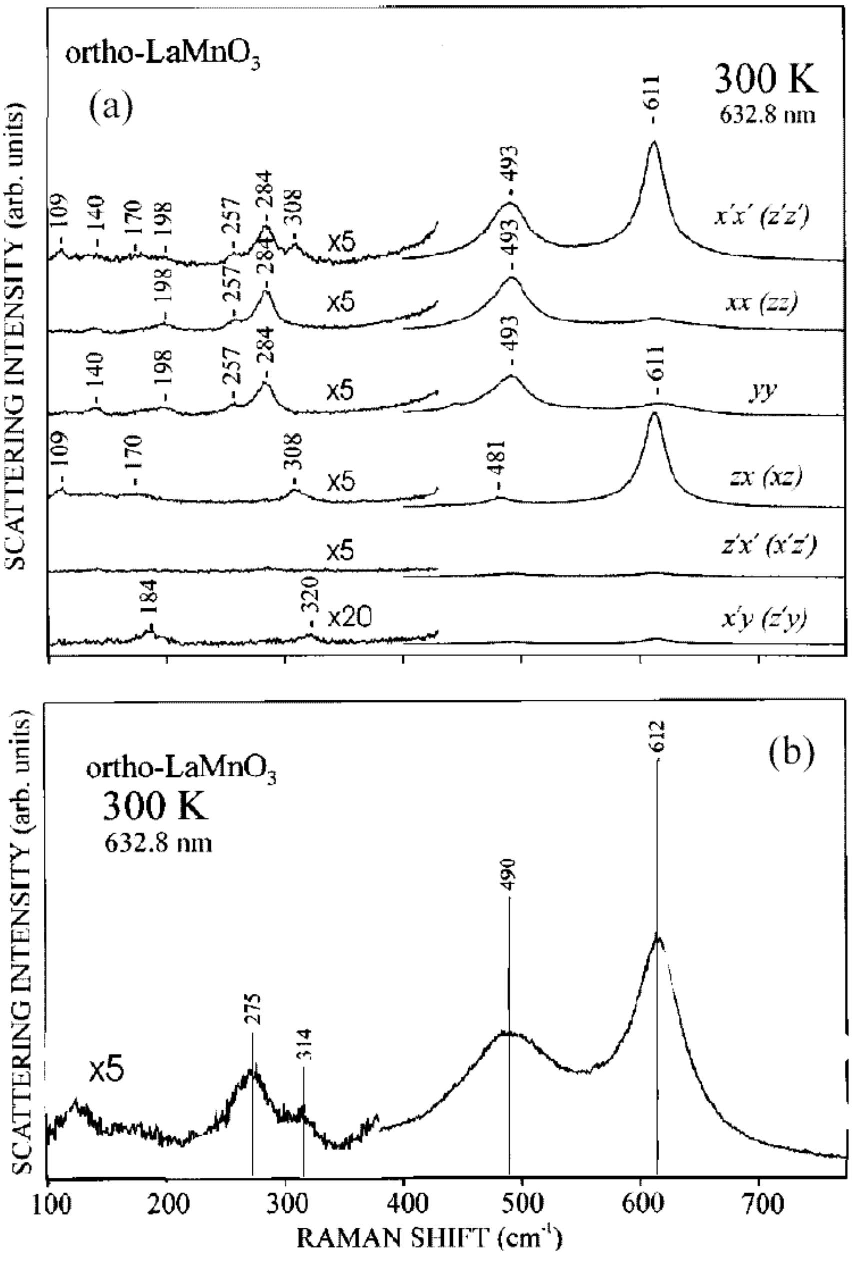

FIGURE 4.2: Raman spectra of LaMnO3 in various polarization configurations (top) and unpolarized configuration (bottom) [87].

spectra of several $La_{1-x}Ae_xMnO_3$ single crystals are compared with that of $LaMnO_3$ [90]. The reduced intensity of Raman signal can be ascribed to the evolution of the structure towards a cubic perovskite on increasing doping, since no Raman-active modes are predicted in the perfect cubic perovskite structure. The further broadening of the Raman bands in doped compounds (in the insulating phase) is due to the lattice disorder induced by the pres-

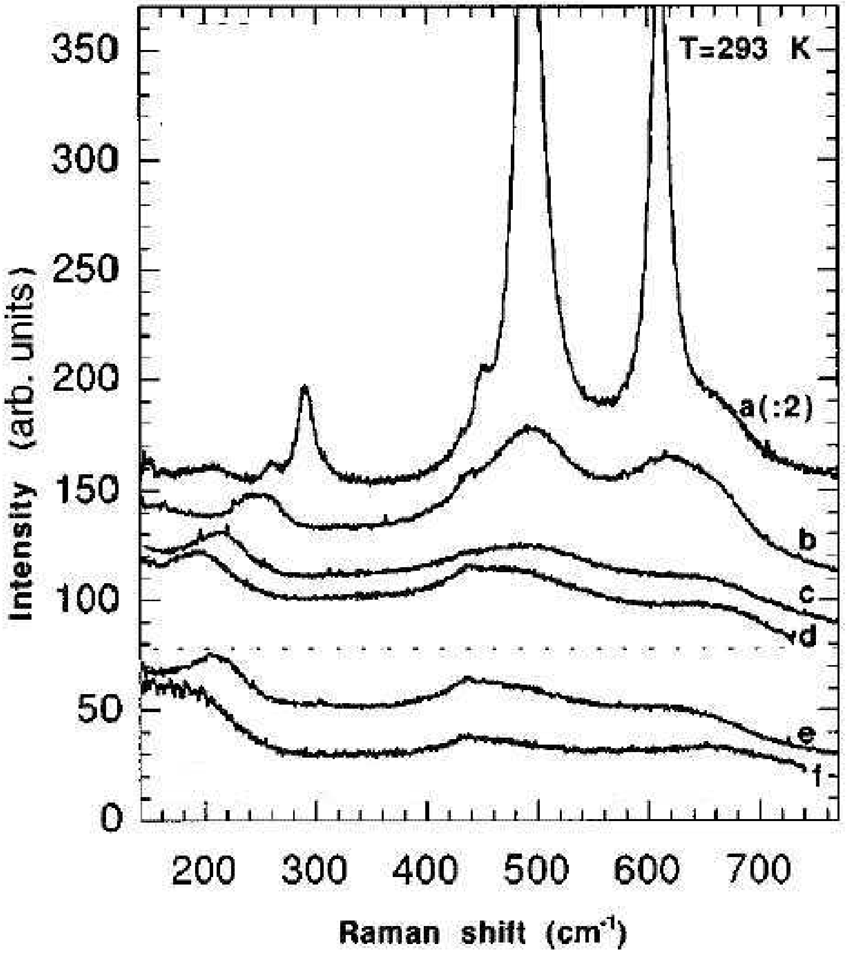

Figure 4.3: Raman spectra of single crystals of of $LaMnO_3$ (a), $La_{1-x}Sr_xMnO_3$ with $x = 0.1$ (b), $x = 0.2$ (c), $x = 0.3$ (d), $La_{0.7}Ca_{0.3}MnO_3$ (e), and $La_{0.7}Pb_{0.3}MnO_3$ (f) [90].

ence of both distorted and undistorted octahedra and it is thus connected to the variance of the distortion [91].

The large width and small intensity of the phonon peaks in doped compounds, combined with the very large number of Raman-active modes predicted, avoid a strict and complete assignment of the phonon bands. It was also proposed that these bands are not pure Γ-point phonons but contain also contributions from the full phonon density of state activated by configurational disorder and/or non coherent JT distortion [89]. Even if such an effect can be present, the similarity with spectrum of undoped compound suggests that the observed bands are mainly due to Γ-point phonons. We will see that the high pressure measurements can give additional information on the assignment. In particular, as will be discussed in sect.4.2.2, the results obtained in this Ph.D. thesis clearly confirm the assignment of the band at around 630 cm^{-1} to the JT stretching mode. In any case, a qualitative classification of the vibrational modes is generally accepted, i.e. phonons laying above 400 cm^{-1} involve modifications of the strong Mn-O bond (i.e. octahedral bending and stretching modes), between 200 and 400 cm^{-1} octahedral rigid rotation should be observed, while rare-earth vibrations are expected to have frequencies smaller than 200 cm^{-1}.

According to the qualitative frequency classification above discussed, and on the basis of the assignment reported in ref. [87], the four main phonon bands, characteristic of doped manganites, can be tentatively ascribed to the $A_g(2)$ (y-rotation), $B_{3g}(4)$ (z-rotation), $A_g(3)$ (apical oxygen bending), and $B_{2g}(1)$ (in-plane oxygen stretching) symmetries on increasing the frequency [49]. A different assignment for the lowest-frequency band was proposed by Yoon et al. [92] who attributed this contribution to rare-earth vibration, but the large part of the authors agree on the octahedral-rotation assignment of this phonon. It is worth to note that the band centered around 500 cm^{-1} can contain also a contribution from the $A_g(1)$ stretching mode, but as we will see in the following, the pressure dependence of the phonon spectrum indicates that this band is substantially dominated by the $A_g(3)$ bending mode. Despite these ambiguities, we will assume the aforementioned tentative assignment in the following.

A doping dependence of the phonon frequency can be also observed in fig.4.3 (curves a-d). A remarkable increase of the JT phonon frequency is indeed apparent on increasing Sr doping from 0% to 30% ($\simeq$ 60 cm^{-1}, curves a-d in fig.4.3). Since the JT distortion is reduced by the introduction of the large Sr ions (see sect.2.3), this finding suggests that the frequency of this phonon is related to the extent of the distortion. This relationship is not surprising since the onset of JT distortions reduces the frequencies of the JT-active phonons (see sect.1.1.1). Although in the literature there are no studies of the x dependence of the frequency of the JT phonon in $La_{1-x}Ca_xMnO_3$, by comparing spectra (a) and (e) in fig.4.3 a moderate frequency shift ($\simeq$ 40 cm^{-1}) can be observed also in the Ca-doping case. It is worth to note that the effect is weaker than in Sr-doped $LaMnO_3$ since Ca^{2+} is quite smaller than Sr^{2+} and therefore it is less efficient in removing the distortion. Indeed Ca-doping removes the distortion mainly by means of the conversion of the JT ions Mn^{3+} to non-JT ions Mn^{4+} while Sr-doping also induces an internal chemical pressure (see sect.2.3). The x dependence of the frequencies of the $A_g(3)$ bending mode (ν_{ben}) and the JT (ν_{JT}) phonons of Ca-doped $LaMnO_3$, as obtained by different experimental works [49, 93–95],

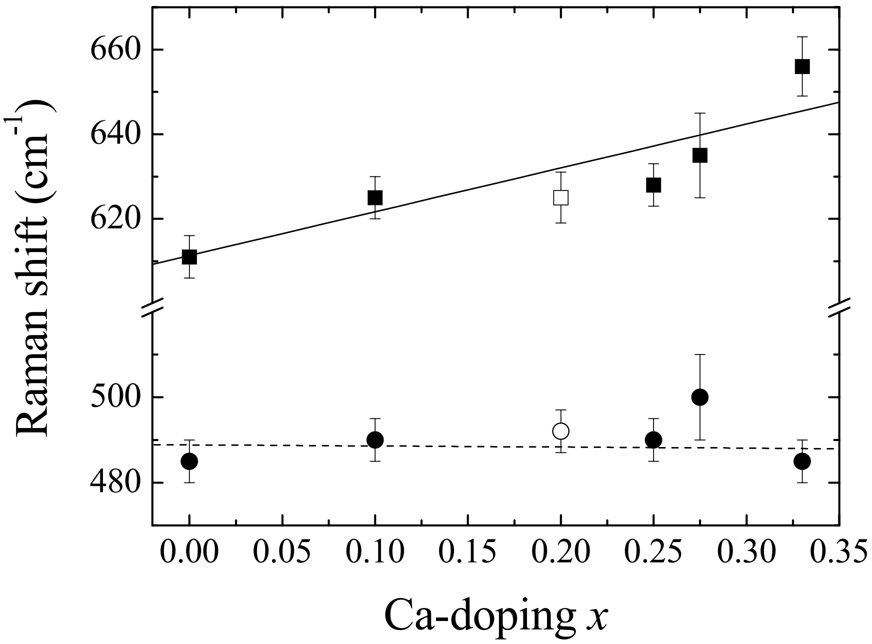

FIGURE 4.4: Doping dependence of the bending (circles) and Jahn-Teller stretching (squares) Raman-active phonons frequencies in $La_{1-x}Ca_xMnO_3$. Full symbols: data from ref. [93] ($x = 0$), ref. [94] ($x = 0.10$ and 0.275), ref. [49] ($x = 0.25$), and ref. [95] ($x = 0.33$). Open symbols: data obtained in this thesis for $x = 0.20$. Lines are linear fits to data.

is shown in fig.4.4. On increasing x, ν_{JT} slightly increases whereas ν_{ben} is almost constant, consistently with the above discussions.

Temperature dependence

The Raman spectrum of $LaMnO_3$ was measured as a function of temperature by Granado et al. who determined the temperature dependence of the peak-frequencies of the phonon modes shown in fig.4.5 [93]. All the three modes show anomalies in correspondence of the AF transition at $T_N = 140$ K, but the effect is larger for the JT phonon which sensibly softens on decreasing temperature below T_N.

The effect of the IM transition on the Raman spectra was investigated by Yoon et al. by studying the temperature dependence of the Raman spectrum for several manganites with different T_C values. The results obtained are shown in fig.4.6 [92]. The spectra have been analyzed by assuming that they are given by two contributions: a phonon spectrum and a continuous background, typical of strongly correlated electron systems, and assigned to a “collision dominated” electronic scattering from free carriers. An additional contribution at around 1100 cm^{-1} was ascribed to a photo-excitation

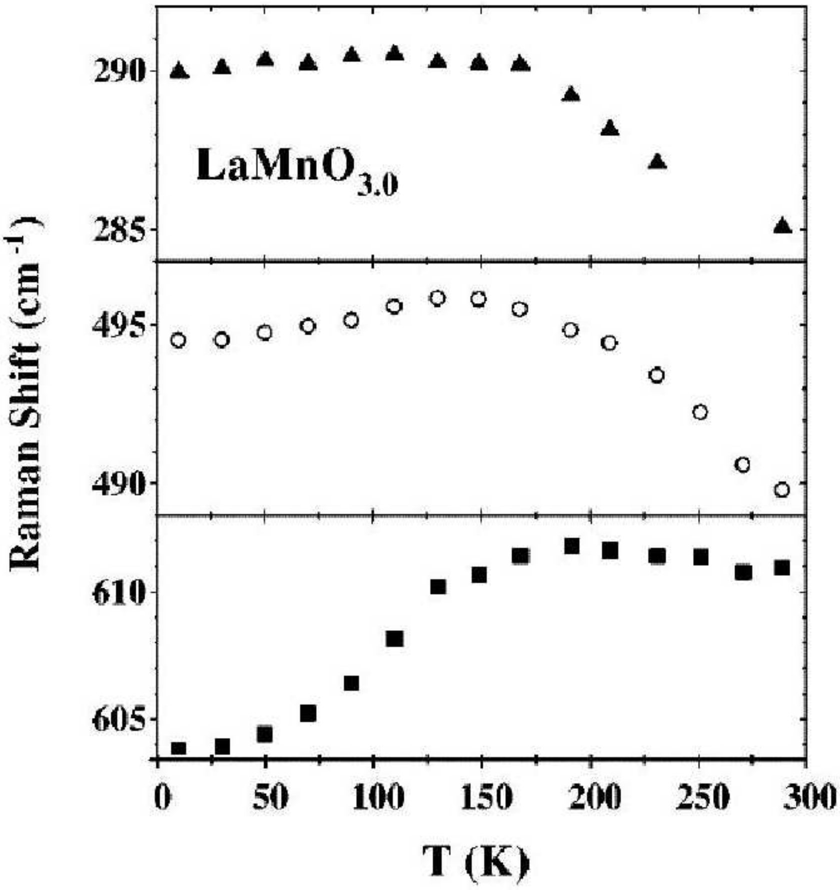

FIGURE 4.5: Temperature dependence of the phonon frequencies of LaMnO$_3$. ▲=x-rotation, ○=bending, ■=Jahn-Teller stretching [93].

of electrons self-trapped in the JT distortion. Data have been fitted by means of [92]:

$$S(\omega) = [1 + n(\omega)] \left[\frac{A\omega\Gamma}{\omega^2 + \Gamma^2} + \sum_{i=1}^{N} \frac{A_i \Gamma_i^2 \omega}{(\omega^2 - \omega_i^2)^2 + \Gamma_i^2 \omega^2} \right] \tag{4.1}$$

where $n(\omega)$ is the Bose thermal factor, A and Γ are the intensity and width of the electronic contribution, $N - 1$ is the number of phonons in the spectrum, and A_i, Γ_i, and ω_i $(i < N)$ are intensity, width, and frequency of the single phonon respectively. The N-th term in the sum of eq.4.1 accounts for the contribution at around 1100 cm^{-1}. Best fit results show a systematic increase of the electronic contribution on increasing the metallic character of the system, i.e. at room temperature in samples with increasing T_C and at fixed T_C on decreasing temperature. Moreover, on decreasing temperature below T_C, a remarkable narrowing of the bending and JT phonon peaks was

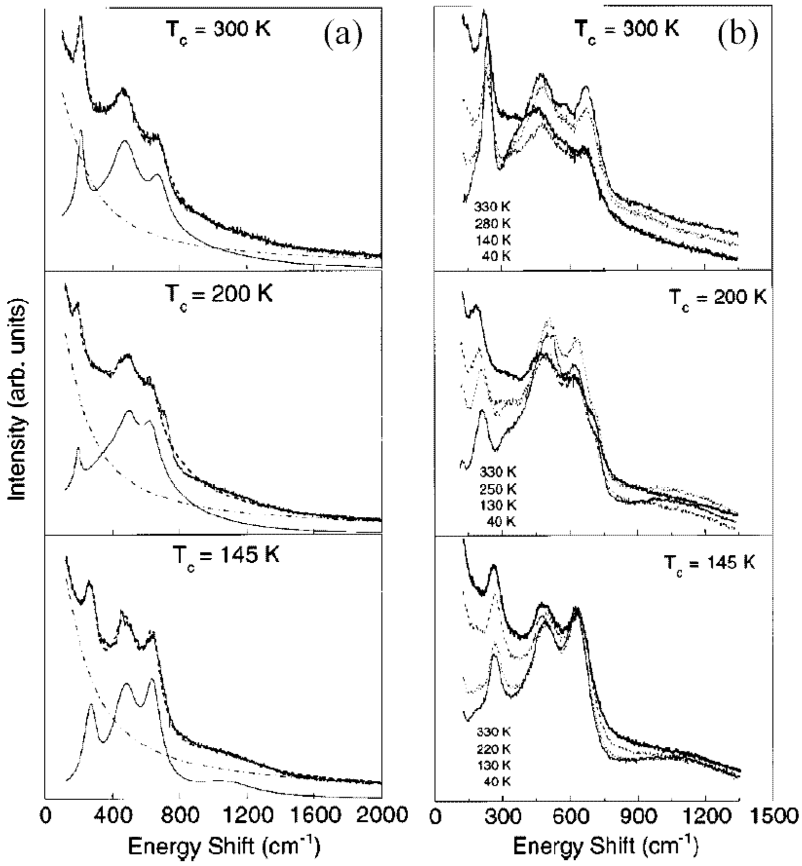

FIGURE 4.6: Room temperature (a) and temperature dependent (b) spectra of different manganites with T_C values indicated in the figure. The fits by means of eq.4.1 (thick solid lines), the phonon contribution (thin solid lines), and the electronic contribution (dashed lines, see text) are also shown in panels (a) [92].

observed [92]. The latter effect can be safely ascribed to the reduction of the JT distortion on entering the metallic phase.

On the basis of the above discussions, the analysis of Raman measurements on manganites could provide the following information:

- The distortion of the cubic structure is directly related to the intensity of the Raman spectrum and in particular of the bending and JT phonons.

- The extent of the JT distortion is related to the frequency of the JT phonon ν_{JT}.

- The JT phonon width Γ_{JT} is a measure of the variance of the JT distortion, i.e. of the degree of disorder.

4.1.1 High-pressure Raman measurements on manganites

The high-pressure investigation of manganites by means of Raman spectroscopy started in 2001 when two successive papers appeared[1]. Loa et al. carried out a high-pressure spectroscopic study on $LaMnO_3$. Raman spectra within the 0-16 GPa pressure range are shown in fig.4.7(a). The overall hardening of the JT phonon is consistent with a reduction of the JT distortion. A splitting of this phonon is also well apparent at around 10 GPa indicating the onset of a local structural rearrangement of the MnO_6 octahedra [2]. This effect was ascribed to the appearance at high pressure of domains containing almost undistorted octahedra which give rise to the higher energy peak.

In a paper of our group the pressure dependence of the Raman spectrum of $La_{0.75}Ca_{0.25}MnO_3$ up to 14 GPa was measured (see fig.4.8(a) [49]). In all spectra four bands at around 240, 330, 480, and 630 cm^{-1} are clearly identified and ascribed to the y-rotation, z-rotation, bending, and JT stretching

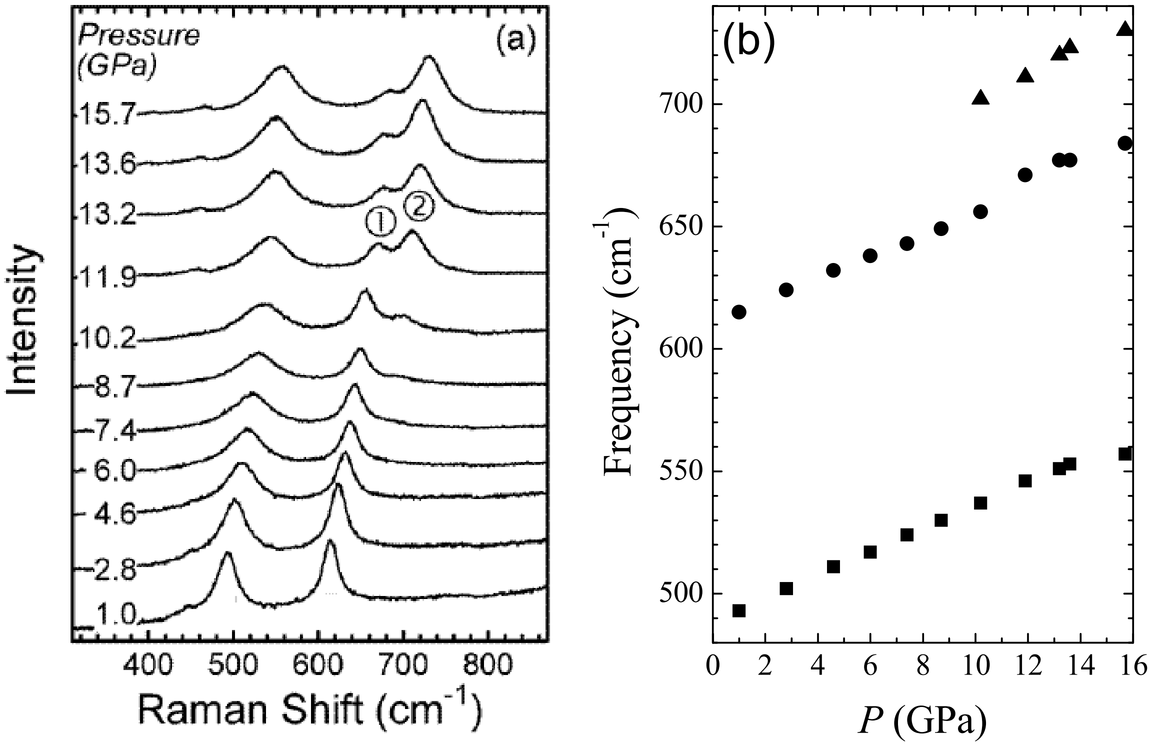

FIGURE 4.7: Pressure dependence of the Raman spectrum of $LaMnO_3$ (a) and of the phonon peak frequencies (b) [8].

---

[1] In this context is simpler to discuss these papers in reversed chronological order.

[2] Since no high-pressure structural transition is observed by means of X-ray diffraction [8], the rearrangement must be local.

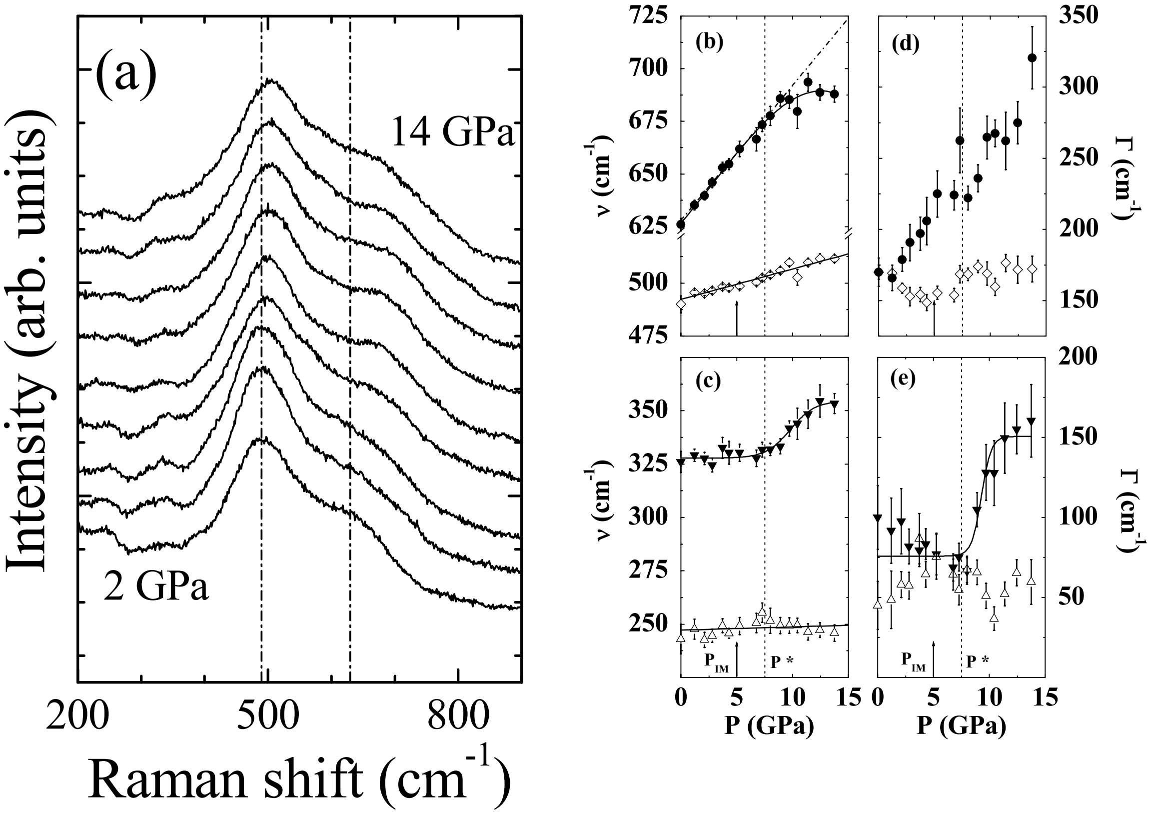

FIGURE 4.8: Pressure dependence of the Raman spectrum of $La_{0.75}Ca_{0.25}MnO_3$ (a), of the phonon frequencies (b) and (c), and linewidths (d) and (e). Lines in panels (b)-(e) are guides to eyes [49].

modes respectively (see the previous section). The spectra in fig.4.8(a) were fitted by means of eq.4.1 with $N = 5$ (the fifth term accounting for the contribution at 1100 cm^{-1} [49,92]). The pressure dependence of the best-fit values of phonon frequencies and linewidths are shown in panels (b)-(c) and (d)-(e) respectively. It is well evident a systematic pressure-induced hardening of the bending and JT phonons. The stronger pressure dependence exhibited by ν_{JT} with respect to ν_{ben}, is in good agreement with the hypothesis that the latter is a volume-conserving mode while the former is not. Therefore these results are well consistent with the assignment of the bending phonon and are in disagreement with the possible alternative assignment of this phonon to the $A_g(1)$ non-volume-conserving stretching mode. The large effect on ν_{JT} is consistent with a pressure-induced reduction of the JT distortions.

The most remarkable observation of this paper is the anomalous high-pressure behavior of the JT phonon in the very high pressure regime. It is worth to notice that on the basis of the low pressure data, a room-temperature IM transition at around 5-6 GPa would be expected for

$La_{0.75}Ca_{0.25}MnO_3$. The absence of phonon narrowing and the apparent very weak pressure dependence of the JT phonon frequency for pressure beyond $P^* = 7 - 8$ GPa are in complete disagreement with a pressure-induced metallization process. On the contrary this behavior indicates the onset of an unexpected localizing mechanism at high pressure. In particular the saturation of ν_{JT} indicates that above P^* pressure becomes inefficient in further removing the JT distortions. The rather abrupt anomaly in the z-rotation frequency ν_{rot} and linewidth Γ_{rot} at P^* suggests a rearrangement of the octahedra. These results are in very good agreement with those obtained on the same sample by Meneghini et al. described in sect.2.4 [52]. One of the purposes of this thesis is to verify the onset of a peculiar high-pressure regime also in other manganites samples and to investigate the nature of the pressure-activated localizing mechanism.

4.2 High-pressure Raman spectroscopy on $La_{1-x}Ca_xMnO_{3-\delta}$

In this section the high-pressure Raman measurements on stoichiometric $La_{0.80}Ca_{0.20}MnO_3$ (LC20S) and oxygen deficient $La_{0.80}Ca_{0.20}MnO_{2.92}$ (LC20D), are reported. The experiments have been carried out at the high-pressure Raman laboratory of our department. We would like to point out that high-pressure far-infrared measurements on the same samples as well as on $La_{0.75}Ca_{0.25}MnO_3$ (LC25S) have been also performed and will be presented in the next chapter.

As discussed in sect.2.2, the introduction of oxygen vacancies represents a way for disentangling the effects of chemical substitution x, which modifies the tolerance factor, and effective hole doping $x_{eff} = x - 2\delta$. In present samples, the large difference in hole doping (x_{eff}=0.20 and 0.04 in LC20S and LC20D respectively) is accompanied by a small variation of the unit cell volume ($\Delta V/V = 0.8\%$ [26]) thus indicating negligible structural modifications (see sect.2.2).

Samples are the same studied in Ref. [26] where a detailed characterization by means of X-ray diffraction, magnetization, and resistivity measurements was performed. It was found that LC20S is a PM insulator at high temperature and a FM metal at low temperature with $T_{IM} \simeq T_C = 194$ K, while LC20D is insulating at all temperatures and shows a FM transition at $T_C = 163$ K. Therefore, the study of these compounds can provide important information on the interplay between magnetic and transport properties.

Raman measurements on LC20S and LC20D were performed, using the experimental configuration described in sect.3.2.1, in the 200-1000 cm^{-1} spectral range. Since the laser spot impinges only a few grains of the sample, possible preferred-orientation effects can induce fluctuations of the scattered intensity for different phonons. In order to overcome this effect, at each pressure, spectra were collected at four different points of the sample and separately analyzed. This procedure also allows to check for pressure gradients. Pressure-dependent representative spectra collected on a given zone of LC20S and LC20D are shown in fig.4.9 (a) and (b) respectively. In all the spectra the four phonon bands already observed in LC25S [49] are apparent. The same analysis procedure of ref. [49] was applied: spectra were separately fitted by means of eq.4.1 with $N = 5$ (see sect.4.1.1) and the fitting parameters obtained from four zones of each sample were averaged. The rather small dispersion of the best-fit parameters (frequencies and widths) shows the absence of large pressure gradients. In the present experiment both frequencies and linewidths of the $A_g(2)$ y-rotation mode do not show variations within the experimental uncertainties over the whole pressure range.

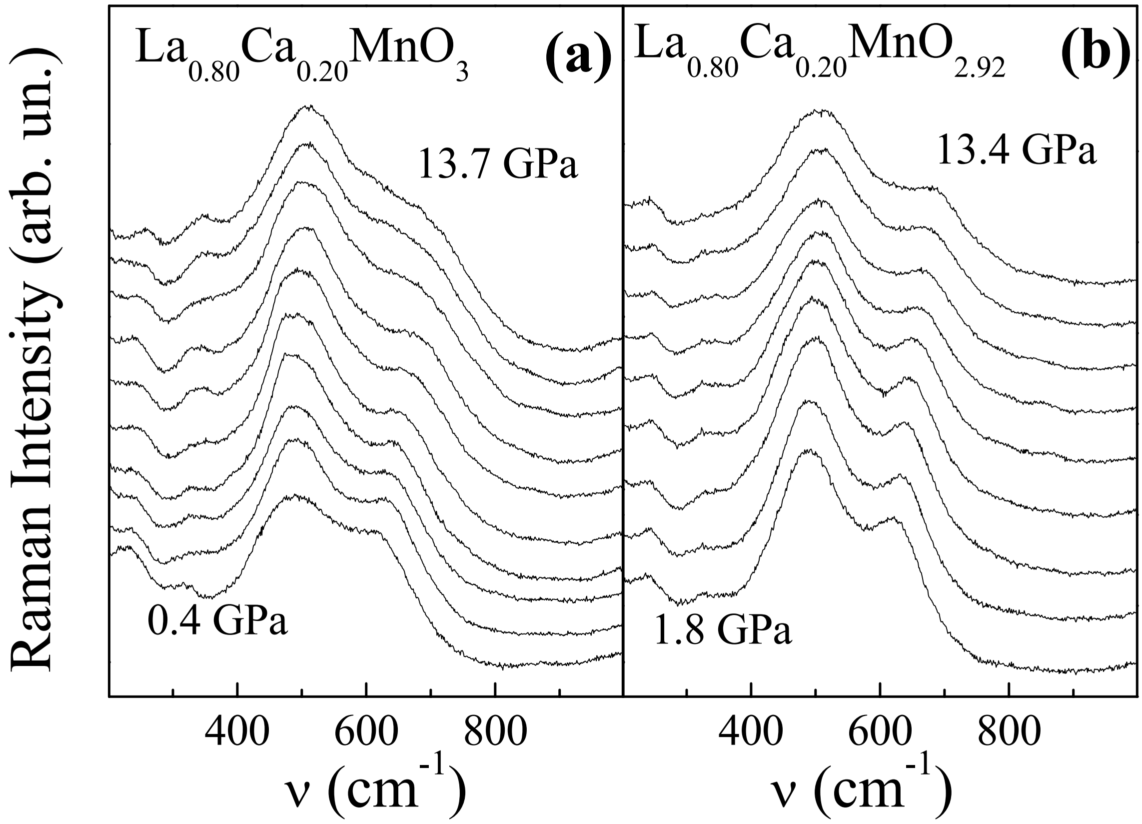

FIGURE 4.9: Raman spectra of $La_{0.80}Ca_{0.20}MnO_3$ (a) and of $La_{0.80}Ca_{0.20}MnO_{2.92}$ (b) as a function of pressure.

The pressure dependence of the frequencies of the $B_{3g}(4)$ z-rotation (ν_{rot}), $A_g(3)$ bending (ν_{ben}), and $B_{2g}(1)$ stretching (ν_{JT}) phonons is shown in fig.4.10 (a) and (b) for LC20S and LC20D, respectively. It is well evident that, similarly to the case of LC25S [49], for both samples the frequency ν_{JT} of the JT phonon has a pressure dependence which is much larger than ν_{ben} and ν_{rot}. Moreover, it is important to note that in LC20S a saturation effect in ν_{JT}, similar to that previously observed in LC25S, can be observed at a slightly larger pressure of about 10 GPa (it was $\simeq$ 7.5 GPa in LC25S). Such an effect is not observed in LC20D over the explored pressure range. The pressure dependence of the linewidths of the rotation (Γ_{rot}), bending (Γ_{ben}), and JT (Γ_{JT}) phonons is shown in fig.4.11 (a) and (b) for LC20S and LC20D, respectively. While Γ_{rot} and Γ_{ben} are quite similar in the two samples, it can be noted that Γ_{JT} in LC20S is larger than in LC20D. This effect can be interpreted in terms of the disorder of the JT distortion induced by hole doping and it is more evident in LC20S where the effective doping is larger. Since there are almost negligible differences between the unit cell volume

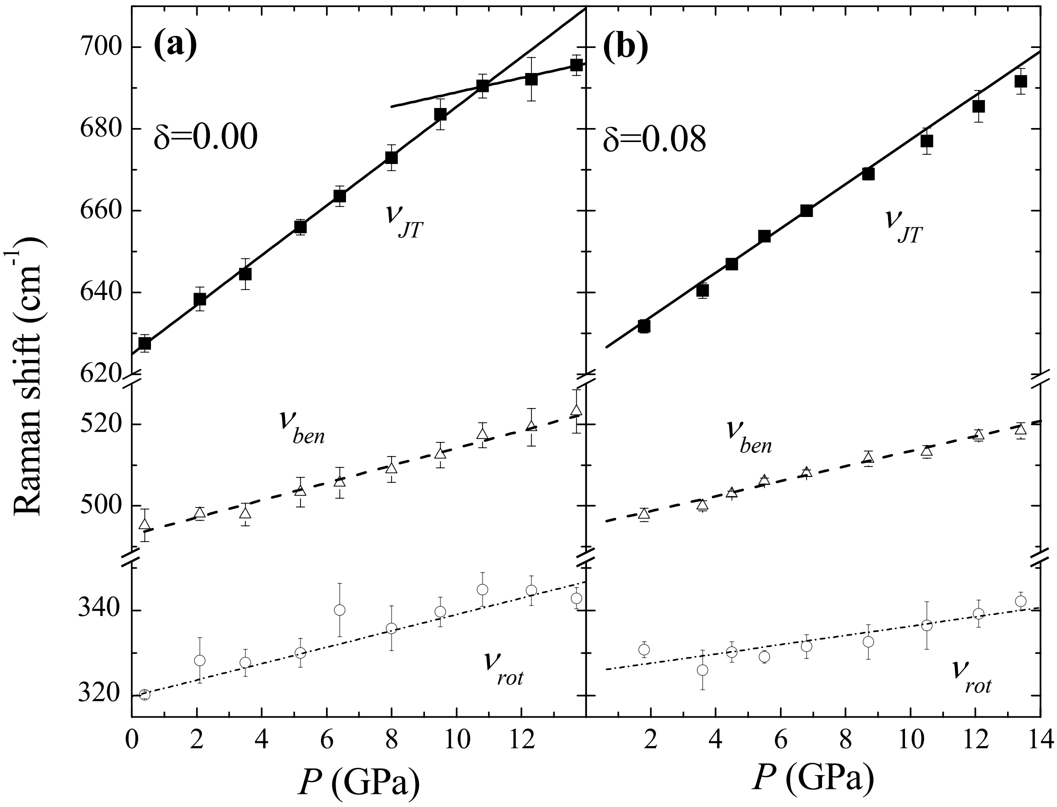

FIGURE 4.10: Pressure dependence of the phonon frequencies for $La_{0.80}Ca_{0.20}MnO_3$ (a) and $La_{0.80}Ca_{0.20}MnO_{2.92}$ (b): $B_{3g}(4)$ z-rotation (ν_{rot}, open circles), $A_g(3)$ bending (ν_{ben}, open triangles), and $B_{2g}(1)$ Jahn-Teller stretching (ν_{JT}, filled squares). Lines are guides to eyes.

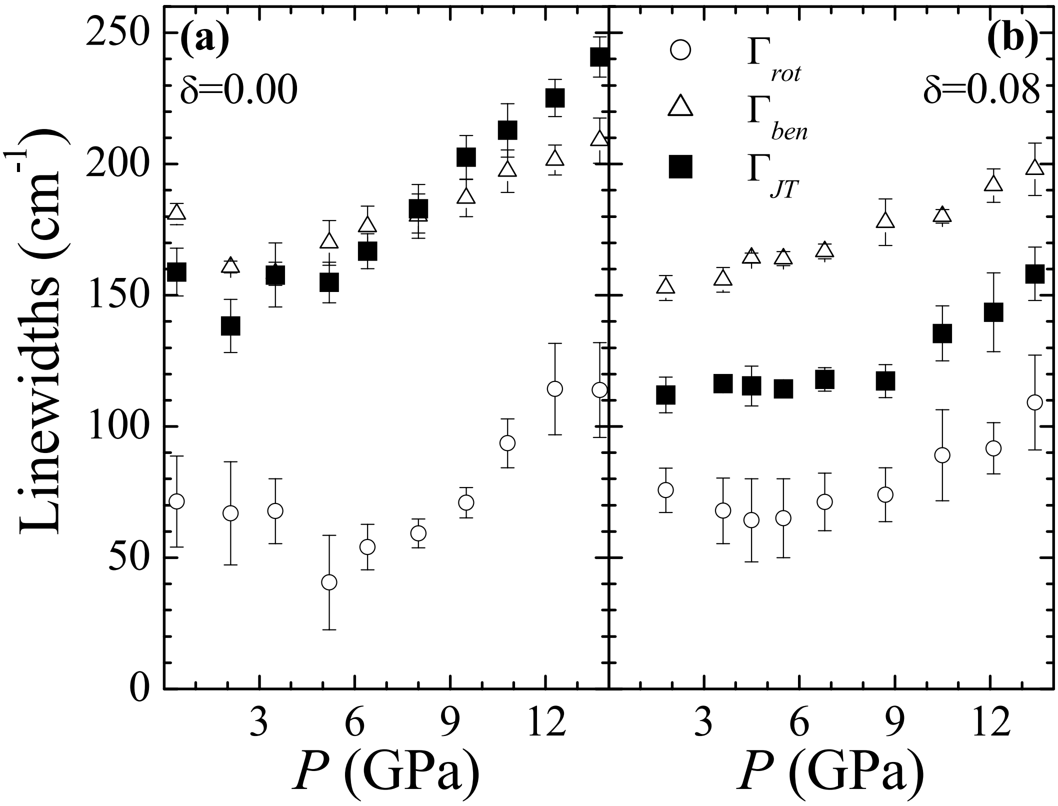

FIGURE 4.11: Pressure dependence of the phonon linewidths for $La_{0.80}Ca_{0.20}MnO_3$ (a) and $La_{0.80}Ca_{0.20}MnO_{2.92}$ (b): $B_{3g}(4)$ z-rotation (Γ_{rot}, open circles), $A_g(3)$ bending (Γ_{ben}, open triangles), and $B_{2g}(1)$ Jahn-Teller stretching (Γ_{JT}, filled squares).

of the two samples [26], the absence of any appreciable difference in Γ_{ben} indicates that the bending phonon is not correlated to carrier density and thus to the JT distortion. This finding supports the assignment of this phonon to the $A_g(3)$ bending mode rather than to the $A_g(1)$ JT-active stretching mode.

4.2.1 Competing interactions at high-pressure

The comparison of the present results with those obtained on LC25S [49] and on $LaMnO_3$ [8] allows a deeper insight in the interplay between electronic and lattice degrees of freedom. The pressure dependencies of ν_{JT} for the $La_{1-x}Ca_xMnO_{3-\delta}$ samples studied in this Ph.D. thesis and those studied in refs. [8,49] are compared in fig.4.12(a). It is quite evident that, on increasing pressure, ν_{JT} increases for all samples indicating that the average distortion is reduced. The rate of increase gets larger as x_{eff} is increased. Bearing in mind the direct relationship between x_{eff} and the average JT distortion, the above finding shows that pressure is more effective in symmetrizing the octahedra in

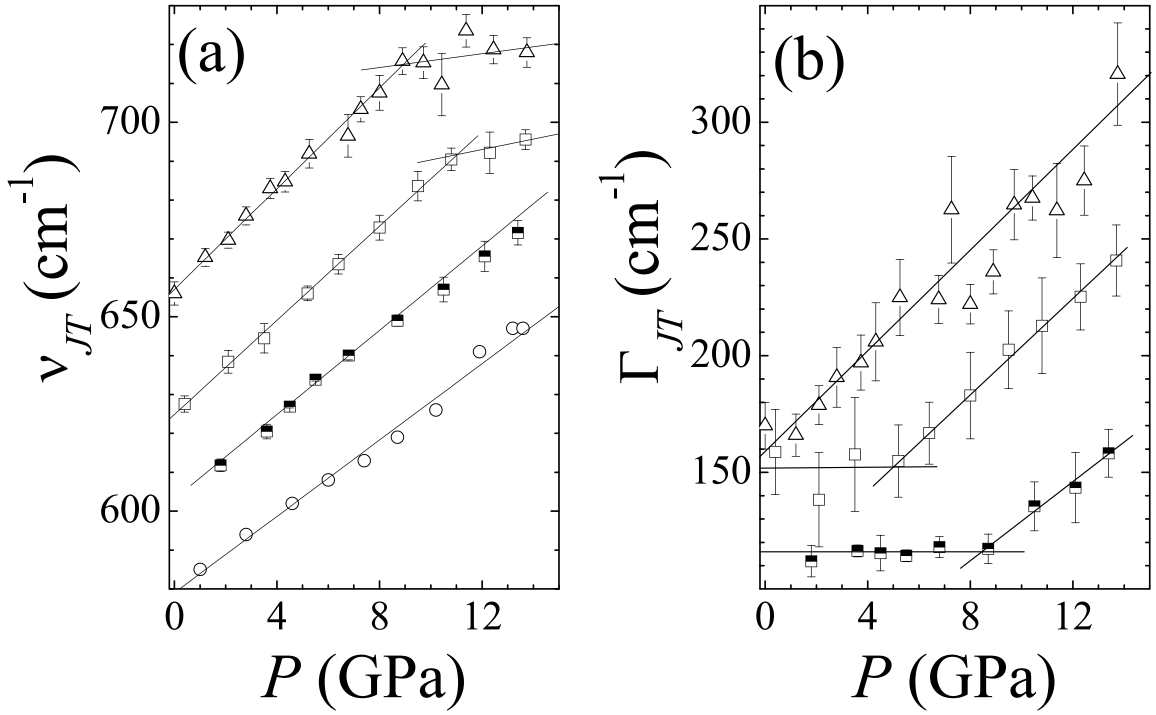

FIGURE 4.12: Pressure dependence of ν_{JT} (a) and Γ_{JT} (b) for $LaMnO_3$ (only in (a) open circles [8]), $La_{0.80}Ca_{0.20}MnO_{2.92}$ (half-filled squares), $La_{0.80}Ca_{0.20}MnO_3$ (open squares), and $La_{0.75}Ca_{0.25}MnO_3$ (open triangles [49]). For sake of clarity, the latter two in (a) have been upshifted of 15 and 40 cm^{-1} respectively. Lines are guides to eyes.

samples which are less distorted at $P = 0$. On the other hand, the saturation effect exhibited by LC25S ($x_{eff} = 0.25$) and LC20S ($x_{eff} = 0.20$) within the high-pressure regime shows the inefficiency of pressure in further reducing the JT distortions. This difference between the low and high pressure behaviors was ascribed to the onset of a new mechanism competing with the pressure-induced reduction of the JT distortion at high pressure [49].

The onset of this mechanism can be seen also in the pressure dependence of the linewidths Γ_{JT} shown in fig.4.12(b) for LC20D, LC20S, and LC25S. A sort of a two-steps behavior can be envisaged for Γ_{JT}: on increasing pressure, at first the linewidth remains constant and, above a threshold, it starts to increase linearly. A threshold value of about 9 GPa is apparent for LC20D whereas it can be only roughly evaluated at around 5 GPa for LC20S. In the case of LC25S we can say that the threshold goes to zero and the linewidth linearly increases starting from ambient pressure. This finding suggests that the onset of the lineshape broadening could be a precursor of the saturation regime shown by the pressure dependence of ν_{JT}. On the other hand the linewidth behavior is also consistent with the onset of a pressure-activated localizing interaction, which competes with the *natural* pressure-induced reduction of the JT distortion. Indeed, the competition favors the coexistence of both distorted and undistorted octahedra leading to a remarkable disorder-induced broadening of the JT phonon. As shown in fig.4.12, the pressure derivatives of both $\nu_{JT}(P)$ and $\Gamma_{JT}(P)$ can be either positive or nearly zero and, within a very simplified scheme, the effect of pressure on the system can be deduced from their values. In particular when $d\nu_{JT}/dP > 0$ the applied pressure symmetrizes the octahedra, thus inducing charge delocalization, whereas when $d\Gamma_{JT}/dP > 0$ a competing localizing interaction is activated and its strength is progressively increased by pressure. The behavior of $\Gamma_{JT}(P)$ has therefore its counterpart in $\nu_{JT}(P)$: in the very high pressure regime the localizing mechanism becomes strong enough to stabilize domains with a coherent distortion [52] and pressure becomes inefficient in further removing the JT distortion, thus leading to the saturation in $\nu_{JT}(P)$. It is finally worth to notice that the threshold pressure for the activation of the localizing mechanism appears to decrease on increasing x_{eff}, that is on increasing the metallic character of the system. This finding suggests that the new pressure activated interaction could be somehow related to the effective Mn-Mn hopping integral t (see sect.1.3.1).

4.2.2 Assignment of the Jahn-Teller phonon

As a final remark we show that the present Raman measurements provide a confirm of the assignment of the bending and JT stretching modes. The $d\nu_{JT}/dP$ and $d\nu_{ben}/dP$ values were calculated for $LaMnO_3$, LC20D, LC20S, and LC25S [3]. The obtained values are shown in fig.4.13 both as a function of Ca doping x (for the JT and bending phonons in panels (a) and (c) respectively) and as a function of effective doping x_{eff} (for the JT and bending phonon in panels (b) and (d) respectively). It appears that $d\nu_{JT}/dP$ is not correlated to x while it shows an almost linear dependence on x_{eff} (compare panels (a) and (b) in fig.4.13). On the other hand, $d\nu_{ben}/dP$ shows the opposite behavior being linearly dependent on x and not correlated to x_{eff}. This behavior can be interpreted considering that the JT phonon is directly connected to the JT distortion while the bending phonon is not. On increasing x_{eff}, pressure is more efficient in reducing the JT distortion (i.e. increasing ν_{JT}) since there is a larger number of undistorted octahedra. On the

---

[3] For $LaMnO_3$ the derivatives were calculated in the pressure range were the additional peak is absent, while for LC20S and LC25S the derivatives were calculated in the pressure range where $\nu_{JT}(P)$ is linear.

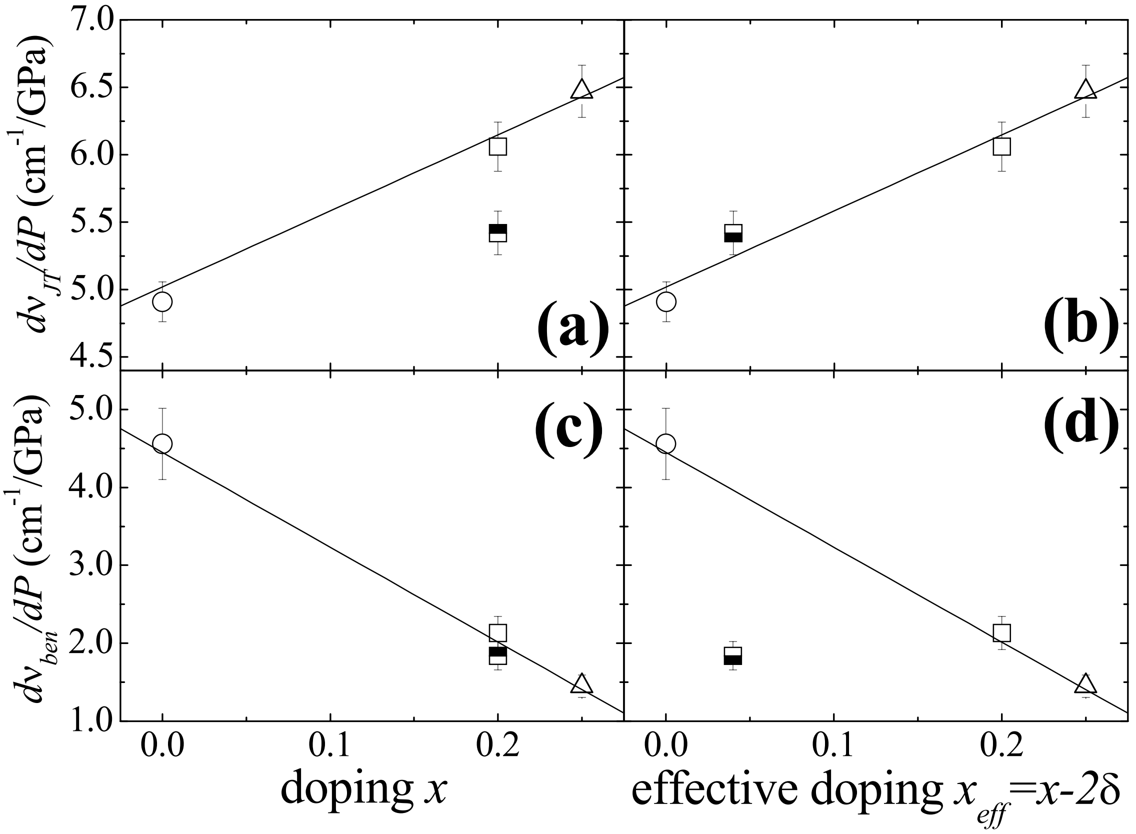

FIGURE 4.13: Pressure derivatives of ν_{JT} (panels (a) and (b)) and ν_{ben} (panels (c) and (d)) as a function of Ca-doping x (panels (a) and (c)) and of effective doping x_{eff} (panels (b) and (d)). Lines are guides to eyes.

other hand, on increasing x the average A-site ionic radius is reduced[4] and the available space for bending the apical oxygen ions increases. Therefore at large x, ν_{ben} is less affected by the pressure-induced lattice compression. The above results strongly support the assignment of the bending and JT phonons.

---

[4] La^{3+} is larger than Ca^{2+} [11].

Chapter 5

Infrared Results at High-Pressure

In this chapter the results obtained by means of high-pressure infrared (IR) spectroscopy are reported. In the first section, the most relevant infrared measurements reported in the literature and the information which can be extracted from this kind of measurements will be reviewed. In the second section, our high-pressure and low-temperature mid-IR measurements on $La_{0.75}Ca_{0.25}MnO_3$ (LC25S) will be shown and discussed. From these data the pressure dependence of the IM transition temperature was determined up to 11 GPa, thus providing for the first time the $P-T$ phase diagram of a manganite over a wide pressure range. A description of the experimental phase diagram performed by means of a simple yet efficient theoretical model based on a two Mn-site cluster will be presented in the third section. Finally, in the fourth section, we will present room-temperature high-pressure far-IR absorption measurements performed on LC25S, $La_{0.80}Ca_{0.20}MnO_3$ (LC20S), and $La_{0.80}Ca_{0.20}MnO_{2.92}$ (LC20D) exploiting the high brilliance of the IR SINBAD beam-line at DAΦNE. These data represent the first high-pressure measurements on manganites in the far-IR range.

5.1 Survey of infrared spectroscopy on manganites

In the last years, a large number of IR experiments on CMR manganites were carried out. In this section we show and discuss several representative examples and in particular we will concentrate on the information which in principle can be obtained from the IR spectrum.

IR reflectance measurements were carried out by Lee et al. on a $Nd_{0.7}Sr_{0.3}$-MnO_3 ($T_C = T_{IM} = 198$ K) single crystal as a function of temperature [96]. The measured reflectivity and the corresponding optical conductivity obtained from Kramers-Kroenig analysis are shown in the left and right panels of fig.5.1 respectively. In the insulating phase the optical spectrum shows small absorption in the far-IR region and at higher frequency the onset of a broad band centered around 1 eV, leading to a gap-like feature ("pseudogap") qualitatively similar to that of a standard semiconductor. This broad band ("polaronic band") was ascribed to the photoionization of small polarons, i.e. the excitation of a charge self-trapped in the local potential well induced by the JT distortion. On decreasing temperature below T_C the polaronic band shifts to low frequency and eventually evolves in a Drude term. The inset in fig.5.1 shows that even at 15 K the spectrum is composed by two main contributions: the Drude peak superimposed to a broad band which seems the evolution of the polaronic band observed at high temperature. In this picture the IM transition can be interpreted in terms of a crossover from small-localized to large-delocalized polaron (see sect.1.3.3). Considering the raw reflectivity spectra, it can be noted that, on entering the metallic phase, phonons become progressively screened but a complete screening is achieved only well below T_C. In particular, the appearance of

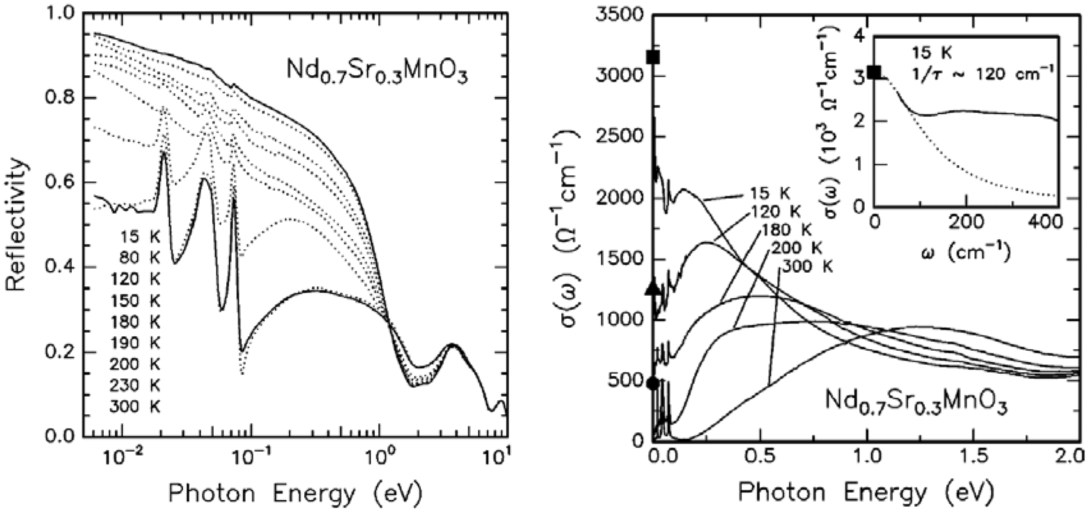

FIGURE 5.1: Temperature dependent infrared reflectivity (left panel) and corresponding optical conductivity (right panel) of a $Nd_{0.7}Sr_{0.3}MnO_3$ single crystal. In the inset: magnification of the optical conductivity at 15 K in the far-infrared range [96].

a Drude contribution completely screens the lowest frequency phonon. A clear signature of the transition can be obtained by means of the standard procedure of calculating the spectral weight n^*, i.e. the integral of the optical conductivity over a suitable spectral range. According to ref. [97], this quantity is simply proportional to the kinetic energy of the charge-carriers. The temperature dependence of the spectral weight obtained integrating the data shown in fig.5.1 from 0 to 0.8 eV is shown in fig.5.2. The rapid increase of $n^*(T)$ around T_{IM}, indicates a rather abrupt increase of the kinetic energy of charge-carriers and thus the IM transition.

A similar behavior was also observed in several single crystals of manganites of the type $R_{0.6}Sr_{0.4}MnO_3$ (R=La, Pr, Nd, Sm) [98]. In figure 5.3 the temperature dependence of the reflectivity (left panels) and optical conductivity (center and right panels) obtained in ref. [98] is shown. In all samples the polaronic band (central panels in fig.5.3) behaves similarly to the case of $Nd_{0.7}Sr_{0.3}MnO_3$ and a progressive screening of phonons is observed both in the reflectivity spectra (left panels) and in the optical conductivity (right panels). These results indicate that the observed behavior of the polaronic band and the phonon screening are quite general features of the IM transition in manganites.

A similar temperature-dependent behavior can be observed also in mea-

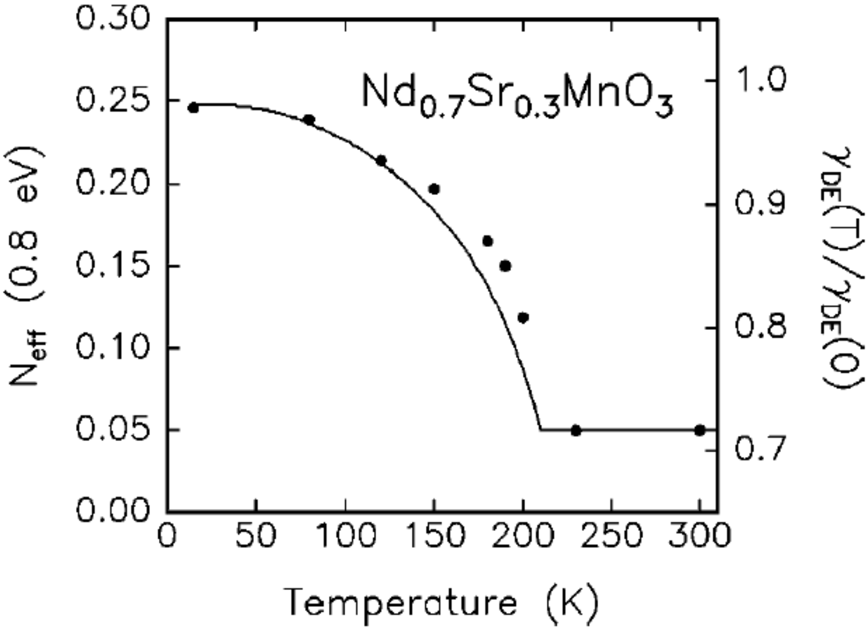

FIGURE 5.2: Temperature dependence of the spectral weight (full circles) of the data of fig.5.1 and theoretical prediction from the double-exchange model (solid line) [96].

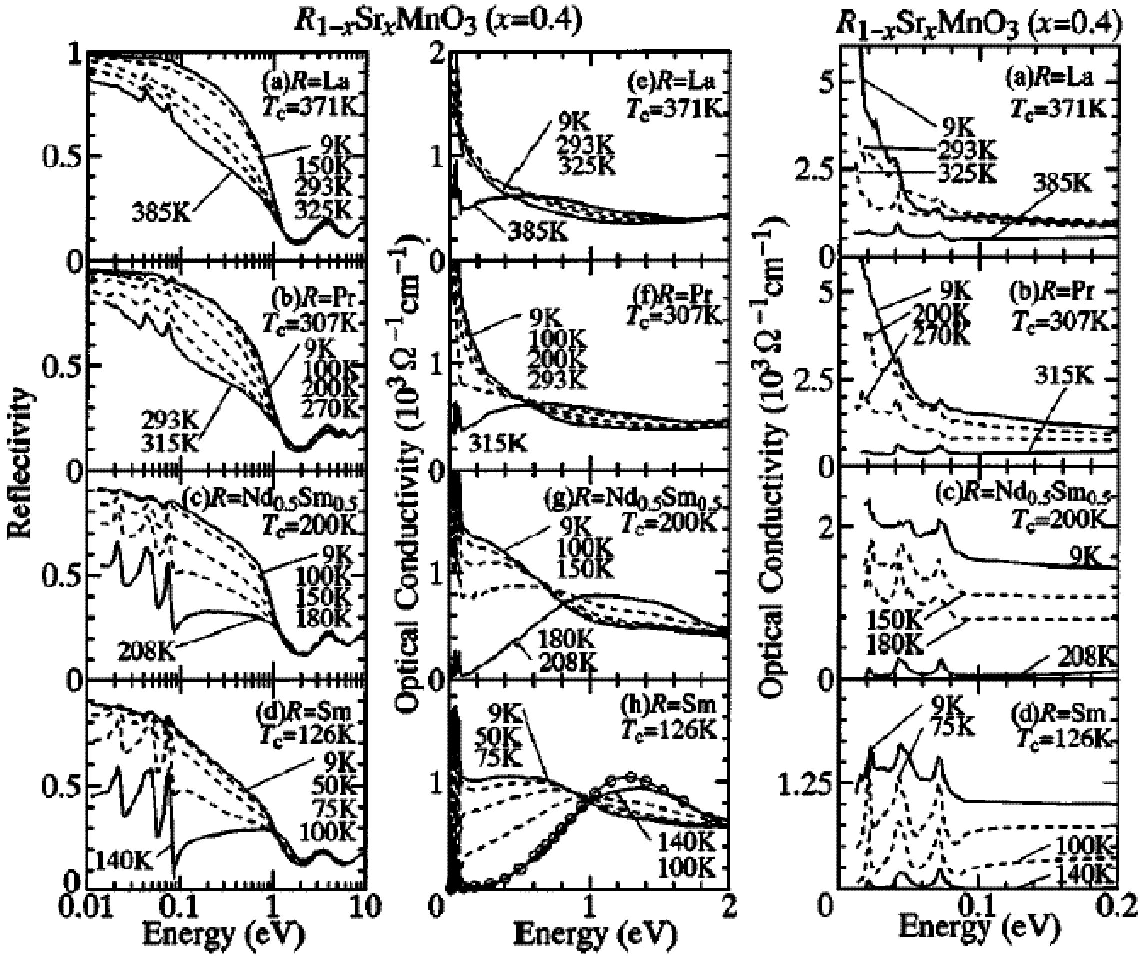

FIGURE 5.3: Temperature dependence of the reflectivity (left panels) and corresponding optical conductivity (center and right panels) of $R_{0.6}Sr_{0.4}MnO_3$ single crystals [98].

surements performed on poly-crystalline samples. Kim et al. measured the reflectivity of a $La_{0.7}Ca_{0.3}MnO_3$ poly-crystalline sample as a function of temperature [99]. The resulting optical conductivity is shown in fig.5.4(a), while in panel (b) the spectral weight analysis is shown. The total spectral weight (open diamonds) is compared with the spectral weight DW of the Drude peak (full squares) obtained by means of:

$$DW = \frac{2m\omega_P^2}{8\pi e^2 N} \tag{5.1}$$

where m is the electron mass, ω_P is the plasma frequency, e is the electron charge, and N is the number of Mn-ions per unit cell. Since ω_P^2 linearly increases on decreasing temperature below T_{IM}, the same behavior is observed in DW. The difference between DW and the total spectral weight

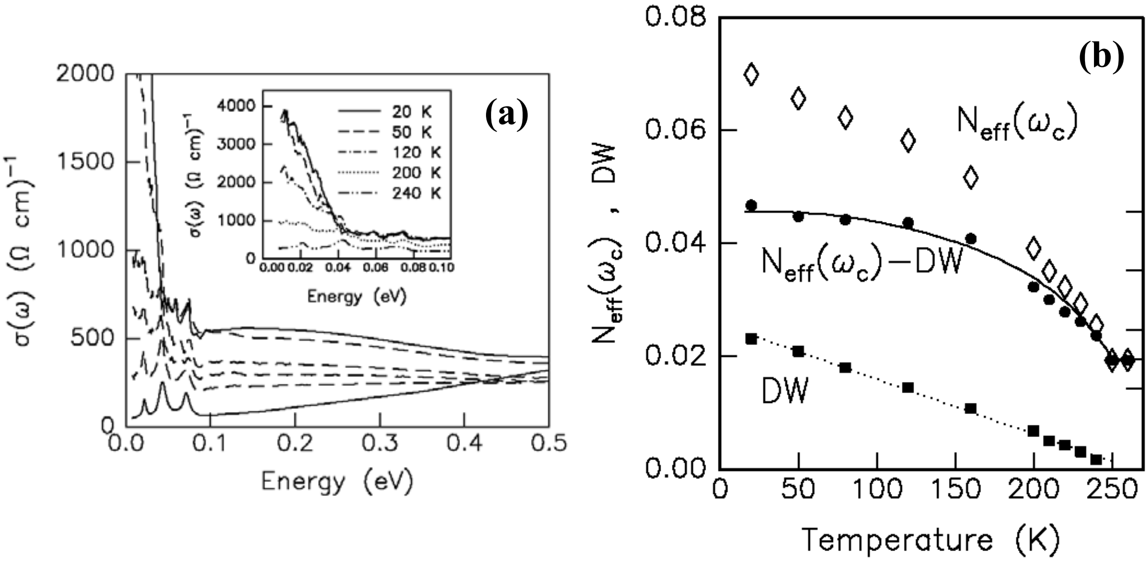

FIGURE 5.4: (a) Optical conductivity obtained by means of reflectivity measurements on $La_{0.7}Ca_{0.3}MnO_3$ poly-crystals. (b) Temperature dependence of the total spectral weight (open diamonds), of the spectral weight of the Drude contribution (full squares) and of the difference between the spectral weights (full circles). Solid line is the double-exchange prediction [99].

(i.e. the spectral weight of the polaronic band) and the theoretical prediction obtained from the DE model are also plotted in fig.5.4(b). It is well evident that the good agreement between the polaronic band spectral weight and the theoretical prediction. Therefore, the spectral weight of the polaronic band gives a clear signature of the IM transition [99, 100].

The same behavior can be observed also by means of transmission measurements. Since manganites are characterized by a strong absorption in the IR region, this kind of measurements must be performed either on very thin samples or on pellets of manganite grains dispersed in a IR-transparent matrix. The latter procedure was exploited in ref. [51] where the intensity transmitted in the mid-IR range both by LC25S dispersed in a pellet of KBr $(I(\nu))$ and a pure-KBr pellet $(I_0(\nu))$ was collected. The optical density $O_d(\nu)$ was then extracted by means of:

$$O_d(\nu) = \ln\left(\frac{I_0(\nu)}{I(\nu)}\right) \tag{5.2}$$

The optical densities so obtained at different temperatures are shown in fig.5.5(a). It is well evident that on decreasing temperature, the pseudogap at around 700 cm^{-1} first deepens and then suddenly starts to fill when entering the metallic phase. This behavior can be evidenced by calculating the

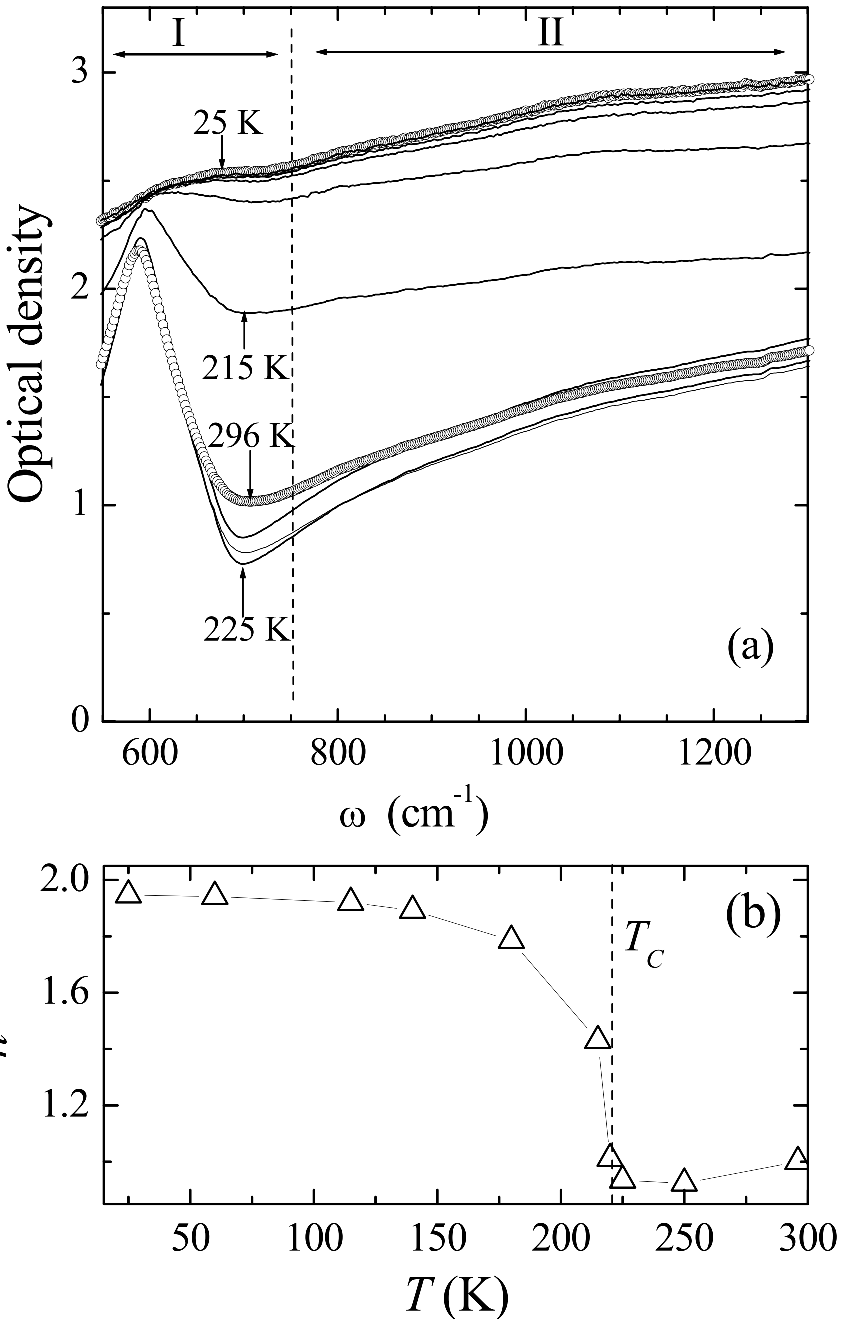

FIGURE 5.5: (a) Temperature dependence of the optical density of $La_{0.75}Ca_{0.25}MnO_3$. (b) Temperature dependence of the integral of the optical density in (a) over the spectral region labelled II [51].

spectral weight of the polaronic band (region II in fig.5.5(a)) as shown in fig.5.5(b). It can be proved that the optical density is roughly proportional to the optical conductivity [101] and therefore the integral of $O_d(\nu)$ is proportional to the spectral weight of the optical conductivity. On the other

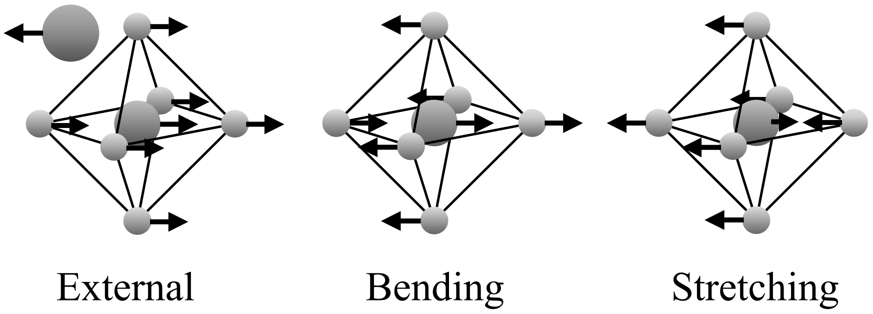

FIGURE 5.6: Atomic displacements of the infrared-active phonons of a cubic perovskite.

hand, the temperature dependence of the spectral weight obtained by the optical density (fig.5.5(b)) shows the same behavior of those obtained by the optical conductivity (figs.5.2 and 5.4(b)). IR absorption measurements are thus a good tool for studying the metallization process in manganites and in particular the temperature at which the inversion of the temperature dependence of the spectral weight occurs can be considered as a good estimate of the IM transition temperature T_{IM}.

Far-IR measurements on manganites allows also to study the IR-active phonon modes. In a cubic ABX_3 perovskite structure, there are three F_{1u} symmetry IR-active phonons: an external vibration of A-site ion, an asymmetric bending of the octahedron, and a stretching of the $B-X$ bonds (see fig.5.6). Since the JT modes are all symmetric (see sect.1.1.1), no JT phonons can be observed with IR measurements, but information on the octahedral distortion can be obtained also in this case. In particular the distortion from the cubic symmetry leads to the appearance of additional phonon peaks in the IR spectrum. The IR phonon spectrum of $\mathrm{La_{0.7}Ca_{0.3}MnO_3}$ was studied by Kim et al. [102] who determined the far-IR optical conductivity from reflectivity measurements, as shown in the left panel of fig.5.7. Three main phonon bands can be observed at around 180, 350, and 550 cm^{-1} and, in analogy with the cubic structure, they are ascribed to the external, bending, and stretching modes respectively[1]. Additional weak peaks can be observed, particularly at low temperature, indicating deviations from the ideal cubic structure. Moreover, a complex fine-structure of the phonon modes was observed by several authors [103–105], particularly for the bending-band at around 350 cm^{-1}. The temperature dependence of the frequency of the three main phonon bands was determined and it is shown in the right panel

---

[1] This assignment is not rigorous, whereas the phonon spectrum of the pseudocubic structures is expected to be similar to the that of the related cubic structure.

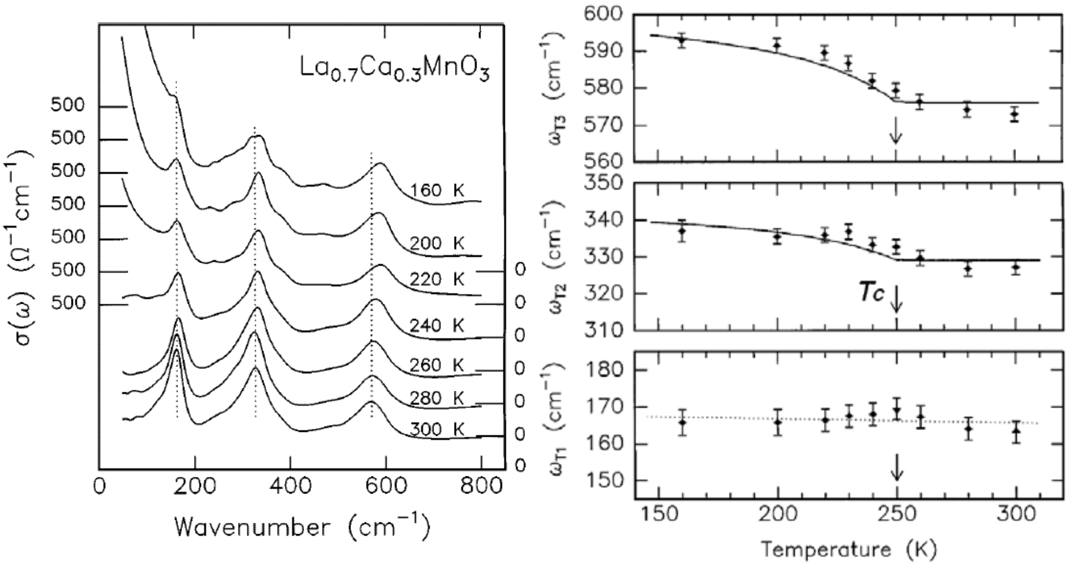

FIGURE 5.7: Left panel: temperature dependence of the far-infrared optical conductivity of $La_{0.7}Ca_{0.3}MnO_3$. Right panels: temperature dependence of the frequencies of the three phonon bands present in the spectra of the left panel [102].

of fig.5.7. A rather abrupt hardening of the stretching phonon at $T = T_C$ is observed, and a similar although less pronounced T-dependence is shown by the bending phonon whereas the external mode is centered at an almost constant frequency. These results are in good agreement with the phonon hardening theoretically predicted in the framework of EPC [23], but this effect was also questioned in successive papers [103, 104]. This issue is still unsolved nowadays.

When this thesis started, there was only one paper reporting on high pressure IR measurements on manganites, in the literature. We conclude this section describing the results reported in this paper. Mid-IR absorption measurements were performed on LC25S at room temperature as a function of pressure up to 10 GPa [51]. Data are shown in the top panel of fig.5.8, while in the bottom panel the spectral weights are plotted as a function of pressure. The effect of increasing pressure is similar to that of lowering temperature and the pseudogap progressively fills, whereas it can be noted that, even at the highest pressure, the phonon is not completely screened. Moreover, the pressure dependence of the integrals of the optical density is quite smooth. As to the pressure dependence of the spectral weight obtained on the layered manganite $Sr_{1.5}La_{0.5}MnO_4$ (which at ambient pressure is insulating at all temperatures) a small and almost linear increase is ob-

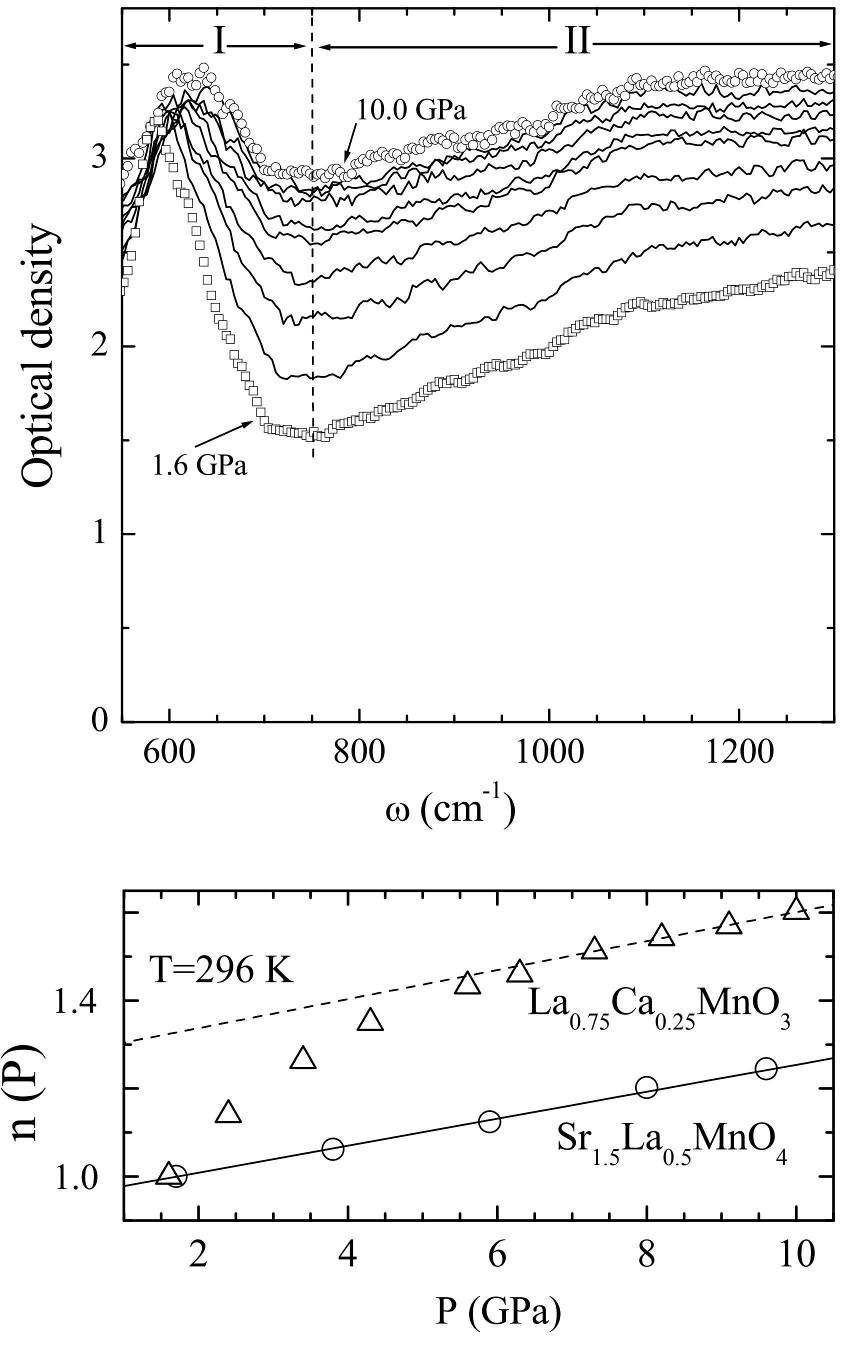

Figure 5.8: Top panel: room-temperature pressure dependence of the optical density for $La_{0.75}Ca_{0.25}MnO_3$. Bottom panel: pressure dependence of the integral of the optical densities in the top panel (triangles) compared with the integral of the optical density for $Sr_{1.5}La_{0.5}MnO_4$ (circles). Lines are guides to eyes [51].

served, suggesting that pressure induces no IM transition in this compound. The high-pressure behavior in LC25S is very similar to that of the layered compound. The whole of these results suggest that no pressure-induced IM transition occurs in LC25S at room temperature, in good agreement with Raman [49] and X-ray diffraction [52] results discussed in sects.4.1.1 and 2.4 respectively.

On the basis of the above discussion, the relevant information on delocalization processes in manganites which can be obtained from IR measurements can be schematically summarized as follows:

- The spectral weight, even if calculated only in the polaronic-band region, describes the charge delocalization extent and the metallic degree of the system.
- The inversion point of the spectral-weight vs. temperature curve is a good estimate of the IM transition temperature.
- Phonon screening (complete for the external phonon and at least partial for the bending and stretching phonons) represents an indication of the onset of free-carrier conduction.

In order to give a clear evidence of the absence of a pressure-induced room-temperature IM transition, in this thesis the optical density of LC25S was measured both as a function of pressure and temperature, thus determining the $P-T$ phase diagram. Moreover, in order to get a deeper insight in the metallization process, high pressure measurements on LC25S, LC20S, and LC20D were performed in the far-IR region were a Drude contribution with screening of the low frequency phonon should be observed when a metallic phase is established.

5.2 Pressure and temperature dependent infrared absorption on $La_{0.75}Ca_{0.25}MnO_3$

Exploiting the experimental setup described in sect.3.3, high-pressure low-temperature mid-IR absorption measurements on LC25S were carried out at the European Laboratories for Non-linear Spectroscopy (LENS) in Florence. The intensity $I(\nu)$ transmitted by the sample+KBr loaded inside the DAC was measured as a function of temperature along seven isobaric paths (0.3, 0.8, 2.1, 4.3, 6.5, 8.8, and 11.2 GPa). The intensity $I_0(\nu)$ transmitted by a pure KBr pellet loaded in the DAC was also measured and the optical density $O_d(\nu) = \ln[I_0(\nu)/I(\nu)]$ calculated for each spectrum. Good quality spectra were obtained within the 500-4500 cm^{-1} range with a spectral resolution of about 4 cm^{-1}.

The $O_d(\nu)$ measured at room temperature and at the minimum pressure is shown in fig.5.9. There can be clearly identified the asymmetric-stretching (AS) phonon at around 600 cm^{-1} and the tail of the polaronic band at higher frequency. Two additional structure at 1000 cm^{-1} ($X1$) and 1500 cm^{-1} ($X2$) are also apparent and they will be discussed in the following. The temperature dependence of $O_d(\nu)$ is shown for three representative pressures in fig.5.10. A strong pressure-induced hardening of the AS phonon can be directly observed in the raw data, whereas no temperature dependence of the phonon peak-frequency is observed. A moderate pressure-induced hardening of $X1$ and $X2$ structures is also observed (60 and 30 cm^{-1} respectively) whereas the temperature dependence of these structures appears to be negligible. The polaronic band shows the aforementioned inversion effect at all pressure thus indicating that the low-temperature metallic phase exist over the whole explored pressure-range. At high-pressure and/or low temperature the high-frequency absorption strongly increases leading to saturation at high frequency.

Before presenting the data analysis, we deal with the nature of the spectral features $X1$ and $X2$. It is important to note that, calculating the differ-

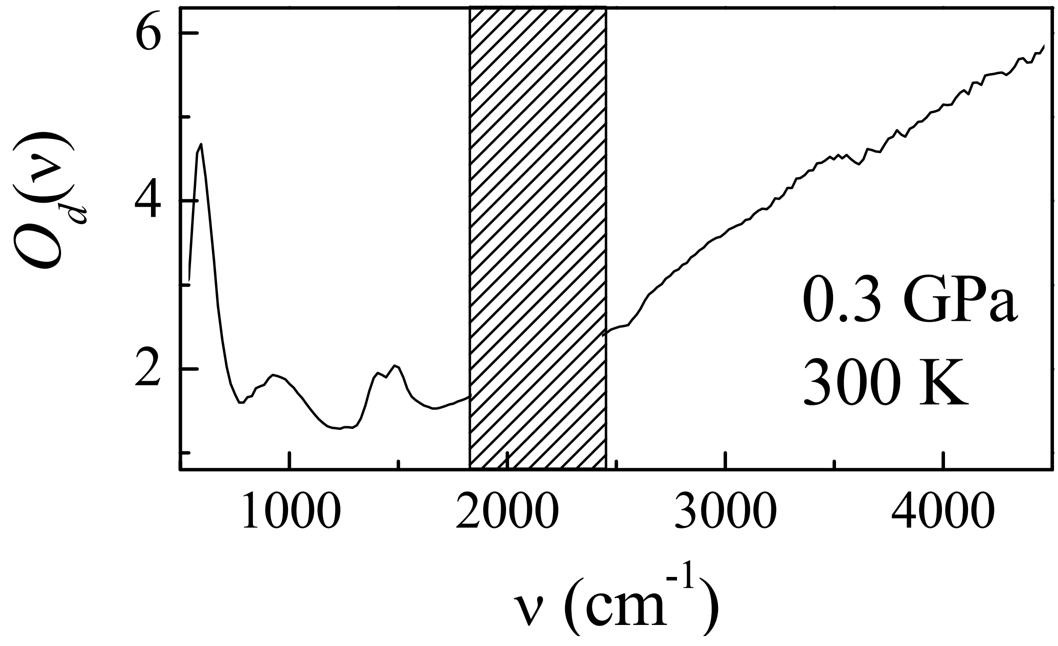

FIGURE 5.9: Room temperature optical density of $La_{0.75}Ca_{0.25}MnO_3$ at 0.3 GPa. The shaded area shadows the region of strong diamond absorption.

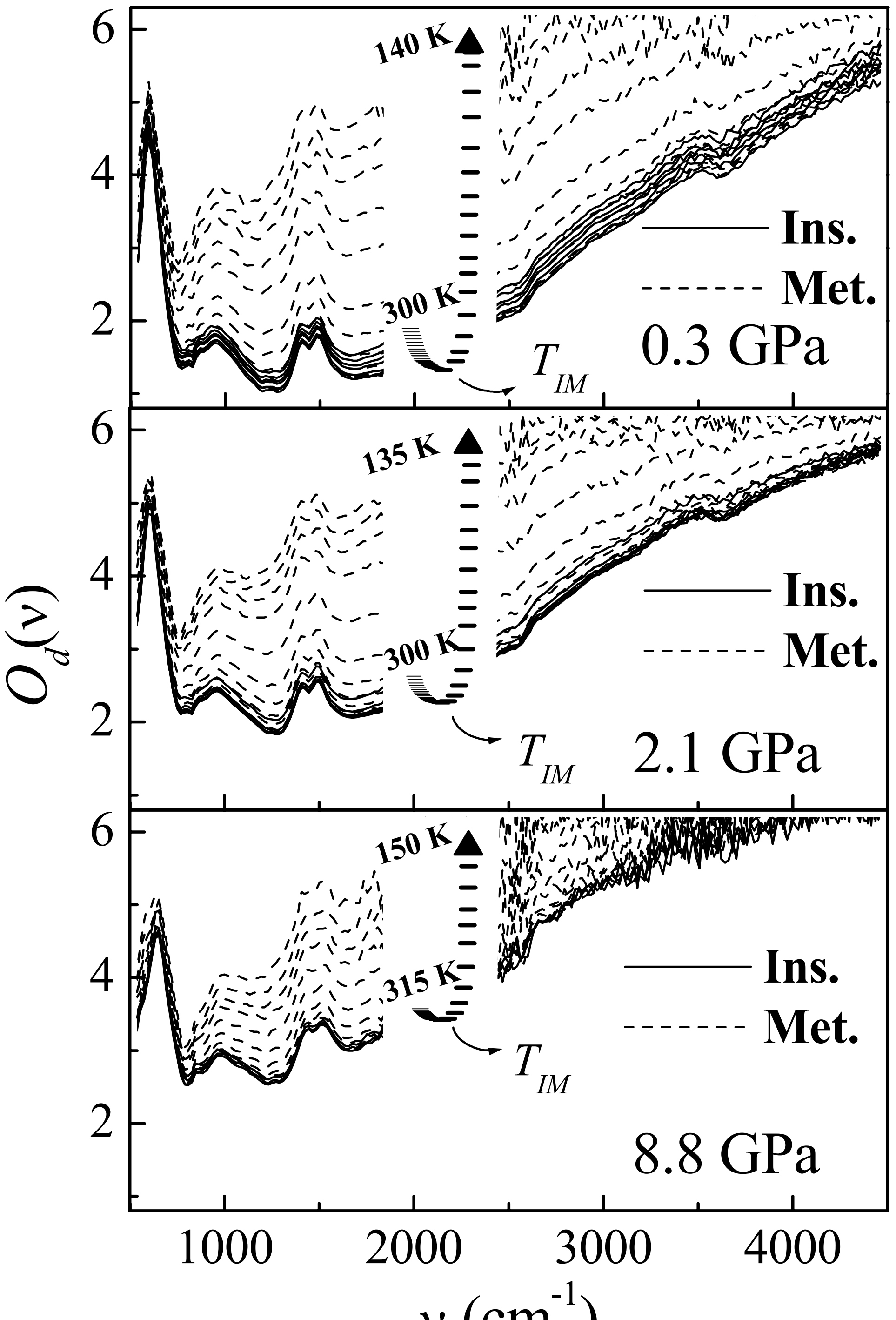

FIGURE 5.10: Temperature dependence of $O_d(\nu)$ along three representative isobars. On cooling, the overall absorption at first decreases (shown by solid curves) and then increases (shown by broken curves). Data over the range 1850-2450 cm^{-1} are not shown because of the strong absorption from diamonds.

ence between the $O_d(\nu)$ at two different temperatures for a given pressure, no residual structures appear around 1000 and 1500 cm^{-1}, indicating that the $X1$ and $X2$ structures are almost temperature independent and their presence does not affect the temperature dependence of the spectral weight n^*. Despite the aforementioned pressure-induced hardening of $X1$ and $X2$, the intensity of these two structures seems not to depend on pressure. Therefore $X1$ and $X2$ can have only very small effects on the pressure behavior of the spectral weight. The physical nature of these two bands is not yet clear. They can be attributed either to multi-phonon bands or to the fine structure of the polaronic band as theoretically predicted [106]. Although a definitive conclusion on the origin of $X1$ and $X2$ cannot be drawn, we want to stress once more that the presence of these structure has negligible effects on the temperature dependence of n^* and hardly affects the pressure dependence of this quantity. On the basis of the above considerations, we can safely apply the spectral-weight analysis.

5.2.1 Spectral weight and phase diagram

In order to avoid the spectral regions where the saturation occurs from high-pressure and low-temperature measurements, the spectral weights were calculated over the 800-1700 cm^{-1} range. The temperature dependence of n^* was calculated at each pressure and it is shown in fig.5.11. The presence of the inversion point is clearly observed at all pressures. As discussed in sect.5.1, the inversion point of $n^*(T)$ is a good estimate of the IM transition temperature T_{IM}. The abscissa of the inversion point was then estimated at each pressure by means of three independent methods and the three results have been averaged, thus obtaining the T_{IM} value and uncertainty given by the maximum semi-dispersion. The resulting $T_{IM}(P)$ values are shown in fig.5.12. It is well evident that on increasing pressure $T_{IM}(P)$ strongly deviates from the linear behavior observed at low pressure (see sect.2.4). In particular two regimes can identified: a low-pressure regime where pressure-induced charge delocalization is strong and $T_{IM}(P)$ rapidly increases and a high-pressure regime where pressure is inefficient in further induce charge delocalization and $T_{IM}(P)$ saturates. The observed $T_{IM}(P)$ behavior is fully consistent with the onset at high pressure of a localizing mechanism which efficiently competes with the natural pressure delocalizing-tendency, as suggest by the results of refs. [49], [51], and [52] (see sects.2.4, 4.1.1, and 5.1).

The experimental values can be fitted by means of the empirical curve:

$$T_{IM}(P) = T_{IM}^{\infty} - (T_{IM}^{\infty} - T_{IM}^{0}) \exp(-P/P_0) \tag{5.3}$$

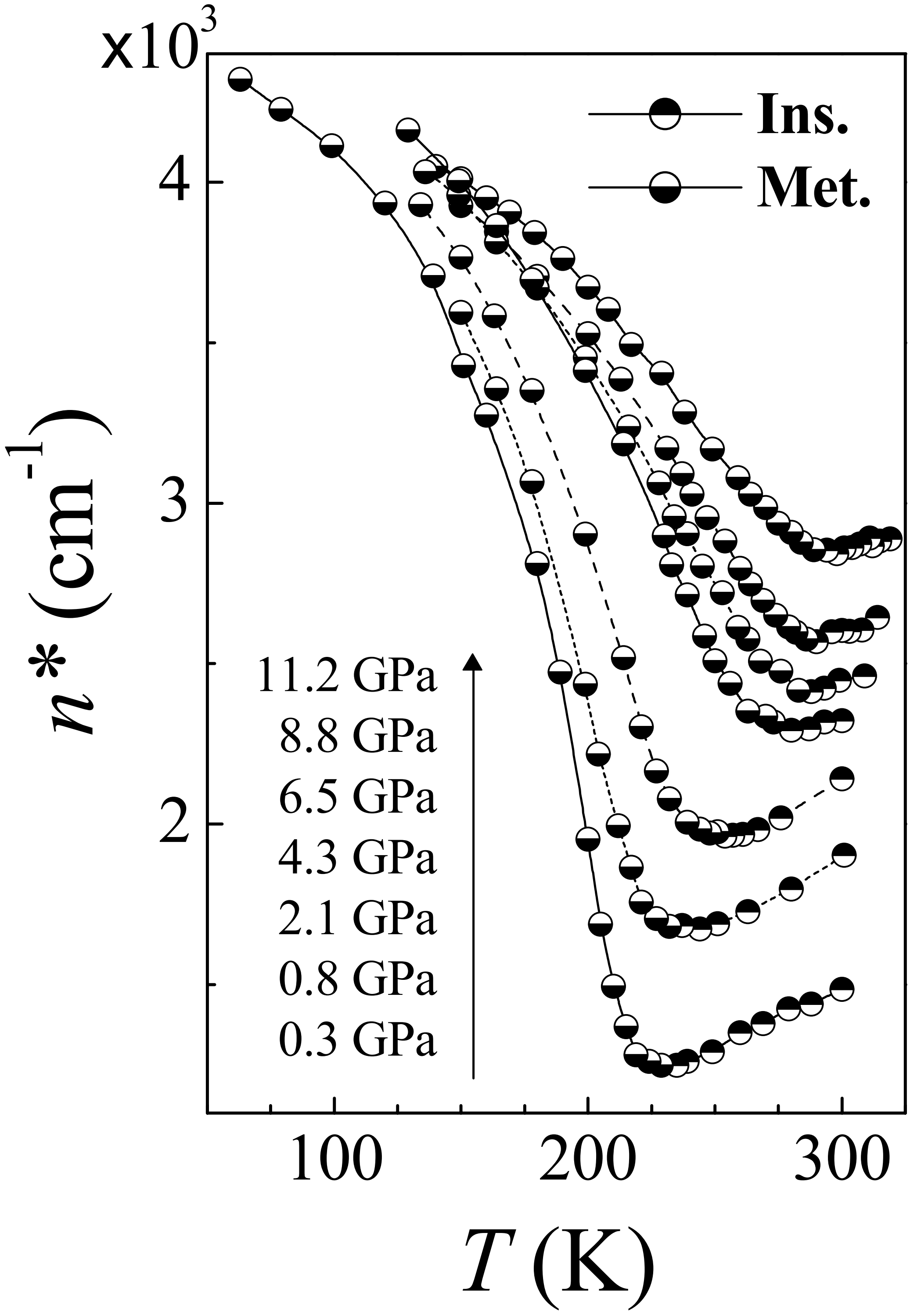

FIGURE 5.11: Temperature dependence of n^* at each measured pressure. Upper half-filled symbols: insulating phase; lower half-filled symbols: metallic phase.

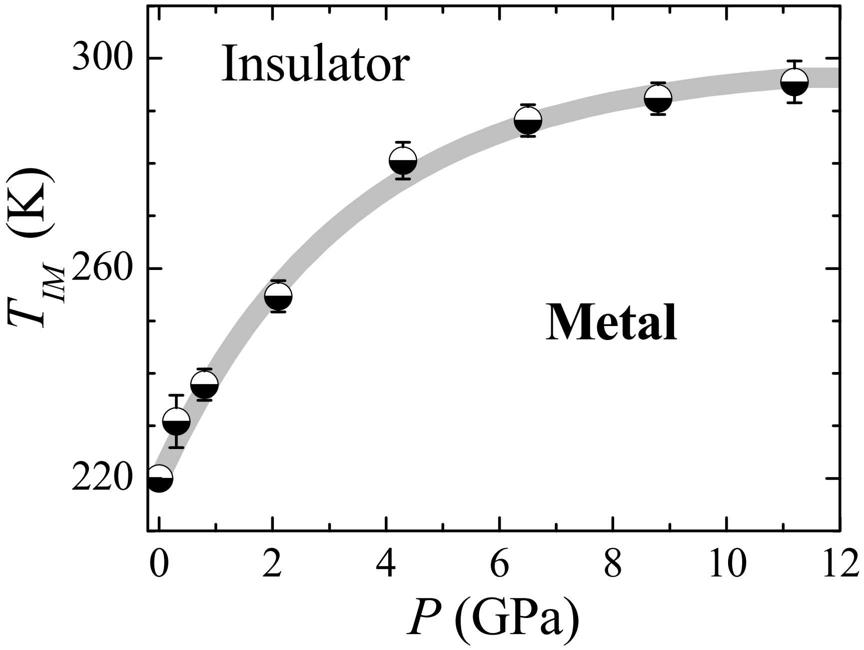

FIGURE 5.12: $P - T$ phase diagram of $La_{0.75}Ca_{0.25}MnO_3$. Symbols: experimental data; solid gray line: fit by means of eq.5.3.

where $T^0_{IM} = 220$ K is the $T_{IM}(P = 0)$ value, and $T^{\infty}_{IM} = 299 \pm 3$ K and $P_0 = 3.4 \pm 4$ GPa are the best-fit values of the two free fitting parameters. The asymptotic value T^{∞}_{IM} confirms the suggestion of refs. [49, 51] where no evidence of pressure induced IM transition at room temperature was observed in LC25S.

5.2.2 Phonon Line

An analysis of the phonon line was also attempted. A best-fit procedure was applied using a model curve given by a dumped harmonic oscillator plus a linear background. The background roughly accounts for possible other spectral contributions within the narrow spectral region of the AS-phonon. The fit interval was varied in order to include the region between the lower data-limit and the minimum between the phonon peak and the polaronic band. It is important to note that, while the phonon frequency best-fit value ν_{AS} is quite stable, the phonon width is strongly dependent on the background. The pressure dependence of ν_{AS} is shown in fig.5.13 at three representative temperatures: 200 K, 260 K, and 300 K. In the inset of the same figure the temperature dependence of ν_{AS} at 0.3 GPa, 4.3 GPa, and 11.2 GPa is shown. At all pressures, the temperature dependence of the ν_{AS} is well below the experimental uncertainty. It is worth to note that, concerning the phase

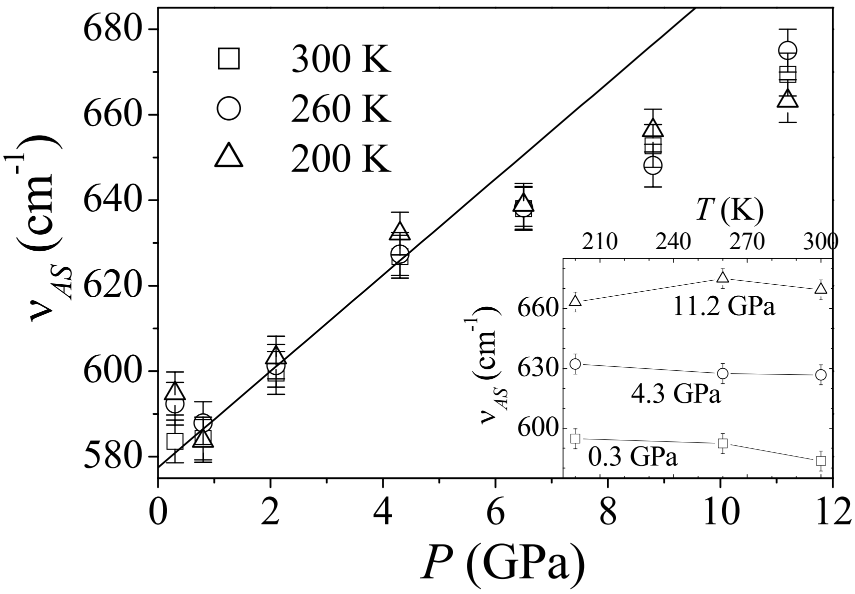

FIGURE 5.13: Pressure dependence of the asymmetric-stretching phonon-frequency at 200 K (triangles), 260 K (circles), and 300 K (squares). Solid line is a linear fit of the first four data at 300 K. Inset: temperature dependence of the same phonon frequency at 0.3 GPa (squares), 4.3 GPa (circles), and 11.2 GPa (triangles).

diagram above discussed, at 300 K the system is always insulating, at 200 K it is always metallic, while at 260 K it undergoes a pressure induced IM transition at around 2 GPa. Therefore, the phonon frequency has a negligible dependence on the metallic character of the system. On increasing pressure a strong hardening is observed, consistently with the lattice compression and the octahedra symmetrization. It is worth to note that, below 6-7 GPa, $\nu_{AS}(P)$ has a slope higher that above, clearly resembling the pressure behavior of the Raman-active symmetric stretching (see sect.4.1.1).

5.3 Two-site model for the $P - T$ phase diagram

As discussed in sect.2.4 a possible explanation of the observed competition between charge localization and delocalization at high pressure is the increasing role of the AF SE coupling. In order to test this hypothesis a simple yet efficient theoretical model for computing the Curie temperature T_C (which is almost coincident with the IM transition temperature T_{IM}) was developed. This model is constituted by a two Mn-site cluster which represents the minimal model including DE, EPC, and SE interactions. The two-site model (TSM) here presented has already been studied in Ref. [107], where it has been shown to successfully catch the relevant physics of manganites at $T = 0$ owing to the extremely short-range nature of the interactions occurring in these systems. The TSM has been extensively employed in the study of polaronic systems, since it is the simplest model able to describe the crossover from a metal to an almost localized small polaron [108]. In particular, it was already successfully applied to the case of manganites [107, 109]. The reliability of the TSM in the case of manganites can be assessed also through the analogy with a completely different theoretical approach, the Dynamical Mean Field Theory (DMFT) [110], which has been applied to a lattice model for the manganites by Millis and coworkers [111]. The DMFT is a powerful non-perturbative approach which freezes spatial fluctuations, but fully retains the local (single-site) quantum dynamics, mapping the original lattice model in the thermodynamic limit onto a self-consistent impurity model which interacts with a quantum bath [110]. In the TSM, the quantum nature of the problem is also completely retained, and each of the two sites "feels" the presence of the other site similarly to the way the impurity site feels the bath within DMFT. Both the methods, despite their differences, are thus expected to well describe the physics of short-range correlations in manganites. In this context we use the TSM model since, besides its intrinsic simplicity, it allows to consider quantum spins and phonons and a SE coupling term between local spins can be easily introduced. On the other hand, such an approach would be quite difficult in the framework of DMFT.

The hamiltonian of our TSM contains the DE term, the EPC, and the SE term [107]:

$$\begin{aligned} H = & -t \sum_{\sigma} \left(c^{\dagger}_{1,\sigma} c_{2,\sigma} + c^{\dagger}_{2,\sigma} c_{1,\sigma} \right) - J_H \sum_{i=1,2} \vec{\sigma}_i \cdot \vec{S}_i \\ & + J_{AF} \vec{S}_1 \cdot \vec{S}_2 - g \left(n_1 - n_2 \right) \left(a + a^{\dagger} \right) + \omega_0 a^{\dagger} a. \end{aligned} \tag{5.4}$$

The standard notation used in chap.1 was employed. It is worth to note that in this model, all the interactions considered are treated at the same level. The simplicity of this model allows complete exact diagonalization of the hamiltonian. In particular the thermal-average of the nearest-neighbor spin correlation operator $\mu = \vec{S}_1 \cdot \vec{S}_2$ can be obtained:

$$\mu(T) = \frac{\sum\limits_{n} \langle \psi_n | \, \mu \, | \psi_n \rangle \exp\left(-E_n / T \right)}{\sum\limits_{n} \exp\left(-E_n / T \right)} \tag{5.5}$$

where $|\psi_n\rangle$ and E_n are the eigenstates and eigenenergies of H respectively. A good estimate of T_C is represented by the temperature at which μ is half of the $T = 0$ saturation value.

Before discussing the calculation at high pressure, the zero-pressure λ-dependence of T_C obtained from the TSM was compared with the same results obtained in the framework of DMFT by Millis and coworkers [111]. The $T_C(\lambda)$ curves calculated with the two methods are very similar, thus making us confident on the reliability of the TSM for describing the physics of manganites. The input parameters of this model are the hopping integral t, the Hund coupling J_H, the phonon frequency ω_0, the SE coupling J_{AF}, and the dimensionless EPC $\lambda = 2g^2/\omega_0 t$. The pressure dependence of t, J_H, ω_0, and λ was estimated combining the results obtained from structural [52], spectroscopic [49], and first principles [112] investigations on $La_{1-x}Ca_xMnO_3$. To our knowledge no estimate of the pressure dependence of J_{AF} is available in the literature. Therefore the calculation was performed following three hypothetical pressure dependencies of J_{AF}: i) $J_{AF}(P) = const.$, ii) $J_{AF}(P) \propto t$, and iii) $J_{AF}(P) \propto t^2$. We want to stress that these three choices correspond to reduce, keep constant, and increase the ratio J_{AF}/t upon increasing pressure.

The pressure dependence of T_C calculated with the TSM in cases i), ii), and iii) is shown in fig.5.14 with dotted, dashed, and solid lines respectively.

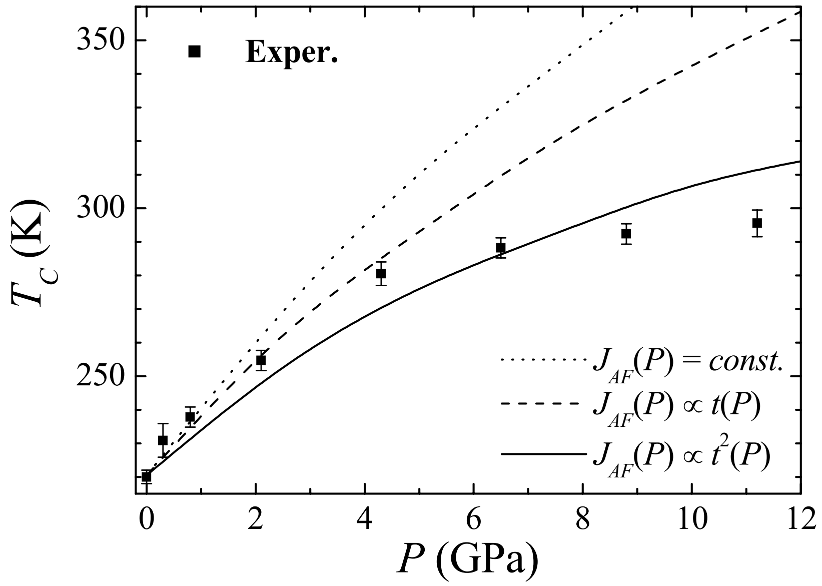

FIGURE 5.14: Pressure dependence of T_C obtained experimentally (full squares) and calculated with the two-site model for $J_{AF} = const.$ (dotted line), $J_{AF} \propto t$ (dashed line), and $J_{AF} \propto t^2$ (solid line).

In the same figure the experimental data described in sect.5.2.1 are shown. For small pressure, the cases i) [$J_{AF} = const$] and ii) [$J_{AF} \propto t$] nicely follow the experimental T_C, while case iii) [$J_{AF} \propto t^2$] gives a lower critical temperature. By increasing the pressure, in the first two cases T_C increases too rapidly with pressure, while the third estimate closely follows the experimental data up to 11 GPa. The ability of the $J_{AF} \propto t^2$ data to reproduce the actual experimental behavior is really encouraging, since the t^2 dependence may be seen as the most "physical" approximation for J_{AF}, as discussed in sect.1.3.2. These findings clearly show that the effects of pressure are not only limited to a reduction of the el-ph coupling but a remarkable pressure dependence of the AF interaction has to be introduced to account for the experimental behavior.

5.4 High-pressure synchrotron radiation infrared absorption on $La_{1-x}Ca_xMnO_{3-\delta}$

Taking full advantage of high brilliance of the IR beam of the SINBAD beamline (see sect.3.4) at DAΦNE (I.N.F.N. Laboratori Nazionali di Frascati, Rome), room temperature far-IR absorption measurements have been carried out on LC25S, LC20S, and LC20D as a function of pressure (0-10 GPa) by means of a DAC. As discussed in sect.3.4, very thin sample slabs (4-5 μm) have been obtained by pressing finely powdered manganite between diamonds and Apiezon grease has been used as pressure transmitting medium. Optical-microscope observation of the sample revealed the presence of fractures over a fraction η of total sample-slab area. The thickness d and fractures-percentage η (estimated from the microscope printed images) are reported in tab.5.1 for each sample. These sample-thicknesses are expected to lead to measurable optical density of the order of 1 in the insulating phase. Taking into account that the far-IR transmittance of a $Nd_{0.7}Sr_{0.3}MnO_3$ film of 0.14 μm thickness decreases from about 0.8 to 0.6 when entering the metallic phase [100], a

Sample	d	η
LC25S	5 μm	4%
LC20S	4 μm	2%
LC20D	4 μm	2%

TABLE 5.1: Thickness and fractures-percentage for the three samples measured with high-pressure far-infrared absorption.

crude estimate for our 4-5 μm thick samples gives an increase of the optical density by a factor ≈ 3 in the metallic phase.

In order to perform correct determination of the optical density of the sample, the intensity transmitted by the DAC filled with the sample ($I(\nu)$) and by the DAC filled with the hydrostatic medium only ($I_0'(\nu)$) must be measured. In the present case, it was found that the transmittance of the DAC filled with Apiezon only is almost flat, i.e. $I_0'(\nu)$ is simply proportional to the intensity $I_0(\nu)$ transmitted by a pinhole. Therefore the optical density was calculated by measuring at each pressure the intensities transmitted by the DAC+sample $I(\nu)$ and by the pinhole $I_0(\nu)$. This approach strongly simplifies the measurement procedure and allows to correct for possible small fluctuations of the synchrotron source. The shape of the $O_d(\nu)$ is unaffected by this simplification, whereas a constant shift is introduced. It is worth to notice that, although the absolute value of O_d is shifted by a constant, internal comparison among the $O_d(\nu)$ measured at different pressures for a given sample is still possible.

The presence of small fractures in the sample-slab, affects the shape of the measured optical density, particularly when the absorption is strong. Indeed, in presence of a fractures-percentage η, the transmitted intensity $I'(\nu)$ effectively measured can be expressed as $I'(\nu) = I_0(\nu)[(1-\eta)e^{-O_d(\nu)}+\eta]$. Therefore the measured optical density $O_d'(\nu)$ can be written as:

$$O_d'(\nu) = \ln \frac{I_0(\nu)}{I'(\nu)} = -\ln \left[(1-\eta)e^{-O_d(\nu)} + \eta\right] \tag{5.6}$$

It is well evident that for large absorption (i.e. large O_d) the measured optical density tends to $-\ln(\eta)$ which represents the maximum measurable $O_d'(\nu)$ and thus its saturation value. This effects, besides altering the shape of the $O_d(\nu)$, allows a rough compensation for the aforementioned uncontrolled level-shift induced by the use of the pinhole reference spectrum. Indeed the saturation level O_d^{sat} can be clearly identified as high-noise region in the measured spectrum of the two stoichiometric samples and all the spectra for a given sample have been shifted by the same constant in order to force $O_d^{sat} = -\ln(\eta)$. For LC20D, where no saturation is observed, the same constant shift of LC20S was applied since these two samples have approximatively the same thickness and η value (see tab.5.1). The application of this correction partially restores the reliability of the absolute value of the optical density and allows comparison of the $O_d(\nu)$ values obtained on different samples.

Spectra corrected with the procedure above described are plotted in the 130-680 cm^{-1} range for the three samples in fig.5.15. In all samples three

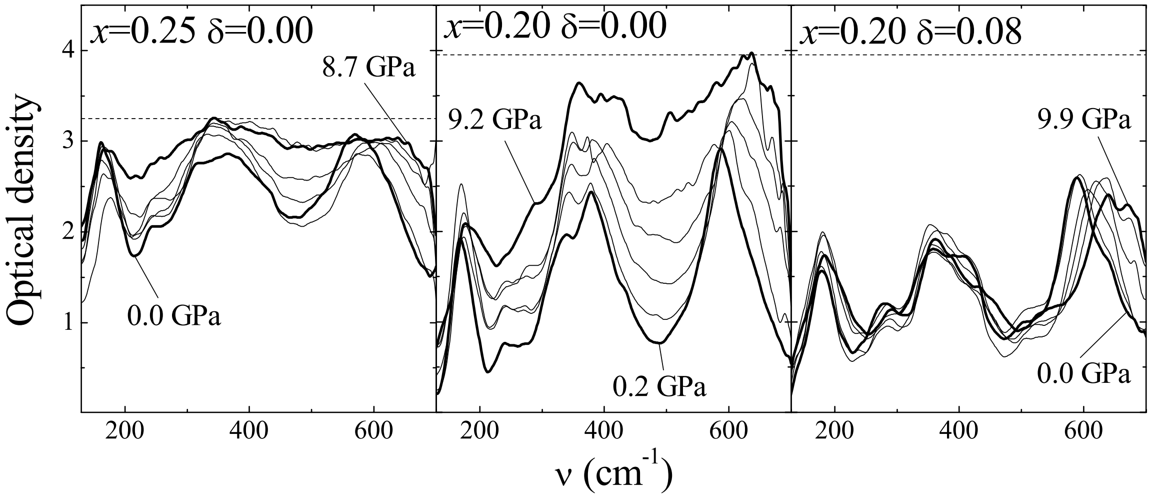

FIGURE 5.15: Optical density of $La_{1-x}Ca_xMnO_{3-\delta}$ for $x = 0.25$, $\delta = 0.00$ (left panel); $x = 0.20$, $\delta = 0.00$ (center panel); and $x = 0.20$, $\delta = 0.08$ (right panel) at different pressures. For each sample the maximum and minimum pressures are evidenced (thick lines) and the saturation values (dashed lines) are also shown.

main phonon bands are observed, namely the external (E), asymmetric bending (AB), and asymmetric stretching (AS) modes centered at ambient pressure at around 180, 350, and 600 cm^{-1} respectively. In LC25S (over the whole pressure range) and in LC20S (at high pressure) the phonon peaks are superimposed to an intense broad band ascribed to the tail of the polaronic band. At the lowest working pressures, the absorption is largest for LC25S. On increasing pressure, a progressive enhancement of the absorption is observed in LC25S and LC20S, while in LC20D the absorption is almost constant. The increase of absorption in LC25S and LC20S indicates that, as expected, the metallic character of the system is enhanced by pressure, whereas the raw data suggest the absence of a complete metallization for three reasons:

- There is no evidence for a Drude contribution even at the highest pressures.
- The phonon screening is not complete and in particular the external mode is well resolved also at the highest pressure.
- The overall absorption is too small since, as discussed above, the optical density should increase of a factor ≈ 3 in the metallic phase.

The absence of a room-temperature pressure-induced metallization is in

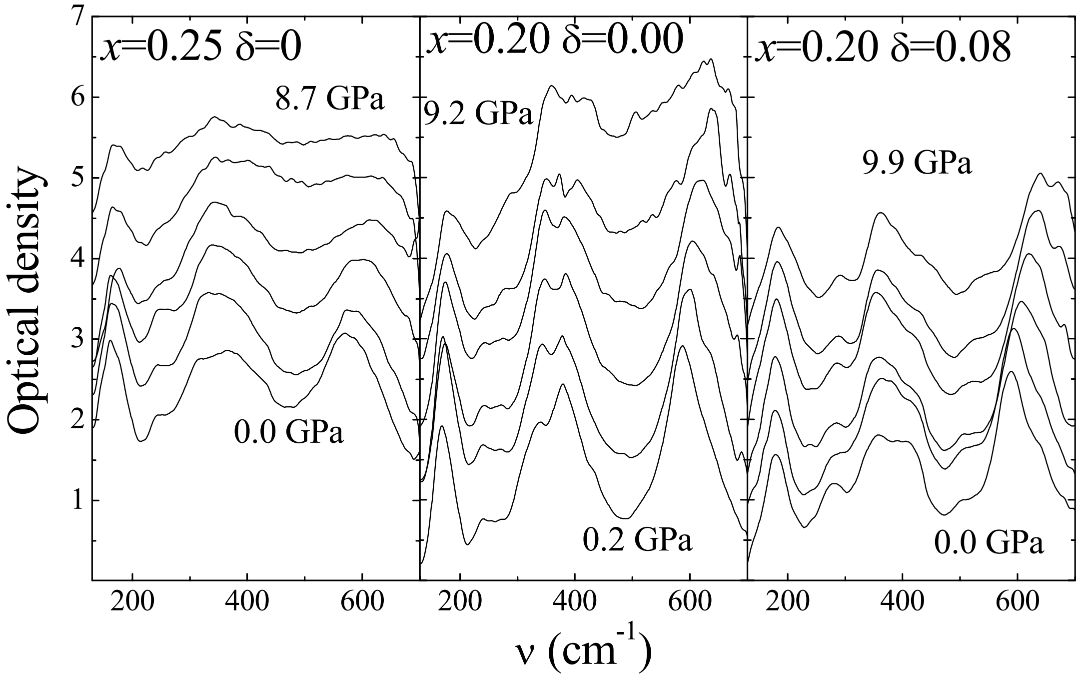

FIGURE 5.16: Optical density of $La_{1-x}Ca_xMnO_{3-\delta}$ for $x = 0.25$, $\delta = 0.00$ (left panel); $x = 0.20$, $\delta = 0.00$ (center panel); and $x = 0.20$, $\delta = 0.08$ (right panel) at different pressures. For each sample spectra have been progressively up-shifted for clarity.

agreement with the refs. [49] and [51] and with the $P - T$ phase diagram described in sect.5.2.1.

In order to evidence the pressure evolution of the spectrum, in fig.5.16 we plot the data properly upshifted. At low pressure a fine structure in the phonon spectrum can be observed, particularly for the less absorbent samples LC20S and LC20D. In all samples a remarkable hardening of the AS phonon is observed, smaller effects occurs in the AB phonon and the E mode is almost pressure independent.

A preliminary analysis of the spectra was performed applying first a correction, by means of eq.5.6, accounting for fractures of the sample slab. Then a simple model function and standard linear combination of damped harmonic oscillators has been used to fit the polaronic band and the phonon spectrum respectively. The empirical model function employed for the description of the polaronic band reads:

$$O_d^{pol}(\nu) = \frac{A\nu^2}{\nu^2 + \Gamma^2} \tag{5.7}$$

This function well reproduces the shape of the polaronic band in the far-IR region and contains only two free parameters A and Γ. As will be discussed

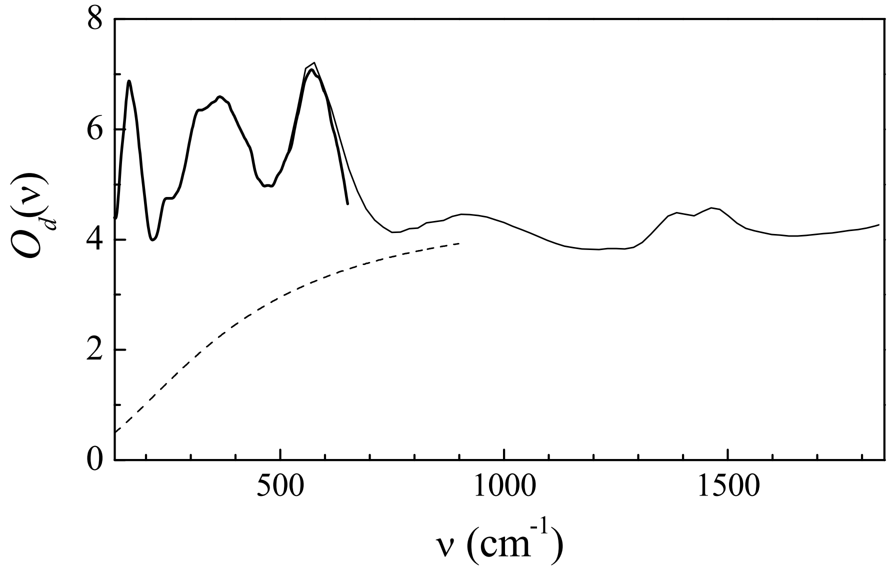

FIGURE 5.17: Room-temperature ambient-pressure $O_d(\nu)$ of $La_{0.75}Ca_{0.25}MnO_3$ in the far (thick solid line) and mid (light solid line) infrared region. The mid-infrared spectrum is properly shifted in order to match the far-infrared one. Dashed line is the best-fit $O_d^{pol}(\nu)$ obtained in the far-infrared region (see text).

in the following, the particular choice of the model function is not very important since we are mainly interested on the spectral weight of the polaronic band and not strictly to its shape. In any case, eq.5.7 well reproduces the shape of the polaronic band also in the mid-IR region. The far-IR and mid-IR spectra obtained on LC25S at ambient P and T are compared in fig.5.17. It is quite evident that the best-fit $O_d^{pol}(\nu)$ (also shown in the same figure) well agrees with the mid-IR data. This finding makes us confident on the reliability of the best-fit procedure. Theoretical hints are required for improving the spectral shape of the polaronic band.

On applying the fitting procedure, we found that a good fit for LC20D at 0 GPa requires 8 phonon contributions (1 for the E mode, 3 for the AB mode, 2 for the AS mode, and 2 accounting for the weak structures at 280 and 500 cm^{-1}), therefore the same number of phonons was employed for fitting all spectra.

5.4.1 Phonon bands

Owing to the saturation effects at high pressure and the limits in the spectral range, a complete determination of the pressure dependence of the frequency of all the observed phonons is not possible. A simplified analysis consists in determining the center frequencies ν_E, ν_{AB}, and ν_{AS} of the three main bands by calculating the weighted average of the peak frequencies of the phonons which compose these bands. For simplicity, in the following we will refer to the main bands as "phonons" *tout court*. The pressure dependence of the phonon frequencies for the three samples is shown in fig.5.18. It is well evident a strong pressure-induced hardening of ν_{AS}, whereas the pressure dependence of ν_{AB} and ν_E is weak. Moreover there is an indication of a saturation effect in $\nu_{AS}(P)$ for LC25S consistently with the high-pressure measurements in the mid-IR region. The saturation effect is absent in the

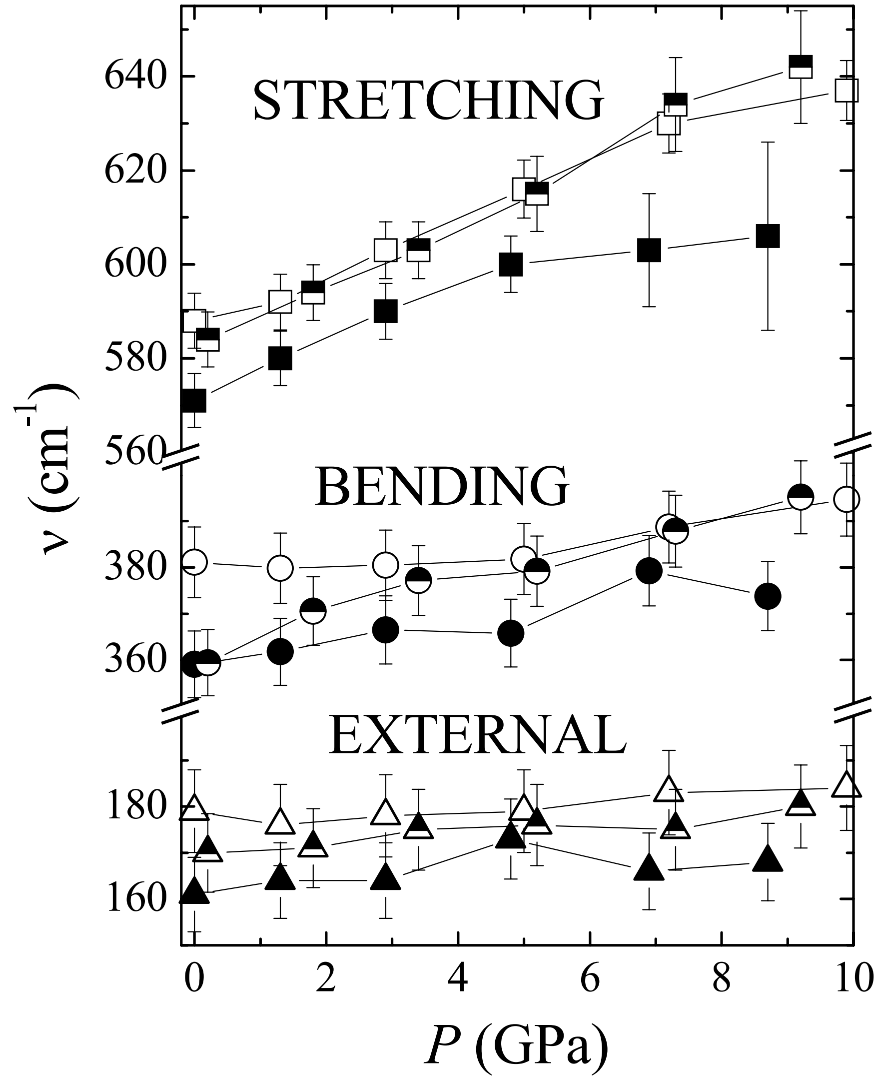

FIGURE 5.18: Pressure dependence of the phonon frequencies of the external (triangles), bending (circles), and stretching (squares) phonon bands for $La_{0.75}Ca_{0.25}MnO_3$ (full symbols), $La_{0.80}Ca_{0.20}MnO_3$ (half-filled symbols), and $La_{0.80}Ca_{0.20}MnO_{2.92}$ (open symbols). Lines are guides to eyes.

other two samples up to 10 GPa. These results are well consistent with the Raman data on the same samples shown in chap.4.

5.4.2 Polaronic band

As above mentioned, a progressive increase of the overall absorption is observed in LC25S and LC20S. Since no Drude contribution is observed, the absorption increase can be ascribed to the softening of the polaronic band with consequent enhancement of the absorption in the far-IR region. This effect can be interpreted in terms of a crossover from small to large polaron. In order to show more clearly and quantitatively this effect, two different procedures have been applied:

- All spectra were corrected for the presence of fractures by means of eq.5.6 and normalized to the same thickness of 4 μm thus obtaining a corrected optical density $O_d^{corr}(\nu)$. A total spectral weight was obtained by integrating the $O_d^{corr}(\nu)$ between 130 and 640 cm^{-1}.
- The polaronic spectral weight was obtained integrating the best-fit $O_d^{pol}(\nu)$ between 130 and 640 cm^{-1}.

The pressure dependence of the total and polaronic spectral weight are shown in the left and right panel of fig.5.19 respectively. The pressure dependence of the spectral weight is very similar for both the analysis procedures and the observed behavior for LC25S closely resembles that observed on the same

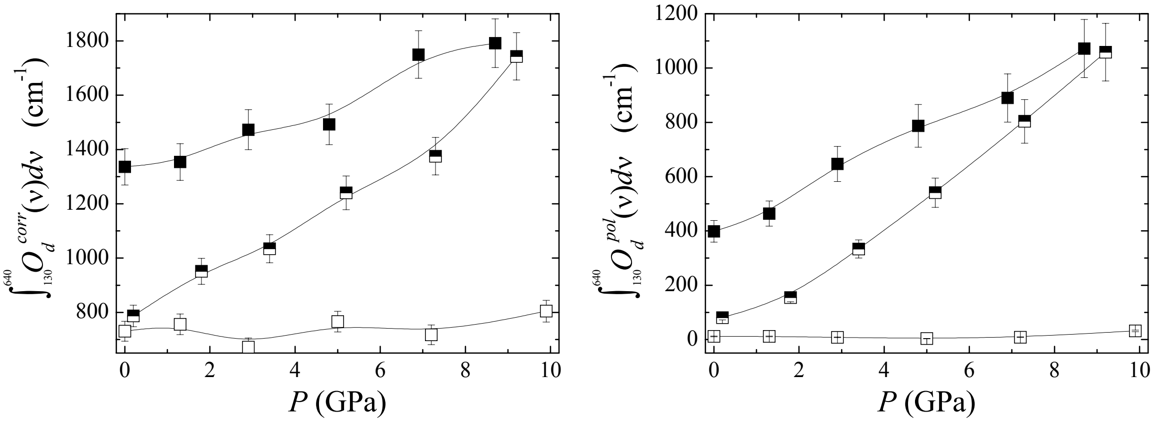

FIGURE 5.19: Pressure dependence of the integrals of the corrected optical density (left panel) and of the polaronic band contribution (right panel) for $La_{0.75}Ca_{0.25}MnO_3$ (full symbols), $La_{0.80}Ca_{0.20}MnO_3$ (half-filled symbols), and $La_{0.80}Ca_{0.20}MnO_{2.92}$ (open symbols). Solid lines are guides to eyes.

sample in the mid-IR region [51]. The integral of $O_d^{corr}(\nu)$ is obviously larger than that of $O_d^{pol}(\nu)$ since the former contains also the spectral weight of the phonon bands which is found to be almost pressure independent. It is well evident that on increasing pressure the spectral weight strongly increases in LC25S and LC20S, while it remains small and constant in LC20D. Moreover, the pressure induced enhancement of the spectral weight is more effective in LC20S where the absorption strongly increases with pressure and approaches the same value of LC25S around 9 GPa. Therefore, although a complete metallization seems not to be achieved, the metallic character of LC25S and LC20S is enhanced with increasing pressure and the effect is more pronounced in LC20S than in LC25S. On the other hand, pressure is ineffective in LC20D where the absorption remains constant.

Chapter 6

Measurements on Thin-Films

As discussed in sect.2.5, the substrate-induced strain in thin films induces anisotropic structural modifications. Therefore the study of manganites thin films allows interesting comparison with the isotropic strain induced by hydrostatic pressure. In this chapter, optical spectroscopy studies on $La_{0.7}Sr_{0.3}MnO_3$ (LSMO) thin film grown on $LaAlO_3$ (LAO) and on $SrTiO_3$ (STO) are reported. In the first section, far-IR reflectivity measurements on LSMO films as are reported. In the second section, Raman measurements on LSMO/LAO thin films are presented in the 40-1000 Å thickness range. To our knowledge, no thickness-dependent spectroscopic investigation on manganites thin films exists in the literature. The data presented in this chapter represent the first systematic investigation of the IR and Raman phonon spectrum of manganite thin-films as a function of film thickness.

6.1 Infrared reflectivity on $La_{0.7}Sr_{0.3}MnO_3$ thin films

Room temperature far-IR reflectivity measurements on LSMO films were performed exploiting the well established collaboration with the IR spectroscopy group of our department.

LSMO films of different thickness d were grown by Pulsed Laser Deposition on $SrTiO_3(001)$ (STO) and $LaAlO_3(001)$ (LAO) substrates. For these samples (first series, probably not fully optimized) the thickness dependence of T_C was already reported in sect.2.5 (see fig.2.15). It is convenient to divide the film/substrate samples in different categories. In thick-film samples ($1000 < d < 2000$ Å), the c-lattice parameter and the T_C value are close to the LSMO bulk values (c = 3.870 Å, T_C = 370 K) indicating that the film is completely relaxed when $d > d_c$ = 1000 Å. In thin-film samples ($d < d_c$), thickness effects become important: c varies and T_C decrease on decreasing d. Hereafter, each sample will be identified by d value (in Å) and substrate (S for STO). Ultra-thick-film samples ($d >$ 4000 Å) were also prepared and studied through IR measurements, although the film crystalline quality is slightly worse than in the thick-film case. Far-infrared reflectance measurements at near-normal incidence were performed at room temperature in the 100-800 cm^{-1} frequency range by using two interferometers equipped with different beam-splitters and detectors [113]. In the vacuum chamber of the interferometer, the sample holder can be rotated in order to measure alternatively the radiation intensity reflected at near-normal incidence by a gold surface ($I_0(\nu)$) or by the film surface ($I(\nu)$). Typically, the diameter of the light spot employed to obtain high-accuracy $R(\nu) = I(\nu)/I_0(\nu)$ reflectance spectra is of the order of 3 mm. Far-IR reflectance measurements showed that, even in ultra-thick-films, the reflection at the film-substrate interface is not avoided. For the LSMO/STO films the $R(\nu)$ spectra plotted in fig.6.1

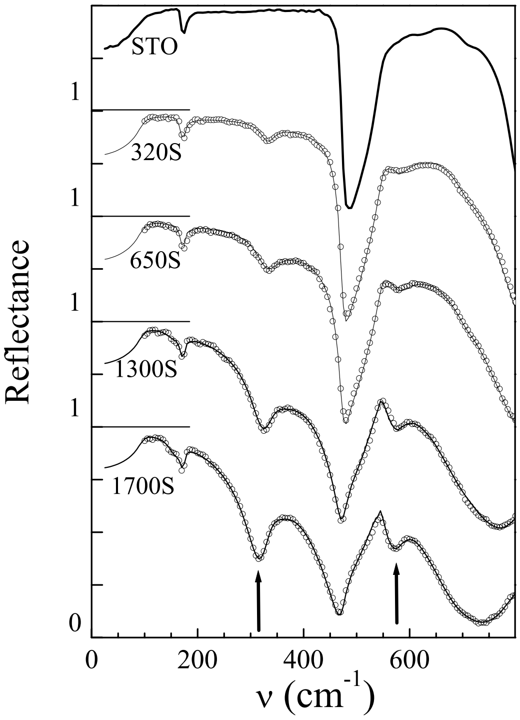

FIGURE 6.1: $R(\nu)$ of $La_{0.7}Sr_{0.3}MnO_3/SrTiO_3$ films with $d <$ 2000 Å (open symbols) and best-fit curves (solid lines). The $R(\nu)$ of $SrTiO_3$ is also plotted for easy comparison. Arrows mark the positions of $La_{0.7}Sr_{0.3}MnO_3$ ν_{AB} and ν_{AS} phonons.

show that the effect on the ν_{AB} and ν_{AS} phonons is evident on decreasing d down to about 300 Å. While for the thinner films, the $R(\nu)$ spectrum is dominated by the STO reflectance. In the case of LSMO/LAO films, the effect of LSMO phonons is hardly detectable because the LSMO phonon frequencies are close to those of LAO. Only LSMO/STO samples have then been studied in detail, in particular the thick-film (1750S and 1300S) and thin-film (650S and 320S) samples (see fig.6.1).

In order to analyze the measured spectra, a procedure which models the optical system vacuum-film-substrate-vacuum and provides exact expression for near-normal-near incidence reflectance of a film of thickness d on a substrate of thickness D [114] was employed. The procedure requires knowledge of the substrate dielectric function, i.e. of its refractive indices $n_s(\nu)$ and $k_s(\nu)$. By using $n_s(\nu)$ and $k_s(\nu)$ data available for STO [115], the model $R(\nu)$ only depends on d, D, and on the refractive indices of the film $n_f(\nu)$ and $k_f(\nu)$. In the present case, D plays no role since the substrate is not transparent in the FIR region and thus a simplified optical system (vacuum-film-semiinfinite substrate) can be considered. The standard Drude-Lorentz (DL) model for the film dielectric function $\tilde{\varepsilon}_f$ provides $n_f(\nu)$ and $k_f(\nu)$ $\left(\sqrt{\tilde{\varepsilon}_f} = n_f + ik_f\right)$ and the optical conductivity $\sigma(\omega) = \omega\varepsilon_2(\omega)/4\pi$ through [116]:

$$\tilde{\varepsilon}_f\,(\omega) = \varepsilon_1 + i\varepsilon_2 = \varepsilon_\infty - \frac{4\pi\Gamma\sigma_0}{\omega^2 + i\omega\,\Gamma} + \sum_{j=1}^{N} \frac{A_j^2\omega_j^2}{\omega_j^2 - \omega^2 - i\gamma_j\omega} \tag{6.1}$$

where $\omega = 2\pi c\nu$. The DL parameters in eq.6.1 are high-frequency dielectric constant ε_∞, damping Γ and zero-frequency conductivity $\sigma_0 = \sigma(\omega = 0)$ in the Drude contribution accounting for free charge-carriers. Peak-frequency ν_j, intensity A_j, and damping γ_j describe the j-phonon in the sum of N lorentzian oscillators.

Good fits of all the measured $R(\nu)$ were obtained, as shown in fig.6.1, by considering, besides the Drude contribution and the three lorentzian components accounting for the expected LSMO phonon lines, a fourth component around 350 cm^{-1}. A fifth component centered above 1500 cm^{-1}, accounting for mid-infrared contributions, was also introduced. For all samples, the best-fit d value is well consistent with the measured one. The LSMO optical conductivity $\sigma(\nu)$ as obtained for different samples is shown in the left panel of fig.6.2, showing no evident effects of the film thickness d, in particular on peak frequencies.

In the case of the thick-film sample 1700S, the different components of $\sigma(\nu)$, reported in fig.6.2, show that the phonon lines are superimposed to

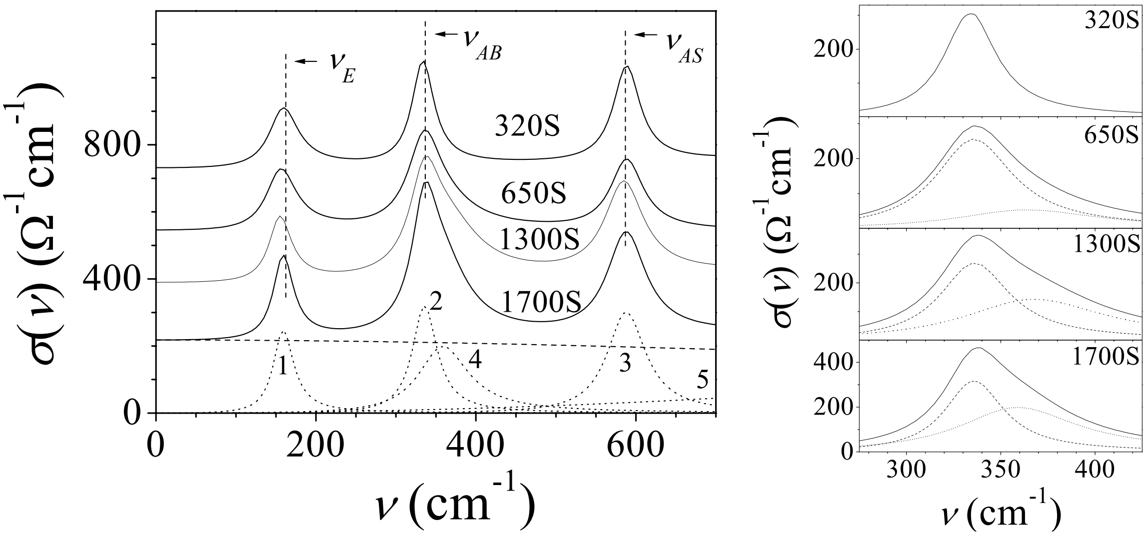

FIGURE 6.2: Left panel: optical conductivity of $La_{0.7}Sr_{0.3}MnO_3$ (solid lines) as obtained for different samples. Successive curves are offset by 200 Ω^{-1}cm^{-1} for clarity. In the case of sample 1700S, the $\sigma(\nu)$ components are plotted (Drude component: dashed line, lorentzian components 1-5: dotted lines). Right panel: line profile (solid lines) of the ν_{AB} phonon contribution. Components 2 (dashed lines) and 4 (dotted lines) are shown separately.

a nearly constant background described by the Drude contribution and by the low-frequency tail of component 5. Owing to the limited spectral range explored, it was not possible to obtain reliable values of the Drude damping Γ (which is higher than 1000 cm^{-1} for all samples) and of the parameters describing component 5. Fig.6.2 shows that the ν_E phonon is described by component 1, ν_{AS} by component 3, while the ν_{AB} phonon line is given by the sum of components 2 and 4. In the case of the thick-film samples ($d > 1000$ Å), parameter values determining the phonon spectrum do not significantly change. Peak-frequency and line-profile of the bending and stretching phonons are thus precisely determined through measurements on thick-film samples. Also in the case of thin-film samples (650S and 320S), the peak-frequency values of the 1-3 components remain nearly constant, although the errors on the best-fit parameter values (in particular the parameters describing component 4) increase since the difference between the $R(\nu)$ of sample and that of bare STO reduces. It can be concluded that, for LSMO/STO samples, the frequencies of components 1, 2, and 3 do not change on varying d. In the 650S spectrum, component 4, although less determined and of reduced intensity, is essential in obtaining a good fit. On the contrary, a good fit of the 320S spectrum can be obtained with a vanishingly small intensity of component 4. The left panel of fig.6.2 shows the ν_{AB} phonon line, given by the superposition of components 2 and 4, for the different samples. Although the phonon line-profile is precisely determined only for thick-film samples (1700S and 1300S), an effect of the film thickness is evident in component 4, which significantly decreases in sample 650S, and nearly vanishes in sample 320S. This finding, although not yet fully understood, should be related to the substrate-induced strain which determines the decrease of the c-lattice parameter observed on decreasing d below 1000 Å. Since in thin epitaxial films the in-plane lattice parameters a and b match the cubic STO lattice giving rise to a square in-plane lattice [117], it can be guessed that such strain effect might modify the lattice symmetry and, consequently, the phonon spectrum. Further studies on thin-film systems are in program in order to verify if IR measurements can monitor the substrate-induced lattice changes, but the obtained results clearly indicate that conventional IR spectroscopy cannot provide information when the film thickness is lower than 300 Å.

6.2 Raman spectroscopy on $La_{0.67}Sr_{0.33}MnO_3$ Thin Films

Since the most intense peaks of the Raman-active phonon spectrum are ascribed to vibrational modes of the MnO_6 octahedra which are crucial in determining transport properties of manganites, Raman spectroscopy is an ideal tool for investigating manganite-films (see sect.4.1). In this section we present a Raman-spectroscopy study of the d-dependence of the phonon spectrum of LSMO films thus demonstrating the capability of Raman spectroscopy in directly probing substrate-induced effects even in very thin films, down to 40 Å. Measurements were performed on a new set of films (second series), having a carefully controlled cation and oxygen stoichiometry, grown by pulsed laser deposition [64]. Raman spectra were measured exploiting the experimental setup described in sect.3.2. The confocal microscope was equipped with a 50× objective which allows to obtain a laser spot about 5 μm^2 wide at the sample surface. Spectra have been collected within the 200-1100 cm^{-1} frequency range with a spectral resolution of about 3 cm^{-1}. A very small confocal diaphragm (50 μm) was used to limit the scattering volume, thus reducing, as much as possible, the signal arising from the substrate.

Preliminary measurements have been carried out on LSMO films grown on different typical substrates such as $NdGaO_3$ (001), $SrTiO_3$ (110) and $LaAlO_3$ (001), to test the feasibility of an accurate Raman analysis. Among these materials the best choice is $LaAlO_3$ (LAO) since its low-intensity and simply structured Raman signal (within the relevant spectral range it mainly consists of a sharp peak at 485 cm^{-1} [118]) allowed us to extract the phonon spectrum of LSMO even for very thin films, when the measured signal is affected by a large contribution arising from the substrate. Several LSMO/LAO films in the 1000-40 Å $d-$range were measured. An acquisition time ranging from 40 min (thicker films) to 90 min (thinner films) was enough to obtain low-noise spectra. Sample characterization has shown a fully relaxed structure for thickness above $d_c \cong 160$ Å, and a disruption of the transport properties for thickness below $d_0 \cong 80$ Å, ascribed to the existence of a dead-layer at the film/substrate interface [64].

Raman spectra of LSMO/LAO films for four representative d values (800, 320, 160, and 80 Å), and the spectrum of one of the thinnest measured films (40 Å) are shown in fig.6.3 (a) and (b), respectively. For sake of comparison, the spectrum of a LAO substrate is also shown in fig.6.3(a). On decreasing d, although the Raman signal arising from the substrate progressively increases, the overall spectral shape due to LSMO film basically does not change and closely resembles those obtained for bulk samples of several CMR manganites [87–91, 93–95, 118]. As discussed in chap.4, the spectrum mainly consists of three broad components around 300, 500, and 620 cm^{-1} usually ascribed to rotational (ν_{rot}), bending (ν_{ben}), and JT stretching (ν_{JT}) modes of the MnO_6 octahedron, respectively (see chap.4). As already reported in literature [118, 119], a weak peak around 430 cm^{-1} (component ν_X) is also observable (see fig.6.3). In some of the measured spectra (e.g. the 160 and 40 Å films in fig.6.3) an unexpected extra component (ν_Y) around 730 cm^{-1} is clearly visible. Its origin is unclear and it was not possible to find out an unambiguous correlation between the growth conditions and its presence and/or its intensity. In any case, by directly comparing Raman spectra obtained by films nominally grown in the same conditions, with or without the ν_Y component, it is clearly observed that this component appears to be an additional contribution with no appreciable influence on the other spectral components.

In order to distinguish and analyze the contribution due to the manganite film and quantitatively determine the d-dependence of the ν_{ben} and ν_{JT} modes a fitting procedure was applied. It is assumed that the measured spectra $S(\nu)$ are given by the sum of two contributions arising from the LSMO film and LAO substrate, i.e. $S(\nu) = S_{LSMO}(\nu) + FS_{LAO}(\nu)$. The model is composed by the measured Raman spectrum of LAO $S_{LAO}(\nu)$ multiplied by the adjustable normalizing factor F and a standard model function, given

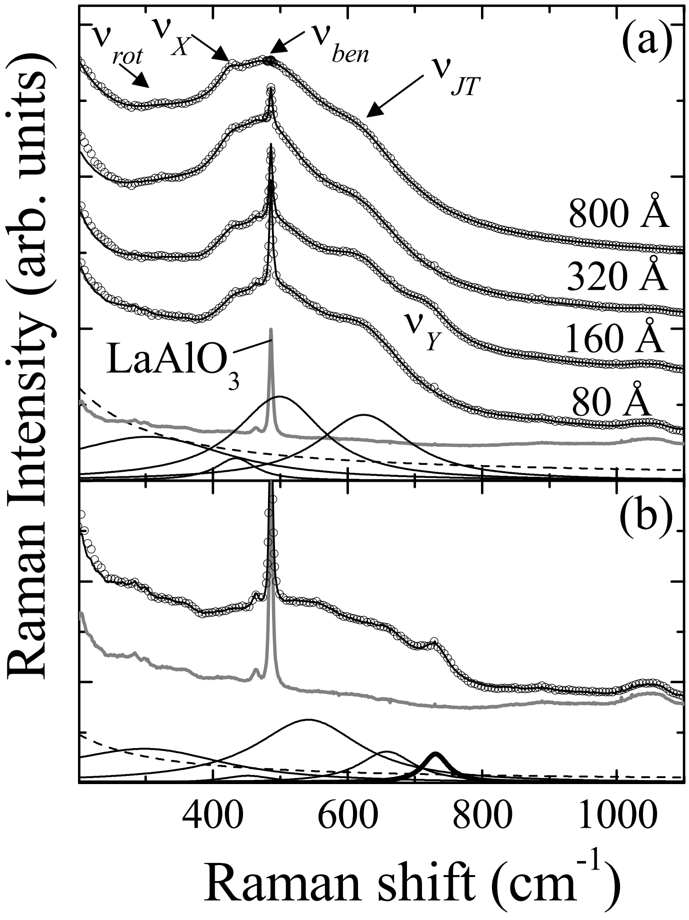

Figure 6.3: Raman spectra (open symbols) and best fit profiles (full lines) of the 800, 320, 160, 80 (panel (a)) and 40 Å (panel (b)) $La_{0.7}Sr_{0.3}MnO_3$ films. In (a), the four components (ν_{rot}, ν_X, ν_{ben}, and ν_{JT}) evident in the 800 Å spectrum, and the ν_Y component in the 160 Å spectrum are indicated. Best fit components of the 80 Å (a) and 40 Å (b) spectra are shown separately ($LaAlO_3$, grey line; electronic background, dashed line; phonon components, full lines). In (b), the ν_Y component is marked by a thick line.

by a linear combination of damped harmonic oscillators plus an electronic term [49, 92], for $S_{LSMO}(\nu)$. The above assumption, although reasonable, is furthermore justified *a posteriori* by the quite good agreement between experimental data and fitting function shown in fig.6.3. In the $S_{LSMO}(\nu)$ all the spectral features above discussed, i.e. the ν_{rot}, ν_X, ν_{ben}, ν_{JT}, and ν_Y (when observed) components, were account for, however, the most interesting results have been obtained for the thickness-dependence of the ν_{ben} and ν_{JT} frequencies, shown in fig.6.4(a). The error bars reported on ν_{ben} and ν_{JT} are representative of both the uncertainty of the best-fit parameter values and the slight differences between best-fit values obtained for different films with

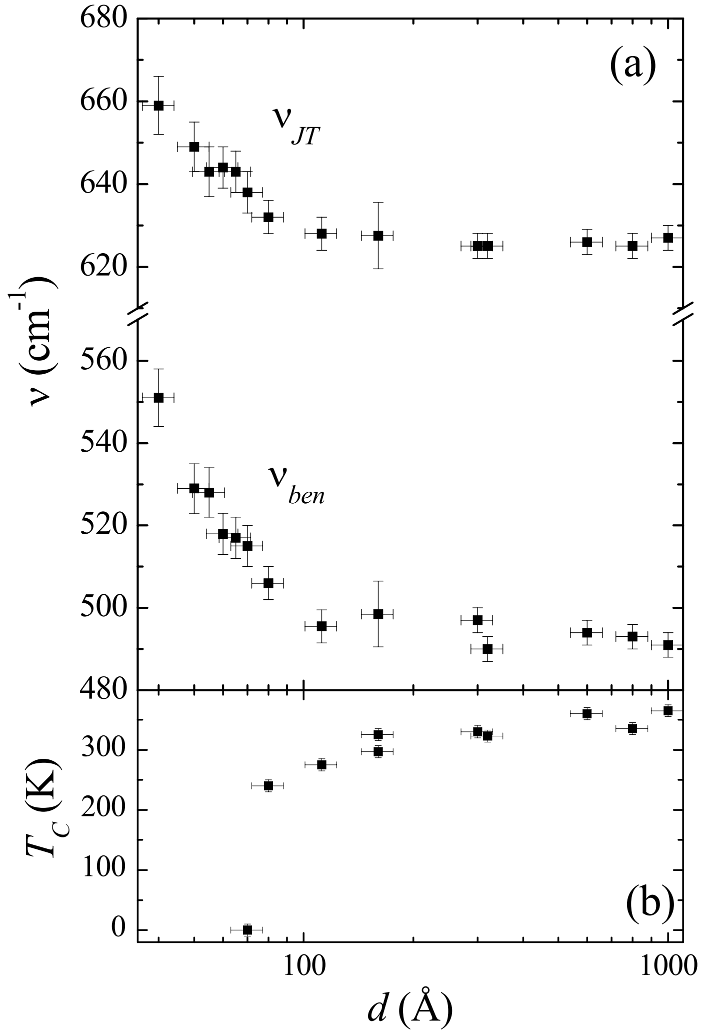

FIGURE 6.4: Peak frequency of the bending (ν_{ben}) and JT stretching (ν_{JT}) phonons (a) and transition temperature T_C (b) as a function of the film thickness d.

the same nominal thickness. We want to stress that films having the same thickness do not show any appreciable difference (within the experimental error) in the ν_{ben} and ν_{JT} values regardless of the ν_Y component. Fig.6.4(a) shows a large and rather abrupt increase of ν_{ben} and ν_{JT} on decreasing d in ultra-thin films ($d < 100$ Å). This behavior, to be ascribed to a remarkable substrate-induced structural effect, appears to be directly related to the measured d-dependence of T_C shown in fig.6.4(b).

The observed continuous evolution of the phonon spectrum on thinning films does not suggest any abrupt structural transition although the small-d behavior of ν_{ben} and ν_{JT} shows up the onset, around $d = 100$ Å, of some kind of a progressive structural rearrangement involving MnO_6 octahedra.

In particular, being the bending mode the mostly affected, a rotation of the octahedra towards new equilibrium positions matching more and more closely the substrate lattice structure is suggested. On the other hand, also the rather abrupt disappearance of the metallic phase, shown in fig.6.4(b), leads to similar conclusions. Indeed this behavior can be traced to an increasing distortion of the octahedra, which can be allocated in the pseudocubic lattice only by varying their structural arrangement and can strongly increase charge-localization. The above interpretation of the Raman results is supported by recent synchrotron X-ray experiments [117, 120]. Indeed, the analysis of an angular resolved absorption study on a LSMO/LAO thin film ($d = 450$ Å) does not show modification of the tilt angle [117] whereas diffraction data on thin and ultra-thin $La_{0.7}Ca_{0.3}MnO_3$ films grown on STO substrate ($24 < d < 800$ Å), clearly show a reorientation of the MnO_6 octahedra for the 24 Å thick film [120].

Within the proposed scenario, the dead-layer, which appears to be responsible [64] of the full disruption of the film transport properties (fig.6.4(b)), consists of a distorted manganite where a structural rearrangement of the MnO_6 octahedra has occurred and charges are strongly localized within distorted octahedra. It is finally worth to notice that at present it is quite difficult to determinate the cause/effect relationship between charge-localization and octahedral rotation since apparently they reinforce each other.

Chapter 7

Study of Non-Pseudocubic MnO_6 Octahedral Networks

In this chapter, measurements performed on $LiMn_2O_4$ (LMO) spinel and on cubic and hexagonal $SrMnO_3$ (SMO) are reported. The physical properties of these two systems have been already discussed in chap.2. Here we only recall that LMO spinel and hexagonal SMO both contain MnO_6 octahedra but the spatial arrangement is different from the pseudocubic structure of $Re_{1-x}Ae_x$MnO$_3$ manganites. In particular, in LMO edge-sharing octahedra are present while SMO contains face-sharing octahedra. The comparison with pseudocubic manganites could give some insight on the role played by the octahedral network.

In the first section, high-pressure high-temperature X-ray diffraction measurements on LMO are reported and discussed. From these data, the $P-T$ structural phase diagram was determined. Raman measurements on LMO are also reported and discussed in comparison with data reported in the literature. In the second section, Raman measurements on hexagonal and cubic SMO with a polarization analysis, devoted to the assignment of the phonon modes of the hexagonal compound, are reported. Finally, low-temperature Raman measurements on SMO are presented.

We would like to stress that although the present results have a relevance in the physics of manganites, they represent the starting point for new research lines focused on studying Li-spinels and electron-doped Sr manganites. The study of Li-spinels is motivated by their potential application for rechargeable batteries and their interesting physical properties. The extension of the study of hole doped manganites to the electron doped regions attracted a lot of attention in the last years but the physics underlying the properties of these compounds is still unknown in large part.

7.1 Experimental results on LiMn$_2$O$_4$ spinel

In the next two sections the experimental data obtained on LMO are reported. As discussed in sect.2.6.1, at ambient pressure LMO undergoes a structural transition from the high-temperature cubic phase to the low-temperature orthorhombic phase at $T_S = 292$ K. High-temperature high-pressure X-ray diffraction measurements were performed in order to determine the structural $P-T$ phase diagram. The reversibility of the transition was also checked increasing pressure up to 20 GPa. Raman measurements on LMO were also performed. Strong sample-heating induced by the laser was observed and the correct Raman spectrum of LMO is obtained only when the laser power is strongly reduced. These results overcome the large discrepancies observed in the Raman spectra of LMO reported in the literature and represent a good starting point for future high-pressure Raman measurements.

7.1.1 X-ray diffraction measurements

Exploiting the experimental setup available at the LURE synchrotron facility, described in sect.3.5, X-ray diffraction measurements have been performed on LMO along three isotherms (T_1=350 K, T_2=385 K and T_3=415 K) over different pressure ranges (between 0 and 20 GPa at T_1 and T_2 and between 0 and 10 GPa at T_3). At the end of each pressure run the force on the anvils was released and a new diffraction pattern was collected in order to check the reversibility of the pressure induced effects. Diffraction patterns collected along the three isotherms at different selected pressures are shown in fig.7.1 where the main Bragg peaks are labelled by capital letters. Owing to the very small sample amount in the small gasket hole, uncontrolled preferred-orientation effects are unavoidable. For this reason a Ritveld refinement of the diffraction data was not attempted. The effect of pressure on the diffraction patterns is quite similar along the three isotherms: beside the obvious overall increase of the peaks energy, due to the lattice contraction, a strong broadening of the peaks B, D and E is well evident, whereas the peaks A and C show the same shape over the whole pressure range, thus indicating that the peak broadening is not due to the onset of pressure gradients. Using the lattice parameter at zero-pressure [71] it is found that the peak assignment is A (111), B $(311, 131, 131)$, C (222), D $(400, 040, 004)$ and E $(331, 313, 133)$.

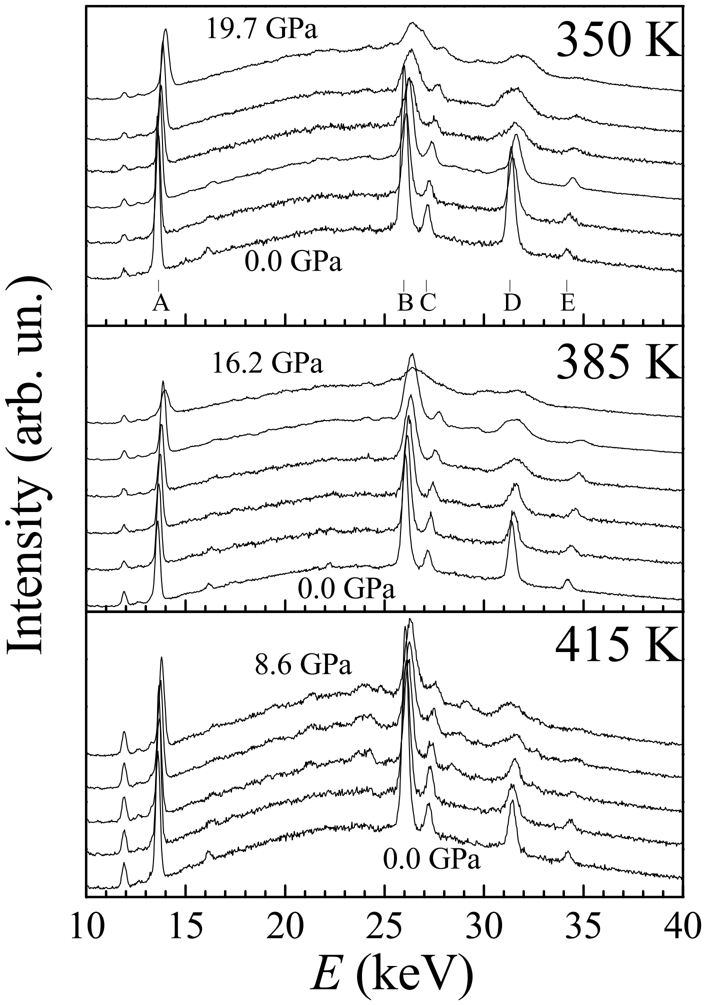

FIGURE 7.1: Energy-dispersion X-ray diffraction patterns of $LiMn_2O_4$ at selected pressures collected along three isotherms. Capital letters label the main Bragg peaks (see text).

On this basis the observed pressure-induced peak broadening can safely be ascribed to the onset of the cubic to orthorhombic structural transition which removes the cubic degeneracy and splits the B, D, and E peaks. Bearing in mind that $T_S(P = 0) = 292$ K is lower than all the working temperatures T_1, T_2, and, T_3 this finding clearly shows, without resorting to any data analysis, that an increase of T_S is achieved on applying a pressure.

Data were analyzed by means of a fitting procedure in order to determine the pressure dependence of the lattice parameters and, above all, to give an estimate of the structural transition pressure along the three measured isotherms. The energy range explored allows to follow the pressure evolution of all the Bragg peaks shown in fig.7.1. The whole diffraction pattern was fitted using a smooth background and 5 gaussian profiles for the cubic phase and 11 for the orthorhombic one. Although the cubic and orthorhombic symmetries are clearly evident from the analysis at low and high pressure respectively, the main problem was that of finely determine the transition pressure, $P_s(T)$ since the instrumental resolution does not allow to observe a clear splitting of the Bragg peaks. In the fitting procedure the experimental resolution was assumed to follow the empirical law:

$$\Delta E(E) = \Delta E_0 \sqrt{\frac{E}{E_0}} \tag{7.1}$$

with $\Delta E_0 = 180$ eV and $E_0 = 5.9$ keV. In this way, by exploiting the Bragg condition, all the gaussian profiles have been modelled using the lattice parameters (1 for the cubic structure and 3 for the orthorhombic one) and the intensity of the single peaks as free fitting parameters. The zero pressure values of the a_{cub} lattice parameter (at $P = 0$ the structure is cubic for all the measured isotherms) are in good agreement at all the working temperatures with those reported in the literature [67, 72]. Up to relatively low pressure when the discrimination between the two phases can be ambiguous, data were fitted using both the cubic and the orthorhombic structure. By taking the ratio of the chi squared values obtained using the cubic and the orthorhombic structure $R_\chi = \chi_{cub}/\chi_{ort}$, $R_\chi \simeq 1.0$ and $a_{ort} \simeq b_{ort} \simeq c_{ort} \simeq a_{cub}$ were systematically obtained at the lowest pressures and a remarkable increase of R_χ on further pressurizing the samples was observed. As a qualitative indication, values of $R_\chi \geq 1.3$ are achieved at pressure larger than about 1.5 GPa, 2.5 GPa and 3.0 GPa at T_1, T_2, and T_3 respectively. Since a 30% of difference in the chi squared values is certainly significant, the above result confirms the presence of a structural transition and gives an upper limit for the transition pressure along the three isotherms. Since the quality of the data does not allow a more accurate and strict statistical analysis, in order to give at least a rough estimate of the transition pressure, an alternative procedure was followed.

We define a dimensionless parameter accounting for the orthorhombic distortion as follows:

$$\delta_{ort} = \frac{1}{m} \sqrt{\frac{(a-m)^2 + (b-m)^2 + (c-m)^2}{3}} \tag{7.2}$$

where $m = (a+b+c)/3$ is a sort of averaged cubic lattice parameter. From the diffraction data collected at ambient pressure as a function of temperature [67, 72] it is observed that δ_{ort} is actually constant over a wide temperature range below T_S. In the temperature range from 80 K to 290 K an averaged value of $\delta^*_{ort} \approx 5.0\ 10^{-3}$ can be calculated. In the present experiment $\delta_{ort}(P)$ was calculated along the three isotherms using the best fit values for the a_{ort}, b_{ort}, and c_{ort} orthorhombic lattice parameters. A typical trend along the isotherms is observed: on increasing pressure at first $\delta_{ort}(P)$ is vanishingly small (cubic phase), then it starts to increase (onset of the orthorhombic phase) and continues to monotonically increase up to about $P_L \approx 10$ GPa approaching a sort of limiting value $\delta^*_{ort}(P_L) \approx 1\ 10^{-2}$ which is basically not exceeded on further pressure increases.

Using δ^*_{ort} as a threshold value, we assume that the system completely entered the orthorhombic phase when $\delta_{ort}(P) \geq \delta^*_{ort}$. The transition pressures values $P_s(T)$ obtained using this procedure along the three isotherms are $P_s(T_1) = 1.8 \pm 0.4$ GPa, $P_s(T_2) = 2.9 \pm 0.7$ GPa, and $P_s(T_3) = 3.2 \pm 0.5$ GPa in agreement with the above reported limiting values obtained using the chi square comparison. It is worth to note that the above pressure values are only a crude estimate of the real transition pressures and that their absolute values can be affected by the criterion adopted; but at the same time it should be emphasized that the occurrence of a pressure-induced structural transition, as well as the increase of $P_s(T)$ on heating the sample, is absolutely evident from the raw data. Consistently with this empirical criterion, we thus assume the cubic structure with the relative best fit values a_{cub} when $\delta_{ort}(P) < \delta^*_{ort}$ and the orthorhombic one with the relative best fit values a_{ort}, b_{ort}, and c_{ort} when $\delta_{ort}(P) \geq \delta^*_{ort}$. The pressure dependence of the cubic and orthorhombic lattice parameters along the three isotherms is shown in fig.7.2 where the arrows mark the $P_s(T)$ values.

A remarkable result is also obtained if looking at the check of the reversibility of the pressure effects. The diffraction patterns collected at ambient pressure before and after each pressure-run at T_1, T_2, and T_3 are shown in fig.7.3(a). At all temperatures an almost perfect reproducibility of the A and C peaks was obtained, whereas it is quite apparent that at T_1 and T_2 the pressure induced broadening of the B, C and D peaks, signature of a non-cubic phase, is still present also after releasing the pressure. In the case of the highest isotherm at T_3 the original cubic structure is perfectly recovered, and also peaks B, C, and D are satisfactorily or thoroughly reproducible. Despite the different behavior, the volume values calculated before and after the pressure run at each working temperature, are coincident within the experimental uncertainties. It is worth to notice that the maximum pressure at the highest working temperature T_3 was limited to be less than P_L, which is the value at which the saturation of $\delta_{ort}(P)$ is observed. Taking into account the above phenomenology, the present data suggest the presence of an

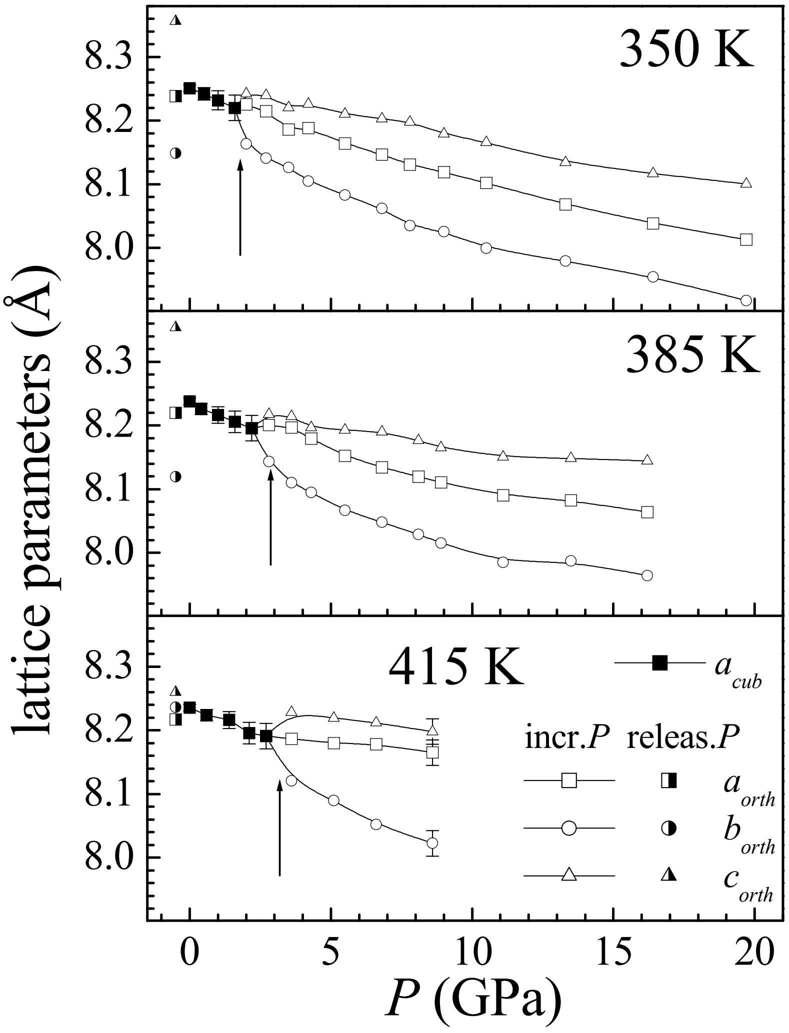

FIGURE 7.2: Pressure dependence of the lattice parameters of LiMn$_2$O$_4$ at fixed temperatures. Open symbols refer to the orthorhombic phase (squares = a_{orth}, circles = b_{orth}, triangles = c_{orth}). Full squares are the lattice parameter in the cubic phase a_{cub}. Half-filled symbols are the zero-pressure values (here shifted at $P < 0$ for sake of clarity) of a (squares), b (circles), and c (triangles) after releasing pressure. Solid lines are guides to eyes. Arrows indicatively mark the transition pressures.

unpredicted metastable distorted phase induced in the high-pressure regime (i.e. $P \geq P_L \approx 10$ GPa). More experimental studies are needed in order to determine on which time scale this phase is stable. The whole of the results obtained can be summarized in the tentative $P - T$ phase diagram reported in fig.7.3(b) where the thermodynamic regions of cubic, orthorhombic and metastable distorted phases are shown.

A last remark concerns the fact that many spinels, like Zn$_2$TiO$_4$, MgFe$_2$O$_4$, CoFe$_2$O$_4$, ZnMn$_2$O$_4$, NiMn$_2$O$_4$, CuMn$_2$O$_4$ and ZnFe$_2$O$_4$ exhibit

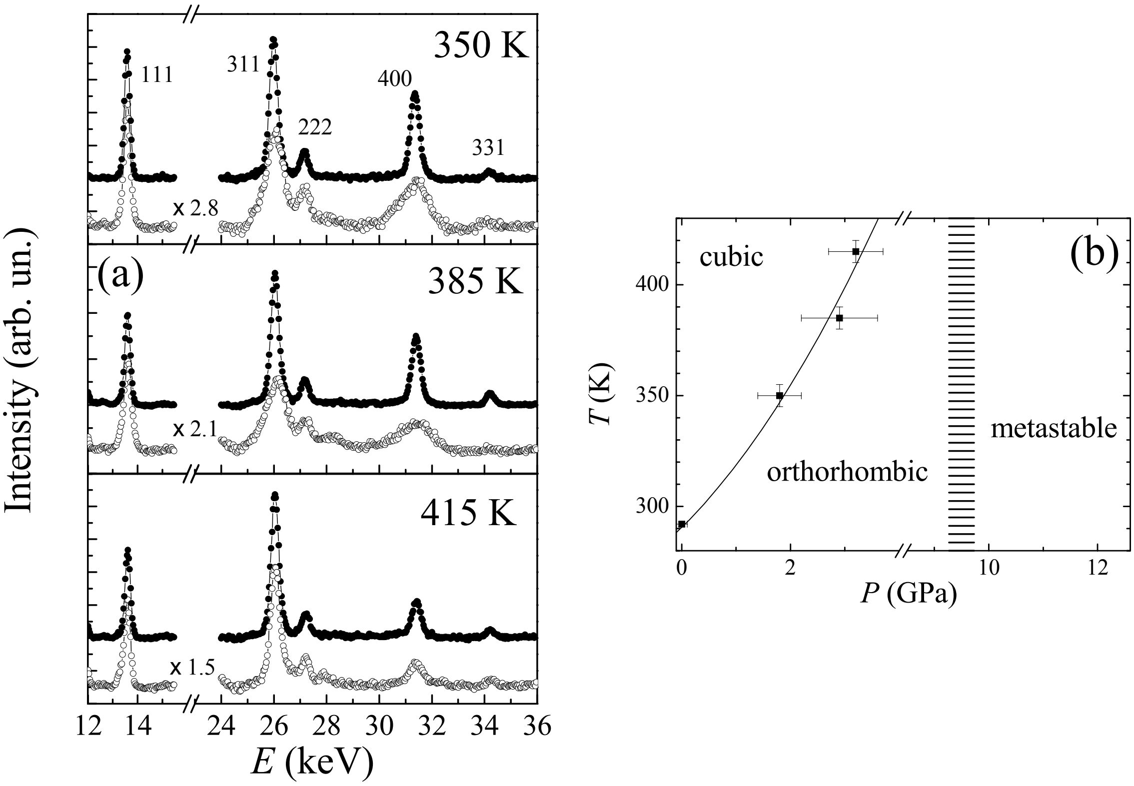

FIGURE 7.3: (a) Zero-pressure X-ray diffraction patterns of $LiMn_2O_4$ at fixed temperatures measured before (full symbols) and after (open symbols) applying pressure. Miller indexes of main Bragg peaks are also indicated. Spectra acquired after releasing pressure are properly magnified for sake of comparison. (b) Tentative structural $P-T$ phase diagram of $LiMn_2O_4$. Solid line is a guide to eyes. Shaded bar indicatively marks the boundary between the reversible orthorhombic and metastable distorted phases (see text).

phase transitions when subject to an external pressure [121]. However, contrarily to the case of LMO, which has been studied in this Ph.D. thesis, the pressure values needed to obtain a phase transformation is usually much higher, i.e. $P_s > 10$ GPa. It is interesting to note that it has been reported that, at least in the first five compounds, the high pressure phase is metastable after the release of the external pressure, similarly to the behavior of LMO here reported.

The phase diagram of LMO will be discussed in chap.8 and compared with that obtained on $La_{0.75}Ca_{0.25}MnO_3$.

7.1.2 Raman measurements

A natural extension of the measurements described in the previous section would be high-pressure Raman measurements. Preliminary test measurements devoted to plan a high-pressure Raman experiment on LMO were thus performed. The obtained results were somehow misleading and deceptive. The spectral shape was found to be hardly reproducible. A careful inspection of the Raman data on LMO reported in the literature showed large discrepancies between the spectra obtained by different authors [122]. These discrepancies can be probably ascribed to laser-induced heating of the sample. In fact using laser sources with a high-focusing optics it is very easy to convey a high photon flux on a small portion of the sample causing a remarkable local heating for strongly absorbing specimen.

In a recent paper, the effects of the chromium substitution in LMO (studying $LiMn_{2-x}Cr_xO_4$ compounds with $0 \leq x \leq 0.5$) have been investigated by means of microRaman spectroscopy and X-ray absorption spectroscopy [123]. The Raman results are shown in fig.7.4. The authors, exploiting the X-ray

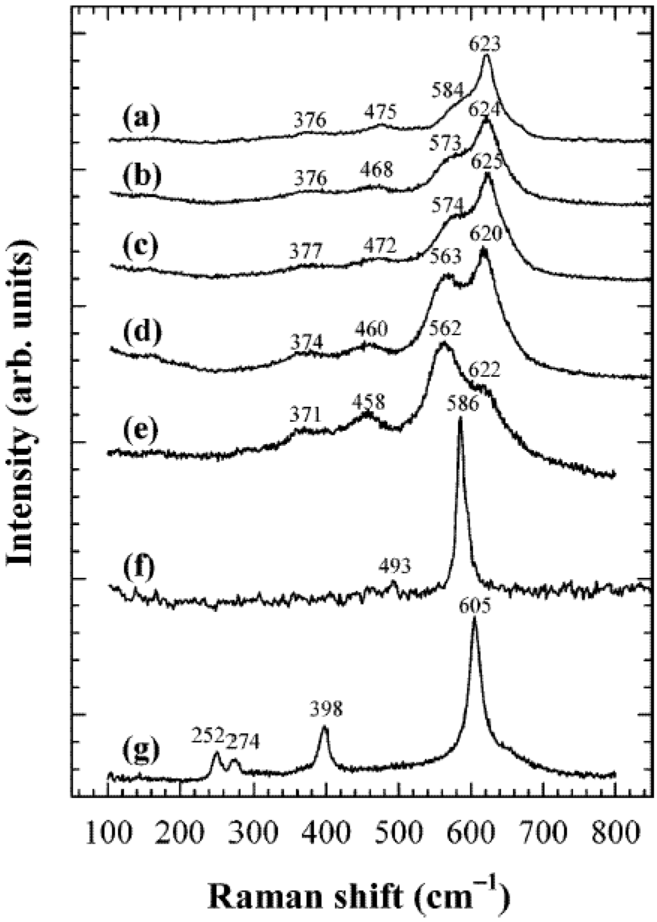

FIGURE 7.4: Micro-Raman spectra for the chromium-substituted $LiMn_{2-x}Cr_xO_4$ spinel compounds with $x = 0$ (a), 0.1 (b), 0.2 (c), 0.3 (d), and 0.5 (e) and for the references cubic spinel λ-MnO_2 (f) and tetragonal spinel $Li_2Mn_2O_4$ (g) [123].

results claim a new interpretation of the Raman spectrum and claim that a simple analysis of the intensity of the two main spectral features they observe in the Raman spectra allows to obtain direct information on the extent of the tetragonal distortion. In particular they ascribe the observed peaks at 580 and 620 cm^{-1} to A_{1g} modes for regular $Mn^{4+}O_6$ octahedra and tetragonally distorted $Mn^{3+}O_6$ octahedra, respectively. This interpretation would be a very important in a high-pressure Raman experiment devoted to the comparison with the high-pressure X-ray diffraction results and can have a particular relevance also in the case of manganites.

In order to verify the reliability of the Raman spectrum of LMO, Raman data were collected as a function of laser power exploiting the experimental apparatus available in the high-pressure Raman laboratory in our department (see sect.3.2) and in particular the available filters. These filters have attenuation factors of 10^0, $10^{-0.3}$, $10^{-0.6}$, 10^{-1}, and 10^{-2} and they will be labelled in the following as D00, D03, D06, D1, and D2 respectively. In fig.7.5 we report the behavior of the Raman spectrum of LMO as a function of the laser intensity. Starting with a low intensity of the laser beam (filter D2), a spectrum with a broad phonon line at 580 cm^{-1} has been obtained. Very broad features are possibly present between 300 and 400 cm^{-1}. Increasing

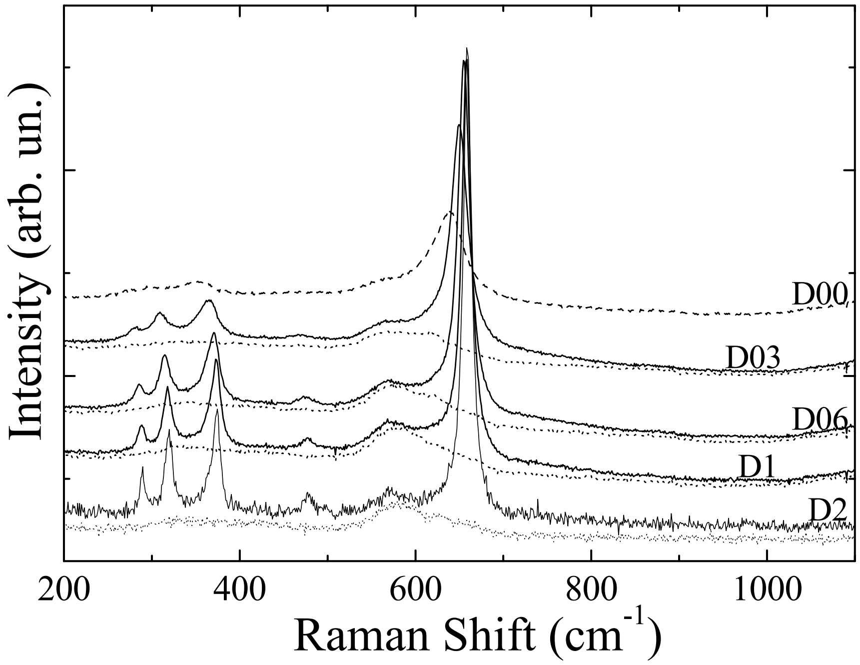

FIGURE 7.5: The Raman spectrum of $LiMn_2O_4$ with different filters for the laser beam. The dashed (solid) lines refer to data collected increasing (decreasing) the laser intensity.

the laser intensity (filters from D1 to D00) the line at 580 cm^{-1} shifts to lower frequency while a feature above 600 cm^{-1} appears as a shoulder for filters D06 and D03 and becomes the most intense peak of the Raman spectrum at the maximum laser power. For filter D00 the original peak at 580 cm^{-1} is a poorly defined shoulder of the peak at 638 cm^{-1}, while at least two broad peaks are visible between 250 and 400 cm^{-1}. On decreasing the laser beam power (continuous lines in fig.7.5) three phonon lines become clearly defined between 250 and 400 cm^{-1}, a peak appears around 475 cm^{-1}, while the line above 600 cm^{-1} is still the most intense peak of the spectrum and the original phonon line between 550 and 600 cm^{-1} becomes more clearly defined. All these phonons shift to higher frequency decreasing the laser power, that is decreasing the local temperature of the small part of the sample impinged by the laser spot. These results suggest the occurrence of a large thermal effect caused by the local heating of the sample induced by the intense laser beam, which determines the local decomposition of the samples into other compounds. To evaluate the temperatures at which LMO is heated, both the Stokes and antiStokes Raman spectra were collected with each filter. The intensity of the same phonon line measured by means of the Stokes or the antiStokes spectrum are linked by the relationship:

$$\frac{I_{antiStokes}}{I_{Stokes}} = \exp\left(-\frac{h\nu}{k_B T}\right) \tag{7.3}$$

so that measuring the energy $h\nu$ of the phonon one can easily calculate the local temperature T of the sample. Since the Raman spectrum of LMO does not present very intense peaks which allow an easy and reliable analysis of the data, the sample was firstly heated up with the maximum laser intensity, obtaining the well defined phonon line above 600 cm^{-1}, and then the Stokes and antiStokes spectra of this sample were collected decreasing the laser intensity (see fig.7.6). In the inset of fig.7.6 the calculated T as a function of the relative laser intensity with the different filters is shown. It can be noticed that T can assume values in a wide range between 330 and 1500 K. Moreover the dependence of T on the laser intensity is linear, and one can check in the inset of fig.7.6 that with zero laser intensity $T \simeq 300$ K, as expected.

The major changes of the Raman spectrum of LMO when measured with the maximum laser intensity suggest that the sample transforms into other compounds in the temperature range between 700 and 1500 K. In the literature various studies of the thermal stability of LMO are available [124, 125]. In particular it was found that at high temperature LMO partially decom-

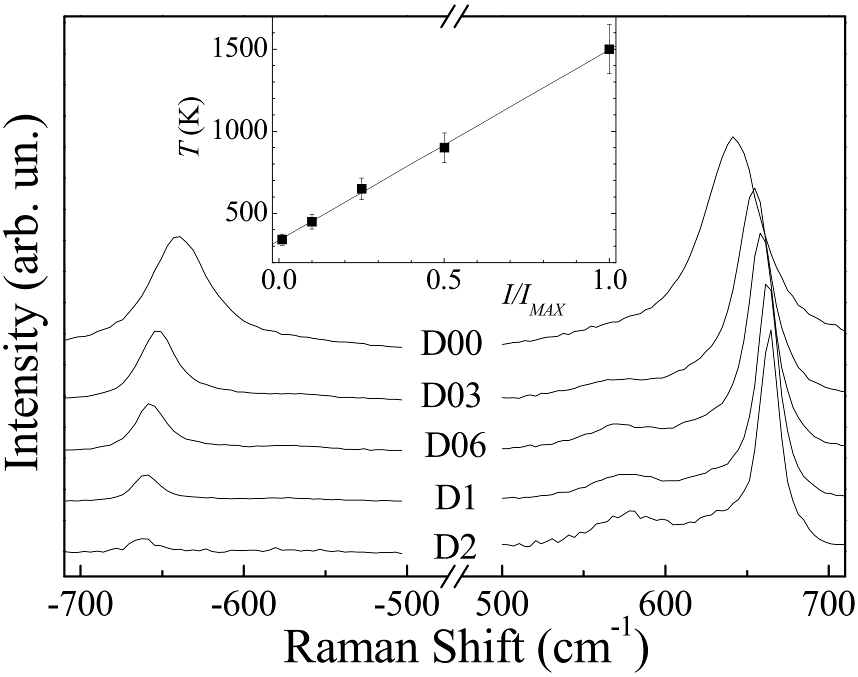

FIGURE 7.6: The Stokes (S) and antiStokes (AS) spectrum of LiMn$_2$O$_4$ with various filters for the laser beam. In the inset the local temperature of the sample calculated from the ratio of the S and AS part of the spectrum vs. the relative intensity of the laser beam is plotted.

poses in Mn$_3$O$_4$ [125]. It is worth to note that the spectrum of LMO measured with D2 filter after heating the sample with D00 is very similar to the Raman spectrum of Mn$_3$O$_4$. It can be thus concluded that, unless a very low laser power is used, LMO tends to decompose when measured with a microRaman apparatus and the Raman spectrum is masked by spurious contributions originating from the decomposition products. The correct Raman spectrum of LMO consists of a broad peak at 580 cm^{-1}, with two poorly defined features between 300 and 400 cm^{-1}, as can be obtained measuring the spectrum with a small laser intensity which heats up the specimen only by ~30 K. It is worth to notice that the phonon structures we ascribe to LMO are in a quite good agreement with the results of a computer simulation reported in ref. [126] where Raman-active peaks are expected within the 350-460 cm^{-1} range and at 597 cm^{-1} whereas at 633 cm^{-1} only an infrared-active phonon peak is predicted.

A remarkable feature of the Raman spectra of LiMn$_{2-x}$Cr$_x$O$_4$ reported in ref. [123] is the variation of the relative intensity, $R(580/620)$ of the phonons at 580 and 620 cm^{-1} as a function of Cr doping, which according to these authors is an additional proof of the link of these lines to the regular and distorted MnO_6 octahedra. The dependence of $R(580/620)$ can be explained in different ways, like a better thermal stability of the doped compound with respect to the undoped sample, or a change of the electronic absorption band centered at the laser frequency as a function of doping, or finally considering that at high temperatures the Raman spectrum of LMO becomes very similar to that of Mn_3O_4, due to the thermal instability of the former compound. It can be supposed that increasing the doping, less Mn is available to form Mn_3O_4, so that the intensity of spectral feature at 625 cm^{-1} due to the presence of the former oxide is reduced.

As to the possibility of performing high-pressure Raman measurements on LMO, it is worth to note that the presence of the diamond window of the DAC can overcome the sample-heating effect owing to the very high thermal conductivity of diamond. Preliminary test measurements on LMO loaded in the DAC showed that in this case the correct LMO Raman spectrum is obtained also at high laser power. Therefore high-pressure Raman measurements on LMO already in planning.

7.2 Raman spectroscopy on cubic and hexagonal $SrMnO_3$

As discussed in sect.2.6.2, SMO can by synthesized in both cubic and hexagonal structure [75]. Therefore, studying the two phases of this compound, allows a direct comparison between a pseudocubic and a non-pseudocubic arrangement of the MnO_6 octahedra. Moreover, the study of SMO represents the starting point of a new research line focused on the investigation of electron-doped manganites. In particular, exploiting the existing collaboration with the group of Prof. B. Raveau (ISMRA-CRISMAT laboratories, Caen France), the Raman spectrum of Ce-doped manganites ($Sr_{1-x}Ce_xMnO_3$, $0 \leq x \leq 0.20$) will be studied in the future. In the following sections, we will report Raman measurements performed at room and low temperature on both cubic and hexagonal SMO.

7.2.1 Room temperature measurements

Since no Raman study of cubic and hexagonal SMO exists in the literature, a first Raman characterization was performed on both samples at room temperature exploiting the Raman apparatus of the high-pressure Raman laboratory of our department and described in sect.3.2. In order to check for homogeneity of the poly-crystalline samples, several spectra have been collected at different points of each sample. Cubic SMO is almost homogeneous whereas in hexagonal SMO strong fluctuations of the intensity of the Raman bands were observed from point to point of the sample. These fluctuations are ascribed to polarization effect. Indeed owing to the poly-crystalline nature of the sample, the intrinsic polarization of the incident laser has random orientation with respect to the crystalline axes from point to point of the sample. The room-temperature Raman spectra of cubic and hexagonal SMO are plotted in fig.7.7. For hexagonal SMO a representative spectrum was selected. It is well evident that a large number of phonon peaks appear in the hexagonal compound whereas the cubic compound is almost structureless and presents only very broad and weak bands. This finding is well consistent with group theory [127] which predicts no Raman-active

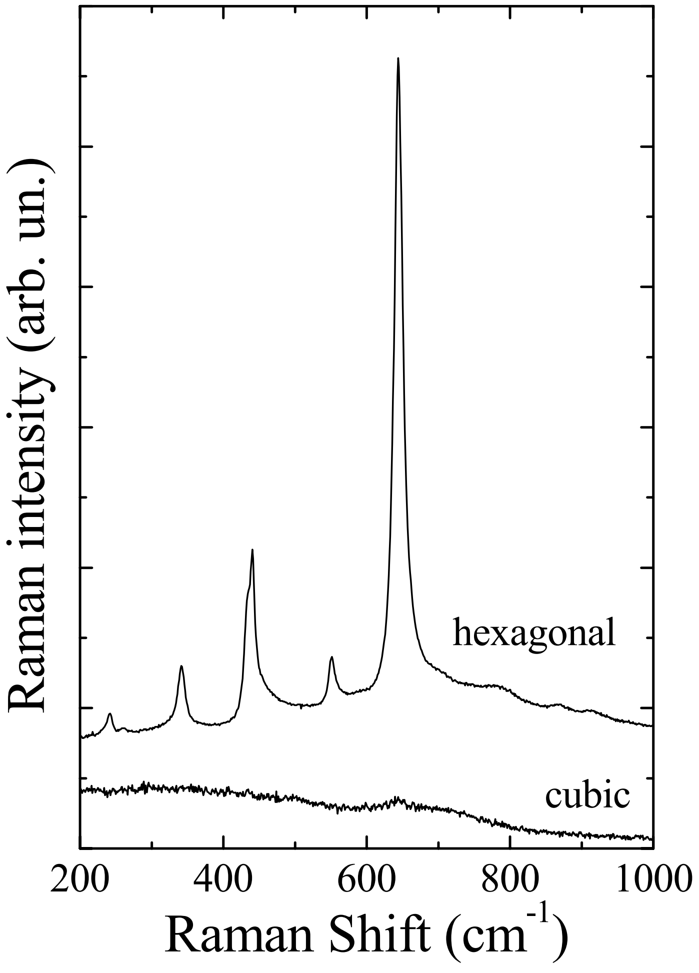

FIGURE 7.7: Room temperature Raman spectra of cubic and hexagonal $SrMnO_3$.

phonons in the cubic perovskite structure ($Pmmm$ space group). On the other hand, 8 Raman active phonons are predicted for the hexagonal symmetry ($P6_3/mmc$ space group). Starting from the point-group symmetry of hexagonal SMO, the total irreducible representation of the Raman active phonons can be determined as [127]:

$$\Gamma_{Ram} = 2A_{1g} + 2E_{1g} + 4E_{2g} \tag{7.4}$$

Spectra of both compounds were fitted by means of a sum of dumped harmonic oscillators and a background term (a linear function for the hexagonal compound and an electronic diffusive term for the cubic compound). The spectrum of cubic SMO can be fitted by means of 3 oscillators, while a good fit of the spectrum of hexagonal SMO can be obtained only employing 9 oscillators. Representative best-fits of the hexagonal and cubic compounds are shown in fig.7.8 (a) and (b) respectively. The corresponding best-fit phonon frequencies ν_0 and widths Γ are reported in tab.7.1 for the two compounds. In hexagonal SMO, six narrow ($\Gamma < 30$ cm^{-1}) and three broad ($\Gamma > 40$ cm^{-1}) structures are observed. The formers are ascribed to 1-phonon processes (labelled P1-P6 in increasing-frequency order), whereas the latter are ascribed to multi-phonon processes. Therefore there can be observed 6 of the 8 allowed phonon modes. It is worth to note the presence of a double 1-phonon peak at around 440 cm^{-1} (see the inset in fig.7.8(a)). In cubic SMO no Raman-active 1-phonon processes are expected. Therefore the presence of the three broad structures is to be ascribed either to multi-phonon process or disorder-induced violation of the selection-rules. In

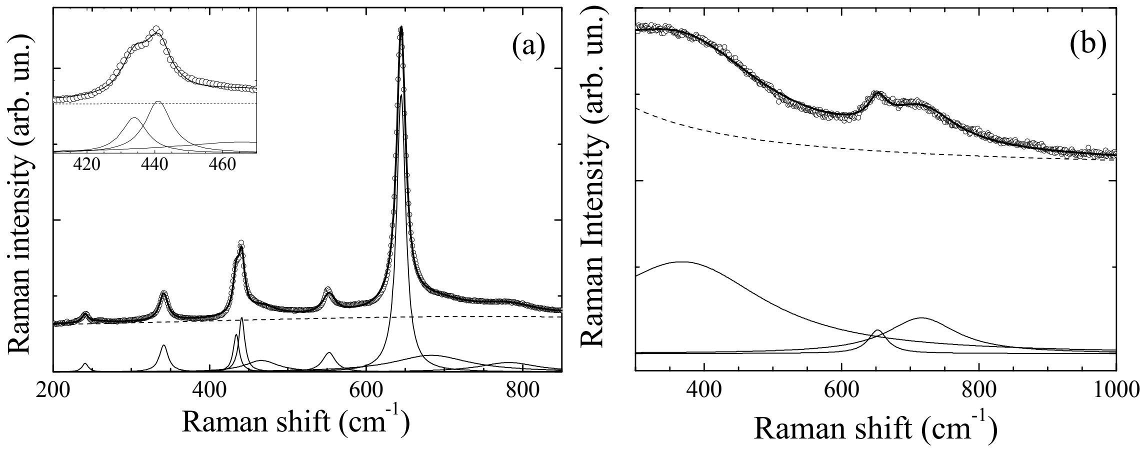

FIGURE 7.8: Raman spectra (open symbols) of hexagonal (a) and cubic (b) $SrMnO_3$. For both samples, best-fit curve (thick solid line), fitting components (solid lines) and background (dashed lines) are also shown.

Hexagonal			
ν_0 (cm^{-1})	Γ (cm^{-1})	1-ph/m-ph	Label
243	9	1-ph	P1
344	13	1-ph	P2
434	9	1-ph	P3
441	9	1-ph	P4
467	52	m-ph	
552	20	1-ph	P5
644	14	1-ph	P6
686	119	m-ph	
783	89	m-ph	

Cubic	
ν_0 (cm^{-1})	Γ (cm^{-1})
405	296
652	33
719	125

Table 7.1: Phonon frequencies ν_0 and widths Γ for hexagonal (left table) and cubic (right table) SrMnO$_3$. For hexagonal SrMnO$_3$ 1-phonon (1-ph) or multi-phonon (m-ph) contributions are also indicated.

this scenario the Raman spectrum of cubic SMO roughly reflects the total phonon density of states.

Despite the poly-crystalline nature of the sample, a polarization analysis of Raman spectrum of hexagonal SMO was attempted in order to assign the observed phonon modes. Scratching the sample, several crystallites were obtained and one having a relatively large flat surface was chosen (see fig.7.9). The crystallite was placed on a holder equipped with tilting and rotation movements. The rotation angle can be measured with 1° accuracy. A polarizer was placed at the entrance of the monochromator in order to select the polarization of the scattered light.

In order to determine the orientation of the crystallite, a preliminary set of measurements was performed rotating the crystal respect to the laser polarization with a step of 5° and covering a total angle of 200°. Scattered polarization parallel to incident polarization was selected. The angle dependence of the spectrum is shown in fig.7.10. The intensity of peaks P2 (344 cm^{-1}), P3 (434 cm^{-1}, with a weak shoulder P4), and P6 (644 cm^{-1}) was obtained at each angle by means of a single fitting procedure. The angle dependence of the intensities of P2, P3, and P6 is shown in fig.7.11. It is well evident that P2 and P3 (left and center panels of fig.7.11) peaks have the same behavior and thus the same symmetry. For each allowed phonon symmetry, a model function for the θ-dependence of the intensity was calculated (see Appendix) exploiting the forms of the Raman tensors obtained from group-theory (see Appendix). Exploiting the calculated model func-

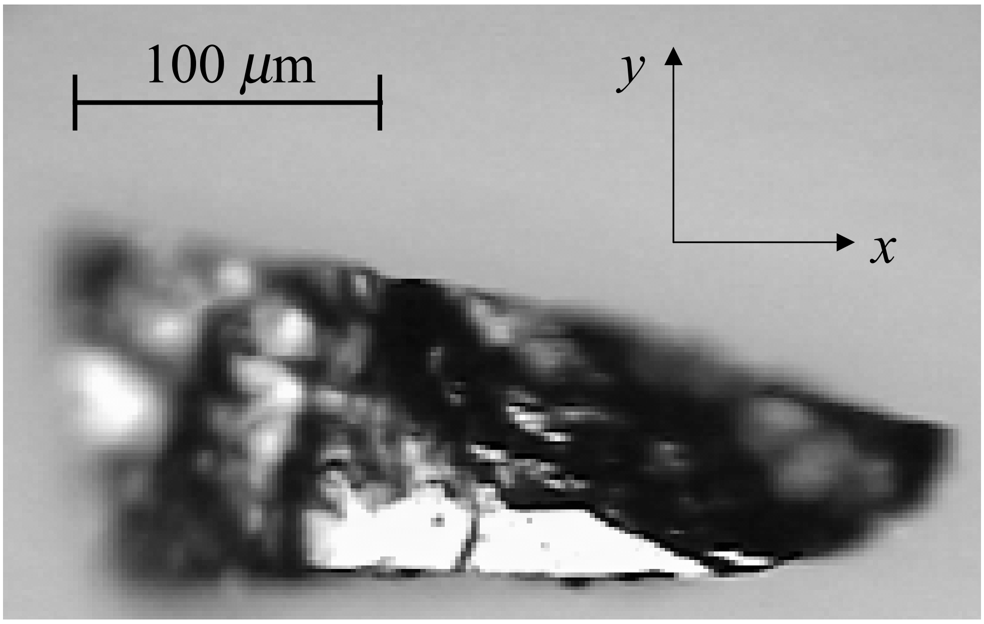

Figure 7.9: Picture of the crystallite employed for polarization dependent measurements taken with the microscope of the micro-Raman apparatus.

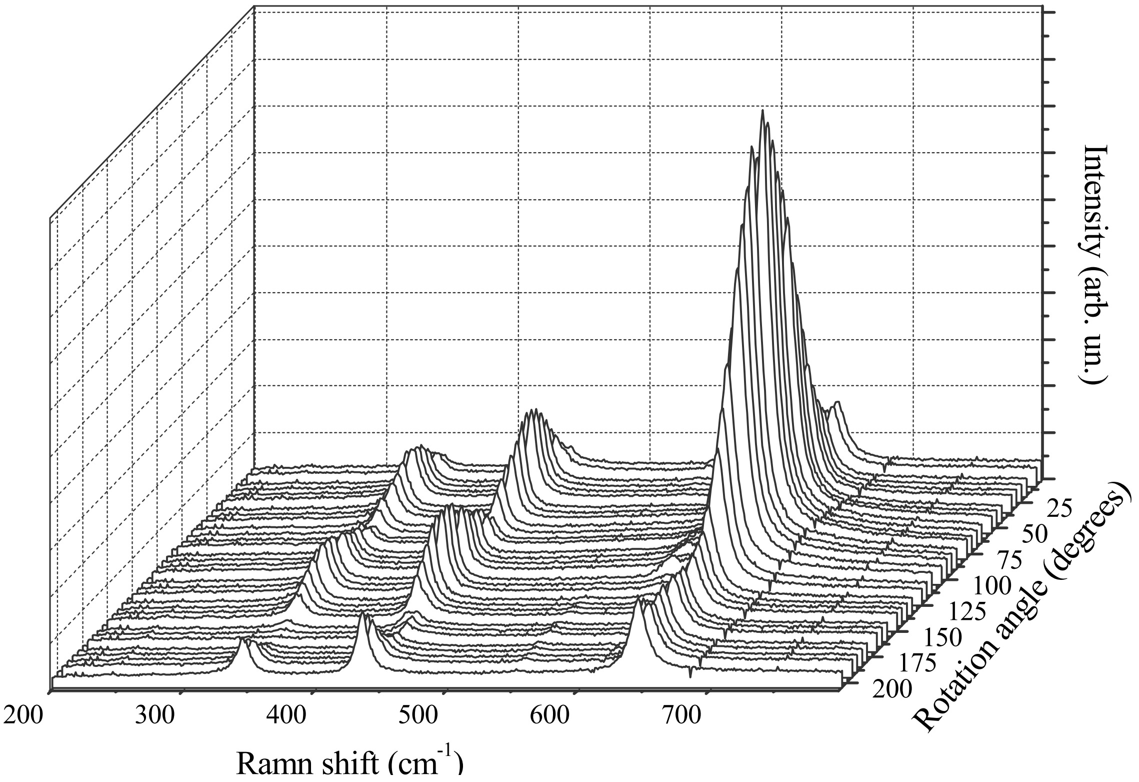

Figure 7.10: Rotation-angle dependence of the Raman spectrum of the crystallite shown in fig.7.9. The origin of the angle scale is arbitrary.

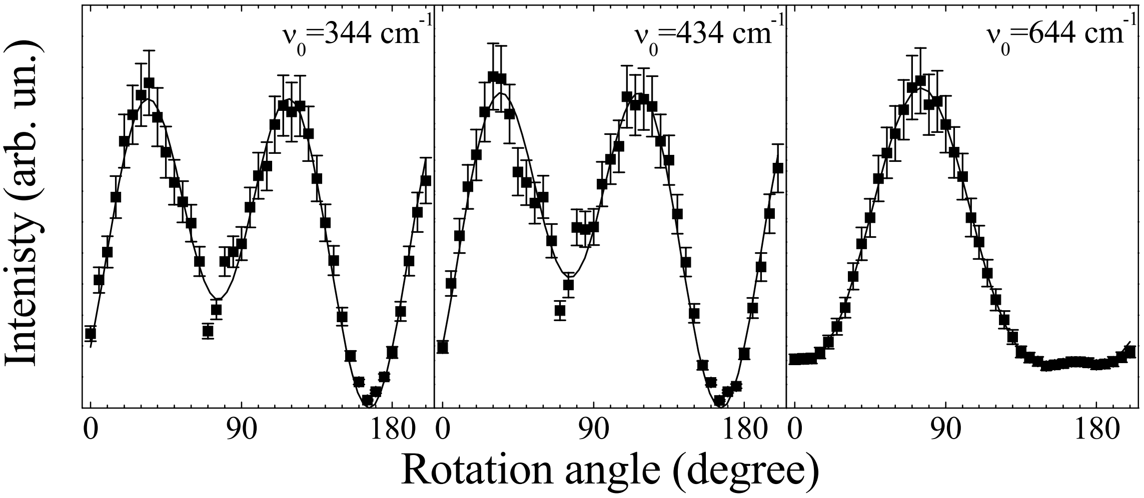

FIGURE 7.11: Angle dependence of the intensity of the main phonon peak of hexagonal $SrMnO_3$ centered at 344 cm^{-1} (P2, left panel), 434 cm^{-1} (P3, center panel), and 644 cm^{-1} (P6, right panel). Solid lines are best-fit curves obtained with the procedure described in the text. The vertical scales are not the same in the three panels. The origin of the angle scale is arbitrary.

tions, we apply a fitting procedure to the data shown in fig.7.11 assuming as free parameters the components of the considered Raman tensor, a tilting angle ϕ between the laser beam and crystal c-axis and an offset θ_0 for the rotation angle θ. Good fits were obtained only assigning the E_{1g} symmetry to the P2 and P3 phonons and the A_{1g} symmetry to the P6 phonon. The fitting results for this choice are shown with solid lines in fig.7.11. A best-fit value of 72° was obtained for ϕ, indicating that the considered flat surface of the crystallite is an ac crystal face slightly tilted ($\sim 18°$) with respect to the laser beam. Moreover, the θ_0 best-fit value allowed to conclude that the c-axis is oriented parallel to the y-axis in fig.7.9. In summary, from these preliminary measurements, the P2, P3, and P6 peaks were assigned to the E_{1g}, E_{1g}, and A_{1g} symmetries respectively and the orientation of the crystallite was determined.

Exploiting the determination of the orientation of the crystallite, long acquisition-time spectra were collected for selected high-symmetry configurations, in order to complete the assignment of the observed phonons P1-P6. Considering the incident ($\hat{\varepsilon}$) and scattered ($\hat{\varepsilon'}$) polarizations both laying in the ac crystal-plane and defining θ as the angle between $\hat{\varepsilon}$ and the a-axis, the selected high-symmetry configurations are $\theta = 0°$ and $\theta = 90°$ with either $\hat{\varepsilon} \| \hat{\varepsilon'}$ (parallel configuration) or $\hat{\varepsilon} \perp \hat{\varepsilon'}$ (orthogonal configuration). The intensities for the three allowed symmetries A_{1g}, E_{1g}, and E_{2g} were calculated in the high-symmetry configurations (see Appendix) and are reported

	$\theta = 0°$	$\theta = 90°$
$I(A_{1g})^{\parallel}$	a^2	b^2
$I(A_{1g})^{\perp}$	0	0
$I(E_{1g})^{\parallel}$	0	0
$I(E_{1g})^{\perp}$	c^2	c^2
$I(E_{2g})^{\parallel}$	d^2	0
$I(E_{2g})^{\perp}$	0	0

TABLE 7.2: Calculated intensities of the three phonon symmetries in both parallel ($\parallel$) and orthogonal ($\perp$) configurations at high-symmetry angles. The constants a, b, c, and d are the components of the Raman tensors (see Appendix).

in tab.7.2. The constants a, b, c, and d are the components of the Raman tensors (see Appendix). Monitoring the Raman signal of the preliminarily assigned phonon peaks we were able to carefully align the flat ac surface of the crystallite orthogonally to the laser beam. Measurements were then performed in both parallel and orthogonal configurations at $\theta = 0°$ and 90°. The results are shown in fig.7.12. The measurements confirm the above preliminary assignment of phonons P2, P3, and P6. The P4 peak behavior is clearly visible in parallel configuration at $\theta = 0°$, whereas its intensity drops to zero at $\theta = 90°$, thus indicating that this phonon is of E_{2g} symmetry. As to the remaining two 1-phonon peaks at 243 cm^{-1} (P1) and at 552 cm^{-1} (P5) their behavior (evidenced in the insets in fig.7.12) is analogous to that of the P4 phonon and opposite to the P6 phonon. Therefore P1 and P5 phonons

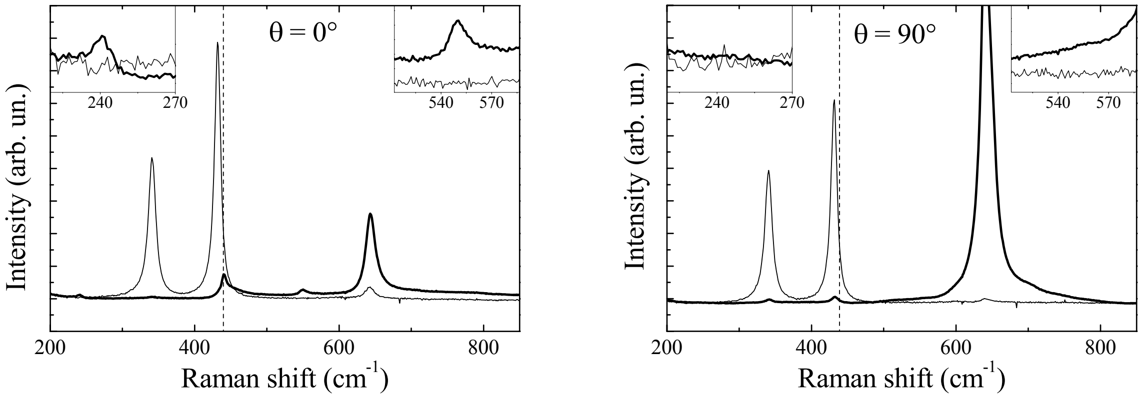

FIGURE 7.12: Raman spectra of hexagonal SrMnO3 at $\theta = 0°$ (left panel) and $\theta = 90°$ (right panel) in both parallel (thin lines) and orthogonal (thick lines) configurations. Vertical dashed lines mark the frequency of the P4 peak. Insets show magnifications in the regions of P1 and P5 peaks.

are ascribed to the E_{2g} symmetry.

From the point-group symmetry of the crystal, the symmetry reduced eigenvectors for each phonon can be determined [127]. In the case of hexagonal SMO, the atomic displacements for the allowed phonon symmetries are shown in fig.7.13. As a rule of thumb we can assume that phonons involving movements of lighter ions have larger frequencies and moreover it is generally correct to assume that stretching modes have frequencies higher than bending modes. On the basis of these assumptions, we ascribe peaks P2 and P3 (having E_{1g} symmetry) to the $E_{1g}(1)$ and $E_{1g}(2)$ modes respectively accordingly with the notation used in fig.7.13. As to the P6 peak (A_{1g} symmetry) it is unlikely that this high-energy phonon could be ascribed to the $A_{1g}(1)$ mode involving Mn-movements and therefore we ascribe this phonon to the $A_{1g}(2)$ mode consistently with the phonon-assignment in isostructural BaRuO$_3$ [79]. Bearing in mind that in BaRuO$_3$ the $E_{2g}(1)$ mode involving Ba-movement is observed at 90 cm^{-1} [79], we expect the corresponding phonon in SMO to have a frequency well below our experimental lower-limit of 200 cm^{-1}.

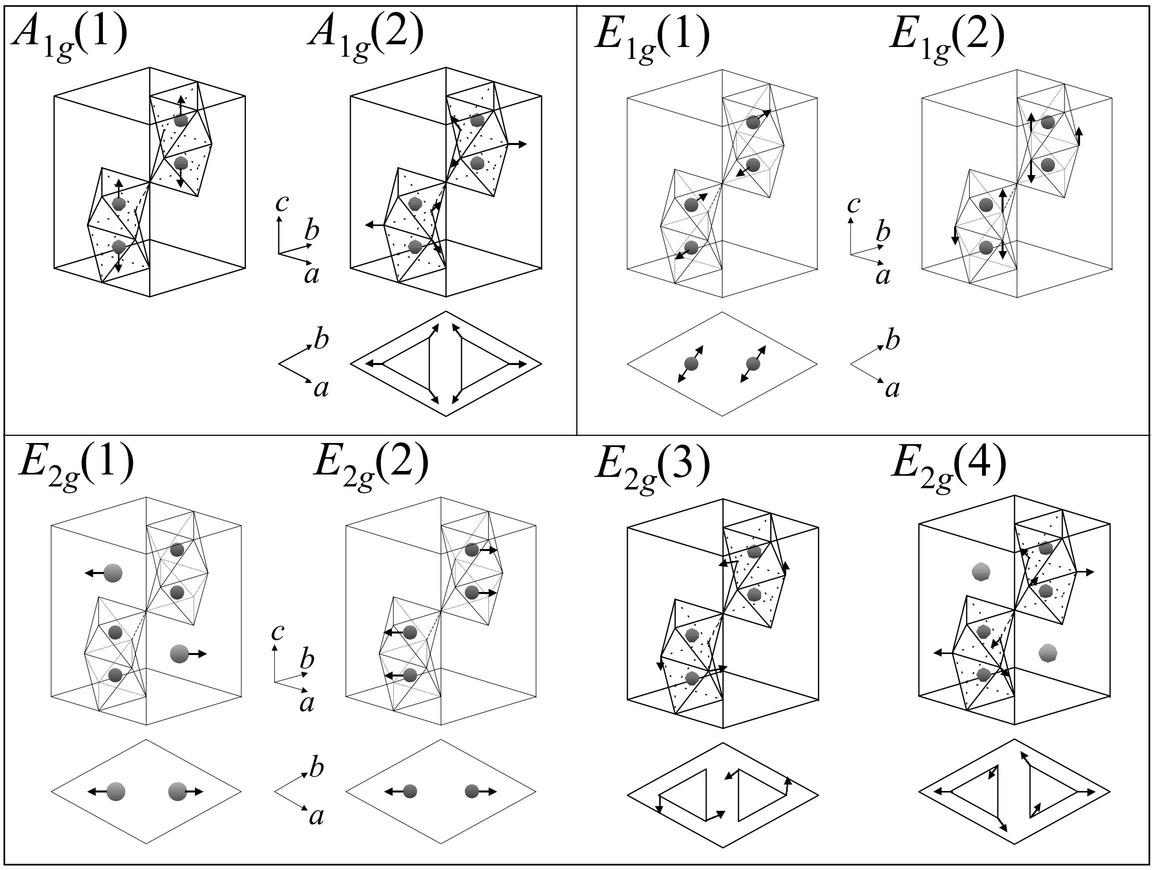

FIGURE 7.13: Symmetry-reduced atomic-displacements for Raman-active phonons in hexagonal SrMnO$_3$.

Label	ν_0 (cm^{-1})	Assignment	Atom
P1	243	$E_{2g}(2)$	Mn
P2	344	$E_{1g}(1)$	Mn
P3	434	$E_{1g}(2)$	O
P4	441	$E_{2g}(3)$	O
P5	551	$E_{2g}(4)$	O
P6	644	$A_{1g}(2)$	O

TABLE 7.3: Assignment of the 1-phonon peaks observed in hexagonal $SrMnO_3$.

Therefore, exploiting the aforementioned assumptions on expected phonon-frequencies, we assign the P1, P4, and P5 phonons to the $E_{2g}(2)$, $E_{2g}(3)$, and $E_{2g}(4)$ modes respectively. The assignment of the six 1-phonon peaks observed in hexagonal SMO is summarized in tab.7.3.

7.2.2 Low temperature measurements

Exploiting the experimental setup described in sect.3.2.2, Raman spectra of both hexagonal and cubic compounds have been collected in the 100-360 K temperature-range in low frequency (200-900 cm^{-1}) and high frequency (1600-3600 cm^{-1}) regions.

Raman spectra of the hexagonal compound in the low frequency region are shown in fig.7.14. On decreasing temperature, the expected narrowing and slight hardening of all phonon peaks is observed. A dramatic change in the phonon spectrum occurs at 100 K where the phonon doublet $E_{1g}(2) - E_{2g}(3)$ at around 440 cm^{-1} splits into four components (see the inset of fig.7.14). Moreover, several additional peaks appear in the spectrum as shown in the top panel of fig.7.14. It is worth to note that at least 11 phonon peaks are observed at 100 K, whereas, as already mentioned, only 8 Raman-active modes are expected for the $P6_3/mmc$ space group of hexagonal SMO. These findings strongly suggest the occurrence of a structural transition between 100 and 200 K, whereas no such effect was observed by means of X-ray diffraction measurements [128]. Since Raman spectroscopy is more sensible to the local structure than diffraction techniques, the observed phonon-splitting can be ascribed to a local structural rearrangement with no change in the average structure.

Bearing in mind the atomic displacements of the $E_{1g}(2)$ and $E_{2g}(3)$ phonon modes (see fig.7.13), a splitting of these two modes accompanied

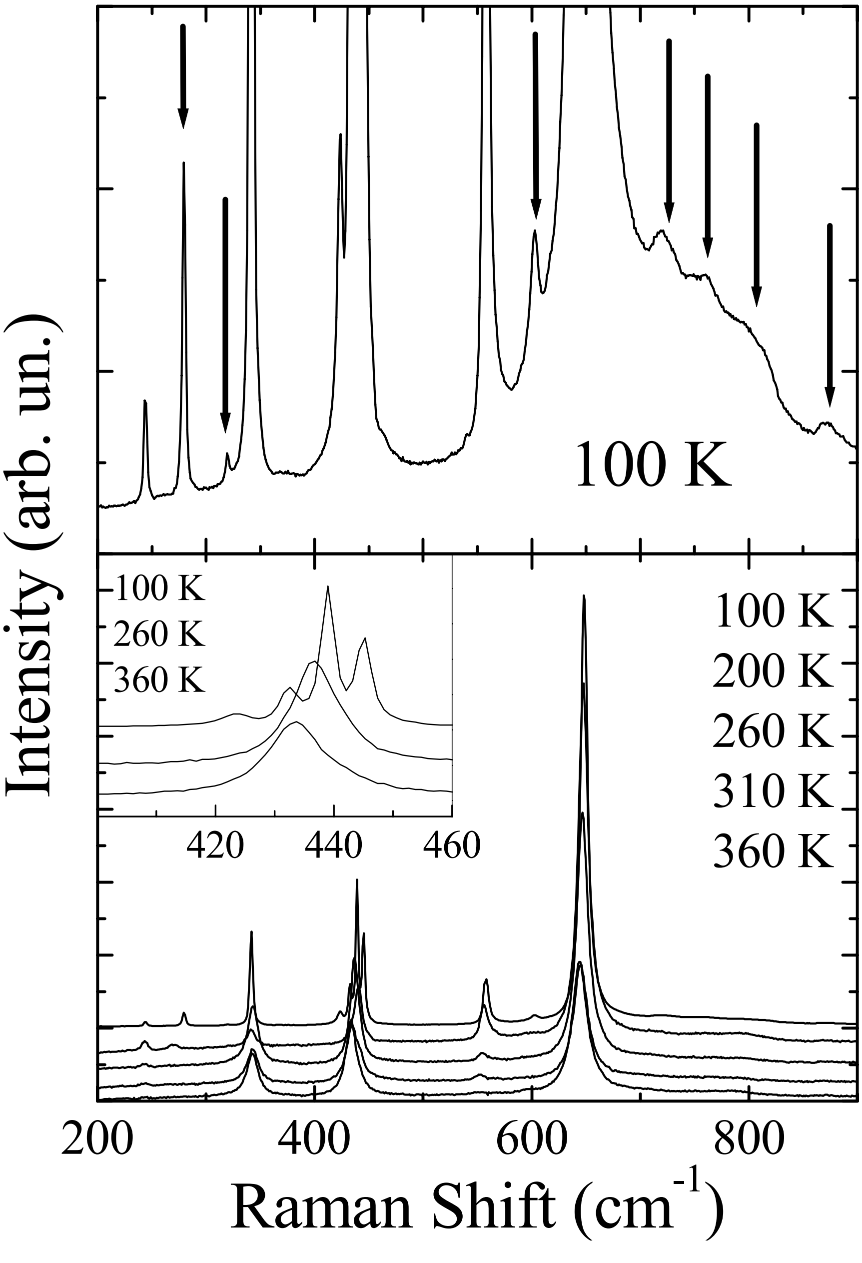

FIGURE 7.14: Bottom panel: Raman spectrum of hexagonal SrMnO$_3$ at different temperatures. Inset: enlargement in the 400-460 cm^{-1} range at selected temperatures. Top panel: detail of the 100 K spectrum. Arrows mark the additional phonon peaks.

by very smaller effects on the other phonons can be possibly explained with a transition which modifies the periodicity of the face-shared octahedra. The observed splitting is well consistent with a structural transitions in which the $P6_3/mmc$ space group is retained (consistently with the diffraction data reported in ref. [128]) whereas the base of the lattice changes for instance from the 4-layers *abac* structure to the 6-layers *abcacb* structure (see sect.2.6.2).

Bearing in mind that the Neél temperature is 278 K, the phonon splitting observed between 100 and 200 K seems not to be correlated with the magnetic structure. Negligible changes in phonon spectrum at low temperature were instead observed in cubic SMO.

Temperature-dependent Raman measurements on hexagonal and cubic SMO were performed also in the high-frequency region (1600-3600 cm^{-1}). Data for the hexagonal compound are shown in fig.7.15. It is well evident a dramatic change of the spectrum below 260 K with the appearance of a broad band centered around 3000 cm^{-1} and whose intensity strongly increases on decreasing temperature. Below 180 K, a fine-structure of this band is observed with the appearance of phonon-like lines. This band can be either ascribed to a Raman process or to a fluorescence band centered at around 1.6 eV (see the top scale in fig.7.15(a)). Unfortunately it was not possible to check this issue either changing the excitation frequency or checking the presence of the antiStokes lines since no alternative laser source are actually available and the possible anti-Stokes counterpart of the observed band is not detectable owing to the very high center-frequency of the band and the relatively low temperature. It is worth to notice that the onset of a fluorescence band around 3 eV was already observed in hexagonal SMO as well as in isostructural BaMnO$_3$ [128]. Therefore the band we observe at 1.6 eV is probably a fluorescence band itself instead of a Raman contribution.

A preliminary analysis of this band was performed simply integrating

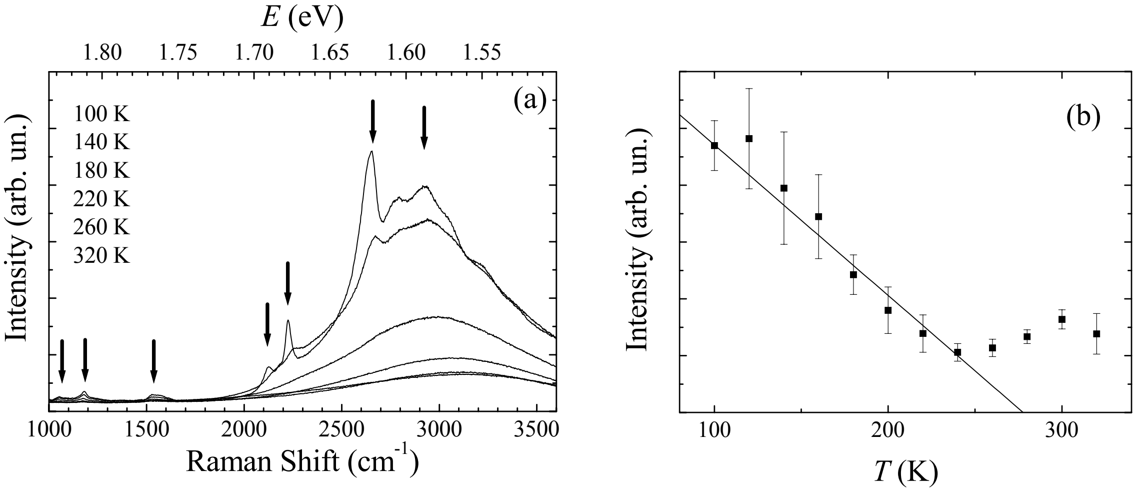

FIGURE 7.15: (a) High-frequency Raman spectrum of hexagonal SrMnO$_3$ at selected temperatures. Absolute energy scale is also shown. Arrows mark the phonon-like structures (see text). (b) Temperature dependence of the integrated area of all measured spectra. Line is linear extrapolation of data below 250 K.

the spectra over the whole frequency-range. The temperature dependence of the integrals so obtained is shown in fig.7.15(b). It is well evident the sudden increase of the area of the spectrum at around 250 K, whereas the low-temperature data linearly extrapolate to zero at a temperature which is very close to the Neél temperature. This finding suggests that the appearance of the broad band observed at low temperature is somehow correlated with the magnetic transition. Finally, it is worth to note that low-temperature measurements performed on cubic SMO in the same frequency range did not show significative changes and in particular there was no evidence of the onset of a broad band similar to the case of hexagonal SMO. We can conclude that, whatever is the nature of the observed band, this contribution is peculiar of the hexagonal phase.

Further experimental and theoretical investigations are required to achieve a complete understanding of the low-temperature phonon-splitting and onset of the high-frequency band.

Chapter 8

Discussions and conclusions

In this final chapter, by the comparison among the results we have previously presented, we will try to further discuss them and to draw some general conclusions. In particular we will discuss the effects induced by the different structure-tuning tools exploited in this research, namely: hydrostatic pressure, substrate-induced strain in thin films, and study of non-pseudocubic compounds with MnO_6 octahedra. Finally we will briefly present the future research perspectives opened by the investigations carried out within this Ph.D. thesis work.

8.1 Pressure effects

The whole of the high-pressure results are consistent with the idea that the anomalous behaviors observed in the high-pressure regime should be ascribed to the onset of a pressure-activated mechanism which competes with the *natural* tendency of pressure to drive the system towards a more symmetric structure with an increased metallic character. In particular, both the anomalous high-pressure behavior of the JT phonon (sect.4.2.1) and the strongly non linear behavior of $T_{IM}(P)$ (sect.5.2.1) support this hypothesis.

It can be shown that, although the high-pressure experiments on manganites have been carried out only on La-Ca compounds, the obtained results can provide a more general description which applies also to other class of manganites. As discussed in sect.5.2.1, the $T_{IM}(P)$ curve is well described by an empirical exponential law (see eq.5.3). To state eq.5.3 in terms of a general law, we applied it to extract at ambient pressure the dependence of T_{IM} on the average ionic radius r_A of the ion at the A-site in the ABX_3 perovskite structure (see sect.2.3), starting from a compound with a given r_A^0.

Without introducing adjustable parameters but exploiting only the known internal/external pressure conversion factor β [34] (see sect.2.4) the insulator-to-metal transition curve can be expressed in term of r_A:

$$T_{IM}(r_A) = T_{IM}^{\infty} - (T_{IM}^{\infty} - T_{IM}(r_A^0)) \exp\left(-\frac{r_A - r_A^0}{\beta P_0}\right) \tag{8.1}$$

The $T_{IM}(r_A)$ is shown in fig.8.1 in comparison with the experimental data of several compounds at constant $x = 0.25$ doping (ref. [129]). The agreement is excellent up to $r_A \sim 1.22$ Å, that is over the region corresponding to intermediate-EPC regime and first order IM transition [129, 130]. At r_A values larger than 1.22 Å the curve fails to describe the experimental data. This finding clearly indicates that the equivalence between internal and external pressure holds only in the low pressure regime. It is worth to notice that for $r_A \gtrsim 1.22$ Å the transition is second order and the EPC is weak [129, 130]. As discussed in sect.2.3, anomalies in the r_A dependence of the Mn-O bond lengths and Mn-O-Mn bond angles were observed at $r_A = 1.23 - 1.24$ Å in $Re_{0.7}Ae_{0.3}$MnO$_3$ samples. In particular, the structure of $Re_{0.7}Ae_{0.3}$MnO$_3$ changes from orthorhombic to rhombohedral at $r_A = 1.23$ Å and the coherent

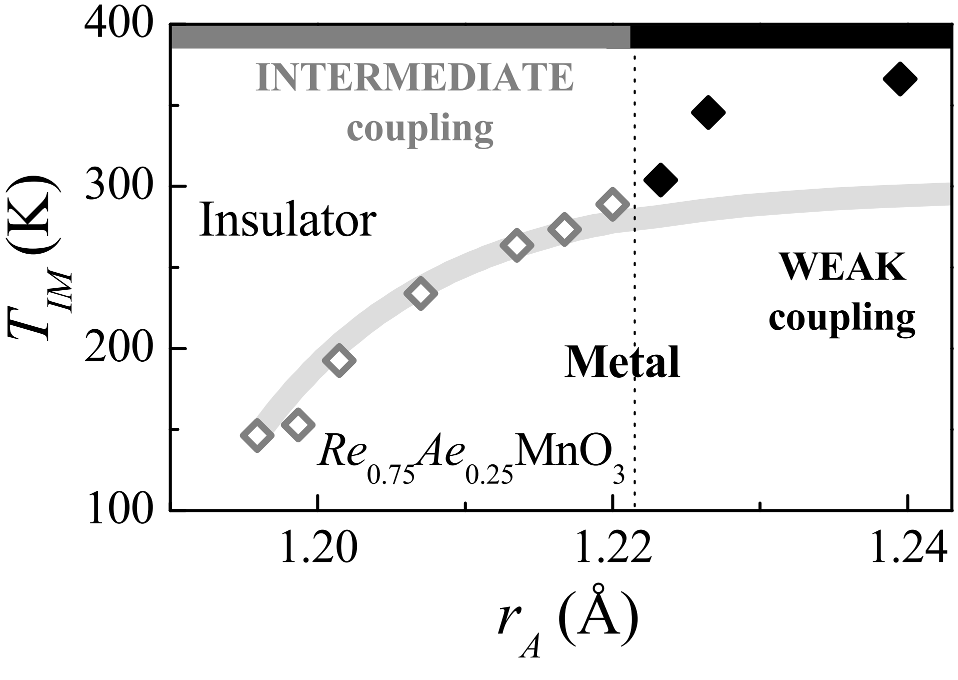

FIGURE 8.1: $r_A - T$ phase diagram for $x = 0.25$ manganites. Diamonds: ref. [129] (Weak coupling compounds: open symbols). Gray line: from eq.8.1 (see text). To make the data internally comparable, the r_A values of ref. [129] have been recalculated using the ionic radii with coordination number 9 as in ref. [34].

JT distortion is suppressed [30].

Eq.5.3 also allows to obtain the pressure derivative of T_{IM}:

$$\frac{dT_{IM}}{dP} = \frac{(T_{IM}^{\infty} - T_{IM}^{0})\exp(-P/P_0)}{P_0} = \frac{T_{IM}^{\infty} - T_{IM}(P)}{P_0} \tag{8.2}$$

thus simply obtaining the linear relationship between dT_{IM}/dP and T_{IM} itself shown in fig.8.2. A set of $(T_{IM}, dT_{IM}/dP)$ values obtained from the experimental $T_{IM}(P)$ data on LC25S reported in sect.5.2 are also shown. In the same figure several data on the T_{IM} pressure derivative within the low pressure regime available in the literature and obtained on several manganites is shown for sake of comparison (see sect.2.4). Also in this case, eq.8.2

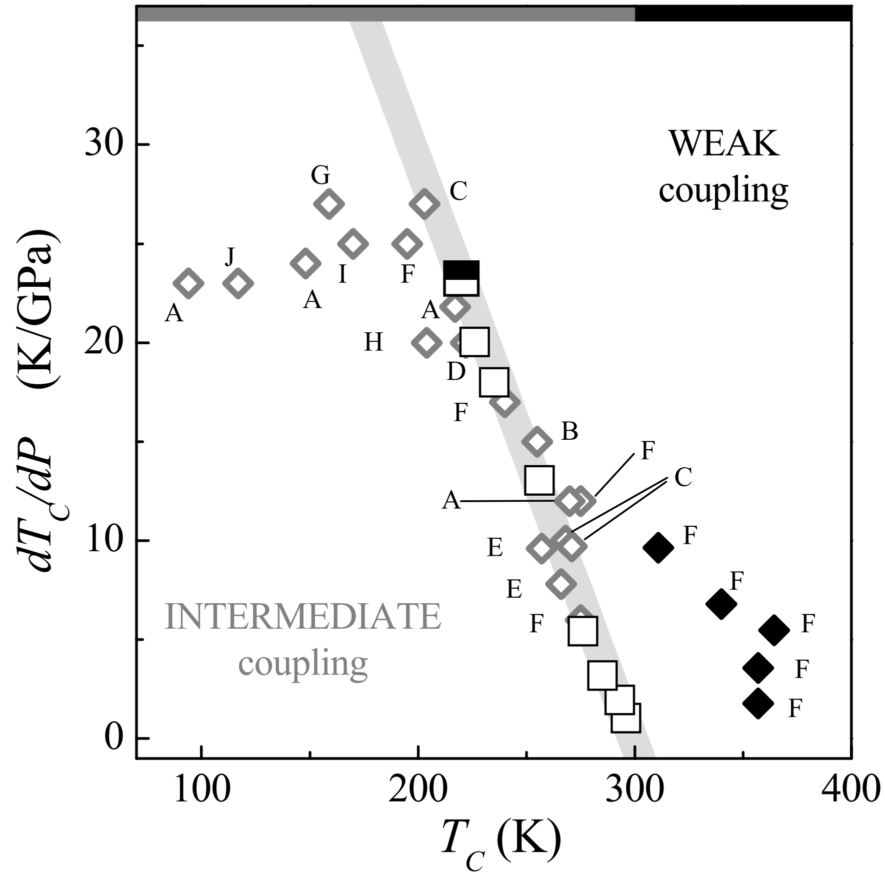

FIGURE 8.2: Pressure derivative of T_{IM} vs. T_{IM}. Open squares: $dT_{IM}(P)/dP \mid_P$ vs. $T_{IM}(P)$ from the present experiment. Gray line: from eq.8.2. The zero pressure limits, $dT_{IM}(P)/dP \mid_{P=0}$ vs $T_{IM}(0)$, are also plotted. Half-filled square: present experiment; diamonds: data from literature (weak coupling compounds: open diamonds, intermediate coupling compounds: full diamonds). References: A= [22], B= [34], C= [48], D= [39], E= [46], F= [36], G= [40], H= [43], I= [44], J= [45].

describes the intermediate coupling regime rather well, at least for $T_{IM} > 200$ K, whereas it is not appropriate for weak coupling compounds. The deviation of the low T_{IM} (≤ 200 K) compounds from eq.8.2 can be explained by the effective EPC getting stronger, with the localizing effect being strengthened by a high cation disorder [31, 32]. More quantitatively, for these samples the mean square deviation σ_{cat} of the $Re - Ae$ ion radii is larger than the mean square thermal displacement σ_{th}, obtained from the experimental vibrational frequencies of the $Re - Ae$ ions. This results in an *effective disorder*: $\Sigma_{eff} = \sigma_{cat}/\sigma_{th} > 1$. The universal behavior here observed (fig.8.2) shows that, regardless of doping or chemical composition, T_{IM} is actually the only relevant parameter for intermediate coupling manganites ($\Sigma_{eff} < 1$).

The far-IR measurements performed on LC25S and LC20S are well consistent with the observed dT_{IM}/dP vs. T_{IM} behavior. Bearing in mind that both T_{IM} and the spectral weight n^* are a measure of the charge delocalization extent, to larger values of n^* correspond larger T_{IM} values. The pressure dependence of n^* for LC25S and LC20S is shown in fig.8.3(a). It is evident that n^* is smaller in LC20S than in LC25S, whereas the rate of increase is much higher in LC20S than in LC25S. Moreover the two spectral weights seem to converge to the same high-pressure value. By comparing the experimental $T_{IM}(P)$ of LC25S with the $T_{IM}(P)$ of LC20S calculated by means of eq.2.2 (fig.8.3(b)), it is apparent that the pressure evolution is qualitatively similar to that observed for $n^*(P)$. At low pressure T_{IM} is different in the two samples whereas on increasing pressure the two curves tend to converge owing to the larger dT_{IM}/dP predicted in LC20S.

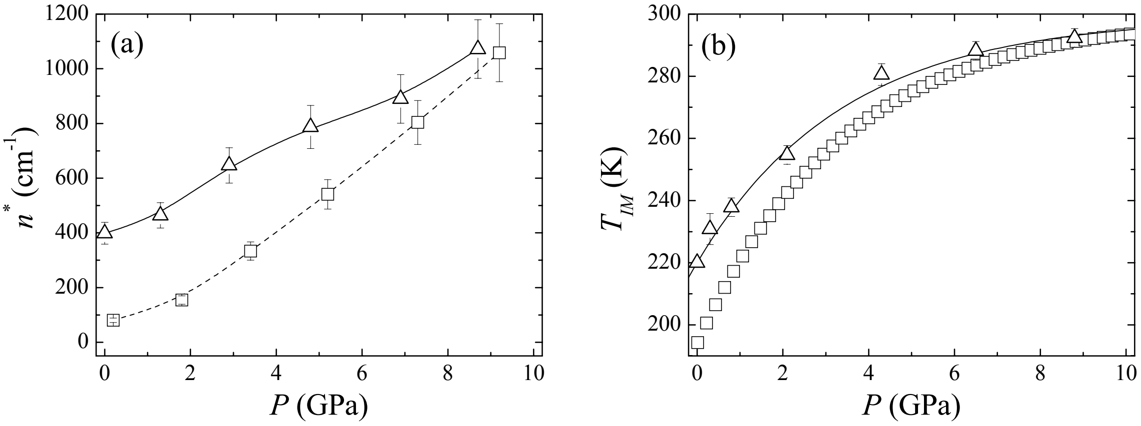

FIGURE 8.3: Pressure dependence of the far-infrared spectral weight (a) and of T_{IM} (b) of $La_{0.75}Ca_{0.25}MnO_3$ (triangles) and $La_{0.80}Ca_{0.20}MnO_3$ (squares). $T_{IM}(P)$ for $La_{0.80}Ca_{0.20}MnO_3$ was calculated by means of eq.5.3. Lines are guides to eyes.

The above results indicate that a certain universality character is associated to the empirical model for describing $T_{IM}(P)$, for its ability to account for a large class of low-disorder manganites characterized by intermediate EPC. Exploiting the Clausius-Clapeyron equation:

$$\frac{dT_{IM}}{dP} = \frac{\Delta V}{\Delta S} \tag{8.3}$$

where ΔV and ΔS are the volume and entropy changes at the transition, the vanishingly small values of dT_{IM}/dP observed at high pressure suggest a reduction of ΔV at high-pressure. This finding can be possibly explained considering that ΔV is large when the system undergoes a transition from a strongly JT-distorted insulating phase to the more symmetric metallic phase, whereas ΔV becomes small when the high-temperature JT distortions are reduced. This hypothesis is qualitatively supported by the Raman data discussed in chap.4. Since the frequency ν_{JT} of the JT stretching-phonon increases as the JT distortion decreases, the Raman data indicate that the distortion is larger in LC20S than in LC25S and that, on increasing pressure, the distortion is reduced in both samples (see left panels in fig.8.4). In LC25S the effect is larger and saturation occurs at a pressure smaller than in LC20S. A similar effect is thus expected in the pressure dependence of

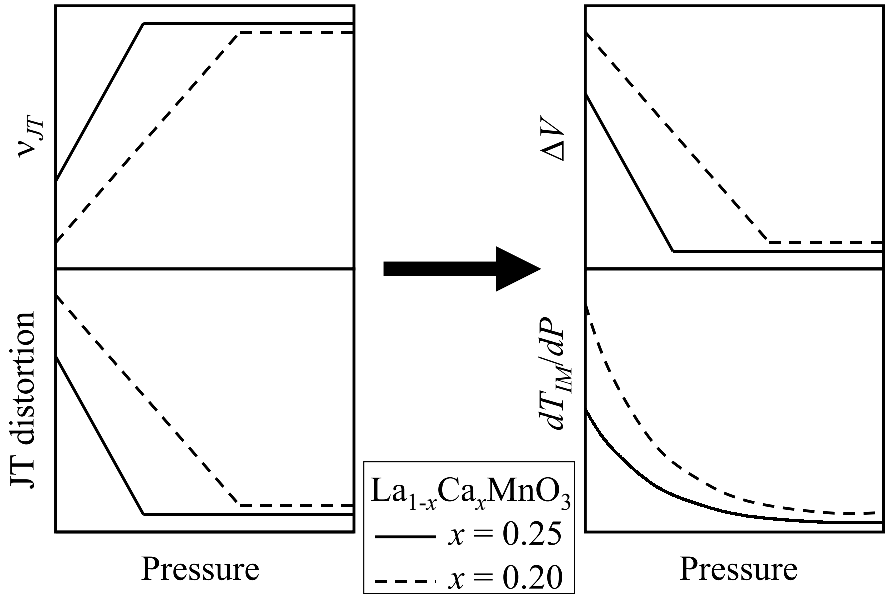

FIGURE 8.4: Schematic representation of the connection between the pressure dependence of the JT phonon-frequency ν_{JT}, the Jahn-Teller distortion, the volume discontinuity ΔV, and dT_{IM}/dP for $La_{0.75}Ca_{0.25}MnO_3$ (solid lines) and $La_{0.80}Ca_{0.20}MnO_3$ (dashed lines).

ΔV consistently with the predicted behavior for dT_{IM}/dP (see right panels in fig.8.4). This suggestion is also consistent with the remarkable decrease of ΔV observed at $r_A \gtrsim 1.22$ Å [130].

8.1.1 Role of superexchange coupling

As discussed in sect.5.3, a two-site model (TSM) was developed for the description of the experimental $P - T$ phase diagram of LC25S. A good agreement between the model and the experimental data is obtained only by introducing a strong pressure dependence of the AF SE interaction. The model can be used in turn to "fit" the experimental $T_{IM}(P)$ values thus obtaining the "experimental" pressure dependence of J_{AF}. This simply amounts to determine, at each pressure, the value of J_{AF} which provides the correct experimental $T_{IM} = T_C$. Since the comparison between the "experimental" $J_{AF}(P)$ (SE interaction) and the pressure dependence of the hopping integral $t(P)$ (DE interaction) could be relevant, the quantities $J_{AF}(P)/J_{AF}(0)$, $t(P)/t(0)$, and $t^2(P)/t^2(0)$ are shown in fig.8.5. The figure clearly

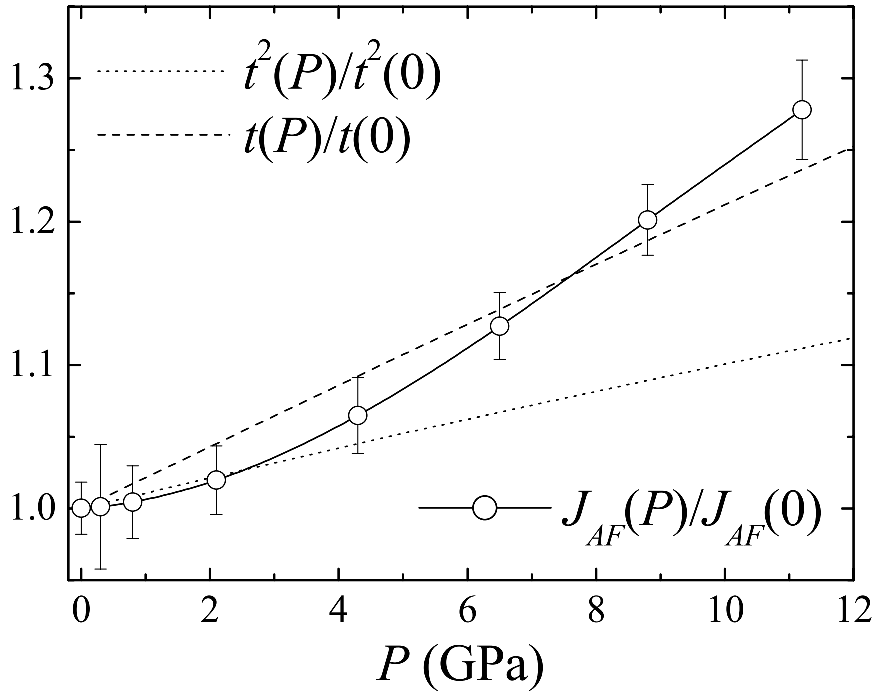

FIGURE 8.5: Open circles: pressure dependence of J_{AF} extracted from the experimental data reported in sect.5.2.1 by means of the two-site model (see text). Solid line is a guide to eyes. For sake of comparison $t^2(P)$ (dashed line) and $t(P)$ (dotted line) are also shown. All curves are normalized to their zero-pressure value.

suggests the $t^2(P)$ proportionality for the $J_{AF}(P)$ term thus strengthening the choice made in sect.5.3. It is worth to notice that the above finding makes reasonable to assume that the DE interaction dominates over the SE at low-pressure, according to well established experimental results, while on increasing pressure the SE contribution becomes more and more important. The onset of a remarkable AF interaction in the high-pressure regime affects the spin alignment weakening the charge-delocalization tendency of the DE interaction.

In this scenario, the low-pressure range where $T_C(P)$ rapidly increases is thus dominated by the DE interaction whereas the high-pressure range where $T_C(P)$ is almost constant is characterized by the competition between the SE and the DE interactions. A direct confirm of this hypothesis has been recently provided by high-pressure neutron diffraction measurements where the onset of magnetic diffraction peaks related to AF ordering was observed in $La_{0.67}Ca_{0.33}MnO_3$ at around 4 GPa [58] (see sect.2.4). In principle, a third regime at very high-pressure could be conjectured on the basis of the $J_{AF}(P) \propto t^2(P)$ dependence. Indeed, on increasing the pressure, the system is expected to evolve from a regime dominated by DE, where the bond compression leads to an increase of T_C, to an intermediate regime, where T_C is almost constant, owing to the competition between SE and DE, and eventually to a regime dominated by the SE contribution where T_C progressively decreases. Although in our measurements the applied pressure allows LC25S to reach only the intermediate regime, this picture is absolutely consistent with the pressure dependence of $T_C(P)$ recently observed in several manganites where the three regimes are apparent, [53–57]. In this case the intermediate regime (T_C almost pressure independent) occurs around 4 GPa [53–57]. This pressure value is lower than that we observed in LC25S but the difference can be ascribed to the presence of high cation disorder ($\Sigma_{eff} > 1$, see sect.8.1) which, as above discussed, strongly affects the $T_C(P)$ behavior.

It is worth to notice that the pressure dependence of the JT phonon discussed in chap.4 can be consistently included within this framework by identifying the conjectured pressure-activated localizing interaction with the SE interaction. Indeed the onset of the competition between SE and DE induces the coexistence of both distorted and undistorted octahedra and leads, in the high-pressure regime, to an increase of lattice disorder and to an inefficiency of pressure in further reducing the JT distortion. The optical counterpart of these structural effects are the broadening of the JT phonon peak (see fig.8.6(a)) and saturation effect for its central frequency (see fig.8.6(b)) observed in our Raman experiments. Moreover the comparison among the

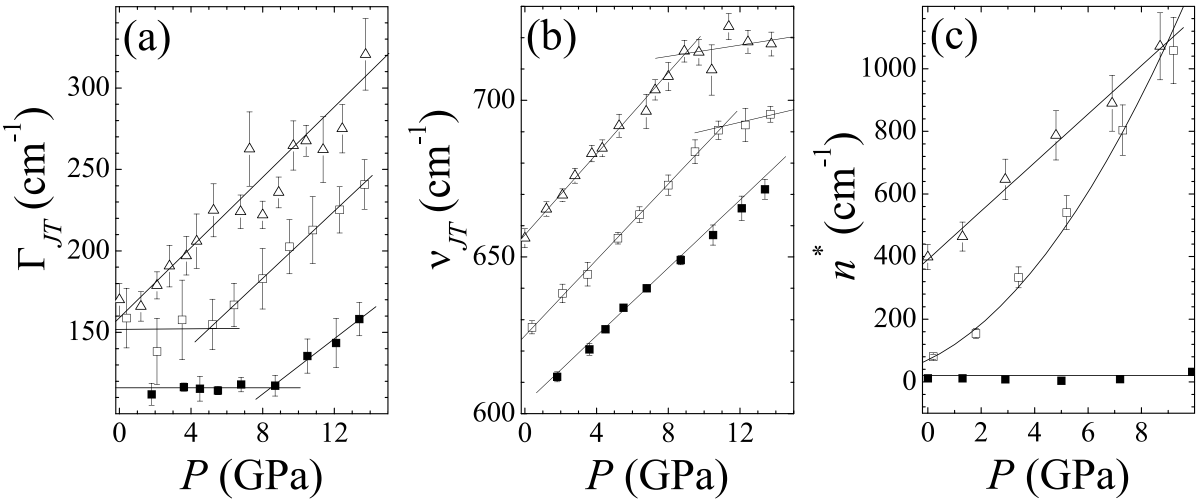

FIGURE 8.6: Pressure dependence of Γ_{JT} (a), ν_{JT} (b), and of n^* (c) for $La_{0.75}Ca_{0.25}MnO_3$ (open triangles), $La_{0.80}Ca_{0.20}MnO_3$ (open circles), and $La_{0.80}Ca_{0.20}MnO_{2.92}$ (full squares). Raman data on $La_{0.75}Ca_{0.25}MnO_3$ are from ref. [49]. The ν_{JT} values are shifted for clarity. Solid lines are guides to eyes.

results obtained for the three samples shows that the threshold pressure for the activation of the SE interaction appear to decrease on increasing the metallic character of the system that is on increasing the hopping integral t. This experimental finding is clearly in agreement with the choice of the $t^2(P)$ proportionality for $J_{AF}(P)$.

The t-dependence of the threshold pressure could also explain the different $n^*(P)$ behavior shown by the LC25S and LC20S samples (see fig.8.6(c)). Indeed the linewidth pressure-dependence suggests the activation of the SE interaction at around ambient pressure and 5 GPa in LC25S and LC20S respectively. The early SE activation in LC25S makes the pressure less effective on increasing n^* and thus charge-delocalization in this compound than in LC20S.

Additional arguments must be given to explain the $n^*(P)$ behavior shown by LC20D which closely resembles that of pure $LaMnO_3$ [8]. Despite the pressure-induced reduction of the JT distortion suggested by the almost linear increase of $\nu_{JT}(P)$, no evidence of charge delocalization in LC20D at least up to 10 GPa can be obtained by the $n^*(P)$ behavior. This finding can be ascribed to the very small number of charge carriers in LC20D and to the spatial arrangement of the distortions. Considering a cluster of N octahedra, the probability that all the octahedra contained in the cluster are distorted (i.e. that all the Mn ions are Mn^{3+}) is $p(N) = (1 - x_{eff})^N$ where x_{eff} is the hole density. Therefore the average size $\overline{N}$ of a cluster of distorted octahedra only is:

$$\overline{N} = \frac{\sum_{N=0}^{+\infty} Np(N)}{\sum_{N=0}^{+\infty} p(N)} = \frac{(1 - x_{eff}/x_{eff}^2)}{1/x_{eff}} = \frac{1 - x_{eff}}{x_{eff}} \tag{8.4}$$

For LC25S ($x_{eff} = 0.25$), LC20S ($x_{eff} = 0.20$), and LC20D ($x_{eff} = 0.04$) eq.8.4 gives $\overline{N}$=3, 4, and 24 respectively. Therefore in the stoichiometric samples the large part of distorted cluster are too small to have a 3-dimensional structure whereas in the oxygen-deficient sample the distorted clusters are much larger and a coherent distortion similar to the case of $LaMnO_3$ can be established. In a coherently-distorted cluster, a distorted octahedron is much more stable than an isolated one. The coherently distorted domains are thus almost unaccessible for holes and charge delocalization is suppressed. In this picture, despite the pressure-induced reduction of the JT distortion in LC20D, the coherency of the distortion and the small number of carriers prevent charge delocalization at least up to 10 GPa. Finally we want to stress that the observed high-pressure charge delocalization process in $LaMnO_3$ [8] has a different nature from that observed in LC25S and LC20S. The behavior of LC20D seems to be similar to that of $LaMnO_3$, whereas the pressure behavior of Γ_{JT} in LC20D can suggest charge delocalization well above 10 GPa.

8.2 Strain effects

As already discussed in chap.2, another important tool for tuning the structure of manganites is the film-substrate lattice mismatch which, differently from the hydrostatic pressure, induces an anisotropic strain to the film lattice. In the chap.6 the optical measurements we carried out on manganite films are reported and discussed. The Raman results are particularly important since we have demonstrated the capability of this technique in probing also very thin films down to 40 Å. In particular a direct correlation between the magneto-transport properties and the frequency of the bending and JT phonons has been proved.

In this section we attempt a comparison between the results obtained on LSMO-LAO thin-films and those obtained at high pressure on LC25S. Despite the different structure[1] and doping of the two compounds, a comparison between the strain effect induced by substrate and pressure can be performed by means of the ratio $R_\nu = \nu_{JT}/\nu_{ben}$ between the JT and bending

---

[1] We recall that LSMO is rhombohedral, whereas LC25S is orthorhombic (see sect.1.2).

phonon frequencies. Indeed, although the frequency of JT phonon was seen as a direct marker of the extent of the octahedral distortion in the previous sections, it can be hardly used in comparing such a different compounds subjected to such a different strain conditions. The division by ν_{ben} should, at least partially, compensate for differences in structure and/or doping and R_ν can be assumed as a comparable parameter measuring the JT distortion. On the basis of the previous discussion, the larger R_ν the weaker the JT effect.

The R_ν dependence of T_C obtained for LSMO films and LC25S under pressure is shown in fig.8.7. Data for $La_{1-x}Ca_xMnO_3$ ($0 \leq x \leq 0.25$) at

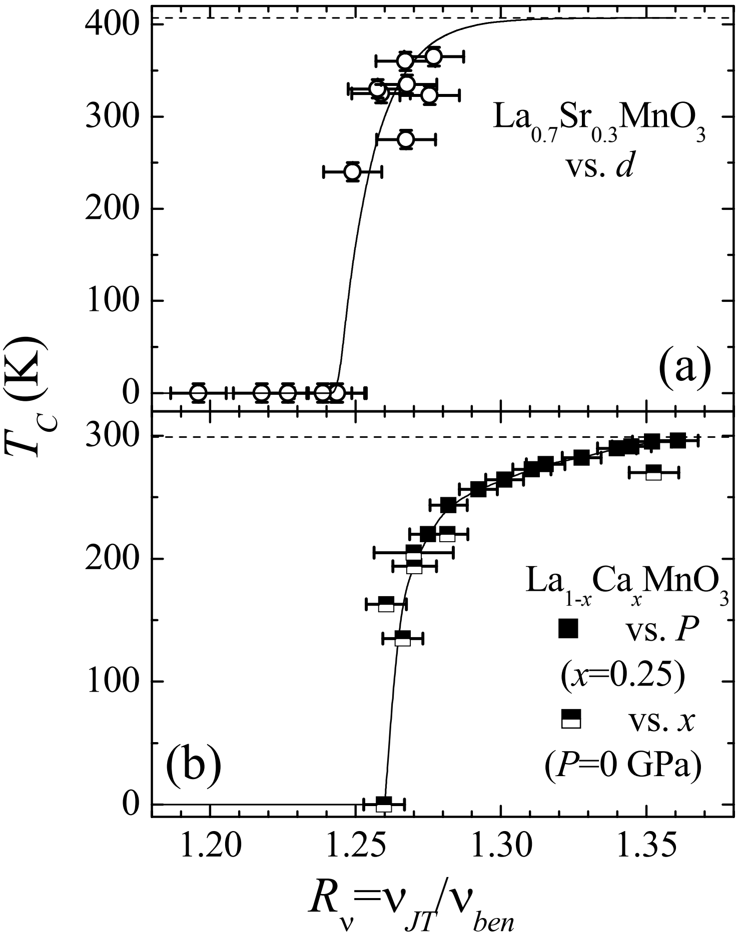

FIGURE 8.7: T_C as a function of the phonon frequency ratio $R_\nu = \nu_{JT}/\nu_{ben}$ (see text) for $La_{0.7}Sr_{0.3}MnO_3/LaAlO_3$ films of different thickness (a), for $La_{1-x}Ca_xMnO_3$ (b) at $x = 0.25$ and different pressures (full symbols), and at $P = 0$ GPa for different x (half-filled symbols). T_C data for $La_{0.7}Sr_{0.3}MnO_3/LaAlO_3$ films are from ref. [64]. Raman data on $La_{1-x}Ca_xMnO_3$ for $x = 0.25$ vs. P are from ref. [49] and for $P = 0$ vs. x are the same of fig.4.4. Solid lines are guides to eyes. Dashed lines mark indicative saturation values (see text).

ambient pressure are also shown. It is apparent that quite a similar behavior for bulk and film samples is shown in fig.8.7 around $R_\nu = 1.25$. The $T_C(R_\nu)$ curve abruptly drops to zero on decreasing R_ν, i.e. on increasing the JT effect. Since it is apparent that the properties of manganites can be efficiently tuned by both isotropic or anisotropic strain, the disruption of the magneto-transport properties which occurs in very thin films should be ascribed to large substrate-induced octahedral distortions and lattice rearrangements. The above discussion suggests that the quantity R_ν is a sort of universal marker of the magneto-transport properties of manganites and that the Raman spectroscopy could play an important role in developing manganite-film based devices.

Finally, on the basis of the saturation observed in $T_C(R_\nu)$ for LC25S on increasing pressure, a similar effect can be expected in LSMO with a $T_C(R_\nu)$ behavior similar to the solid line in fig.8.7(a). The T_C saturation value, estimated from the pressure dependent data on La-Sr manganites [36] shown in fig.8.2, is about 400 K (dashed line in fig.8.7). Further investigations are needed to verify the above suggestions.

8.3 Importance of pseudocubic structure

In order to verify the relevance of the octahedra network, two samples, the LMO spinel and the SMO manganite, with a non-pseudocubic skeletal array of MnO_6 octahedra have been investigated. The results obtained for these samples are rather different from those reported for pseudocubic manganites confirming the paramount relevance of the octahedra spatial arrangement on the physical properties of these MnO_6-based compounds (chap.7). In this section the tentative structural $P-T$ phase diagram of LMO determined with high-pressure X-ray diffraction measurements, is compared in fig.8.8 with the phase diagram obtained for LC25S by infrared spectroscopy. In both systems the transition temperature increases as pressure increases but the JT-distorted phase is at low-temperature for LMO, and at high-temperature for LC25S. Therefore applied pressure has the opposite effect on the two samples: it favors the undistorted phase in LC25S and the distorted phase in LMO. Moreover, in LMO at $P \gtrsim 10$ GPa the distorted phase becomes metastable and persists on releasing pressure down to 0 GPa. On the basis of the discussion reported in the previous sections it is not unlikely that pressure could strengthen the distortion but this effect is apparent in pseudocubic manganites only in a very high pressure regime. The different

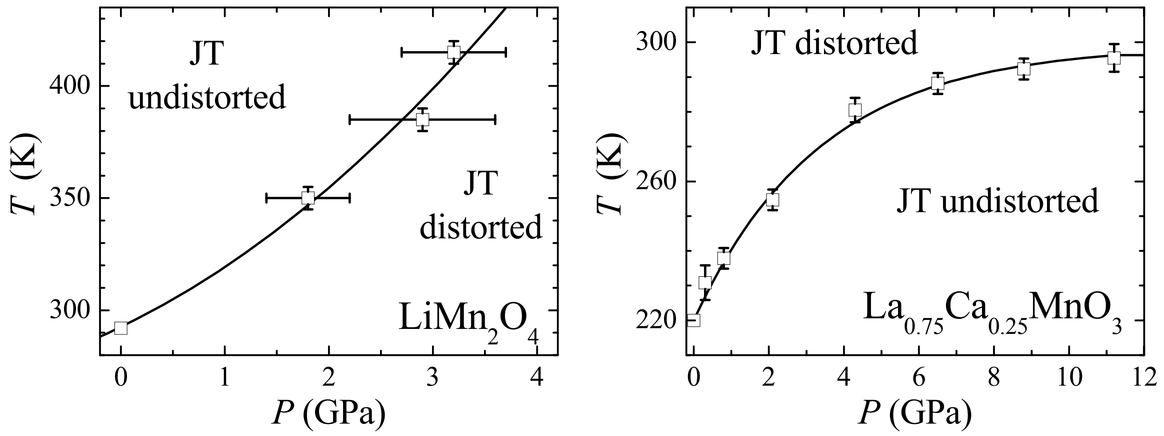

FIGURE 8.8: $P - T$ phase diagram of LiMn$_2$O$_4$ (left panel) and of La$_{0.75}$Ca$_{0.25}$MnO$_3$ (right panel). Solid lines are guides to eyes.

behavior shown by LMO should be ascribed to the presence of soft LiO$_4$ tetrahedra intercalated among the MnO$_6$ octahedra which allow the JT distortion to occur. Further relevant information on this topic could be provided by the comparison between the high-pressure Raman results on manganites reported in this thesis and those obtainable from the planned high-pressure Raman experiment on LMO. The importance of the octahedral arrangement is evidenced also by the strongly different behaviors observed in cubic and hexagonal SMO. In particular, the very intense band observed in the spectrum of hexagonal compound at low temperature in the high-frequency range (sect.7.2.2) suggests the presence of differences in the electronic structure with respect to the cubic structure. On the basis of the interesting results obtained, further investigations on LMO and SMO are in planning to clarify this point.

8.4 Conclusions

In this Ph.D. thesis, the effects of the JT distortion of the MnO$_6$ octahedra on the properties of CMR manganites and related compounds were investigated mainly by means of spectroscopic techniques and exploiting different tools for tuning the structure. Within the sphere of the research activity carried out for this thesis we have demonstrated the feasibility of high-pressure far-infrared measurements on bulk manganites and of Raman measurements on very thin manganite films (down to 40 Å). To our knowledge, the present are the first results obtained by these kind of challenging experiments. The analysis of the data allows to obtain clear spectroscopic markers of the magneto-transport properties of the investigated compounds and to gain a deeper insight of the microscopic interaction at work, finely discriminating the delicate balance among them. In particular the role of the superexchange interaction has been experimentally evidenced with the help of a simple theoretical model purposely developed. Connection and correlation between the effects of isotropic (hydrostatic pressure) and anisotropic (film-lattice mismatch) strains have been established and discussed. Finally the role of the skeletal array of MnO_6 octahedra has been pointed out by comparing the experimental results achieved on pseudocubic manganites with those obtained on other MnO_6-based compounds.

The main results obtained in this thesis are schematically summarized as follows:

- Room temperature high-pressure Raman measurements on $La_{0.80}$-$Ca_{0.20}MnO_{3-\delta}$ (δ=0.00, 0.08) and their comparison with existing results allowed the unambiguous identification of the Raman-active JT phonon. Occurrence of anomalous behavior of the JT phonon at high pressure was observed in agreement with previous results. These data are well consistent with the activation of a localizing mechanism competing with charge delocalization at high pressure.

- Pressure (0-11 GPa) and temperature (130-320 K) dependent mid-infrared absorption measurements on $La_{0.75}Ca_{0.25}MnO_3$ provided the first $P-T$ phase diagram of a manganite over a wide pressure range and the previously proposed absence of a pressure-induced room-temperature insulator to metal transition was confirmed. The phase diagram so determined indicates the existence of a kind of universal pressure behavior of the transition temperature for a large class of manganites.

- A simple theoretical model was developed for the description of the experimental $P-T$ phase diagram. Good agreement between theory and experiment is obtained only introducing the onset of an antiferromagnetic superexchange interaction at high pressure. It was argued that this interaction can represent the above mentioned localizing mechanism which competes with charge delocalization at high pressure.

- Room-temperature high-pressure far-infrared absorption measurements on $La_{1-x}Ca_xMnO_{3-\delta}$ (three samples: x = 0.25, δ = 0.00; x = 0.20, δ = 0.00; x = 0.20, δ = 0.08) by means of synchrotron radiation were carried out, thus demonstrating the feasibility of this kind of experiment. The results confirmed the absence of a pressure-induced insulator to metal transition at room temperature in all measured samples. The universal behavior suggested by the mid-infrared data on $La_{0.75}Ca_{0.25}MnO_3$ was qualitatively confirmed.

- $La_{0.70}Sr_{0.30}MnO_3$ thin films were studied by means of far-infrared reflectivity measurements (thickness from 320 Å to 6800 Å on $SrTiO_3$ substrate) and Raman spectroscopy (thickness from 40 Å to 1000 Å on $LaAlO_3$ substrate). Film thickness was found to affect the phonon spectrum and in particular the Raman spectrum dramatically changes in the 100-40 Å thickness range. The comparison with the high-pressure measurements suggests that the effect induced by hydrostatic pressure and substrate-induced strain are of the same nature.

- The importance of the octahedral arrangement characterizing pseudocubic manganites was pointed out by the study of compounds with MnO_6 octahedra in a non-pseudocubic arrangement such as hexagonal $SrMnO_3$ and $LiMn_2O_4$ spinel. The results obtained on these compounds represent a good starting point for a research line to be developed in parallel with the study of manganites.

8.5 Future work

The research activity carried out during the present Ph.D. thesis allowed to answer some open questions, whereas new issues have arisen from the interpretation of the results. In order to confirm the universal behavior we proposed for the transition temperature, the high-pressure phase diagram of other manganites should be investigated, in particular the study must be focused on both high and low disorder manganites. Moreover, the predicted onset of the antiferromagnetic interaction requires investigations by means of magnetic techniques such as high-pressure neutron diffraction, magnetization, and magneto-optics measurements. The study of manganites will be extended also to electron-doped systems (e.g. $Sr_{1-x}Ce_xMnO_3$ compounds) starting in particular from the parent compound $SrMnO_3$ with a detailed investigation of its peculiar low-temperature properties observed in the present Ph.D. thesis.

As to manganites thin-films, the strain effects will be investigated studying films of different manganites and in particular $La_{1-x}Ca_xMnO_3$ thin films. Moreover the study of multilayer hetero-structures could provide an important tool for finely tuning the strain exploiting the presence of multiple interfaces.

Finally the investigation performed on $LiMn_2O_4$ in the present Ph.D. thesis provides a good starting point for a new research activity focused on the study of other Li-spinels, such as Cr-doped $LiMn_2O_4$, possibly with high-pressure experiments.

Appendix

A.1 Calculated angle-dependence of phonons intensities in hexagonal $SrMnO_3$

During the measurements devoted to the assignment of the Raman-active phonon peaks of hexagonal $SrMnO_3$ (SMO), the angle dependence of the phonons intensity was calculated for non-oriented and oriented crystal. The calculation is based on the form of the Raman tensors for the three allowed phonon symmetries:

$$A_{1g}: \begin{pmatrix} a & 0 & 0 \\ 0 & a & 0 \\ 0 & 0 & b \end{pmatrix} \quad E_{1g}: \begin{pmatrix} 0 & 0 & 0 \\ 0 & 0 & c \\ 0 & c & 0 \end{pmatrix}, \begin{pmatrix} 0 & 0 & c \\ 0 & 0 & 0 \\ c & 0 & 0 \end{pmatrix}$$

$$E_{2g}: \begin{pmatrix} -d & 0 & 0 \\ 0 & d & 0 \\ 0 & 0 & 0 \end{pmatrix}, \begin{pmatrix} 0 & d & 0 \\ d & 0 & 0 \\ 0 & 0 & 0 \end{pmatrix} \tag{A-1}$$

where a, b, c, and d are constants, here assumed to be real for simplicity. The E symmetries are associated with two different Raman tensors owing to their two-fold degeneracy.

The case of non-oriented crystal can be treated assuming that the incident polarization $\hat{\varepsilon}$ forms an angle ϕ with crystal c-axis and the projection of $\hat{\varepsilon}$ on the crystal ab plane forms an angle θ' with the crystal a-axis (see fig.9). Since the orientation of the crystal is unknown *a priori*, the measured rotation angle $\theta = \theta' - \theta_0$ where θ_0 is an unknown offset value. The polarization $\hat{\varepsilon}$ can be written in the base of crystal axes as $(\sin\phi\cos\theta', \sin\phi\sin\theta', \cos\phi)$. Exploiting the well-known Raman intensity equation:

$$I \propto |\hat{\varepsilon}\alpha\hat{\varepsilon}'|^2 \tag{A-2}$$

where $\hat{\varepsilon}$ and $\hat{\varepsilon}'$ are the polarization of the incident and scattered light respectively and α is the Raman tensor of the considered phonon and considering

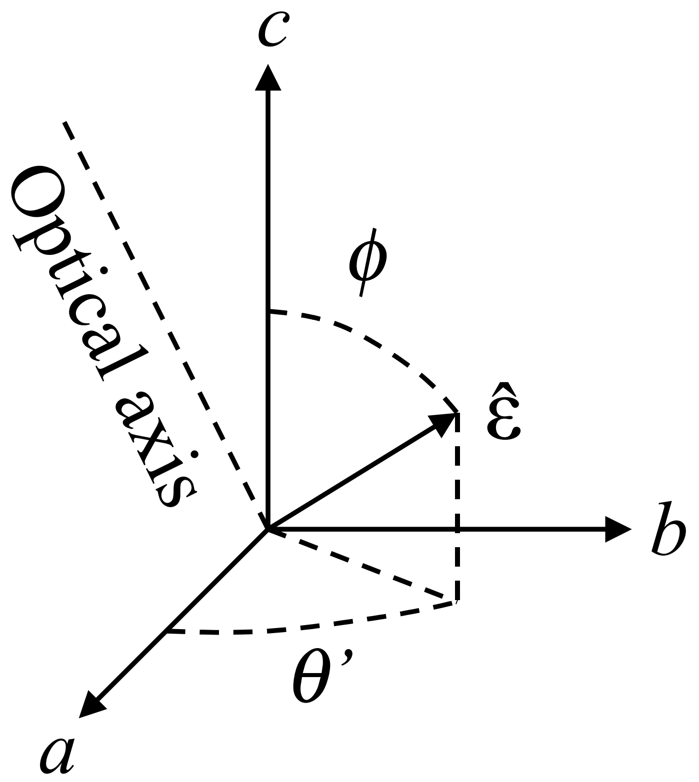

FIGURE 9: Geometrical configuration in the case of non-oriented crystal.

the parallel ($\hat{\varepsilon}'\|\hat{\varepsilon}$) and orthogonal ($\hat{\varepsilon}'\perp\hat{\varepsilon}$) configurations, the θ-dependence of the phonon intensity can be calculated analytically for a given phonon symmetry and given ϕ and θ_0 values. For the two-fold degenerate E symmetries, the intensities associated with the two possible forms of the Raman tensor are calculated separately by means of eq.A-2 and then summed. The analytical forms we obtain are the followings:

$$\begin{aligned} I(A_{1g})^{\|} = \; & a^2\cos^4\phi\sin^4\theta' + \cos^2\phi(2ab\sin^2\phi\sin^4\theta' + \\ & 2a^2\sin^2\theta'\cos^2\theta') + b^2\sin^4\phi\sin^4\theta' + \\ & 2ab\sin^2\phi\sin^2\theta'\cos^2\theta' + a^2\cos^4\theta' \end{aligned}$$

$$I(A_{1g})^{\perp} = \; (a-b)^2\sin^4\phi\sin^2\theta'\cos^2\theta'$$

$$I(E_{1g})^{\|} = \; 4c^2\sin^2\phi\cos^2\phi\sin^4\theta' + 4c^2\sin^2\phi\sin^2\theta'\cos^2\theta'$$

$$\begin{aligned} I(E_{1g})^{\perp} = \; & 4c^2\sin^2\phi\cos^2\phi\sin^2\theta'\cos^2\theta' + \\ & \sin^2\phi(c^2 - 4c^2\sin^2\theta'\cos^2\theta') \end{aligned}$$

$$I(E_{2g})^{\parallel} = \quad d^2(\cos^2\phi\sin^2\theta' + \cos^2\theta')^2$$

$$\begin{aligned} I(E_{2g})^{\perp} = \quad & d^2\cos^4\phi\sin^2\theta'\cos^2\theta' + \cos^2\phi(d^2 - \\ & 2d^2\sin^2\theta'\cos^2\theta') + d^2\sin^2\theta'\cos^2\theta' \end{aligned} \tag{A-3}$$

In the case of oriented crystal, $\hat{\varepsilon}$ can be either parallel to the ac (or equivalently ab) crystal face or to an ab crystal face. The former case corresponds to $\phi = \pi/2$ and the latter corresponds to $\phi = 0$. The orientation of the crystal can be chosen such that $\theta_0 = 0$. The analytical forms of the θ-dependence of the intensity are strongly simplified in this case. In particular, for $\hat{\varepsilon}\|ab$ the intensity in the parallel ($\hat{\varepsilon}\|\hat{\varepsilon}'$) and orthogonal ($\hat{\varepsilon}\perp\hat{\varepsilon}'$) configurations for the three phonon symmetries read:

$$\begin{array}{ll} I(A_{1g})^{\parallel} = a^2 & I(A_{1g})^{\perp} = 0 \\ I(E_{1g})^{\parallel} = d^2 & I(E_{1g})^{\perp} = d^2 \\ I(E_{2g})^{\parallel} = 0 & I(E_{2g})^{\perp} = 0 \end{array} \tag{A-4}$$

For $\hat{\varepsilon}\|ac$ the above equations read:

$$\begin{array}{ll} I(A_{1g})^{\parallel} = [(a-b)\cos^2\theta + b]^2 & I(A_{1g})^{\perp} = (a-b)^2\sin^2\theta\cos^2\theta \\ I(E_{1g})^{\parallel} = d^2\cos^4\theta & I(E_{1g})^{\perp} = d^2\sin^2\theta\cos^2\theta \\ I(E_{2g})^{\parallel} = 4c^2\sin^2\theta\cos^2\theta & I(E_{2g})^{\perp} = c^2(1-\sin^2\theta\cos^2\theta) \end{array} \tag{A-5}$$

The intensities in the high-symmetry configurations $\theta = 0$ and $\theta = \pi/2$ can be easily calculated from the above equations.

Bibliography

[1] S. Jin, T.H. Tiefel, M. McCormack, R.A. Fastnacht, R. Ramesh, and L.H. Chen, *Science* **264**, 413 (1994); R. Von Helmolt, J. Wecker, B. Holpzapfel, L. Schultz, and K. Samwer, *Phys. Rev. Lett.* **71**, 2331 (1993); R. Von Helmolt, J. Wecker, K. Samwer, L. Haupt, and K. Barner, *J. Appl. Phys.* **76**, 6925 (1994); R. Von Helmolt, J. Wecker, T. Lorenz, and K. Samwer, *Appl. Phys. Lett.* **67**, 2093 (1995).

[2] S.-W. Cheong, H.Y. Hwang, in *Colossal Magnetoresistance Oxides. Monograph in Condensed Matter Science*, edit by Y. Tokura (Gordon and Breach, New York, 2000).

[3] J.M.D. Coey, M. Viret, S. Molnar, *Adv. Phys.* **48**, 167 (1999).

[4] E. Dagotto, *Nanoscale Phase Separation and Colossal Magnetoresistance* (Springer-Verlag, Berlin, 2002).

[5] D.J. Lam, B.W. Veal, D.E. Ellis, *Phys. Rev. B* **22**, 5730 (1980).

[6] H.A. Jahn and E. Teller, *P. Roy. Soc. Lond. A Mat.* **161**, 220 (1937).

[7] E. Tarnow, *J. Phys.-Condens. Mat.* **5**, 1863 (1993).

[8] I. Loa, P. Adler, A. Grzechnik, K. Syassen, U. Schwarz2 M. Hanfland, G.Kh. Rozenberg, P. Gorodetsky, and M. P. Pasternak, *Phys. Rev. Lett.* **87**, 125501 (2001).

[9] P.G. Radaelli, D.E. Cox, M. Marezio,S.-W. Cheong, P.E. Schiffer, A.P.Ramirez, *Phys. Rev. Lett.* **75**, 4488 (1995).

[10] S. Jin, T.H. Tiefel, M. McCormack, R.A. Fastnacht, R. Ramesh, and L.H. Chen, *Science* **264**, 413 (1994); R. Von Helmotz, J. Wecker, T. Lorenz, and K. Samwer, *Appl Phys. Lett.* **67**, 2093 (1995).

[11] R.D. Shannon, *Acta Crystallogr. A* **32**, 751 (1976).

[12] J. Hemberger, A. Krimmel, T. Kurz, H.-A. Krug von Nidda, V.Yu. Ivanov, A.A. Mukhin, A.M. Balbashov, and A. Loidl, *Phys. Rev. B* **66**, 094410 (2002).

[13] C. Zener, *Phys. Rev.* **82**, 403 (1951).

[14] K. Kubo and N. Ohata, *J. Phys. Soc. Jpn.* **33**, 21 (1972).

[15] A.J. Millis, P.B. Littlewood, B.I. Shraiman, *Phys. Rev. Lett.* **74**, 5144 (1995).

[16] P. Norby, I.G. Krogh Andersen, E. Krogh Andersen, and N.H. Andersen, *J. Solid State Chem.* **119**, 191 (1995).

[17] C.H. Booth, J. Bridges, G.H. Kwei, J.M. Lawrence, A.L. Cornelius, J.J. Neumeier, *Phys. Rev. Lett.* **80**, 853, (1998); A. Lanzara, N.L. Saini, M. Brunelli, F. Natali, A. Bianconi, P.G. Radaelli, and S.-W. Cheong, *ibid.* **81**, 878 (1998).

[18] G. Zaho, K. Conder, H. Keller, K.A. Müller, *Nature* **381**, 676 (1996).

[19] T. Holstein, *Ann. Phys.* (New York) **8**, 325 (1959); *ibid.* **8**, 343 (1959).

[20] H. Fröhlich, *Adv. Phys.-New York* **3**, 325 (1954).

[21] W.A. Harrison, *The Electronic Structure and Properties of Solids* (Freeman, San Francisco, 1980).

[22] V. Laukhin, J. Fontcuberta, J.L. Garcia-Muñoz, and X. Obradors, *Phys. Rev. B* **56**, R10009 (1997).

[23] J.D. Lee and B.I. Min, *Phys Rev. B* **55**, 12454 (1997).

[24] A.J. Millis, T. Darling, and A. Migliori, *J. Appl. Phys.* **83**, 1588 (1998).

[25] I.O. Troyanchuk, S.V. Trukhanov, H. Szymczak, J. Przewoznik, and K. Bärner, *J. Exp. Theor. Phys.* **93**, 161 (2001).

[26] T.L. Aselage, D. Emin, S.S. McCready, E.L. Venturini, M.A. Rodriguez, J.A. Voigt, and T.J. Headley, *Phys. Rev. B* **68**, 134448 (2003).

[27] S.V. Trukhanov, N.V. Kasper, I.O. Troyanchuk, M. Tovar, H. Szymczak, and K. Bärnere, *J. Solid State Chem.* **169**, 85 (2002).

[28] H.L. Ju and H. Sohn, *J. Magn. Magn. Mater.* **167**, 200 (1997).

[29] H.Y. Hwang, S.-W. Cheong, P.G. Radaelli, M. Marezio, and B. Batlogg, *Phys. Rev. Lett.* **75**, 914 (1995).

[30] P.G. Radaelli, G. Iannone, M. Marezio, H.Y. Hwang, S-W. Cheong, J.D. Jorgensen, and D.N. Argyriou, *Phys. Rev. B* **56**, 8265 (1997).

[31] J. Fontcuberta, V. Laukhin, and X. Obradors, *Appl. Phys. Lett.* **72**, 2607 (1998).

[32] L.M. Rodriguez-Martinez and J.P. Attfield, *Phys. Rev. B* **54**, 15622 (1996).

[33] Y. Moritomo, H. Kuwahara, and Y. Tokura, *J. Phys. Soc. Jpn.* **66**, 556 (1997).

[34] H.Y. Hwang, T.T.M. Palstra, S.-W. Cheong, and B. Batlogg, *Phys. Rev. B* **52**, 15046 (1995).

[35] Y. Moritomo, A. Asamitsu, and Y. Tokura, *Phys. Rev. B* **56**, 12190 (1997).

[36] Y. Moritomo, H. Kuwahara, and Y. Tokura, *Physica B* **237-238**, 26 (1997).

[37] J.S. Zhou, W. Archibald, and J.B. Goodenough, *Nature* **381**, 770 (1996).

[38] J.S. Zhou and J.B. Goodenough, *Phys. Rev. Lett.* **80**, 2665 (1998).

[39] J.M. De Teresa, M.R. Ibarra, J. Blasco, J. Garca, C. Marquina, P.A. Algarabel, Z. Arnold, K. Kamenev, and C. Ritter, *Phys. Rev. B* **54**, 1187 (1996).

[40] Z. Arnold, K. Kamenev, M.R. Ibarra, P.A. Algarabel, C. Marquina, J. Blasco, and J. Garca, *Appl. Phys. Lett.* **67**, 2875 (1995).

[41] K. Kamenev, G. Balakrishnan, M.R. Lees, D.McK. Paul, Z. Arnold, and O. Mikulina, *Phys. Rev. B* **56**, 2285 (1997).

[42] T. Okuda, Y. Tomioka, A. Asamitsu, and Y. Tokura, *Phys. Rev. B*, **61** 8009 (200).

[43] K. Khazeni, Y.X. Jia, L. Lu, V.H. Crespi, M.L. Cohen, and A. Zettl, *Phys. Rev. Lett.* **76**, 295 (1996).

[44] K. Khazeni, Y.X. Jia, V.H. Crespi, L. Lu, A. Zettl, and M.L, Cohen, *J. Phys.-Condens. Mat.* **8**, 7723 (1996).

[45] H. Kuwahara, Y. Moritomo, Y. Tomioka, A. Asamitsu, M. Kasai, R. Kumai, and Y. Tokura, *Phys. Rev. B* **56**, 9386 (1997).

[46] Y.S. Wang, A.K. Heilman, B. Lorenz, Y.Y. Xue, C.W. Chu, J.P. Franck, and W.M. Chen, *Phys. Rev. B* **60**, R14998 (1999).

[47] B. Lorenz, A.K. Heilman, Y.S. Wang, Y.Y. Xue, C.W. Chu, G.Zhang, and J.P. Franck, *Phys. Rev. B* **63**, 144405 (2001).

[48] J.J. Nuemeier, M.F. Hundley, J.D. Thompson, and R.H. Heffner, *Phys. Rev. B* **52**, 7006 (1995).

[49] A. Congeduti, P. Postorino, E. Caramagno, M. Nardone, A. Kumar, and D.D. Sarma, *Phys. Rev. Lett.* **86**, 1251 (2001).

[50] P. Postorino, A. Congeduti, E. Degiorgi, J.P. Itie, and P. Munsch, *Phys. Rev. B* **65**, 224102 (2002).

[51] A. Congeduti, P. Postorino, P. Dore, A. Nucara, S. Lupi, S. Mercone, P. Calvani, A. Kumar, and D.D. Sarma, *Phys. Rev. B* **63**, 184410 (2001).

[52] C. Meneghini, D. Levy, S. Mobilio, M. Ortolani, M. Nuñez-Reguero, A. Kumar, and D.D. Sarma, *Phys. Rev. B* **65**, 012111 (2002).

[53] C. Cui, T.A. Tyson, Z. Zhong, J.P. Carlo, and Y. Qin, *Phys. Rev. B* **67**, 104107 (2003).

[54] C. Cui and T.A. Tyson, *Appl. Phys. Lett.* **83**, 2856 (2003).

[55] C. Cui, T.A. Tyson, Z. Chen, and Z. Zhong, *Phys. Rev. B* **68**, 214417 (2003).

[56] C. Cui and T.A. Tyson, *Appl. Phys. Lett.* **84**, 2856 (2004).

[57] C. Cui and T.A. Tyson, *Phys. Rev. B* **70**, 094409 (2004).

[58] D.P. Kozlenko, V.P. Glazkov, R.A. Sadykov, B.N. Savenko, V.I. Voronin, and I.V. Medvedeva, *J. Magn. Magn. Mater.* **258-259**, 290 (2003).

[59] D.P. Kozlenko, I.N. Goncharenko, B.N. Savenko, and V.I. Voronin, *J. Phys.-Condens. Mat.* **16**, 6755 (2004).

[60] A.M. Haghiri-Gosnet and J.P. Renard, *J. Phys. D Appl. Phys.* **36** R127 (2003).

[61] J.Z. Sun, D.W. Abraham, R.A. Rao, and C.B. Eom, *Appl. Phys. Lett.* **74**, 3017 (1999).

[62] H.S. Wang, E. Wertz, Y.F. Hu, Qi Li and D.G. Schlom, *J. Appl. Phys.* **87**, 7409 (2000).

[63] M. Bibes, L. Balcells, S. Valencia, J. Fontcuberta M. Wojcik, E. Jedryka, and S. Nadolski, *Phys. Rev. Lett.* **87**, 067210 (2001).

[64] M. Angeloni, G. Balestrino, N. Boggio, P.G. Medaglia, P. Orgiani, and A. Tebano, submitted to *J. Appl. Phys.*

[65] R.P. Borges, W. Guichard, J.G. Lunney, J.M.D. Coey, and F. Ott, *J. Appl. Phys.* **89**, 3868 (2001).

[66] M. Bibes, S. Valencia, L. Balcells, B. Martnez, J. Fontcuberta, M. Wojcik, S. Nadolski, and E. Jedryka, *Phys. Rev. B* **66**, 134416 (2002).

[67] G. Rousse, *Ordre de charge, Magnétisme et Electrochimie du spinelle $LiMn_2O_4$*, Ph.D. thesis, Univerité de Paris-Sud (2000).

[68] Y. Shimakawa, T. Numata, and J. Tabuchi, *J. Solid State Chem.* **131**, 138 (1997).

[69] C.C. Yang, S.Y. Wua, W.-H. Li, K.C. Lee, J.W. Lynn, R.S. Liu, and C.H. Shen, *Mat. Sci. Engin. B-Solid* **95**, 162 (2002).

[70] A. Yamada, *J. Solid State Chem.* **122**, 160 (1996).

[71] J. Rodriguez-Carvajal, G. Rousse, C. Masquelier, M. Hervieu, *Phys. Rev. Lett.* **81**, 4660 (1998).

[72] E. Wolska, P. Piszora, J. Darul, W. Nowicki, *J. Phys. Chem. Solids* **65**, 223 (2004).

[73] J. Goodenough, J.M. Longo, in *Magnetic and other properties of Oxides and Realted Compound*, edited by K.-H. Hellewege and A.M. Hellewege, Landolt-Borstein (Berlin 1970).

[74] Y. Syono, S. Akimoto, K. Kohn, *J. Phys. Soc. Jpn* **26**, 993 (1969).

[75] T. Negas, R. Roth, *J. Solid State Chem.* **1**, 409 (1970).

[76] T. Takeda, S. Ohara, *J. Phys. Soc. Jpn* **37**, 275 (1974).

[77] A. Sundaresan, J.L. Tholence, A. Maignan, C. Martin, M. Hervieu, B. Raveau, and E. Suard, *Eur. Phys. J. B.* **14**, 431 (2000).

[78] S. Hashimoto and H. Iwahara, *J. Electroceram.* **1**, 225 (2000).

[79] Y.S. Lee, T.W. Noh, J.H. Park, K.-B. Lee, G. Cao, J.E. Crow, M.K. Lee, C.B. Eom, E.J. Oh, and I.-S. Yang, *Phys. Rev. B*, **65**, 235113 (2002).

[80] A. Jayaraman, *Rev. Sci. Instrum.* **57**, 1013 (1986).

[81] C. Narayana, H. Luo, J. Orloff, and A.L. Ruoff, *Nature* **393**, 46 (1998).

[82] P. Dore, A. Nucara, D. Cannav, G. De Marzi, P. Calvani, A. Marcelli, R.S. Sussmann, A.J. Whitehead, C.N. Dodge, A.J. Krehan, and H.J. Peters, *Appl. Optics* **37**, 5731 (1998).

[83] G.J. Piermarini and S. Block, *Rev. Sci. Instrum.* **46**, 973 (1975).

[84] H.K. Mao, J. Xu, and P.M. Bell, *J. Geophys. Res.* **91**, 4673 (1986).

[85] D.R. Ragan, R. Gustacsen, and D. Schieferl, *J. Appl. Phys.* **72**, 5539 (1992).

[86] B. Chen, D.V.S. Muthu, Z.X. Liu, A.W. Sleight, and M.B. Kruger, *Phys. Rev. B* **64**, 214111 (2001).

[87] M.N. Iliev, M.V. Abrashev, H.G. Lee, V.N. Popov, Y.Y. Sun, C. Thomsen, R.L. Meng, and C.W. Chu, *Phys. Rev. B.* **57**, 2872 (1998).

[88] E. Liarokapis, T. Leventouri, D. Lampakis, D. Palles, J.J. Neumeier, and D.H. Goodwin, *Phys. Rev. B* **60**, 12758 (1999).

[89] M.N. Iliev, M.V. Abrashev, V.N. Popov, and V.G. Hadjiev, *Phys. Rev. B* **67**, 212301 (2003).

[90] V.B. Podobedov, A. Weber, D.B. Romero, J.P. Rice, and H.D. Drew, *Phys. Rev. B* **58**, 43 (1998).

[91] L. Martin-Carron, A. de Andres, M.J. Martinez-Lope, M.T. Casais, and J. A. Alonso, *Phys. Rev. B* **66**, 174303 (2002).

[92] S. Yoon, H.L. Liu, G. Schollerer, S.L. Cooper, P.D. Han, D.A. Payne, S.-W. Cheong, Z. Fisk, *Phys. Rev. B* **58**, 2795 (1998).

[93] E. Granado, N.O. Moreno, A. Garcia, J.A. Sanjurjo, C. Rettori, I. Torriani, S.B. Oseroff, J.J. Neumeier, K.J. McClellan, and S.-W. Cheong, Y. Tokura, *Phys. Rev. B* **58**, 11435 (1998).

[94] A.E. Pantoja, H.J. Trodahl, R.G. Buckley, Y. Tomioka, and Y. Tokura, *J. Phys.-Condens. Mat.* **13**, 3741 (2001).

[95] P.X. Zhang, S.J. Huang, H.U. Habermeier, and G.M. Zhao, *J. Raman Spectrosc.* **32**, 812 (2001).

[96] H.J. Lee, J.H. Jung, Y.S. Lee, J.S. Ahn, T.W. Noh, K.H. Kim, and S.-W. Cheong, *Phys. Rev. B* **60**, 5251 (1999).

[97] M. Quijada, J. Cerne, J.R. Simpson, H.D. Drew, K.H. Ahn, A.J. Millis, R. Shreekala, R. Ramesh, M. Rajeswari, T. Venkatesan, *Phys. Rev. B* **58**, 16093 (1998).

[98] E. Saitoh, Y. Okimoto, Y. Tomioka, T. Katsufuji, Y. Tokura, *Phys. Rev. B* **60**, 10362 (1999).

[99] K.H. Kim, J.H. Jung, and T.W. Noh, *Phys. Rev. Lett.* **81**, 1517 (1997).

[100] S.G. Kaplan, M. Quijada, H.D. Drew, D.B. Tanner, G.C. Xiong, R. Ramesh, C. Kwon, and T. Venkatesan, *Phys. Rev. Lett.* **77**, 2081 (1996).

[101] A. Paolone, P. Giura, P. Calvani, P. Dore, S. Lupi, P. Maselli, *Physica B* **244**, 33 (1998).

[102] K.H. Kim, J.Y. Gu, H.S. Choi, G.W. Park, and T.W. Noh, *Phys. Rev. Lett.* **77**, 1877 (1996).

[103] A.V. Boris, N.N. Kovaleva, A.V. Bazhenov, P.J.M. Van Bentum, Th. Rasing, S.-W. Cheong, A.V. Salimov, N.-C. Yeh, *Phys. Rev. B* **59**, R697 (1999).

[104] J.P. Franck, I. Isaac, W. Chen, J. Chrzanowski, J.C. Irwin, and C.C. Homes, *J. Supercond.* **12**, 263 (1999).

[105] F. Gao, R.A. Lewis, X.L. Wang, and S.X. Dou, *J. Alloy. Compd.* **347**, 314 (2002).

[106] P.B. Allen and V. Perebeinos, *Phys. Rev. Lett.* **83**, 4828 (1999).

[107] M. Capone and S. Ciuchi, *Phys. Rev. B* **65**, 104409 (2002).

[108] F. De Pasquale, S. Ciuchi, J. Bellissard, and D. Feinberg, *Reviews of Solid State Science* edited by A. K. Gupta, S. K. Joshi, and C.N.R. Rao (World Scientific, Singapore, 1988), Vol. **2**, p. 443; J. Ranninger and U. Thibblin, *Phys. Rev. B* **45**, 7730 (1992); M. Acquarone, J.R. Iglesias, M. A. Gusmão, C. Noce, and A. Romano, *ibid.* **58**, 7626 (1998); E.V.L. De Mello and J. Ranninger, *ibid.* **55**, 14872 (1997).

[109] S. Satpathy, *Sol. State Comm.* **112**, 195 (1999); M. Mitra, P. A. Sreeram, and S. Dattagupta, *Phys. Rev. B* **67**, 132406 (2003).

[110] A. Georges, G. Kotliar, W. Krauth, and M. J. Rozenberg, *Rev. Mod. Phys.* **68**, 13 (1996).

[111] A. J. Millis, R. Mueller, and B. I. Shraiman, *Phys. Rev. B* **54**, 5405 (1996).

[112] J. W. Liu, Z. Zheng, Q. Q. Zheng, H. Q. Lin, and H. K. Wong, *J. Appl. Phys.* **85**, 5426 (1999).

[113] S. Cunsolo, P. Dore, S. Lupi, P. Maselli, and C.P. Varsamis, *Infrared Phys. Techn.* **33**, 539 (1992).

[114] P. Berberich, M. Chiusuri, S. Cunsolo, P. Dore, H. Kinder, and C.P. Varsamis, *Infrared Phys. Techn.* **34**, 269 (1993).

[115] P. Dore, A. Paolone, and R. Trippetti, *J. Appl. Phys.* **80**, 5270 (1996); P. Dore, G. De Marzi, and A. Paolone, *Int. J. Infrared Milli.* **18**, 125 (1997).

[116] F. Wooten, *Optical Properties of Solids*, Academic Press, London (1972).

[117] A. de Andres, J. Rubio, G. Castro, S. Taboada, J.L. Martinez, and J.M. Colino, *Appl. Phys. Lett.* **83**, 713 (2003).

[118] M. N. Iliev and M.V. Abrashev, *J. Raman Spectrosc.* **32**, 805 (2001).

[119] V.B. Podobedov, A. Weber, D.B. Romero, J.P. Rice, and H.D. Drew, *Solid State Commun.* **105**, 589 (1998).

[120] N.M. Souza-Neta, A.Y. Ramos, H.C. N. Tolentino, E. Favre-Nicolin, and L. Ranno, *Appl. Phys. Lett.* **83**, 3587 (2003).

[121] A. Waśkowska, L. Gerward, J. Staun Olsen, S. Steenstrup, and E. Talik, *J. Phys.-Condens. Mat.* **13**, 2549 (2001); S. Åsbrink, A. Waśkowska, J. Staun Olsen, L. Gerward, *Phys. Rev. B* **57**, 4972 (1998); S. Åsbrink, A. Waśkowska, L. Gerward, J. Staun Olsen, and E. Talik, *ibid.* **60**, 12651 (1999); Z.W. Wang, S.K. Saxena, and C.S. Zha, *ibid.* **66**, 024103 (2002); Zhongwu Wang, R.T. Downs, V. Pischedda, R. Shetty, S.K. Saxena, C.S. Zha, Y.S. Zhao, D. Schiferl, and A. Waśkowska, *ibid.* **68**, 094101 (2003); D. Levy, A. Pavese, and M. Hanfland, *Phys. Chem. Miner.* **27**, 638 (2000); D. Andrault and N. Bolfan-Casanova, *ibid.* **28**, 211 (2001); Y.W. Fei, D.J. Frost, H.K. Mao, C.T. Prewitt, and D. Hausermann, *Am. Mineral.* **84**, 203 (1999); C. Haavik, S. Stolen, H. Fjellvag, M. Hanfland, and D. Hausermann, *ibid.* **85**, 514 (2000); Z.W. Wang, P. Lazor, S.K. Saxena, and H.S.C. O'Neill, *Mater. Res. Bull.* **37**, 1589 (2002).

[122] S. Chitra, P. Kalyani, T. Mohan, R. Gangadharan, B. Yebka, S. Castro-Garcia, M. Massot, C. Julien, and M. Eddrieff, *J. Electroceram.* **3-4**, 433 (1999); W. Huang and R. Frech, *J. Power Sources* **81-82**, 616 (1999); C. Julien, E. Haro-Poniatowski, M.A. Camacho-Lopez, L. Escobar-Alarcon, and J. Jimenez-Jarquin, *Mat. Sci. Engin. B-Solid* **72** , 36 (2000); S. Nieto-Ramos and M.S. Tomar, *Int. J. Hydrogen Energ.* **26**, 159 (2001); S.R.S. Prabaharan, N.B. Saparil, S.S. Michael, M. Massot, C. Julien, *Solid State Ionics* **112**, 25 (1998); C. Wu, Z. Wang, F. Wu, L. Chen, and X. Huang, *ibid.* **144**, 277 (2001); N. Anzue, T. Itoh, M. Mohamedi, M. Umeda, and I. Uchida, *ibid.* **156**, 301 (2003).

[123] S.J. Hwang, D.H. Park, J.H. Choy, G. Campet, *J. Phys. Chem. B* **108**, 12713 (2004).

[124] J.M. Tarascon and D. Guyomard, *Electrochim. Acta* **38**, 1221 (1993); M.M. Tackeray, M.F. Masueto, D.W. Dees, and D.R. Vissers, *Mater. Res. Bull.* **31**, 133 (1996); M.M. Tackeray, *Prog. Solid State Ch.* **25**, 1 (1997); A. Yamada, K. Miura, K. Hinokuma, and M. Tanaka, *J. Electrochem. Soc.* **142**, 2149 (1995).

[125] V. Massarotti, D. Capsoni, and M. Bini, *Solid State Commun.* **122**, 317 (2002).

[126] B. Ammundsen, G.R. Burns, M. Saiful Islam, H. Kanoh, and J. Rozière, *J. Phys. Chem. B* **103**, 5175 (1999).

[127] W.G. Fately, F.R. Dollish, N.T. McDevitt, F.F. Bentley, *Infrared and Raman selection rules for molecular and lattice vibrations: the correlation method* John Wiley & Sons (New York, 1972).

[128] J. Heiras, E. Pichardo, A. Mahmood, T. Lopez, R. Perez-Salas, J.M. Siqueiros, O. Blanco, and M. Castellanos, *J. Phys. Chem. Solids* **63**, 591 (2002).

[129] H. Fujishiro, M. Ikebe, T. Kikuchi, and H. Ozawa, *Physica B* **281& 282**, 491 (2000).

[130] J. Mira, J. Rivas, L.E. Hueso, F. Rivadulla, M.A. Lopez Quintela, M.A. Señaris Rodriguez, and C. A. Ramos, *Phys. Rev. B* **65**, 024418 (2001).

Acknowledgments

The real number of persons I should acknowledge for their contribution to this work is so large that a complete list would be probably larger than the entire thesis. Therefore I first acknowledge all the people I will forget to mention in the following.

I am gratefully indebted to Paolo Postorino for teaching, supporting, and supervising me during the three years of the Ph.D. and for critical revising of the thesis. For the same reasons I thank Paolo Dore whose contribution was indispensable. I want to thank the colleagues of the IRS group in our department: Paolo Calvani, Stefano Lupi, Alessandro Nucara, Mariangela Cestelli and Michele Ortolani for fruitful collaboration and helpful discussions. Thanks are due to the other young researchers of our group: Daniele Di Castro, Emanuele Arcangeletti, Maria Baldini, Tommaso Corridoni, Rosario Giambelluca, and Michela Lavagnini for their collaboration. I want to thank for fruitful collaboration and warm hospitality the colleagues in Florence: Lorenzo Ulivi and Federico Gorelli, in Frascati: Claudio Marcelli and Massimo Piccinini, and in Paris: Jean-Paul Itié, Alberta Congeduti, and Pascal Munch. I also thank Annalisa Paolone for the scientific collaboration.

I gratefully thank my family and in particular my mother and my father for supporting me all long these years and for teaching me the pleasure of knowledge. I also thank my aunt Paola for hosting me during the last 7 years.

I gratefully thank my friends... at least those who proved to be TRUE friends: Camillo, Carla, Corradino, Marco, and Serena.

A very special acknowledgment, with infinite love, is for the best fuel for the engine of my hearth: Beatrice. There are no words to describe the importance of the role she played in this work and in the last two years of my life, in general.

Finally I want to thank my beloved cousin Sara, for teaching me loving life and never stop fighting... never. I still miss her a lot.